# Microstructure evolution in functional magnetic materials

von der Fakultät Maschinenbau
der Technischen Universität Dortmund
zur Erlangung des akademischen Grades

**Doktor-Ingenieur (Dr.-Ing.)**

genehmigte Dissertation

von

**Karsten Buckmann**

aus Datteln

| | |
|---|---|
| Referent: | Prof. Dr.-Ing. A. Menzel |
| Korreferenten: | Prof. Dipl.-Ing. B. Kiefer, Ph. D. |
| | Prof. Dr.-Ing. F. Walther |
| Tag der Einreichung: | 08.01.2019 |
| Tag der mündlichen Prüfung: | 12.04.2019 |

**Bibliografische Information Der Deutschen Bibliothek**
Die Deutsche Bibliothek verzeichnet diese Publikation in der Deutschen Nationalbibliografie; detaillierte bibliografische Daten sind im Internet über **http://dnb.ddb.de** abrufbar.

**Bibliographic information published by Die Deutsche Bibliothek**
Die Deutsche Bibliothek lists this publication in the Deutsche Nationalbibliografie; detailed bibliographic data is available in the Internet at **http://dnb.ddb.de**.

Schriftenreihe des Instituts für Mechanik

Herausgeber: Institut für Mechanik
Fakultät Maschinenbau
Technische Universität Dortmund
Leonhard-Euler-Str. 5
D-44227 Dortmund

Druck: Koffler DruckManagement GmbH

© by Karsten Buckmann 2019

This work is subject to copyright. All rights are reserved, whether the whole or part of the material is concerned, specifically the rights of translation, reprinting, reuse of illustrations, recitation, broadcasting, reproduction on microfilm or in any other way, and storage in data banks. Duplication of this publication or parts thereof is permitted in connection with reviews or scholarly analysis. Permission for use must always be obtained from the author.

Alle Rechte vorbehalten, auch das des auszugsweisen Nachdrucks, der auszugsweisen oder vollständigen Wiedergabe (Photographie, Mikroskopie), der Speicherung in Datenverarbeitungsanlagen und das der Übersetzung.

Als Manuskript gedruckt. Printed in Germany.

ISSN 2191-0022
ISBN 978-3-947323-09-8

# Acknowledgements

This thesis is based on my work as a research assistant at the Institute of Mechanics at TU Dortmund university from September 2012 to August 2018. At this point I would like to thank some people.

First of all I would like to thank my supervisor Professor Andreas Menzel for the many years of cooperation and good support, which began with my employment as a student assistant in May 2008. In particular, his enthusiasm and the great working atmosphere at the Institute of Mechanics encouraged me at the end of my studies to take a closer look at mechanics. I am deeply thankful for his lasting trust in me.

Furthermore, I would like to thank Professor Björn Kiefer, also for many years of cooperation and intense support, especially during the time of my diploma thesis and the following first years of my time as a research assistant. The time we spent together from the beginning of 2011, first in the context of exercises and tutorials and then due to his supervision—especially of my research work—until his appointment in 2016, has left a lasting impression on me. Without his support and the always helpful discussions, this work would not have been possible.

I would like to thank Professor Frank Walther for his interest in my research work and for acting as third referee of my thesis. I would like to thank Dr. Andreas Zabel for taking over the chairmanship of the examination committee.

My thanks also go to Dr. Thorsten Bartel who has become an integral part of the institute with his entrance in 2008. I will have good memories of the many discussions, also beyond the field of mechanics. I do not know anyone who can distinguish so well between private and professional fields. I am also very thankful for his support during my time as a research assistant.

I would also like to take this opportunity to thank Dr. Vadim Palnau. The joint educational activities that began with my employment as a student assistant in 2008 also had a lasting influence on me. Through his supervision of my student research project, my interest in further exploring the field of mechanics has increased.

Kerstin Walter and Christina McDonagh have made a significant contribution to the excellent atmosphere at the institute through their work, in particular due to the organisation of excursions, joint breakfasts, and Christmas parties. Kerstin Walter was always the first contact person for administrative questions. I would like to thank Christina McDonagh for proofreading this thesis. I thank Matthias Weiss for his support and help in the area of IT. A solution for each of my problems could always be found.

I would like to take this opportunity to thank my two former office colleagues for the time we spent together. I shared an office with Dr. Dinesh Dusthakar for over four years.

Besides many discussions on a professional level, a real friendship developed during this time. I always have positive memories of the evenings and business trips we had together. I would also like to thank Robin Schulte for his pleasant and sociable manner. I like to remember the discussions we had together on a professional and private level.

I would also like to thank Professor Jörn Mosler. In my opinion, his leadership and the integration of his co-workers have created a large joint institute rather than two separate groups.

I would like to thank all other current and former employees of the institute for their professional manner, the many common moments, and the discussions in the kitchen, also beyond the topic of mechanics. Dr. Alexander Bartels and Rolf Berthelsen deserve special mention. I have always enjoyed spending time together, also outside the institute.

I would like to express my deepest gratitude to my friends. Some of them have been with me for almost all of my life. Especially during the past years as a research assistant, I have learned what it means to have real friends. I hope our friendship will last forever.

Last but not least I would like to thank my family and my girlfriend very much. I will never forget your moral support, especially during the time I worked on this document.

Dortmund, May 2019 Karsten Buckmann

# Zusammenfassung

Die vorliegende Arbeit befasst sich mit der Modellierung und Simulation der Mikrostrukturentwicklung in funktionalen magnetischen Materialien, insbesondere in magnetischen Formgedächtnislegierungen (MSMAs). Das Ziel der Arbeit ist die Entwicklung eines Materialmodells, in dem Informationen über die Mikrostruktur in einem effektiven Sinne erfasst werden, und dessen Einbettung in die Finite Elemente Methode (FEM). Zunächst wird ein mikromagnetisch inspirierter variationeller Modellierungsrahmen eingeführt. Die zugrunde liegende Mikrostruktur wird parametrisiert und sowohl zugehörige Energiedichten als auch Dissipationsfunktionale werden spezifiziert. Dabei wird unter anderem das Konzept der Energierelaxierung angewandt. Mit Hilfe von Demagnetisierungsfaktoren lassen sich makroskopisch homogene Zustände simulieren und die Eigenschaften des Materialmodells untersuchen. Anschließend liegt der Fokus auf der Implementierung solcher Materialmodelle in die FEM. In dem vorgeschlagenen Ansatz werden unter anderem Zustandsvariablen als globale Feldgrößen aufgelöst und Ungleichheits-Nebenbedingungen auf globaler Ebene berücksichtigt. Anhand von magnetostatischen und darauf aufbauenden vollständig gekoppelten Simulationen werden die Vorteile der FEM demonstriert.

# Abstract

This thesis deals with the modelling and simulation of the microstructure evolution in functional magnetic materials, especially in magnetic shape memory alloys (MSMAs). The objective of this work is the development of a material model, where information regarding the microstructure is taken into account in an effective sense, and its embedding into the finite element method (FEM). Firstly, a micromagnetics-inspired variational modelling framework is introduced. The underlying microstructure is parametrised and the corresponding energy densities as well as dissipation functionals are specified. Amongst others, the concept of energy relaxation is applied. Using demagnetisation factors, macroscopically homogeneous states are simulated and the properties of the material model are analysed. Afterwards, the focus lies on the implementation of such material models into the FEM. In the proposed approach, state variables are resolved as global fields and inequality constraints are taken into account on the global level. The advantages of the FEM is demonstrated for magnetostatic simulations and—based on them—fully coupled simulations.

# Publications

Key parts of this thesis are based on three peer-reviewed journal articles and one book contribution, which were either published or submitted during the progress of this doctoral work. The original articles are partially modified wherever it is considered necessary.

1. B. Kiefer, K. Buckmann, and T. Bartel:

   *Numerical energy relaxation to model microstructure evolution in functional magnetic materials*, GAMM-Mitteilungen, 38(1):171–196, 2015 [112].

2. B. Kiefer, T. Bartel, and K. Buckmann:

   *A variational framework for the modeling of phase transforming solids using energy relaxation methods — application to conventional and magnetic SMA*, submitted for publication, 2016 [114].

3. T. Bartel, B. Kiefer, K. Buckmann, and A. Menzel:

   *An energy-relaxation-based framework for the modelling of magnetic shape memory alloys — simulation of key response features under homogeneous loading conditions*, submitted for publication, 2018 [10].

4. K. Buckmann, B. Kiefer, T. Bartel, and A. Menzel:

   *Simulation of magnetised microstructure evolution based on a micromagnetics-inspired FE framework: application to magnetic shape memory behaviour*, available online, 2018 [21].

The articles were prepared in collaboration with two or three co-authors. The author of this thesis contributed essential aspects with regard to the outline of the theory in [10, 21], carried out the numerical implementation and simulations completely in [10, 21, 112], respectively partially in [114], and contributed essential parts to the preparation of all contributions listed above.

# Contents

**Notation** ix

**1 Introduction** 1

1.1 Magnetic functional materials . . . . . . . . . . . . . . . . . . . . . . . . . 1
1.2 Modelling approaches . . . . . . . . . . . . . . . . . . . . . . . . . . . . . 12
1.3 Structure of the thesis . . . . . . . . . . . . . . . . . . . . . . . . . . . . 15

**2 An energy relaxation-based MSMA model** 17

2.1 Variational framework . . . . . . . . . . . . . . . . . . . . . . . . . . . . 18
  2.1.1 Global field variables . . . . . . . . . . . . . . . . . . . . . . . . . 18
  2.1.2 Continuous variational principle . . . . . . . . . . . . . . . . . . . 18
  2.1.3 Incremental variational principle . . . . . . . . . . . . . . . . . . . 21
  2.1.4 Simplifications for homogeneous problems . . . . . . . . . . . . . 22
2.2 Constitutive framework . . . . . . . . . . . . . . . . . . . . . . . . . . . 24
  2.2.1 General aspects of quasiconvexity . . . . . . . . . . . . . . . . . . 24
  2.2.2 Representation of MSMA microstructure . . . . . . . . . . . . . . 25
  2.2.3 Specific constitutive model . . . . . . . . . . . . . . . . . . . . . . 30
  2.2.4 Summary of constitutive equations . . . . . . . . . . . . . . . . . 34
2.3 Numerical examples . . . . . . . . . . . . . . . . . . . . . . . . . . . . . 35
  2.3.1 Variant switching diagrams . . . . . . . . . . . . . . . . . . . . . . 35
  2.3.2 The connection of effective material responses to microstructure evolution . . . . . . . . . . . . . . . . . . . . . . . . . . . . . . . 43
  2.3.3 The influence of the shape anisotropy and a closer look at the demagnetisation effect . . . . . . . . . . . . . . . . . . . . . . . . 47
2.4 Summary and outlook . . . . . . . . . . . . . . . . . . . . . . . . . . . . 49
2.5 Appendix . . . . . . . . . . . . . . . . . . . . . . . . . . . . . . . . . . . 50
  2.5.1 Dependencies among the domain magnetisations . . . . . . . . . . 50
  2.5.2 Analysis of the martensite twin boundary orientation . . . . . . . 52

**3 A micromagnetics-inspired FE-framework — spatial resolution of magnetic degrees of freedom** 55

3.1 Variational framework . . . . . . . . . . . . . . . . . . . . . . . . . . . . 56
3.2 Constitutive model . . . . . . . . . . . . . . . . . . . . . . . . . . . . . . 60
3.3 Finite element discretisation . . . . . . . . . . . . . . . . . . . . . . . . . 64

3.4 Numerical examples . . . . . . . . . . . . . . . . . . . . . . . . . . . . . 70
3.5 Summary and outlook . . . . . . . . . . . . . . . . . . . . . . . . . . . 80
3.6 Appendix . . . . . . . . . . . . . . . . . . . . . . . . . . . . . . . . . . 80

**4 A micromagnetics-inspired FE-framework — spatial resolution of mechanical and magnetic degrees of freedom 83**
4.1 Variational framework . . . . . . . . . . . . . . . . . . . . . . . . . . . 84
4.2 Constitutive model . . . . . . . . . . . . . . . . . . . . . . . . . . . . . 90
4.3 Implementation and algorithmic treatment . . . . . . . . . . . . . . . . . 101
4.4 Numerical examples . . . . . . . . . . . . . . . . . . . . . . . . . . . . . 114
  4.4.1 Magnetic field-induced easy- and hard-axis magnetisation response 115
  4.4.2 Magnetic field-induced martensite reorientation . . . . . . . . . . 120
  4.4.3 Stress level dependency of the magnetic field-induced response behaviour . . . . . . . . . . . . . . . . . . . . . . . . . . . . . . . 127
  4.4.4 Stress-induced martensite reorientation under constant magnetic field . . . . . . . . . . . . . . . . . . . . . . . . . . . . . . . . . 132
  4.4.5 Biaxial magnetic field-induced martensite reorientation . . . . . . 135
  4.4.6 Investigation of a complex geometry . . . . . . . . . . . . . . . . 141
4.5 Summary and outlook . . . . . . . . . . . . . . . . . . . . . . . . . . . 144
4.6 Appendix . . . . . . . . . . . . . . . . . . . . . . . . . . . . . . . . . . 145
  4.6.1 Dependencies among the domain magnetisations . . . . . . . . . . 145
  4.6.2 Constitutive driver routine . . . . . . . . . . . . . . . . . . . . . . 146
  4.6.3 Shape functions . . . . . . . . . . . . . . . . . . . . . . . . . . . . 152
  4.6.4 Stiffness matrix contributions . . . . . . . . . . . . . . . . . . . . 153

**5 Concluding remarks 157**

**Bibliography 161**

# Notation

Most of the notations used in this thesis become obvious from the context. For the sake of the reader's convenience, the essential relations are briefly summarised below. Here, Einstein's summation convention is used for a compact representation.

**Tensors** The three-dimensional Euclidean space is represented by a set of basis vectors $\{\boldsymbol{e}_i\}$, with $i = 1, 2, 3$. First- to fourth-order tensors are expressed in terms of their coefficients by

$$
\begin{aligned}
\boldsymbol{a} &\mathrel{\widehat{=}} a_i \, \boldsymbol{e}_i && \text{(first-order tensor)} \ , \\
\boldsymbol{A} &\mathrel{\widehat{=}} A_{ij} \, \boldsymbol{e}_i \otimes \boldsymbol{e}_j && \text{(second-order tensor)} \ , \\
\boldsymbol{\mathsf{a}} &\mathrel{\widehat{=}} a_{ijk} \, \boldsymbol{e}_i \otimes \boldsymbol{e}_j \otimes \boldsymbol{e}_k && \text{(third-order tensor)} \ , \\
\boldsymbol{\mathsf{A}} &\mathrel{\widehat{=}} A_{ijkl} \, \boldsymbol{e}_i \otimes \boldsymbol{e}_j \otimes \boldsymbol{e}_k \otimes \boldsymbol{e}_l && \text{(fourth-order tensor)} \ .
\end{aligned}
$$

Non-bold letters are used for scalars, bold-face lower-case italic letters for vectors and first-order tensors, bold-face upper-case italic letters for second-order tensors, bold-face lower-case sans-serif letters for third-order tensors, and bold-face upper-case sans-serif letters for fourth-order tensors.

**Inner tensor products** Inner tensor products are represented by dots. The number of dots is equivalent to the number of contractions, e.g.

$$
\begin{aligned}
\boldsymbol{a} \cdot \boldsymbol{b} &\mathrel{\widehat{=}} a_i \, b_i \ , \\
\boldsymbol{A} \cdot \boldsymbol{b} &\mathrel{\widehat{=}} A_{ij} \, b_j \, \boldsymbol{e}_i \ , \\
\boldsymbol{A} \cdot \boldsymbol{B} &\mathrel{\widehat{=}} A_{ij} \, B_{jk} \, \boldsymbol{e}_i \otimes \boldsymbol{e}_k \ , \\
\boldsymbol{A} : \boldsymbol{B} &\mathrel{\widehat{=}} A_{ij} \, B_{ij} \ , \\
\boldsymbol{\mathsf{A}} : \boldsymbol{B} &\mathrel{\widehat{=}} A_{ijkl} \, B_{kl} \, \boldsymbol{e}_i \otimes \boldsymbol{e}_j \ .
\end{aligned}
$$

The colon is used for a contraction of a pair of neighbouring indices. A scalar results for the special case of $n$-fold contraction of two $n$-th-order tensors.

**Outer tensor products** Outer tensor products, respectively dyadic products, are represented by the symbol $\otimes$. The non-standard symbols $\overline{\otimes}$ and $\underline{\otimes}$ are used for special tensor products for pairs of second-order tensors.

$$
\begin{aligned}
\boldsymbol{a} \otimes \boldsymbol{b} &\mathrel{\widehat{=}} a_i \, b_j \, \boldsymbol{e}_i \otimes \boldsymbol{e}_j \ , \\
\boldsymbol{A} \otimes \boldsymbol{b} &\mathrel{\widehat{=}} A_{ij} \, b_k \, \boldsymbol{e}_i \otimes \boldsymbol{e}_j \otimes \boldsymbol{e}_k \ , \\
\boldsymbol{A} \otimes \boldsymbol{B} &\mathrel{\widehat{=}} A_{ij} \, B_{kl} \, \boldsymbol{e}_i \otimes \boldsymbol{e}_j \otimes \boldsymbol{e}_k \otimes \boldsymbol{e}_l \ , \\
\boldsymbol{A} \, \overline{\otimes} \, \boldsymbol{B} &\mathrel{\widehat{=}} A_{ik} \, B_{jl} \, \boldsymbol{e}_i \otimes \boldsymbol{e}_j \otimes \boldsymbol{e}_k \otimes \boldsymbol{e}_l \ , \\
\boldsymbol{A} \, \underline{\otimes} \, \boldsymbol{B} &\mathrel{\widehat{=}} A_{il} \, B_{jk} \, \boldsymbol{e}_i \otimes \boldsymbol{e}_j \otimes \boldsymbol{e}_k \otimes \boldsymbol{e}_l \ .
\end{aligned}
$$

**Identity tensors** The second-order identity tensor $\boldsymbol{I}$ is

$$
\boldsymbol{I} \mathrel{\widehat{=}} \delta_{ij} \, \boldsymbol{e}_i \otimes \boldsymbol{e}_j \ ,
$$

wherein $\delta_{ij} \mathrel{\widehat{=}} \boldsymbol{e}_i \cdot \boldsymbol{e}_j$ is the Kronecker delta with $\delta_{ij} = 1$ for $i = j$ and otherwise $\delta_{ij} = 0$. The fourth-order symmetric $\boldsymbol{\mathsf{I}}_{\mathrm{sym}}$, volumetric $\boldsymbol{\mathsf{I}}_{\mathrm{vol}}$, and deviatoric $\boldsymbol{\mathsf{I}}_{\mathrm{dev}}$ identity tensors are specified using the tensor products introduced above as

$$
\begin{aligned}
\boldsymbol{\mathsf{I}}_{\mathrm{sym}} &= \frac{1}{2} \left[ \boldsymbol{I} \, \overline{\otimes} \, \boldsymbol{I} + \boldsymbol{I} \, \underline{\otimes} \, \boldsymbol{I} \right] \ , \\
\boldsymbol{\mathsf{I}}_{\mathrm{vol}} &= \frac{1}{3} \left[ \boldsymbol{I} \otimes \boldsymbol{I} \right] \ , \\
\boldsymbol{\mathsf{I}}_{\mathrm{dev}} &= \boldsymbol{\mathsf{I}}_{\mathrm{sym}} - \boldsymbol{\mathsf{I}}_{\mathrm{vol}} \ .
\end{aligned}
$$

**Operators** In the following, a comma is used to represent the partial derivative of a quantity w.r.t. $\boldsymbol{x}_\bullet$. The symbol $\nabla_{\boldsymbol{x}}$ represents the Nabla operator.
The (spatial) gradient of a scalar or tensor is represented by, e.g.,

$$
\nabla_{\boldsymbol{x}} a \mathrel{\widehat{=}} a_{,i} \, \boldsymbol{e}_i \ , \quad \nabla_{\boldsymbol{x}} \boldsymbol{a} \mathrel{\widehat{=}} a_{i,j} \, \boldsymbol{e}_i \otimes \boldsymbol{e}_j \ , \quad \nabla_{\boldsymbol{x}} \boldsymbol{A} \mathrel{\widehat{=}} A_{ij,k} \, \boldsymbol{e}_i \otimes \boldsymbol{e}_j \otimes \boldsymbol{e}_k \ .
$$

The (right) divergence of a first- and second-order tensor is represented by

$$
\mathrm{div}_{\boldsymbol{x}} \boldsymbol{a} = \nabla_{\boldsymbol{x}} \cdot \boldsymbol{a} \mathrel{\widehat{=}} a_{i,i} \ , \quad \mathrm{div}_{\boldsymbol{x}} \boldsymbol{A} = \nabla_{\boldsymbol{x}} \cdot \boldsymbol{A} \mathrel{\widehat{=}} A_{ij,j} \, \boldsymbol{e}_i \ .
$$

The (right) curl of a first- and second-order tensor is represented by

$$
\mathrm{curl}_{\boldsymbol{x}} \boldsymbol{a} = \nabla_{\boldsymbol{x}} \times \boldsymbol{a} \mathrel{\widehat{=}} - a_{i,j} \, \epsilon_{ijk} \, \boldsymbol{e}_k \ , \quad \mathrm{curl}_{\boldsymbol{x}} \boldsymbol{A} = \nabla_{\boldsymbol{x}} \times \boldsymbol{A} \mathrel{\widehat{=}} - A_{ij,k} \, \epsilon_{jkl} \, \boldsymbol{e}_i \otimes \boldsymbol{e}_l \ ,
$$

wherein $\epsilon_{ijk}$ is the Levi-Civita symbol with $\epsilon_{ijk} = 1$ for $i, j, k$ being an even permutation and $\epsilon_{ijk} = -1$ for $i, j, k$ being an odd permutation.

# 1 Introduction

The present thesis is based on work that was carried out in the context of the research unit *FOR 1509: Ferroic Functional Materials* funded by the German Research Foundation (DFG). The research unit has set itself the goal of achieving a new quality in the modelling, simulation, and experimental characterisation of multifield couplings in multiferroic materials across various length scales, see [1]. Project P7 focusses on the modelling of the effect of microstructure evolution in magnetostrictive materials using numerical energy relaxation approaches. In this chapter, a brief introduction to magnetic functional materials and, in particular, magnetic shape memory alloys (MSMAs) is presented, followed by a short summary of established modelling approaches. The structure of the thesis is outlined at the end of this chapter.

## 1.1 Magnetic functional materials

According to [112], functional materials are by definition materials that provide additional engineering functionality due to intrinsic properties on top of the usual structural requirements. Typical applications are their use as sensors, actuators, or energy harvesters. One subclass of these materials are magnetic functional materials, in particular magnetostrictive materials that are used in sensors, actuators, transducers, or to store information, see [47, 214]. The magnetic field-induced strain in giant magnetostrictive materials is approximately two orders of magnitude above the strain that is observable in magnetostrictive elements, such as iron. Typical examples are Terfenol-D [37, 149] and Galfenol [102]. Due to the commercial availability of these materials, the research interest has increased during the last years. Exemplary applications are the use as magnetostrictive transducers in the cutting head of a milling machine to achieve tolerances of approximately $1\,\mu$m at frequencies in the kHz region, see [192]. Other applications are their use in sonar equipment due to the greater bandwidth, reliability, and reduced transducer size and weight, see [2], or in high pressure fuel injectors [184], see also [48]. Another group of materials that recently gained much research interest is the group of (multi)ferroic materials. Ferroic materials exhibit a spontaneous magnetisation (ferromagnetics), a spontaneous polarisation (ferroelectrics), or a spontaneous straining (ferroelastics). They are promising canditates for the development of novel applications that require functional materials. Multiferroics typically occur in composite form and are designed to have desired, e.g. magnetoelectrical, coupling properties. The individual constituents are usually weakly coupled or even uncoupled, see [48]. Magnetic shape memory alloys, however, are intrinsically multiferroic materials, since a spontaneous straining and a spontaneous magnetisation occurs, when below both the phase transformation and Curie temperatures. The probably best-known MSMA is $Ni_2MnGa$, where magnetic field-induced strains of up to 6–10 % [74, 90, 106, 134, 160, 164, 172, 195, 197, 200] in a large bandwidth of up to 1–2 kHz [25, 79, 106, 139, 209, 210], respectively 5 kHz in thin films [192], have been reported in the literature. In addition to strong magnetomechanical coupling, they possess the conventional shape memory effect. Due to their nonlinear, hysteretic, and highly stress level-dependent response behaviour under combined magnetomechanical loading conditions, $Ni_2MnGa$ is considered to be a challenging model problem. For the development of, e.g., actuator and sensor applications, modelling approaches are required which can accurately predict the real material behaviour and which are, moreover, numerically robust. Major parts of this work focus on the modelling and simulation of magnetomechanically coupled materials, in particular $Ni_2MnGa$ single crystals. The shape dependent demagnetisation effect that heavily influences the response behaviour is explicitly taken into account in the present modelling approaches. In the following, the terms magnetic order and disorder in materials are discussed. A brief overview is presented of the topic of magnetic functional materials and shape memory alloys (SMAs), including their historical discovery, and MSMAs are introduced in detail.

The state of the magnetisation of a material is defined as the magnetic moment density per unit volume. It depends on the individual magnetic moments of the individual ions, atoms, or molecules of a material and their dipole interactions as well as interactions with external magnetic fields. “Magnetism is inseparable from quantum mechanics, for a strictly classical system in thermal equilibrium can display no magnetic moment, even in a magnetic field”, see [116]. The following classification of magnetic (dis)order in terms of diamagnetism, paramagnetism, ferromagnetism, antiferromagnetism, and ferrimagnetism, among others is adopted from [92, 167]. According to [92], “all materials exhibit a diamagnetic susceptibility, although not all are classified as diamagnets. Some materials have a net magnetic moment per atom, due to an unpaired electron spin in each atom which leads to paramagnetism or even ordered magnetism.” The magnetisation is very weak in materials classified as diamagnets and opposes the applied magnetic field. The typical order of the susceptibility $\chi$ in such materials is $-10^{-5}$ or $-10^{-6}$, with $\chi$ being defined as $\chi = m/h$, wherein $m$ is the magnetisation and $h$ is the magnetic field strength. In paramagnetic materials, the magnetic field is slightly amplified and the susceptibility is positive and typically of the order of $10^{-5}$ to $10^{-3}$. Ferromagnetism, antiferromagnetism, and ferrimagnetism are different types of magnetic order that might occur in solids. In ferromagnetic materials such as iron, nickel, and cobalt, a transition from the paramagnetic to the ferromagnetic state is observable at temperatures below the Curie temperature $T_C$. This transition is accompanied with the occurrence of a spontaneous magnetisation $m_s$. Magnetic domains, viz. regions of equal spontaneous magnetisation, form, wherein the magnetic moments are aligned parallel even in the absence of an external magnetic field. The initial susceptibility in such materials is typically of the order of 10 to $10^5$. The individual domains are separated by domain walls, wherein the magnetisation vectors rotate to ensure a continuous transition to the adjacent domain. Domain wall thicknesses are typically between $10\,\mathrm{nm}$ and $1\,\mu\mathrm{m}$, see [106, 170]. According to [127], domains form to reduce the magnetostatic energy and minimise the internal energy in the material, see also [36, 85, 106, 116, 170]. Heusler alloys are also ferromagnetic, although their alloy elements are not. In antiferromagnetic and ferrimagnetic materials, the nearest-neighbour moments are aligned antiparallel. However, the magnetic moments in the different sublattices in ferrimagnetic materials have different magnitudes, see also [168]. Ferrimagnets also possess a spontaneous magnetisation below the Curie temperature and a domain structure is observable.

Magnetostriction refers to strains that occur during the second-order paramagnetic to ferromagnetic phase transition at the Curie temperature or as a response of the ferromagnetic phase to an applied magnetic field, see [192]. The following outlined historical discovery of magnetostrictive materials and further evolution is, in large parts, adopted from [192]. James P. Joule discovered magnetostrictive materials in 1842 when he observed that an iron sample changed its length under the application of a magnetic field. The effect was termed the Joule effect. The inverse effect, where an applied stress changes the magnetisation, also known as the Villari effect, was discovered shortly thereafter. Two additional effects are the Wiedemann effect where a twisting in a specimen is observed under a helical magnetic field, and the inverse Wiedemann effect, respectively Matteucci effect. Nickel, cobalt, and their alloys were typical materials used in transducers during the first half of the 20th century, with saturation magnetostrictions—i.e. the maxima of the magnetic field-induced strains—of the order of $50\,\mu\,\mathrm{L/L}$. Giant magnetostrictive materials were initially discovered in 1963 in terbium and dysprosium alloys, where strains of the order of $10.000\,\mu\,\mathrm{L/L}$ were observed at cryogenic temperatures. Giant magnetostriction at room temperature was discovered shortly thereafter, see [33, 122], by a combination of these rare earth elements and iron as the transition metal. This resulted in the development of Terfenol-D (Ter: terbium, fe: iron, nol: Naval Ordnance Laboratory, D: dysprosium) shortly thereafter, where strains of the order of $1.600\,\mu\,\mathrm{L/L}$ were observed that increase up to $3.600\,\mu\,\mathrm{L/L}$ at resonance. Magnetic field-induced strains of the order of 4–7 % were observed in terbium and dysprosium single crystals in large magnetic fields of the order of 10–40 T in 1965 and 1975, see [31, 133, 200]. Therein, mechanical twins form and deform plastically, which is similar to the effect observed in MSMAs.

The macroscopic response of a magnetostrictive specimen is directly related to the underlying microscale mechanisms that are briefly discussed in this section. The representation is based on [192]. Even though the magnetisation vectors are non-zero at every point inside a ferromagnetic specimen, the macroscopic magnetisation might be zero, which is identical to a completely demagnetised specimen. As already pointed out, multiple domains form on the underlying microscale to lower the overall magnetostatic energy. Domains with opposingly oriented easy-axes, i.e. the preferred directions of the spontaneous magnetisation vectors that minimise the magnetocrystalline anisotropy energy [31, 92], are separated by 180° domain walls. Additional 90° closure domains might form in, e.g., cubic materials to close the magnetic flux path. This results in an even lower magnetostatic energy and allows the macroscopic magnetisation to vanish. The deviations of the spontaneous magnetisation vectors from the magnetic easy-axes, termed rotation of the magnetisation vectors, is accompanied with additional magnetocrystalline anisotropy energy. The overall configuration results from a balance of the exchange energy that favours an alignment of neighbouring magnetic moments, also referred to as domain wall energy, and the magnetocrystalline anisotropy energy in addition to the magnetostatic energy. The domain walls in ferromagnetic materials are usually thicker than their counterparts in ferroelectrics. In a macroscopically fully magnetised specimen, all spontaneous magnetisation vectors point in the same direction and are completely aligned. The macroscopic magnetisation saturates. The two mechanisms that allow the magnetic state to change are domain wall motion, where favourable domains grow at the expense of the others, and rotation of the magnetisation vectors, see also [36, 106, 116, 170] and the discussion of the microscale mechanisms in MSMAs below. In single crystals, the easy- and hard-axes, i.e. the directions with the largest magnetocrystalline anisotropy energy, magnetisation response curves are typically diverse, whereas a polycrystalline material might respond isotropic due to the variety of differently oriented grains. Due to the magnetostrictive effect, a deviation of the magnetisation vectors from the preferred directions results in a deformation of the crystalline lattice. Consequently, the magnetocrystalline anisotropy energy and (reversible) strains are intrinsically magnetomechanically coupled. The initial magnetostriction that occurs during the paramagnetic to ferromagnetic phase transformation is termed spontaneous magnetostriction $\lambda_0$, whereas the largest additional magnetic field-induced strain is termed saturation magnetostriction $\lambda_s$. The above introduced linear relation between the magnetisation and the magnetic field strength is only a coarse approximation that is not capable of predicting hysteretic response behaviour. Microscale pinning and other phenomena might result in a strong internal resistance to magnetic domain wall motion that is exploited to built permanent magnets, where the macroscopic magnetisation remains in the absence of an external magnetic field, see [36, 50, 106, 170]. The universal relation $\boldsymbol{b} = \mu_0\,[\,\boldsymbol{h} + \boldsymbol{m}\,]$, wherein $\boldsymbol{b}$ is the magnetic induction and $\mu_0$ is the vacuum permeability, can, however, always be used. Figure 1.1 shows experimentally determined magnetic field-induced strain and magnetisation response curves of Terfenol-D and Galfenol. In order to model such a complex response, a detailed knowledge of the underlying mechanisms is indispensable. Another class of materials that was not mentioned so far includes piezomagnetic materials as a subgroup of the antiferromagnetic materials. The material behaviour is similar to the behaviour in ferromagnetic materials. The two main differences in piezomagnetic materials are: the strain depends on the sign of the magnetic field and a strain can induce a magnetic induction in the absence of a magnetic field, see also IEEE-Standard 319-1990.

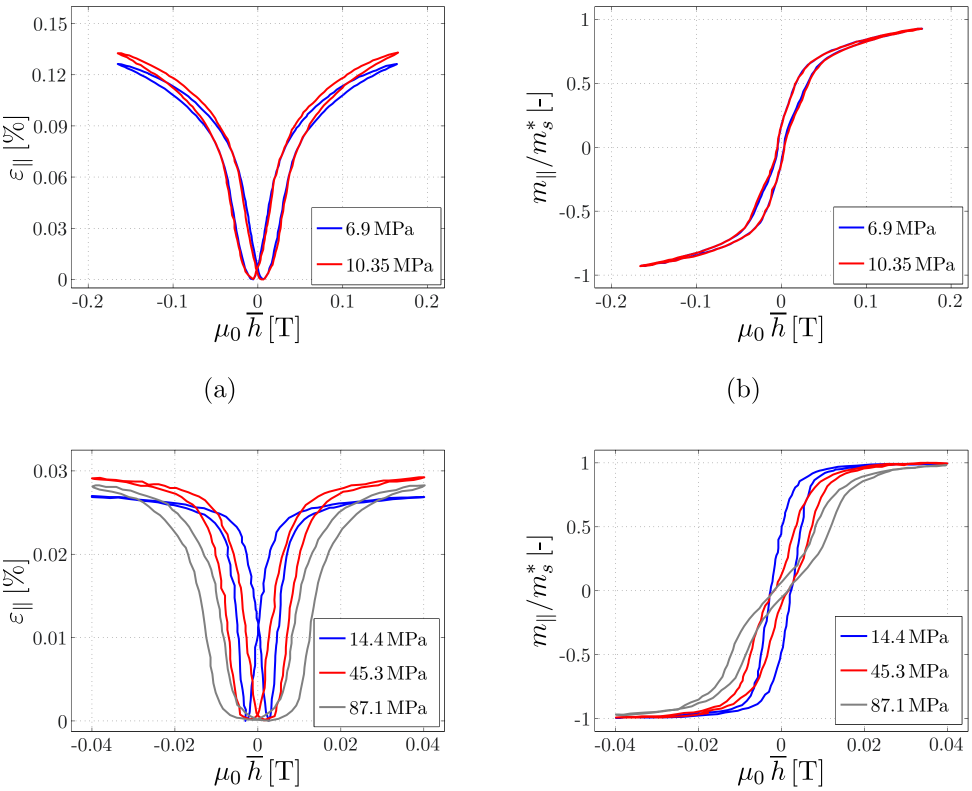

(a) (b)

(c) (d)

**Figure 1.1:** Experimentally measured magnetic field-induced (a), (c) strain and (b), (d) normalised magnetisation responses under multiple levels of constant compression stress and cyclic magnetic field loading (0.05 Hz in (c), (d)) of (a), (b) a Terfenol-D ($Tb_{0.3}Dy_{0.7}Fe_{1.92}$) transducer reported by [37] and (c), (d) Galfenol ($Fe_{0.81}Ga_{0.19}$) reported by [102].

Shape memory alloys (SMAs) belong to the group of functional materials. The following outline of their historical discovery, their properties, and the underlying mechanisms is adopted in large parts from [192]. The first observed materials that returned to their original shape when heated were AuCd alloys. The shape memory effect (SME) was discovered by Arne Ölander in 1932 [176]. A temperature-dependent nucleation and disappearance of martensite phases was observed in 1938 in CuZn. In 1951 [24], it was discovered that the application of the SME allows work as an output. The probably most widely known SMA is NiTi and its alloys. Its discovery started in 1961 at the Naval Ordnance Laboratory, see [22], and is known as Nitinol (Nickel Titanium Naval Ordnance Laboratory). Several other SMAs were discovered later, such as CuAlNi, CuZnAl, FeMnSi. Up to 10% of temperature and stress induced strain are observable in SMAs, due to an induced phase transformation, respectively variant switching. The operating frequencies reach up to 100 Hz in thin films and are mainly limited by heat transfer, see [16, 106]. The martensitic transformation from the high temperature austenite parent phase to the lower temperature martensite product phase, according to [187] typically lower symmetric, is a first-order diffusionless, displacive, shear-like, and reversible phase transition that occurs during cooling, see [141, 179]. Four critical temperatures characterise the martensitic transformation, see [62]. During cooling, the martensite start temperature $M_s$ and martensite finish temperature $M_f$ mark the points where 1 %, respectively 99 %, of the material have converted to martensite. The reverse transformation from martensite to austenite during heating is characterised by the austenite start temperature $A_s$ and austenite finish temperature $A_f$, where 1 %, respectively 99 %, of the material have converted to austenite. Generally, the multiple variants of martensite are energetically equivalently favourable. They may occur in twinned and de-twinned form. A macroscopic strain is typically not observable when cooling below the phase transformation temperature, due to the self-accommodating arrangement of the martensite variants, see also [15]. SMAs are considered to be ferroelastic materials due to the occurrence of domains of austenite and the multiple martensite variants. The one-way shape memory effect is typically observable at low temperatures when the self-accommodated martensite is strained. After an initial linear response, a stress plateau occurs for increasing strain until, again, a linear response is observable in the now completely de-twinned configuration. After unloading a remanent strain occurs. This behaviour is termed pseudoplastic or quasiplastic behaviour, since the initial shape may be recovered during heating. At sufficiently high temperatures, one starts in the initial austenite phase and switches into the martensite phase during straining. The initial austenite phase and the shape is recovered during unloading. This behaviour is termed pseudoelastic or superelastic, since the phase transformation is dissipative in nature and a visible hysteresis occurs. The two-way shape memory effect allows two different shapes of a workpiece by training, where plastic deformations produce material or stress anisotropies that favour certain martensite variants. Although the SME allows unique actuator and potentially sensor capabilities, single crystal SMAs suffer from functional degradation during cyclic loading, see [9, 55, 190]. Nevertheless, SMA are for instance used for vibration attenuation in civil structures or as stents, see [9, 68, 124, 144], also for further applications.

The martensitic transformation and conventional shape memory effect was also observed in the NiMnGa Heusler alloys, see [25, 29, 98, 106, 140, 185, 226, 232]. The magnetic shape memory effect (MSME) was discovered in 1996 in stoichiometric $Ni_2MnGa$ [215], where 0.2% magnetic field-induced strain were measured in magnetic fields of 0.8 T. Unlike in conventional magnetostrictive materials, the magnetic field was able to induce a switching of the martensite phase into the magnetic field-favoured martensite variant—hence the name, magnetostriction of martensite, see also [171, 200]. Shortly thereafter, 4–6% strain under magnetic fields of the order of 1 T were observed in slightly off-stoichiometric 5M $Ni_2MnGa$ single crystals, see [74, 90, 106, 134, 164, 200]. Up to 10% strain is achievable for 7M martensite, see [106, 160, 172, 195, 197, 200]. In addition to the large magnetic field-induced strains, that are directly related to the lattice parameters [75, 84, 106, 135, 226, 232], MSMAs allow operation frequencies of 1 kHz

[25, 79, 106, 139, 209, 210] and up to 5 kHz in thin films [192]. They possess nearly perfect efficiency of coupling magnetic energy to mechanical load [78, 80, 139, 171, 200, 210]. The previously discussed mechanism of domain wall motion and rotation of the magnetisation vectors occur likewise in $Ni_2MnGa$, since it is a ferromagnetic material, see also [36, 106, 116]. The Curie temperature shows only a slight variation for different compositions, but the transition temperature from austenite to martensite may differ significantly, see [3, 4, 72, 106, 217]. Three different martensite morphologies might occur in $Ni_2MnGa$ alloys, see [76, 106, 136, 185]. The most common morphology is five layered modulated (5M) martensite, which has an approximately tetragonal unit cell that is modulated by a five layer periodic shuffling, see [181, 196, 200]. A maximum of 6% magnetic field-induced strain occurs due to the rearrangement of the three possible martensite variants. In contrast, the seven layered modulated (7M) martensite has an approximately orthorhombic structure which is modulated by a seven layer periodic shuffling. A maximum of 10% magnetic field-induced strain occurs due to the rearrangement of the six possible martensite twin variants, see [160, 195, 200]. The non modulated (NM) martensite has a tetragonal unit cell. A magnetic field can slightly influence the mechanical behaviour, but has no influence on the shape, see [193, 198, 200]. Several other alloys can also be assigned to the group of MSMAs, such as NiMnGaFe [228], NiMnGaB [121], NiMnAl [52], NiCoMnSn [180], NiFeGa [67, 131, 175, 208], FeNiCoTi [163], FePd [35, 89, 132, 191, 219, 231], FePt [96, 186], CoNiGa [152, 230], CoNiAl [98, 150, 153, 174], and $LaSrCuO_4$ [128], see also the overviews in [25, 106, 200, 229]. FePd is more ductile than $Ni_2MnGa$ and CoNiAl contains no expensive elements, see [25, 153]. Due to the antiferromagnetic order in $LaSrCuO_4$, the term magnetic shape memory alloys is more appropriate than the also common name ferromagnetic shape memory alloys (FSMAs), see [50, 83, 90, 106, 164, 171, 194, 200]. A magnetic field-induced austenite martensite phase transformation has been reported in FePt [95], NiMnGa [100], and NiMnFeGa [28], see also [106]. One drawback of MSMAs that limits possible applications is the relatively low compression stress that completely suppresses the magnetic field-induced variant reorientation, also termed blocking stress, that is typically well below 10 MPa, see [25, 56, 57, 73, 99, 108, 151, 164]. Nevertheless, MSMAs are promising materials for, e.g., sensors, actuators, and to control the structure of the material itself, see [106, 182, 193, 200, 210]. A list of applications is provided in [25]: Linear actuators [58, 206, 210], micro and nano actuators [103, 119], and bending actuators [117, 118] are exemplary applications as actuators. The application as sensors and energy harvesters is outlined in [101, 120, 199, 207]. Possible damping applications are reported in [225, 233]. The magnetic field induced strain in polycrystalline MSMAs is significantly smaller than the strain in single crystals, see [28, 91, 106, 138, 162, 216, 219]. One idea to alleviate this restriction is the texturing of polycrystalline materials, see [25, 32, 53, 54]. Two other things have not been mentioned so far. Another mechanism to change the magnetic state of the material by inducing a phase transformation is discussed in [63]. In the magnetocaloric effect, an external magnetic field induces an isothermal entropy change, respectively an adiabatic temperature change, see [25] for a detailed discussion.

The focus of this work lies on the micromagnetics-inspired modelling and simulation of the ferromagnetic nearly tetragonal (5M modulated) martensite variants of $Ni_2MnGa$ under magnetomechanical loading conditions. This approach necessitates a fundamental understanding of the underlying microstructure and the mechanisms that occur on the microscale. Experimentally determined microstructures of ferromagnetic 5M modulated martensite in $Ni_2MnGa$, that occur below both the Curie and the phase transformation temepratures, are shown in Figure 1.2 and 1.3, reported by [60] and [136]. Both figures clearly show the occurrence of order in terms of martensite twins that are subdivided into magnetic domains with internal domain walls.

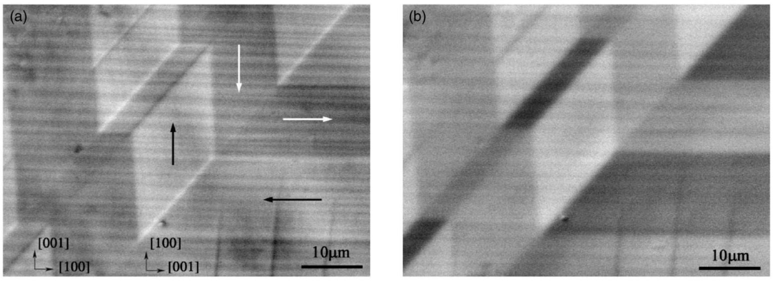

**Figure 1.2:** Experimentally determined microstructure (scanning electron microscopy) of a nearly tetragonal (5M modulated) $Ni_2MnGa$ MSMA specimen. Type II magnetic contrast of the two-variant specimen in (left) COMPO mode and (right) TOPO mode. Reprinted from [60] with kind permission.

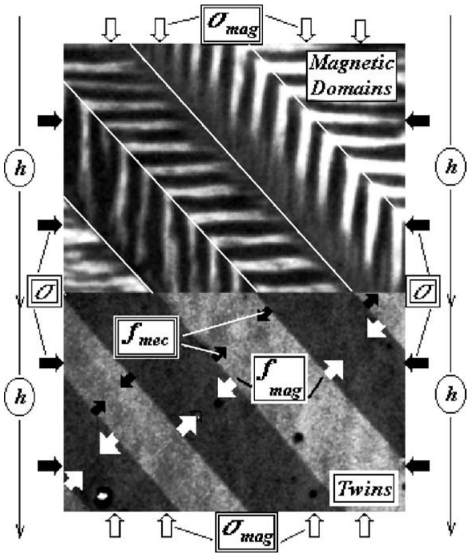

**Figure 1.3:** Experimentally determined twin and magnetic microstructure (situ optical and magneto-optical) of nearly tetragonal (5M modulated) $Ni_2MnGa$ MSMA specimen. Multiple magnetic domains are observable in each twin band of the martensite variants. Reprinted from [136] with kind permission.

A schematic representation of the ferromagnetic product phase and its higher symmetric cubic parent austenite phase is shown in Figure 1.4, see also [106, 112, 161, 165]. The three (tetragonal) martensite variants are distinguishable by their distinct transformation strains. Each variant has two opposingly oriented magnetic easy-axes, i.e. preferred directions of the spontaneous magnetisation vectors, along the short c-edge of the unit cell. In the absence of magnetomechanical loading, the overall six variant and domain configurations are generally energetically equally favourable. The complex interaction of these six states, possible deviations from the sketched energy well states, and the evolution of the microstructure result in the complex response behaviour of Ni$_2$MnGa under magnetomechanical loading conditions.

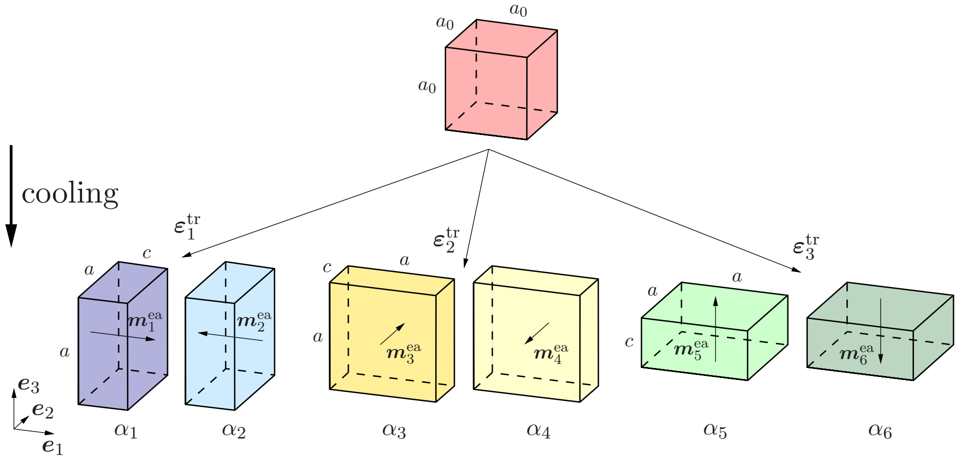
$a_0$
$a_0$
$a_0$
cooling
$\varepsilon_1^{\mathrm{tr}}$
$\varepsilon_2^{\mathrm{tr}}$
$\varepsilon_3^{\mathrm{tr}}$
$a$
$c$
$a$
$c$
$a$
$a$
$a$
$a$
$c$
$\boldsymbol{m}_1^{\mathrm{ea}}$
$\boldsymbol{m}_2^{\mathrm{ea}}$
$\boldsymbol{m}_3^{\mathrm{ea}}$
$\boldsymbol{m}_4^{\mathrm{ea}}$
$\boldsymbol{m}_5^{\mathrm{ea}}$
$\boldsymbol{m}_6^{\mathrm{ea}}$
$\boldsymbol{e}_3$
$\boldsymbol{e}_2$
$\boldsymbol{e}_1$
$\alpha_1$
$\alpha_2$
$\alpha_3$
$\alpha_4$
$\alpha_5$
$\alpha_6$

**Figure 1.4:** Schematic representation of the parent cubic austenite phase and the lower symmetric ferromagnetic martensite product phase. Adopted from [112] with kind permission.

Typical experimentally determined response curves of nearly tetragonal (5M modulated) single crystalline Ni$_2$MnGa specimens are shown in Figure 1.5. The (a) strain and (b) magnetisation responses depend highly on the level of the applied constant compression stress. Prior to the experiments, the sample is compressed to obtain a single martensite variant configuration. In the actual experiments, multiple levels of constant compression stresses which favour the initial single martensite variant state are applied. In addition, one cycle of an external magnetic field is applied perpendicular to the compression stress, favouring the other martensite variant. Initially, the change in strain is almost negligible, whereas a linear magnetisation response is observable during loading. The underlying mechanism is the rotation of the magnetisation vectors away from their preferred magnetic easy-axes in the direction of the external magnetic field. At a certain point, the onset of the martensite reorientation is visible in the strain response, where an almost vertical response behaviour is observable and large strains are measured, and the magnetisation response curves, where the slopes of the curves drastically increase, for low and medium compression stresses. The magnetic field induces the martensite variant switching into the magnetic field-favoured martensite variant, which is magnetised in one of its easy-axes directions. After the almost vertical strain response, both curves flatten and approach asymptotically a certain strain level until the magnetisation saturates and the switching process stops. The higher the compression stress, the lower the maximum magnetic field-induced strain and the later the onset of the reorientation until the compression stress completely suppresses the variant switching. Here, the variant switching is nearly completely suppressed for high compression stresses, where the strain remains mostly zero and where the magnetisation response is almost linear for the whole loading cycle. During unloading, the onset of the martensite switching process is delayed due to dissipation associated with the martensite reorientation. The initial martensite variant is completely/partially recovered for medium/low compression stresses during unloading. In the absence of the external magnetic field, the magnetisation reduces to zero. The mechanism of domain wall motion is activated in the magnetic field-favoured martensite variant. The second half of the loading cycle is almost identical to the first half for medium and high compression stresses, but differs significantly for low compression stresses due to the initial occurrence of both martensite variants and all domains at zero magnetic field. This effect is known in the literature as the first cycle effect. For low compression stresses, the magnetisation response is almost linear with a higher slope during this second half, since domain wall motion requires less energy than the rotation of the magnetisation vectors. At a certain point, the martensite switching process is initiated. From this point on, the response is almost identical to the first half of the loading cycle. The highly nonlinear strain and magnetisation response of $Ni_2MnGa$ under magnetomechanical loading conditions is due to the (simultaneous) occurrence of all magnetisation mechanisms on the microscale. In the following, the three mechanisms are isolated in some thought experiments.

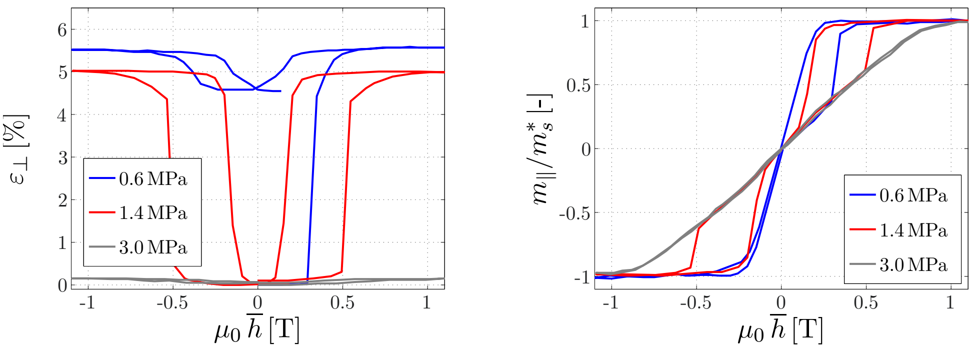

(a) (b)

**Figure 1.5:** Experimentally measured magnetic field-induced (a) strain and (b) normalised magnetisation responses under three levels of constant compression stress and perpendicular cyclic magnetic field loading of a $Ni_{50.7}Mn_{28.4}Ga_{20.9}$ MSMA specimen reported by [71].

The magnetic response of MSMAs such as $Ni_2MnGa$ under magnetic field loading is mainly governed by three mechanisms that are schematically sketched in Figure 1.6. The first mechanism is called (180°) *magnetic domain wall motion*, see Figure 1.6 (top). Here, a single variant of martensite is considered with two opposingly oriented magnetic easy-axes. Areas of equal magnetisation are known as domains and are separated by 180° domain walls. In the initial configuration in the absence of externally applied magnetic fields, the total areas of both domain types are of equal size and the macroscopically observable net magnetisation is zero. Under the application of an external magnetic field, the mechanism of (180°) magnetic domain wall motion is initiated. The sizes of all magnetic field-favoured domains, where the spontaneous magnetisations are oriented in the direction of the external magnetic field, grow at the expense of the others and a non-zero net magnetisation is observable. During this magnetisation, the demagnetisation self-field acting against the magnetisation builds up and the magnetostatic energy of the self-field increases. At certain magnetic fields, the unfavourable domains vanish completely and the magnetisation saturates. For the considered ideal case, the magnetisation response is completely linear. During this whole process, the magnetisation is always oriented along the easy-axes. In experiments one tries to isolate this easy-axis response by applying a magnetic field in one of the easy-axes of a single crystalline $Ni_2MnGa$ specimen, see Figure 1.7 taken from [134] for an experimentally measured magnetisation response curve. The response is almost linear. The single martensite variant configuration is maintained by the application of a suitable compression stress. The easy-axis magnetisation response in $Ni_2MnGa$ is nearly hysteresis-free. The second mechanism is called *rotation of the magnetisation vectors*, see Figure 1.6 (middle). Again, a single variant of martensite with an initially zero net magnetisation is considered. A suitable compression stress above the blocking stress is applied in the easy-axes direction to maintain the single martensite variant configuration and to suppress the third mechanism, see below. An external magnetic field is applied perpendicular to the magnetic easy-axes. The spontaneous magnetisation vectors within all domains start to rotate towards the direction of the applied magnetic field, resulting in a macroscopically observable magnetisation. For high magnetic fields, the spontaneous magnetisation vectors fully align with the external field and the magnetisation saturates. Magnetostatic energy is stored in the demagnetisation field that builds up during the magnetisation. In addition, magnetocrystalline anisotropy energy is stored due to the reversible deviation of the spontaneous magnetisation vectors from the magnetic easy-axes. This additional energy storage usually results in the requirement of higher externally applied magnetic fields to magnetise a specimen in its hard-axes directions. An experimentally determined magnetic field-induced hard-axis magnetisation response curve of a single crystalline $Ni_2MnGa$ specimen is shown in Figure 1.7 taken from [134]. Like in the thought experiment, a suitable compression stress is applied to the specimen. The response curve is almost linear and dissipation is hardly if at all observable. Conventional magnetostriction is neglected in this thought experiment, due to the relatively low strains in contrast to the strains obtained by the third mechanism named *marten-*

*site variant reorientation*, respectively variant switching which is unique to MSMAs, see Figure 1.6 (bottom). For the sake of clarity, the magnetisation vectors permanently point in the easy-axes directions for this schematical representation. Initially, a single martensite variant is considered with zero net magnetisation. An external magnetic field is applied in the hard-axis direction. At a certain magnetic field, the martensite reorientation process in initiated, accompanied by large magnetic field-induced strains. Due to the relatively high magnetocrystalline anisotropy energy in $Ni_2MnGa$ and the relatively low threshold for the martensite reorientation, it is favourable to switch to the magnetic field-favoured martensite variant to reduce the overall energy. The arising second martensite variant is magnetised in its easy-axis direction. Higher magnetic fields are required to complete the switching process. Unlike for the other two mechanisms, the initial configuration is not regained during unloading. There are two reasons for this behaviour. Firstly, the mechanism of martensite reorientation is dissipative in nature. Secondly, the two martensite variants are energetically equally favourable in the absence of external loads. During unloading, domains with the spontaneous magnetisation oriented in the other easy-axis direction will form and allow a reduction to zero net magnetisation at zero applied magnetic field. Figure 1.5, taken from [71], shows magnetic field-induced (a) strain and (b) magnetisation response curves of a single crystal $Ni_2MnGa$ specimen. Large magnetic field-induced strains and dissipative switching behaviour is observable. Unlike for the other two mechanisms, it is not possible to isolate the martensite reorientation process in experiments. It should be mentioned that it is possible to initiate and complete the variant switching process by applying suitable mechanical loading conditions, see, e.g., [71].

## 1.2 Modelling approaches

This section briefly introduces modelling approaches that were used to model and simulate the response behaviour of magnetic shape memory alloys under magnetomechanical loading conditions. Several other authors have provided overviews over established modelling approaches, see, for instance, [25, 48, 104, 106, 110, 220, 222]. These publications were used as a basis for the following representation.

One of the earliest models provided in [89] is based on the constrained theory of magnetoelasticity which was developed for materials with high anisotropy, see also [41, 213]. One central assumption is the large body limit where not all details of the underlying laminate type microstructure, such as domain arrangements and domain walls, are resolved. The martensite variants and magnetic domains are both mechanically and magnetically compatible, since deviations from the energy well states, i.e. elastic deformations and rotated magnetisation vectors, are not considered. The overall response results from the solution of a constrained optimisation problem.

The model proposed in [169] assumes two variants that are separated by a single twin boundary to study the magnetic field-induced martensite reorientation. The driving

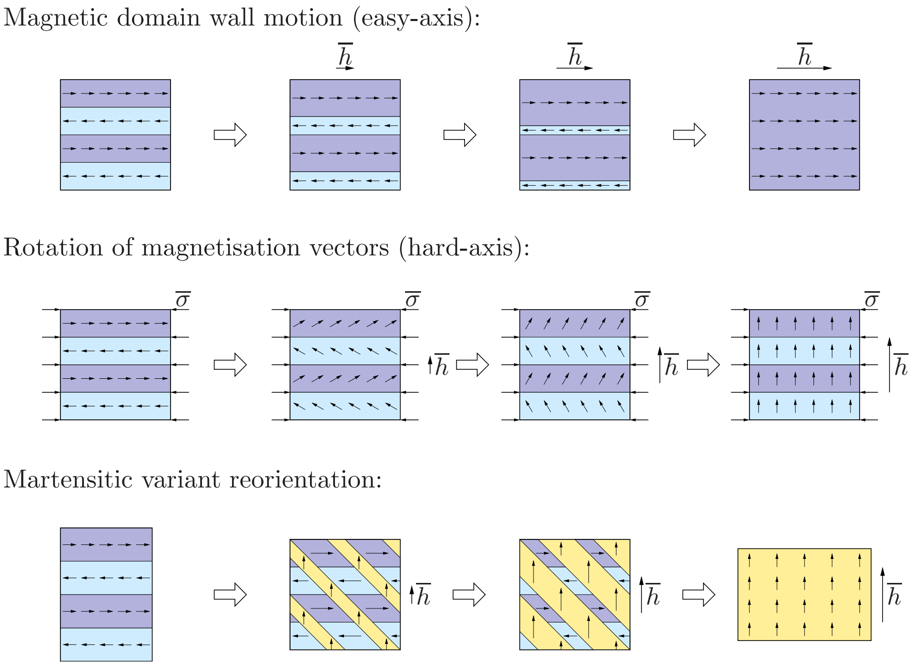
Magnetic domain wall motion (easy-axis):
$\overline{h}$
Rotation of magnetisation vectors (hard-axis):
$\overline{\sigma}$
$\overline{h}$
Martensitic variant reorientation:
$\overline{h}$

**Figure 1.6:** Schematic representation of the magnetic field-induced microscale mechanism. The mechanism of 180° domain wall motion (top) and the rotation of the magnetisation vectors (middle) occur in all ferromagnetic materials. For the latter, a stress is applied to suppress the mechanism of martensitic variant reorientation (bottom), respectively variant switching, which is unique to MSMAs and accompanied with large magnetic field-induced strains. For the sake of clarity, the latter mechanism is sketched isolated without rotations of the magnetisation vectors.

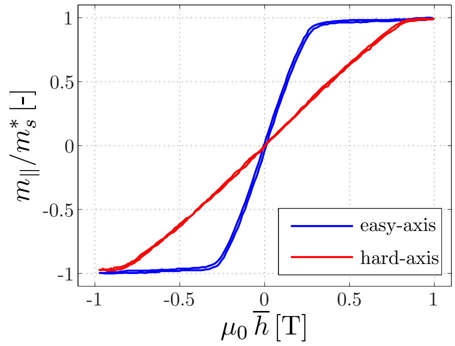

**Figure 1.7:** Experimentally measured magnetic field-induced normalised magnetisation response in easy- and hard-axis direction of a single variant $\mathrm{Ni_{48}Mn_{30}Ga_{22}}$ MSMA specimen reported by [134].

force for the twin boundary motion is the difference between the magnetic energies of the two variants across the boundary. The model was extended by considering an additional mechanical potential in [166] and further in [157] by considering magnetisation vectors that may deviate from the magnetic easy-axes. Hysteretic effects and generalised magnetomechanical loading conditions are considered in [69, 70]. The models predict an abrupt switching whenever the energy changes its sign or the difference of the energies reach a certain threshold, but qualitatively capture the magnetic fields and stresses where switching occurs. In addition, the energy analysis outlined in [69, 70] suggests that magnetic field-induced variant switching might occur in MSMAs at high stress levels, even above the blocking stress, under multiaxial stresses. The experiments outlined in [26] suggest that the intrinsic hysteresis of the material and strain change due to variant switching are constant under various biaxial compression stresses.

Another early model was proposed in [134]. It requires only a few parameters, respectively energies, that can be determined by experiments, e.g. by integration of experimental magnetisation response curves in easy- and hard-axis direction of a single martensite variant. The driving force for the twin boundary motion is introduced so as to depend on the ratio between the magnetic anisotropy energy difference of the two variants in addition to the strain change that occurs during the martensite reorientation. The onset of the twin boundary motion is independent of the physical nature of the driving force and starts at equivalent load levels. Several other models are based on this work, such as [104, 105, 201].

The modelling of the macroscopic behaviour using statistical approaches is outlined in, e.g., [30, 61, 158]. Therein, the evolution of the variant volume fractions is determined as a function of the effective stress acting on the specimen. Thermally activated variant switching is considered in [20, 123, 173]. The switching rates of the variants are related to an energy barrier.

The path dependency of the response behaviour and dissipative effects are taken into account in thermodynamics-based models. In these approaches, internal state variables are introduced that characterise the state of the underlying microstructure. A Helmholtz or Gibbs free energy is typically proposed. The constitutive equations that correspond to the different independent variables are derived and used to determine the magnetomechanical response as well as the evolution equations for the internal state variables. A one-dimensional constitutive model with two internal state variables was proposed in [82] to capture the martensite reorientation of two variants. The models outlined in [34, 59] additionally allow the magnetisation to rotate away from the preferred magnetic easy-axes. This is also true for the models proposed in [107, 108, 110], but they provide a more systematic thermodynamic treatment. Therein, internal variables describe the crystallographic and magnetic microstructure. Hysteretic effects that occur under magnetic field-induced variant reorientation are captured. A special emphasis is placed to capture the nonlinearity and stress level-dependency of the strain and magnetisation response. Experimental data is provided in [111] and compared to simulated response curves. The model is used for the simulation of magnetic boundary value problem in [64, 109, 125]. The spatial influence of the demagnetisation effect is analysed in detail in [65]. Three dimensional models are proposed in [5, 14, 27]. In [220], a variational approach is proposed and applied to derive the governing system of equations. The shape dependency of the response behaviour is taken into account. The embedding of this model into a finite element framework requires a special numerical treatment in terms of an iterative scheme, see [221]. Overall, the outlined models generally predict the magnetic field-induced strain and magnetisation response curves as well as the stress induced strain response curves quite well. The evolution of the state variables can be utilised to investigate the underlying mechanisms that are responsible for the response behaviour observable in experiments.

Phase field models allow the spatial resolution of the microstructure. Different order parameters may be used to capture the evolution of the martensite variants that are subdivided in magnetic domains with internal domain walls. Examples are the models outlined in [93, 129, 130, 142, 143, 183, 234]. The non-local nature of the response is directly taken into account in micromagnetics-based phase field models.

A series of papers [222–224] deals with the establishment of a material model for MSMAs and its finite element implementation to investigate the twin interface movement in single crystalline MSMAs under magnetomechanical loading conditions. Therein, the properties of the configurational force on the twin interfaces are analysed in three-dimensional cuboid bodies. In their finite element simulations, a finite size free space box is used and the demagnetisation effect is directly taken into account.

## 1.3 Structure of the thesis

The objective of this thesis is described in two different parts. The first part focusses on the development of a suitable material model to capture and simulate the nonlinear, hysteretic, and stress level-dependent response of $Ni_2MnGa$ MSMAs under magnetomechanical loading conditions for macroscopically homogeneous states. The second part, however, focusses on the implementation of such models into a finite element framework to simulate macroscopically inhomogeneous material and structural responses. The following chapters are independent of each other and are briefly summarised below.

Chapter 2 deals with the development of a suitable material model for the simulation of $Ni_2MnGa$ MSMAs single crystals. Three global primary fields, viz. the displacement field, the magnetic potential of the demagnetisation field, and a general set of state variables, are introduced, followed by the micromagnetics-inspired variational framework. The assumption of macroscopically homogeneous states allows the reduction to a constrained minimisation problem to determine the evolution of the state variables for the coupled magnetomechanical problem. After a short discussion regarding numerical relaxation techniques, the underlying microstructure is parametrised by a set of state variables and the stored energy density as well as a dissipation functional are specified. Several numerical examples demonstrate the capabilities of the specific constitutive model. The chapter ends with a short summary and an appendix, wherein the stored energy density is further analysed.

Chapter 3 can be regarded as the first step in the implementation of these kinds of material models into a finite element framework. The focus of this chapter lies on the simultaneous solution of the magnetostatic boundary value problem and the evolution equations for the state variables, since the non-local demagnetisation field heavily influences the evolution of the state variables. The assumption of homogeneous stress and strain distributions allows a reduction of the number of primary field variables of the micromagnetics-inspired variational framework to two. The first variation of the continuous variational framework serves as a basis for the finite element implementation, where arising Karush-Kuhn-Tucker (KKT) conditions are directly taken into account. The state variables and the constitutive model are briefly summarised. The finite element implementation and the algorithmic treatment are discussed with an emphasis on a newly introduced mixed element formulation and the treatment of the constraints. The magnetostatic boundary value problem as well as the evolution equations are solved monolithically using a global Newton-Raphson scheme. Several numerical examples demonstrate the capabilities of the finite element implementation. The chapter closes with a short summary and an analysis of the stored energy density.

Chapter 4 can be regarded as an extension of the finite element implementation. To be precise, the focus lies on the simultaneous solution of the fully coupled magnetomechanical boundary value problem and the evolution equations for the state variables. Again, the first variation of the continuous variational framework, including the arising KKT conditions, serves as a basis for the finite element implementation. Multiple parametrisations of the underlying microstructure are discussed and the constitutive model is introduced, including the application of numerical relaxation techniques for the elastic strain energy density of the phase mixture and the rate-dependent evolution equations for all state variables. The finite element implementation and the algorithmic treatment are discussed in detail. Many numerical examples demonstrate the capabilities of the fully coupled finite element implementation in comparison to experimental findings and calculated macroscopically homogeneous response curves. The chapter is briefly summarised, followed by an appendix, wherein the different parametrisations are connected, the constitutive driver is detailed, and the shape functions as well as the stiffness matrix contributions are listed.

Chapter 5 concludes the thesis and the main achievements of this work are briefly summarised. The chapter closes with an outlook on future research perspectives.

# 2 An energy relaxation-based MSMA model

---

The material presented in this chapter is, in large parts, based on the ideas outlined in the recent work [10]. A constitutive modelling framework is presented for magnetic shape memory alloys, $Ni_2MnGa$ in particular, that builds on global variational principles. The approach relies on concepts of energy relaxation and generalised notions of convexity to compute effective energy hulls of the non-convex energy landscape associated with the underlying multi-phase solid, from which the prediction of microstructure evolution results. In this sense, it fundamentally distinguishes itself from MSMA models that essentially follow phenomenological concepts of classic plasticity, see, e.g., [108, 110]. The microstructure is not spatially resolved, but microscale quantities are taken into account in an effective sense by internal state variables and appropriate mixture rules. The model allows all mechanisms central to MSMA behaviour to occur simultaneously. The modelling approach can quantitatively capture key characteristics of single-crystalline MSMA response under magnetomechanical loading conditions, such as variant switching diagrams, magnetic field-biased pseudo-elasticity and the influence of specimen shape anisotropy, see also [112]. Moreover, the global variational framework is formulated in a manner that lends itself to the finite element implementation. In this chapter, however, numerical examples are considered in which the non-local nature of the demagnetisation field is taken into account in an approximate sense through appropriate shape factors.

The chapter is structured as follows: Section 2.1 introduces the three global primary fields and presents the general micromagnetics-inspired variational modelling framework. Section 2.2 begins by introducing the general concept of energy relaxation and thereby ties the modelling of microstructure evolution to the notion of the loss of material stability (quasiconvexity). Afterwards, the global energy storage and dissipation potentials are specified for the proposed MSMA model. A number of insightful numerical examples are presented in Section 2.3. The chapter closes with a short summary of the key findings and conclusions drawn from this work and an outlook on future work in Section 2.4. A further analysis of the stored energy density is given in the appendix in Section 2.5.

## 2.1 Variational framework

In this section, the general variational framework for the modelling of magnetisable solids with evolving microstructure under the consideration of dissipative effects is introduced. Although the focus of this chapter is set on spatially homogeneous problems—since it already allows comparisons to experiments—the governing variational principle shall be introduced in a general manner.

### 2.1.1 Global field variables

First, the spatial positions are denoted as $\boldsymbol{x} \in \mathbb{R}^3$, which partly refer to a magnetisable body $\mathcal{B} \subset \mathbb{R}^3$ and the surrounding free space $\mathbb{R}^3 \backslash \mathcal{B}$. In general, the underlying state variables are introduced as

$$\boldsymbol{u} : \begin{cases} \mathcal{B} \times \mathcal{I} \to \mathbb{R}^3 \\ (\boldsymbol{x}, t) \mapsto \boldsymbol{u}(\boldsymbol{x}, t) \end{cases}, \quad \boldsymbol{h} : \begin{cases} \mathbb{R}^3 \times \mathcal{I} \to \mathbb{R}^3 \\ (\boldsymbol{x}, t) \mapsto \boldsymbol{h}(\boldsymbol{x}, t) \end{cases}, \quad \boldsymbol{m} : \begin{cases} \mathcal{B} \times \mathcal{I} \to \mathbb{R}^3 \\ (\boldsymbol{x}, t) \mapsto \boldsymbol{m}(\boldsymbol{x}, t) \end{cases}, \tag{2.1}$$

where $\boldsymbol{u}$ denotes the displacement field, $\boldsymbol{h}$ the magnetic field strength, $\boldsymbol{m}$ the magnetisation, and $\mathcal{I} \subset \mathbb{R}_{\geq 0}$ the considered time interval. In the absence of free currents, the magnetic field may be related to a scalar magnetic potential $\phi$ via $\boldsymbol{h} := -\nabla_{\boldsymbol{x}} \phi$, which a priori fulfils Ampère's law, with $\nabla_{\boldsymbol{x}} \bullet$ defined as the gradient with respect to the underlying Cartesian frame. Furthermore, the magnetic field can be subdivided into prescribed spatially homogeneous contributions $\overline{\boldsymbol{h}}$ and demagnetisation field $\widetilde{\boldsymbol{h}}$, so that $\boldsymbol{h} = \overline{\boldsymbol{h}} + \widetilde{\boldsymbol{h}}$ holds. As a consequence, an analogous decomposition can be applied to the scalar magnetic potential as well, hence one obtains $\phi = \overline{\phi} + \widetilde{\phi}$, $\overline{\boldsymbol{h}} = -\nabla_{\boldsymbol{x}} \overline{\phi}$, and $\widetilde{\boldsymbol{h}} = -\nabla_{\boldsymbol{x}} \widetilde{\phi}$. In the present micromagnetics-inspired framework, magnetisation $\boldsymbol{m}$ is not treated as a field variable itself, but is rather parametrised by a set of additional state variables $\boldsymbol{p}$, so that $\boldsymbol{m}(\boldsymbol{p})$. As elaborated in Section 2.2, these state-dependent variables—whose total number of scalar-valued coefficients is $n_p$—describe the material's microstructure. With these modifications at hand, the alternative set of global field variables is given by

$$\boldsymbol{u} : \begin{cases} \mathcal{B} \times \mathcal{I} \to \mathbb{R}^3 \\ (\boldsymbol{x}, t) \mapsto \boldsymbol{u}(\boldsymbol{x}, t) \end{cases}, \quad \widetilde{\phi} : \begin{cases} \mathbb{R}^3 \times \mathcal{I} \to \mathbb{R} \\ (\boldsymbol{x}, t) \mapsto \widetilde{\phi}(\boldsymbol{x}, t) \end{cases}, \quad \boldsymbol{p} : \begin{cases} \mathcal{B} \times \mathcal{I} \to \mathbb{R}^{n_p} \\ (\boldsymbol{x}, t) \mapsto \boldsymbol{p}(\boldsymbol{x}, t) \end{cases}, \tag{2.2}$$

which serves as a basis for the subsequent model development.

### 2.1.2 Continuous variational principle

Conceptionally in line with [49], the micromagnetics inspired functional

$$\Pi(\boldsymbol{u}, \widetilde{\phi}, \boldsymbol{p}) := \Pi^{\text{int}}(\boldsymbol{u}, \boldsymbol{p}) + \Pi^{\text{free}}(\widetilde{\phi}) + \Pi^{\text{ext}}(\boldsymbol{u}, \boldsymbol{p}) \tag{2.3}$$

is defined, wherein $\mathit{\Pi}^{\text{int}}$ accounts for the energy stored in the magnetisable and deformable solid, $\mathit{\Pi}^{\text{free}}$ accounts for the magnetostatic energy stored in the body and the surrounding free space, and $\mathit{\Pi}^{\text{ext}}$ accounts for the external magnetomechanical loading. To be precise, the individual contributions are defined as

$$\mathit{\Pi}^{\text{int}}(\boldsymbol{u},\boldsymbol{p}) := \int_{\mathcal{B}} \psi^{\text{mat}}(\boldsymbol{\varepsilon},\boldsymbol{p})\,\mathrm{d}v \ , \tag{2.4}$$

$$\mathit{\Pi}^{\text{free}}(\widetilde{\phi}) := \frac{\mu_0}{2}\int_{\mathbb{R}^3} \|\widetilde{\boldsymbol{h}}\|^2\,\mathrm{d}v \ , \tag{2.5}$$

$$\mathit{\Pi}^{\text{ext}}(\boldsymbol{u},\boldsymbol{p}) := -\mu_0\int_{\mathcal{B}} \overline{\boldsymbol{h}}\cdot\boldsymbol{m}(\boldsymbol{p})\,\mathrm{d}v - \int_{\partial\mathcal{B}_t} \overline{\boldsymbol{t}}\cdot\boldsymbol{u}\,\mathrm{d}a \ , \tag{2.6}$$

with the small strain $\boldsymbol{\varepsilon} := \nabla^{\text{sym}}_{\boldsymbol{x}}\boldsymbol{u} = \frac{1}{2}\left[\,\nabla_{\boldsymbol{x}}\boldsymbol{u} + \nabla_{\boldsymbol{x}}\boldsymbol{u}^{\,\text{t}}\,\right]$ and $\overline{\boldsymbol{t}}$ denoting prescribed tractions on the boundary $\partial\mathcal{B}_t$. Hence, the functional $\mathit{\Pi}(\boldsymbol{u},\widetilde{\phi},\boldsymbol{p})$ is specified as follows

$$\mathit{\Pi} := \int_{\mathcal{B}} \psi^{\text{mat}}(\boldsymbol{\varepsilon},\boldsymbol{p})\,\mathrm{d}v + \frac{\mu_0}{2}\int_{\mathbb{R}^3} \|\widetilde{\boldsymbol{h}}\|^2\,\mathrm{d}v - \mu_0\int_{\mathcal{B}} \overline{\boldsymbol{h}}\cdot\boldsymbol{m}(\boldsymbol{p})\,\mathrm{d}v - \int_{\partial\mathcal{B}_t} \overline{\boldsymbol{t}}\cdot\boldsymbol{u}\,\mathrm{d}a \ . \tag{2.7}$$

Assuming, that the demagnetisation potential vanishes at infinity, the following identity holds, see [41, 88],

$$-\frac{\mu_0}{2}\int_{\mathbb{R}^3} \|\nabla_{\boldsymbol{x}}\widetilde{\phi}\|^2\,\mathrm{d}v = -\frac{\mu_0}{2}\int_{\mathbb{R}^3} \|\widetilde{\boldsymbol{h}}\|^2\,\mathrm{d}v \equiv \frac{\mu_0}{2}\int_{\mathcal{B}} \widetilde{\boldsymbol{h}}\cdot\boldsymbol{m}\,\mathrm{d}v \ . \tag{2.8}$$

This allows the formulation of an alternative energy-enthalpy functional $\widetilde{\mathit{\Pi}}(\boldsymbol{u},\widetilde{\phi},\boldsymbol{p})$ derived from (2.7), which is in line with [146] and defined as follows

$$\widetilde{\mathit{\Pi}} := \int_{\mathcal{B}} \psi^{\text{mat}}(\boldsymbol{\varepsilon},\boldsymbol{p})\,\mathrm{d}v - \frac{\mu_0}{2}\int_{\mathbb{R}^3} \|\widetilde{\boldsymbol{h}}\|^2\,\mathrm{d}v - \mu_0\int_{\mathcal{B}} \left[\overline{\boldsymbol{h}} + \widetilde{\boldsymbol{h}}\right]\cdot\boldsymbol{m}(\boldsymbol{p})\,\mathrm{d}v - \int_{\partial\mathcal{B}_t} \overline{\boldsymbol{t}}\cdot\boldsymbol{u}\,\mathrm{d}a \ . \tag{2.9}$$

Exchange energy terms are not considered in the present approach in (2.7) as well as (2.9), due to the assumption of the large body limit, cf. [41].

The functional (2.9) is used for the definition of a power-type potential, cf. [23, 145, 178],

$$\mathcal{L} := \dot{\widetilde{\mathit{\Pi}}} + \int_{\mathcal{B}} \zeta(\dot{\boldsymbol{p}},\boldsymbol{p})\,\mathrm{d}v \ , \tag{2.10}$$

where $\dot{\bullet}$ denotes the material time derivative and where $\zeta$ is a dissipation potential according to, e.g., [17, 46, 235], which is used to account for the dissipation associated with the evolution of the state variables. In addition, equality and inequality constraints—depending on the chosen set of $\boldsymbol{p}$—may need to be considered in order to limit the evolution of the state variables. The application of the—at this point unconstrained—mixed minimisation/maximisation principle

$$\{\dot{\boldsymbol{u}}, \dot{\widetilde{\phi}}, \dot{\boldsymbol{p}}\} = \arg\left[\inf_{\dot{\boldsymbol{u}}}\ \sup_{\dot{\widetilde{\phi}}}\ \inf_{\dot{\boldsymbol{p}}}\ \{\mathcal{L}\}\right] \tag{2.11}$$

yields the set of stationarity conditions, respectively Euler-Lagrange equations, of the variational principle

$$\begin{aligned}
\mathrm{div}_{\boldsymbol{x}}\boldsymbol{\sigma} &= \boldsymbol{0} && \text{in } \mathcal{B}\ , && (2.12)\\
\boldsymbol{\sigma}\cdot\boldsymbol{n} &= \overline{\boldsymbol{t}} && \text{on } \partial\mathcal{B}_t\ , && (2.13)\\
\mathrm{div}_{\boldsymbol{x}}\widetilde{\boldsymbol{b}} &= 0 && \text{in } \mathcal{B}\ , && (2.14)\\
\mathrm{div}_{\boldsymbol{x}}[-\nabla_{\boldsymbol{x}}\widetilde{\phi}\,] &= 0 && \text{in } \mathbb{R}^3\setminus\mathcal{B}\ , && (2.15)\\
[\![\widetilde{\boldsymbol{b}}]\!]\cdot\boldsymbol{n} &= 0 && \text{on } \partial\mathcal{B}\ , && (2.16)\\
\boldsymbol{0} \in -\boldsymbol{\mathcal{F}} + \partial_{\dot{\boldsymbol{p}}}\zeta + \partial_{\boldsymbol{p}}\zeta & && \text{in } \mathcal{B}\ , && (2.17)
\end{aligned}$$

with

$$\begin{aligned}
\boldsymbol{\sigma} &:= \partial_{\boldsymbol{\varepsilon}}\psi^{\mathrm{mat}}\ , && (2.18)\\
\widetilde{\boldsymbol{b}} &:= \mu_0\left[\widetilde{\boldsymbol{h}} + \boldsymbol{m}(\boldsymbol{p})\right]\ , && (2.19)\\
\boldsymbol{\mathcal{F}} &:= -\,\partial_{\boldsymbol{p}}\psi^{\mathrm{mat}} + \mu_0\left[\overline{\boldsymbol{h}} + \widetilde{\boldsymbol{h}}\right]\cdot\partial_{\boldsymbol{p}}\boldsymbol{m}\ , && (2.20)
\end{aligned}$$

introduced as stresses $\boldsymbol{\sigma}$, magnetic induction of the demagnetisation field $\widetilde{\boldsymbol{b}}$, and the generalised thermodynamical driving forces $\boldsymbol{\mathcal{F}}$ and $[\![\widetilde{\boldsymbol{b}}]\!] = \widetilde{\boldsymbol{b}}_+ - \widetilde{\boldsymbol{b}}_-$ denoting the jump in $\widetilde{\boldsymbol{b}}$ between the sides $\partial\mathcal{B}_+$ and $\partial\mathcal{B}_-$ of the interface $\partial\mathcal{B}$. The definition of $\widetilde{\boldsymbol{b}}$ introduced above—with the magnetisation as a part of the magnetic induction of the demagnetisation field—is used here for a compact notation of the underlying equations. As mentioned above, the exact relation between the magnetisation and the internal state variables $\boldsymbol{p}$ will be provided subsequently—resulting in the exact expression for $\partial_{\boldsymbol{p}}\boldsymbol{m}$. The stationarity conditions reflect the balance of linear momentum (2.12), Gauss's law for magnetism (2.14)–(2.16), and the Biot-type evolution equations for the internal state variables $\boldsymbol{p}$

(2.17), whereas (2.13) denotes Neumann boundary conditions. In addition, one has to consider the Dirichlet boundary conditions

$$\boldsymbol{u} = \overline{\boldsymbol{u}} \quad \text{on } \partial\mathcal{B}_u \ , \tag{2.21}$$

with $\partial\mathcal{B}=\partial\mathcal{B}_t \cup \partial\mathcal{B}_u$, and the magnetic potential vanishes at infinity, i.e. $\widetilde{\phi}=0$, cf. (2.8), in order to solve the complete boundary value problem.

### 2.1.3 Incremental variational principle

As an alternative to the aforementioned approach, one may also consider an incremental variational principle, cf. [9, 12, 23, 145, 178]. The functional

$$\mathit{\Psi} := \int_{t_n}^{t_{n+1}} \mathcal{L}\,\mathrm{d}t = \int_{t_n}^{t_{n+1}} \left[ \dot{\widetilde{\mathit{\Pi}}} + \int_{\mathcal{B}} \zeta(\dot{\boldsymbol{p}}, \boldsymbol{p})\,\mathrm{d}v \right] \mathrm{d}t \tag{2.22}$$

is based on the potential $\mathcal{L}$ introduced in (2.10) and is defined for the time interval $t \in \{t_n, t_{n+1}\}$, cf. [9]. This functional can be transformed into the equivalent form

$$\mathit{\Psi} = \widetilde{\mathit{\Pi}}_{n+1} - \widetilde{\mathit{\Pi}}_n + \int_{t_n}^{t_{n+1}} \int_{\mathcal{B}} \zeta(\dot{\boldsymbol{p}}, \boldsymbol{p})\,\mathrm{d}v\,\mathrm{d}t \ , \tag{2.23}$$

where

$$\widetilde{\mathit{\Pi}}_\bullet := \widetilde{\mathit{\Pi}}(\boldsymbol{u}_\bullet, \widetilde{\phi}_\bullet, \boldsymbol{p}_\bullet) = \widetilde{\mathit{\Pi}}(\boldsymbol{u}(t_\bullet), \widetilde{\phi}(t_\bullet), \boldsymbol{p}(t_\bullet)) \ . \tag{2.24}$$

The actual values of the underlying variables, i.e. the values of $\boldsymbol{u}$, $\widetilde{\phi}$, and $\boldsymbol{p}$ at time $t_{n+1}$, are determined by the following—at this point likewise unconstrained—mixed minimisation/maximisation problem, cf. (2.11),

$$\{\boldsymbol{u}_{n+1}, \widetilde{\phi}_{n+1}, \boldsymbol{p}_{n+1}\} = \arg \left[ \inf_{\boldsymbol{u}_{n+1}} \sup_{\phi_{n+1}} \inf_{\boldsymbol{p}_{n+1}} \{\mathit{\Psi}\} \right] \equiv \arg \left[ \inf_{\boldsymbol{u}_{n+1}} \sup_{\phi_{n+1}} \inf_{\boldsymbol{p}_{n+1}} \left\{ \widehat{\mathit{\Psi}} \right\} \right] \ , \tag{2.25}$$

where the alternative functional

$$\widehat{\mathit{\Psi}} := \widetilde{\mathit{\Pi}}_{n+1} + \int_{t_n}^{t_{n+1}} \int_{\mathcal{B}} \zeta(\dot{\boldsymbol{p}}, \boldsymbol{p})\,\mathrm{d}v\,\mathrm{d}t \tag{2.26}$$

can be used, since the values of $\boldsymbol{u}$, $\widetilde{\phi}$, and $\boldsymbol{p}$ at time $t_n$ and $\widetilde{\mathit{\Pi}}_n$ are known. In general, the solution of (2.25) requires a time-discretisation of the rates present in the dissipation potential $\zeta(\dot{\boldsymbol{p}}, \boldsymbol{p})$. They are approximated by $\dot{\boldsymbol{p}} \approx [\boldsymbol{p}_{n+1} - \boldsymbol{p}_n]/\Delta t$ with $\Delta t = t_{n+1} - t_n$, which is covered by

$$D([\boldsymbol{p}_{n+1} - \boldsymbol{p}_n]/\Delta t, \boldsymbol{p}_{n+1}) \approx \int\limits_{t_n}^{t_{n+1}} \zeta(\dot{\boldsymbol{p}}, \boldsymbol{p}) \, \mathrm{d}t \; . \tag{2.27}$$

With this quantity at hand and, in addition, by defining

$$\mathfrak{D}(\boldsymbol{p}_{n+1}, \boldsymbol{p}_n) := \int\limits_{\mathcal{B}} D([\boldsymbol{p}_{n+1} - \boldsymbol{p}_n]/\Delta t, \boldsymbol{p}_{n+1}) \, \mathrm{d}v \; , \tag{2.28}$$

the functional to be minimised/maximised is expressed by

$$\widehat{\varPsi} = \widetilde{\varPi}_{n+1} + \mathfrak{D}(\boldsymbol{p}_{n+1}, \boldsymbol{p}_n) \; , \tag{2.29}$$

so that

$$\{\boldsymbol{u}_{n+1}, \widetilde{\phi}_{n+1}, \boldsymbol{p}_{n+1}\} = \arg \left[ \inf_{\boldsymbol{u}_{n+1}} \sup_{\phi_{n+1}} \inf_{\boldsymbol{p}_{n+1}} \left\{ \widetilde{\varPi}_{n+1} + \mathfrak{D}(\boldsymbol{p}_{n+1}, \boldsymbol{p}_n) \right\} \right] \; . \tag{2.30}$$

It should be mentioned that the application of variational calculus in order to optimise $\varPsi$ as introduced in (2.22) yields identical stationarity conditions as given in Section 2.1.2.

### 2.1.4 Simplifications for homogeneous problems

The main aim of the present study is to establish a material model that is capable of reproducing essential phenomena of MSMA, which were observed in experiments conducted by using single crystals, see, e.g., [71, 202, 211, 212]. In order to investigate the material behaviour itself, the underlying problem—in experimental investigations and concerning the simulations—should be as simple as possible, preferably providing homogeneous states of the essential fields. In this section, the model introduced so far will be specified for such cases.

In particular, deformations are assumed to yield homogeneous total strains $\boldsymbol{\varepsilon}(\boldsymbol{p})$ and consequently homogeneous stresses $\boldsymbol{\sigma}$ without the necessity of considering compatibility or boundary conditions. Furthermore, the demagnetisation field is directly expressed as a function of the magnetisation. Inside specifically shaped bodies, e.g. ellipsoids, an on the considered length scale spatially homogeneously distributed magnetisation $\boldsymbol{m}$ minimises the magnetostatic energy, see [41]. In analogy to the Eshelby solution for the purely mechanical case, the homogeneous magnetisation and the likewise homogeneous demagnetisation field inside the magnetisable body $\mathcal{B}$ are then related by the analytical solution, cf. [115, 155],

$$\widetilde{\boldsymbol{h}} = -\nabla_{\boldsymbol{x}}\widetilde{\phi} = -\boldsymbol{D}\cdot\boldsymbol{m} \;, \tag{2.31}$$

with $\boldsymbol{D}$ as the second-order demagnetisation tensor depending on the shape of the body, which is symmetric and positive definite. For bodies with a homogeneous distribution of the magnetisation and an inhomogeneous demagnetisation field, (2.31) holds for the averaged quantities. From now on, we will only consider bodies with a spatially homogeneous distribution of the magnetisation. The inhomogeneous demagnetisation field outside the magnetisable body is of no interest and consequently not calculated. For the shape dependent demagnetisation tensors, either analytical solutions may be used, cf. [36, 155, 170, 188], or they may be calculated in advance in magnetostatic finite element simulations, see also the discussion in [65].

By the combination of (2.31) and (2.8), the specific functional $\widetilde{\Pi}^{\mathrm{hom}}$, based on (2.9), can, for the considered homogeneous case, be expressed as

$$\widetilde{\Pi}^{\mathrm{hom}}(\boldsymbol{p}) = \Big[\,\psi^{\mathrm{mat}}(\boldsymbol{p}) + \frac{\mu_0}{2}\,\boldsymbol{m}(\boldsymbol{p})\cdot\boldsymbol{D}\cdot\boldsymbol{m}(\boldsymbol{p}) - \mu_0\,\overline{\boldsymbol{h}}\cdot\boldsymbol{m}(\boldsymbol{p})\Big]\,V_{\mathcal{B}} - \int\limits_{\partial\mathcal{B}_t}\bar{\boldsymbol{t}}\cdot\boldsymbol{u}\,\mathrm{d}a \;, \tag{2.32}$$

with $V_{\mathcal{B}}$ as the volume of the magnetisable body $\mathcal{B}$. Finally, the surface integral can be transformed into a volume integral via

$$\int\limits_{\partial\mathcal{B}_t}\bar{\boldsymbol{t}}\cdot\boldsymbol{u}\,\mathrm{d}a = \int\limits_{\partial\mathcal{B}_t}[\overline{\boldsymbol{\sigma}}\cdot\boldsymbol{n}]\cdot\boldsymbol{u}\,\mathrm{d}a \equiv \int\limits_{\mathcal{B}}\overline{\boldsymbol{\sigma}}:\nabla_{\boldsymbol{x}}\boldsymbol{u}\,\mathrm{d}v = \int\limits_{\mathcal{B}}\overline{\boldsymbol{\sigma}}:\boldsymbol{\varepsilon}\,\mathrm{d}v = \overline{\boldsymbol{\sigma}}:\boldsymbol{\varepsilon}\,V_{\mathcal{B}} \;, \tag{2.33}$$

so that one obtains

$$\widetilde{\Pi}^{\mathrm{hom}}(\boldsymbol{p}) = \Big[\,\psi^{\mathrm{mat}}(\boldsymbol{p}) + \frac{\mu_0}{2}\,\boldsymbol{m}(\boldsymbol{p})\cdot\boldsymbol{D}\cdot\boldsymbol{m}(\boldsymbol{p}) - \mu_0\,\overline{\boldsymbol{h}}\cdot\boldsymbol{m}(\boldsymbol{p}) - \overline{\boldsymbol{\sigma}}:\boldsymbol{\varepsilon}(\boldsymbol{p})\Big]\,V_{\mathcal{B}} \tag{2.34}$$

as the final representation of the energy-enthalpy function for homogeneous states inside the body. It should be emphasised here that $\overline{\boldsymbol{h}}$ and $\overline{\boldsymbol{\sigma}}$ are prescribed quantities, whereas $\boldsymbol{m}$ as well as $\boldsymbol{\varepsilon}$ are outcomes of the material model and thus generally depend on the internal state variables $\boldsymbol{p}$. These can now be determined by applying (2.30) for the dissipative case, which results in

$$\boldsymbol{p}_{n+1} = \arg\inf_{\boldsymbol{p}_{n+1}}\Big\{\widetilde{\Pi}^{\mathrm{hom}}_{n+1}(\boldsymbol{p}_{n+1}) + \mathfrak{D}(\boldsymbol{p}_{n+1},\boldsymbol{p}_n)\Big\} \quad \text{s.t. } \boldsymbol{p}_{n+1} \text{ being admissible} \;. \tag{2.35}$$

The precise representation of the functions $\psi^{\mathrm{mat}}(\boldsymbol{p}), \boldsymbol{m}(\boldsymbol{p})$, and $\boldsymbol{\varepsilon}(\boldsymbol{p})$ and the arising equality/inequality constraints are, however, part of the specific constitutive model and will thus comprehensively be discussed in the following section.

**Remark 1** *The constrained minimisation problem* (2.35) *for the non-dissipative case, i.e.* $\mathfrak{D} = 0$*, without considering energy stored in the magnetisable and deformable body, i.e.* $\psi^{\mathrm{mat}} = 0$*, and the magnetisation* $\boldsymbol{m}$*, respectively the strain* $\boldsymbol{\varepsilon}$*, as convex combinations of the energy well states, i.e. easy-axes magnetisations* $\boldsymbol{m}_j^{\mathrm{ea}}$ *and transformation strains* $\boldsymbol{\varepsilon}_i^{\mathrm{tr}}$*, represents the minimisation problem in the context of the constrained theory of magnetoelasticity introduced by [41].*

## 2.2 Constitutive framework

After having introduced the overall thermodynamical framework, the precise material model for the considered MSMA shall now be discussed in detail.

### 2.2.1 General aspects of quasiconvexity

In this section, the concept of energy relaxation shall be outlined and its relation to constitutive modelling shall be discussed. Energy relaxation methods—as used for the development of material models by, e.g., [7, 12, 177]—stem from quasiconvex analysis and the direct methods in the calculus of variations. If one considers a minimisation problem of the form

$$\min_{\boldsymbol{u}} \left\{ \int_{\mathcal{B}} \psi^{\mathrm{mat}}(\nabla_{\boldsymbol{x}}^{\mathrm{sym}} \boldsymbol{u}) \, \mathrm{d}v - \ell(\boldsymbol{u}) \right\} , \tag{2.36}$$

where $\ell(\boldsymbol{u})$ is a linear function w.r.t. $\boldsymbol{u}$, this problem is mathematically well-posed if the energy density $\psi^{\mathrm{mat}}$ is (i) bounded, (ii) coercive, and most essentially (iii) quasiconvex. The first two aspects may be interpreted as certain (i) smoothness and (ii) growing assumptions which can be taken into account rather easily in the context of the present modelling approach. The notion of quasiconvexity has been introduced by [154] who showed that quasiconvex potentials are indeed weakly lower semicontinuous and thus the existence of minimisers and solutions can be proved. The condition for $\psi^{\mathrm{mat}}(\boldsymbol{\varepsilon})$ to be quasiconvex, viz.

$$\psi^{\mathrm{mat}}(\nabla_{\boldsymbol{x}}^{\mathrm{sym}} \boldsymbol{u}) \leq \frac{1}{V_{\mathcal{B}}} \int_{\mathcal{B}} \psi^{\mathrm{mat}}(\nabla_{\boldsymbol{x}}^{\mathrm{sym}} \boldsymbol{u} + \nabla_{\boldsymbol{x}}^{\mathrm{sym}} \boldsymbol{w}) \, \mathrm{d}v \tag{2.37}$$

with

$$\int_{\mathcal{B}} \nabla_{\boldsymbol{x}} \boldsymbol{w} \, \mathrm{d}v = 0 \qquad \text{and} \qquad \boldsymbol{w} = \boldsymbol{0} \quad \text{on } \partial\mathcal{B} , \tag{2.38}$$

also exhibits an intuitive physical interpretation in terms of a material (in)stability condition: As long as the energy associated with homogeneous strain states is lower than or equal to energy densities obtained by any admissible displacement perturbation field $\boldsymbol{w}$, this energy density is said to be quasiconvex. In contrast, if (2.37) does not hold, it means that perturbation fields $\boldsymbol{w}$—which may be related to specific microstructure models as discussed in the subsequent section—further minimise the underlying energy and a phase mixture will occur accordingly.

As a consequence, the energy density $\psi^{\text{mat}}$ present in (2.36) should be substituted by its quasiconvex envelope

$$Q\psi^{\text{mat}}(\nabla_{\boldsymbol{x}}^{\text{sym}}\boldsymbol{u}) := \min_{\boldsymbol{w}} \left\{ \int_{\mathcal{B}} \psi^{\text{mat}}(\nabla_{\boldsymbol{x}}^{\text{sym}}\boldsymbol{u} + \nabla_{\boldsymbol{x}}^{\text{sym}}\boldsymbol{w}) \, \mathrm{d}v \right\} \quad \text{subject to (2.38)} \tag{2.39}$$

in order to guarantee well-posedness of the overall problem, which is now given by

$$\min_{\boldsymbol{u}} \left\{ \int_{\mathcal{B}} Q\psi^{\text{mat}}(\nabla_{\boldsymbol{x}}^{\text{sym}}\boldsymbol{u}) \, \mathrm{d}v - \ell(\boldsymbol{u}) \right\} \, . \tag{2.40}$$

It is well known that the quasiconvex envelope of a formerly non-quasiconvex energy landscape is hardly, if at all achieveable, see, e.g., [40] for a rare case in which this optimal energy bound has been determined. In general, approximations of the quasiconvex hull have to be applied. Such approximations can be conducted by calculating the convex hull $C\psi^{\text{mat}}$ (see, e.g., [94, 112]), the polyconvex hull $P\psi^{\text{mat}}$ (see, e.g., [7]), or the rank-one convex hull $R_n\psi^{\text{mat}}$ w.r.t. laminates of n-th-order (see, e.g., [9] for laminates of first order), where it can be proved that

$$C\psi^{\text{mat}} \leq P\psi^{\text{mat}} \leq Q\psi^{\text{mat}} \leq R_\infty\psi^{\text{mat}} \leq \ldots \leq R_n\psi^{\text{mat}} \leq \ldots \leq R_1\psi^{\text{mat}} \, . \tag{2.41}$$

In this work, first-order laminates will be used in order to determine an upper bound of the quasiconvex hull, as will be explained in the following section.

### 2.2.2 Representation of MSMA microstructure

We generally consider a multi-phase solid which, for the considered model material system—a magnetic shape memory alloy (MSMA), such as $\text{Ni}_2\text{MnGa}$—typically consists of ferromagnetic martensite at the relevant operating temperature, see Figure 2.1. As a basis for our micromechanically-motivated constitutive model, we assume the idealised representation of the microstructure illustrated in Figure 2.2. The assumption of such (first-order) laminate-type arrangements does not necessarily always need to directly correspond to an actual microstructure. In the case of the rank-one relaxation, they may represent rather generic realisations of perturbation states used to approximate the quasiconvex hull. However, such twinned martensite patterns with internal domains have actually been experimentally observed in MSMAs [60, 205]. Moreover, the assumption of neglecting the third crystallographic variant, see Figure 2.1, is in line with typical experiments [202], provided that the single crystal specimens are carefully cut along selected crystallographic directions, that the (virtual) coordinate system is placed accordingly and that the magnetomechanical loading is applied only in the $\boldsymbol{e}_1$-$\boldsymbol{e}_2$-plane.

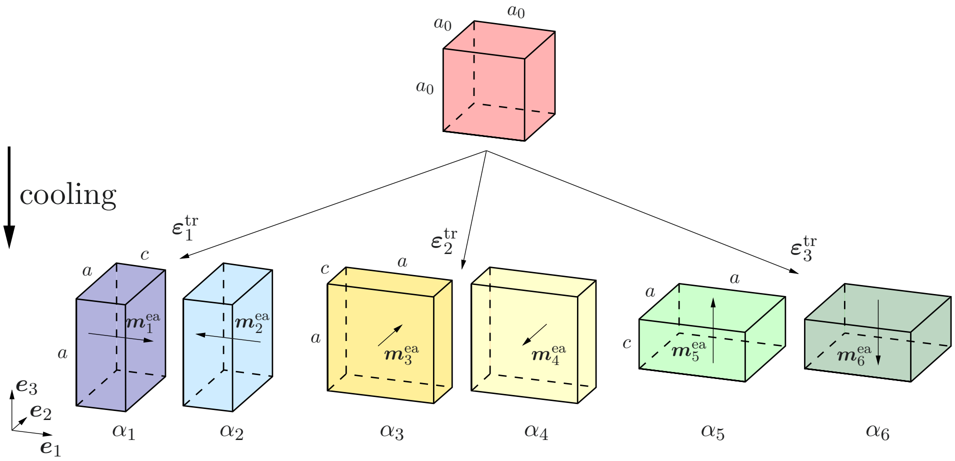
$a_0$
$a_0$
$a_0$
cooling
$\boldsymbol{\varepsilon}_1^{\mathrm{tr}}$
$\boldsymbol{\varepsilon}_2^{\mathrm{tr}}$
$\boldsymbol{\varepsilon}_3^{\mathrm{tr}}$
$a$
$c$
$a$
$\boldsymbol{m}_1^{\mathrm{ea}}$
$\boldsymbol{m}_2^{\mathrm{ea}}$
$c$
$a$
$a$
$\boldsymbol{m}_3^{\mathrm{ea}}$
$\boldsymbol{m}_4^{\mathrm{ea}}$
$a$
$a$
$c$
$\boldsymbol{m}_5^{\mathrm{ea}}$
$\boldsymbol{m}_6^{\mathrm{ea}}$
$\boldsymbol{e}_3$
$\boldsymbol{e}_2$
$\boldsymbol{e}_1$
$\alpha_1$
$\alpha_2$
$\alpha_3$
$\alpha_4$
$\alpha_5$
$\alpha_6$

**Figure 2.1:** Crystallographic variants. Below both the Curie and the phase transformation temperatures, typical MSMAs consist of ferromagnetic martensites, here of tetragonal structure. The variants of this lower symmetry phase—compared to the cubic austenite parent phase—are distinguishable by their respective transformation strains. While the easy-axis of each variant is always along the short edge of the unit cell, the sense of direction (positive/negative) of the spontaneous magnetisation can be used to further distinguish different domain types. Consequently, a total of six domain/variant combinations can be identified as individual "phases". Adopted from Kiefer et al. [112] with kind permission .

In this two-dimensional arrangement, the martensite variants may form perfectly coherent interfaces, with a twin boundary whose orientation is described by the unit normal vector $\hat{\boldsymbol{n}}_{12}^{\mathrm{tw}}$, with $\|\hat{\boldsymbol{n}}_{12}^{\mathrm{tw}}\| = 1$. The orientation of $\hat{\boldsymbol{n}}_{12}^{\mathrm{tw}}$ is one of the micromechanical degrees of freedom, cf. [9]. The two martensite variants, which may coexist, are associated with the transformation strains (cf. Figure 2.1)

$$\boldsymbol{\varepsilon}_1^{\mathrm{tr}} = b_2\, \boldsymbol{e}_1 \otimes \boldsymbol{e}_1 + b_1 [\, \boldsymbol{e}_2 \otimes \boldsymbol{e}_2 + \boldsymbol{e}_3 \otimes \boldsymbol{e}_3 \,] \,, \quad \boldsymbol{\varepsilon}_2^{\mathrm{tr}} = b_2\, \boldsymbol{e}_2 \otimes \boldsymbol{e}_2 + b_1 [\, \boldsymbol{e}_1 \otimes \boldsymbol{e}_1 + \boldsymbol{e}_3 \otimes \boldsymbol{e}_3 \,] \,, \tag{2.42}$$

with $b_1$, $b_2$ as Bain strain coefficients, that are related to the lattice parameters, cf. Figure 2.1, by $b_1 = [\, a - a_0 \,]/a_0$ and $b_2 = [\, c - a_0 \,]/a_0$. As also indicated by Figures 2.1 and 2.2, each of the two crystallographic variants of martensite decomposes into two distinct domains exhibiting converse spontaneous magnetisation directions basically aligned with the crystallographic easy-axes—depicted as $\boldsymbol{m}_j^{\mathrm{ea}}$—, which correspond to the short axes of the tetragonal crystals. The orientation of those may vary and deviate from the respective easy-axis under applied magnetic loading. Therefore, the angles $\theta_j$ with $j = 1, \ldots, 4$

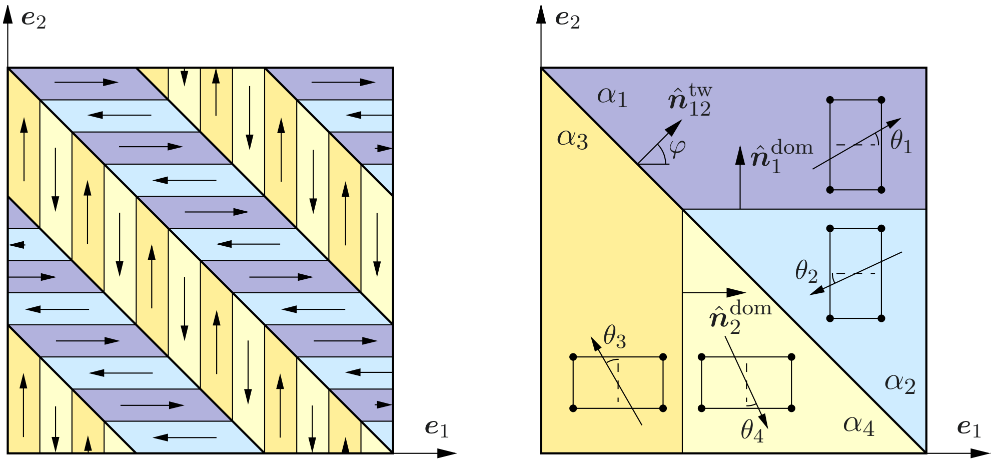
$\boldsymbol{e}_2$
$\boldsymbol{e}_1$
$\boldsymbol{e}_2$
$\alpha_1$
$\hat{\boldsymbol{n}}_{12}^{\mathrm{tw}}$
$\alpha_3$
$\varphi$
$\hat{\boldsymbol{n}}_1^{\mathrm{dom}}$
$\theta_1$
$\theta_2$
$\hat{\boldsymbol{n}}_2^{\mathrm{dom}}$
$\theta_3$
$\alpha_2$
$\theta_4$
$\alpha_4$
$\boldsymbol{e}_1$

(a) (b)

**Figure 2.2:** (a) Two-dimensional idealisation of the MSMA microstructure. Twinned arrangement of the martensite variants introduced in Figure 2.1, with each twin band further separated into magnetic domains. (b) The microstructure is parametrised in terms of the volume fractions $\alpha_i$, the fixed 180° domain wall orientations $\hat{\boldsymbol{n}}_i^{\mathrm{dom}}$, and the orientation of the twin boundary $\hat{\boldsymbol{n}}_{12}^{\mathrm{tw}}(\varphi)$, which also represents a 90° domain wall. The planar rotation of the local magnetic moments away from their respective easy-axes is measured in terms of the angles $\theta_i$. See also Kiefer and Lagoudas [108].

are introduced as well as the relations for the the domain magnetisations $\boldsymbol{m}_j^{\mathrm{dom}}(\theta_j)$, cf. Figure 2.2 and [108],

$$\boldsymbol{m}_1^{\mathrm{dom}}(\theta_1) := \quad m_s[\cos(\theta_1)\,\boldsymbol{e}_1 + \sin(\theta_1)\,\boldsymbol{e}_2]\;, \tag{2.43}$$

$$\boldsymbol{m}_2^{\mathrm{dom}}(\theta_2) := -\,m_s[\cos(\theta_2)\,\boldsymbol{e}_1 + \sin(\theta_2)\,\boldsymbol{e}_2]\;, \tag{2.44}$$

$$\boldsymbol{m}_3^{\mathrm{dom}}(\theta_3) := -\,m_s[\sin(\theta_3)\,\boldsymbol{e}_1 - \cos(\theta_3)\,\boldsymbol{e}_2]\;, \tag{2.45}$$

$$\boldsymbol{m}_4^{\mathrm{dom}}(\theta_4) := \quad m_s[\sin(\theta_4)\,\boldsymbol{e}_1 - \cos(\theta_4)\,\boldsymbol{e}_2]\;, \tag{2.46}$$

where the magnitudes of the domain magnetisations are treated as a constant material parameter, viz. $\|\boldsymbol{m}_j^{\mathrm{dom}}\| = m_s$, with $m_s$ as the saturation magnetisation.

It is worth noting that the angles $\theta_j$ are generally not restricted to a certain value range. In order to be able to distinguish the different domains throughout the calculations it is, however, necessary to define the limits

$$-\,\pi/2 \le \theta_j \le \pi/2\;. \tag{2.47}$$

We assume conservation of mass in terms of negligible density changes and identical densities for all martensite variants and for the underlying domains. The volume fractions of the individual domains are introduced as $\alpha_j$ with $j = 1, \ldots, 4$. The variant volume fractions $\xi_1$ and $\xi_2$ are related to the domain volume fractions via

$$\xi_1 = \alpha_1 + \alpha_2 \ , \quad \xi_2 = \alpha_3 + \alpha_4 \ . \tag{2.48}$$

In addition, the net magnetisations of each domain $\eta_1$ and $\eta_2$ are introduced, which are related to the domain volume fractions via

$$\eta_1 = \alpha_1 - \alpha_2 \ , \quad \eta_2 = \alpha_3 - \alpha_4 \ . \tag{2.49}$$

The inverse relations are then given by

$$\alpha_{2\,i-1} = \frac{1}{2}[\,\xi_i + \eta_i\,] \ , \quad \alpha_{2\,i} = \frac{1}{2}[\,\xi_i - \eta_i\,] \ , \quad \text{with } i = 1, 2 \ . \tag{2.50}$$

The introduction of the domain volume fractions, respectively alternative representation in terms of variant volume fractions and net magnetisations, are inevitably accompanied by the consideration of equality and inequality constraints, i.e.

$$\alpha_j \geq 0 \ , \quad \sum_{j=1}^{4} \alpha_j = 1 \ , \quad \xi_i \geq 0 \ , \quad \xi_1 + \xi_2 = 1 \ , \quad |\eta_i| \leq \xi_i \ . \tag{2.51}$$

With these quantities at hand, the total magnetisation is obtained by averaging over all domains, which results in

$$\boldsymbol{m}(\alpha_j(\xi_i, \eta_i), \theta_j) := \sum_{j=1}^{4} \alpha_j(\xi_i, \eta_i)\, \boldsymbol{m}_j^{\text{dom}}(\theta_j) \tag{2.52}$$

and which yields the precise relation between the magnetisation and the internal state variables that were formerly introduced as $\boldsymbol{p}$.

The interfaces of the respective domains referring to one martensite variant are perpendicular to the interface normal directions $\hat{\boldsymbol{n}}_1^{\text{dom}}$ and $\hat{\boldsymbol{n}}_2^{\text{dom}}$. These orientations are initiated and kept fixed as shown in Figure 2.2, namely

$$\hat{\boldsymbol{n}}_1^{\text{dom}} = \boldsymbol{e}_2 \ , \qquad \hat{\boldsymbol{n}}_2^{\text{dom}} = \boldsymbol{e}_1 \ . \tag{2.53}$$

The last aspect of the microstructure model deals with compatibility conditions, cf. [15]. In order to fulfil mechanical compatibility at the intermartensitic twin boundaries with respect to the local displacement field within the assumed underlying microstructure in an idealised representative volume element (RVE) consisting of two martensite variants, cf. Figure 2.2, the Hadamard condition implies a rank one connection in terms of the jump $[\![\boldsymbol{F}]\!]$ between the deformation gradients of the two martensite variants $\boldsymbol{F}_i$, cf., e.g., [9],

$$[\![\boldsymbol{F}]\!] := \boldsymbol{F}_1 - \boldsymbol{F}_2 = \boldsymbol{a} \otimes \hat{\boldsymbol{n}}_{12}^{\mathrm{tw}} \ , \tag{2.54}$$

where $\boldsymbol{a} \in \mathbb{R}^3$ reflects another internal state variable, which can be interpreted as the jump in the deformation gradient or the strain jump—in the small strain setting—projected onto the interface normal $\hat{\boldsymbol{n}}_{12}^{\mathrm{tw}}$. It is also possible to relate jump $\boldsymbol{a}$ to the amplitude of a perturbation field that yields homogeneous deformation gradients, see [9]. The mechanical compatibility between the respective domains present in one variant do not need to be taken into account, since these are fulfilled a priori due to identical crystal orientations. In addition to the compatibility conditions at the twin boundary, the averaged deformation gradients present in the RVE need to be identical to the macroscopic counterpart, i.e.

$$\boldsymbol{F} \doteq \sum_{i=1}^{2} \xi_i \, \boldsymbol{F}_i \ . \tag{2.55}$$

The combination of (2.54) and (2.55) yields the deformation gradients $\boldsymbol{F}_i$ of both martensite variants

$$\boldsymbol{F}_1 = \boldsymbol{F} + \xi_2 \, \boldsymbol{a} \otimes \hat{\boldsymbol{n}}_{12}^{\mathrm{tw}} \ , \quad \boldsymbol{F}_2 = \boldsymbol{F} - \xi_1 \, \boldsymbol{a} \otimes \hat{\boldsymbol{n}}_{12}^{\mathrm{tw}} \ . \tag{2.56}$$

Equation (2.54) represents the invariant plane condition. A vector $\boldsymbol{v}$, which lies on the interface with the interface normal $\hat{\boldsymbol{n}}_{12}^{\mathrm{tw}}$ satisfying $\boldsymbol{v} \cdot \hat{\boldsymbol{n}}_{12}^{\mathrm{tw}} = 0$, is equally deformed by $\boldsymbol{F}_1$ and $\boldsymbol{F}_2$, cf. [15],

$$\boldsymbol{F}_1 \cdot \boldsymbol{v} - \boldsymbol{F}_2 \cdot \boldsymbol{v} = [\, \boldsymbol{a} \otimes \hat{\boldsymbol{n}}_{12}^{\mathrm{tw}} \,] \cdot \boldsymbol{v} = \boldsymbol{a} \, [\, \boldsymbol{v} \cdot \hat{\boldsymbol{n}}_{12}^{\mathrm{tw}} \,] = \boldsymbol{0} \ . \tag{2.57}$$

In the present small strain setting, relations (2.54) to (2.56) are symmetrised using the relation $\boldsymbol{\varepsilon} = \frac{1}{2} \, [\, \boldsymbol{F} + \boldsymbol{F}^{\mathrm{t}} \,] - \boldsymbol{I}$, with $\boldsymbol{I}$ being the second-order unit tensor. The Hadamard condition in terms of total strains of the individual martensite variants $\boldsymbol{\varepsilon}_i$ is introduced as the symmetrised version of (2.54), viz.

$$[\![\boldsymbol{\varepsilon}]\!] := \boldsymbol{\varepsilon}_1 - \boldsymbol{\varepsilon}_2 = [\, \boldsymbol{a} \otimes \hat{\boldsymbol{n}}_{12}^{\mathrm{tw}} \,]^{\mathrm{sym}} = \frac{1}{2} \, [\, \boldsymbol{a} \otimes \hat{\boldsymbol{n}}_{12}^{\mathrm{tw}} + \hat{\boldsymbol{n}}_{12}^{\mathrm{tw}} \otimes \boldsymbol{a} \,] \ . \tag{2.58}$$

In analogy to (2.55), the averaged strains present in the RVE need to be identical to the macroscopic counterpart, i.e.

$$\boldsymbol{\varepsilon} \doteq \sum_{i=1}^{2} \xi_i \, \boldsymbol{\varepsilon}_i \ . \tag{2.59}$$

Combining (2.58) and (2.59), i.e. the small strain version of (2.56), yields the strains $\boldsymbol{\varepsilon}_i$ of both martensite variants

$$\boldsymbol{\varepsilon}_1 = \boldsymbol{\varepsilon} + \xi_2 [\, \boldsymbol{a} \otimes \hat{\boldsymbol{n}}_{12}^{\mathrm{tw}} \,]^{\mathrm{sym}} \ , \quad \boldsymbol{\varepsilon}_2 = \boldsymbol{\varepsilon} - \xi_1 [\, \boldsymbol{a} \otimes \hat{\boldsymbol{n}}_{12}^{\mathrm{tw}} \,]^{\mathrm{sym}} \ . \tag{2.60}$$

The magnetic compatibility at the domain interfaces, viz.

$$[\, \boldsymbol{m}_{2\,i-1}^{\mathrm{dom}} - \boldsymbol{m}_{2\,i}^{\mathrm{dom}} \,] \cdot \hat{\boldsymbol{n}}_i^{\mathrm{dom}} = 0 \ , \quad \text{with } i = 1, 2 \tag{2.61}$$

as well as similar conditions across the twin boundary are, however, not taken into consideration in the present framework. This is justified by the fact that the overall model could be too restrictive in the sense that the complete set of restrictions may not allow a continuous evolution of the variables which parametrise the microstructure. In other words, the compliance of these constraints could directly result in the values of the related variables. Furthermore, it is generally still a topic in scientific discussions as to whether magnetisation compatibility between domains need to be enforced or if violations may be allowed and then accounted for by additional contributions to the excess energy, see, e.g., [41], without creating unphysical magnetic monopoles.

In order to summarise this section, the complete set of internal state variables used in the subsequent calculations is given by

$$\boldsymbol{p} := \{\xi_1, \xi_2, \eta_1, \eta_2, \theta_1, \theta_2, \theta_3, \theta_4, \boldsymbol{a}, \varphi\} \ , \tag{2.62}$$

where the twin interface normal

$$\hat{\boldsymbol{n}}_{12}^{\mathrm{tw}} := \cos(\varphi)\, \boldsymbol{e}_1 + \sin(\varphi)\, \boldsymbol{e}_2 \tag{2.63}$$

has been parametrised by the angle $\varphi$, cf. Figure 2.2.

### 2.2.3 Specific constitutive model

On the basis of the microstructure model introduced above, the constitutive model in terms of suitable energy densities shall now be discussed. More precisely speaking, the energy density $\psi^{\mathrm{mat}}$ introduced in Section 2.1.2 shall be specified. To this end, this energy density is generally defined by

$$\psi^{\mathrm{mat}} := \sum_{i=1}^{2} \xi_i \, \psi_i \ , \tag{2.64}$$

where the phase energy densities $\psi_i$ further decompose into an elastic part $\psi_i^{\mathrm{el}}$ and contributions due to the magnetocrystalline anisotropy $\psi_j^{\mathrm{an}}$, viz.

$$\psi_i := \psi_i^{\mathrm{el}} + \frac{1}{\xi_i} \sum_{j=2\,i-1}^{2\,i} \alpha_j \, \psi_j^{\mathrm{an}} \;, \quad \text{with } i = 1, 2 \;. \tag{2.65}$$

The elastic energy densities are chosen as quadratic forms

$$\psi_i^{\mathrm{el}} := \frac{1}{2}\, \boldsymbol{\varepsilon}_i^{\mathrm{el}} : \mathbf{E}_i : \boldsymbol{\varepsilon}_i^{\mathrm{el}} \;, \quad \text{with } i = 1, 2 \;, \tag{2.66}$$

wherein $\mathbf{E}_i$ denotes the fourth-order elasticity tensor of the $i$-th martensite variant. The additive decomposition of the strain tensors introduced in (2.60) into elastic $\boldsymbol{\varepsilon}_i^{\mathrm{el}}$ and transformation $\boldsymbol{\varepsilon}_i^{\mathrm{tr}}$ parts, viz. $\boldsymbol{\varepsilon}_i = \boldsymbol{\varepsilon}_i^{\mathrm{el}} + \boldsymbol{\varepsilon}_i^{\mathrm{tr}}$, yields the elastic strains present in each martensite variant as

$$\boldsymbol{\varepsilon}_1^{\mathrm{el}} = \boldsymbol{\varepsilon} + \xi_2 [\, \boldsymbol{a} \otimes \hat{\boldsymbol{n}}_{12}^{\mathrm{tw}} \,]^{\mathrm{sym}} - \boldsymbol{\varepsilon}_1^{\mathrm{tr}} \;, \quad \boldsymbol{\varepsilon}_2^{\mathrm{el}} = \boldsymbol{\varepsilon} - \xi_1 [\, \boldsymbol{a} \otimes \hat{\boldsymbol{n}}_{12}^{\mathrm{tw}} \,]^{\mathrm{sym}} - \boldsymbol{\varepsilon}_2^{\mathrm{tr}} \;. \tag{2.67}$$

In line with, e.g., [116, 170], the magnetocrystalline anisotropy energy density is chosen as

$$\psi_j^{\mathrm{an}} := k_1 \left[ 1 - \left[ \frac{\boldsymbol{m}_j^{\mathrm{dom}}}{m_s} \cdot \boldsymbol{n}_j^{\mathrm{ea}} \right]^2 \right] \equiv k_1 \, \sin^2(\theta_j) \;, \tag{2.68}$$

with $k_1$ as a material parameter and $\boldsymbol{n}_j^{\mathrm{ea}} = \boldsymbol{m}_j^{\mathrm{ea}} / m_s$ as the orientation of the easy-axis for the $j$-th domain, cf. Figure 2.1.

Having specified the individual contributions and having assumed identical elasticity tensors for both martensite variants, i.e. $\mathbf{E}_1 = \mathbf{E}_2 = \mathbf{E}$, the energy density $\psi^{\mathrm{mat}}$ in (2.64) is specified as follows

$$\begin{aligned} \psi^{\mathrm{mat}} &= \frac{1}{2}\, \boldsymbol{\varepsilon} : \mathbf{E} : \boldsymbol{\varepsilon} + \frac{1}{2}\, \xi_1 \, \xi_2 \, [\, \boldsymbol{a} \otimes \hat{\boldsymbol{n}}_{12}^{\mathrm{tw}} \,]^{\mathrm{sym}} : \mathbf{E} : \big[ [\, \boldsymbol{a} \otimes \hat{\boldsymbol{n}}_{12}^{\mathrm{tw}} \,]^{\mathrm{sym}} + 2 \, [\, \boldsymbol{\varepsilon}_2^{\mathrm{tr}} - \boldsymbol{\varepsilon}_1^{\mathrm{tr}} \,] \big] \\ &\quad + \frac{1}{2} \sum_{i=1}^{2} \xi_i \, \boldsymbol{\varepsilon}_i^{\mathrm{tr}} : \mathbf{E} : \big[ \, \boldsymbol{\varepsilon}_i^{\mathrm{tr}} - 2 \, \boldsymbol{\varepsilon} \, \big] + k_1 \sum_{j=1}^{4} \alpha_j(\xi_i, \eta_i) \, \sin^2(\theta_j) \;. \end{aligned} \tag{2.69}$$

For the sake of simplicity, and since the anisotropy of the inelastic response dominates the overall behaviour, the elastic properties of all martensite variants are assumed to be identical and isotropic, so that the elasticity tensor can be expressed as

$$\mathbf{E} \mathrel{\widehat{=}} [\, \lambda \, \delta_{ij} \, \delta_{kl} + \mu \, [\, \delta_{ik} \, \delta_{jl} + \delta_{il} \, \delta_{jk} \,] \,] \; \boldsymbol{e}_i \otimes \boldsymbol{e}_j \otimes \boldsymbol{e}_k \otimes \boldsymbol{e}_l \;, \tag{2.70}$$

with the Lamé constants $\lambda = \nu\, E/[\,[\,1+\nu\,]\,[\,1-2\,\nu\,]\,]$, $\mu = E/[\,2\,[\,1+\nu\,]\,]$ and $E$, $\nu$ denoting Young's modulus and Poisson's ratio, respectively.

In order to fully specify the total potential $\widehat{\varPsi}^{\mathrm{hom}}$ in (2.35), the dissipation potential needs to be defined and a suitable time discretisation needs to be chosen, see Section 2.1.3. In advance, it is necessary to distinguish variables whose evolution cause a noticeable amount of dissipation and those where this is not the case. A reliable indicator for this is exemplified by the question as to whether or not the evolution of one specific internal state variable is associated with local heating of the material and if hysteresis loops occur in diagrams revealing the effective material behaviour.

In the present framework, the martensite variant volume fractions are chosen to be dissipative in nature so that the dissipation function becomes

$$\zeta := \widehat{\zeta}(\dot{\xi}_1, \xi_1, \dot{\xi}_2, \xi_2)\ . \tag{2.71}$$

This is motivated by experimental observations, see [211, 212], where the mechanism of domain wall motion (evolution of $\eta_i$ at constant $\xi_i$) and magnetisation rotation (evolution of $\theta_j$) causes negligible dissipation, while the mechanism of martensite reorientation is clearly dissipative in nature, see [71, 202]. The evolution of the strain jump $\boldsymbol{a}$ and the interface orientation $\hat{\boldsymbol{n}}_{12}^{\mathrm{tw}}(\varphi)$ are also assumed to cause no dissipation. More precisely speaking, the dissipation function is chosen to be positively homogeneous of degree one, so that Euler's Lemma $\partial_{\dot{\boldsymbol{p}}}\zeta \cdot \dot{\boldsymbol{p}} \equiv \zeta$ holds, cf. [9, 147], viz.

$$\zeta := \sum_{i=1}^{2} \mathsf{Y}_\xi(\xi_1)\,|\dot{\xi}_i|\ , \tag{2.72}$$

where

$$\mathsf{Y}_\xi(\xi_1) := \begin{cases} \mathsf{Y}_\xi^0 + \xi_1\,\Delta\mathsf{Y}_\xi\ , & \text{if } \dot{\xi}_1 > 0 \Leftrightarrow \dot{\xi}_2 < 0 \\ \mathsf{Y}_\xi^0 + [\,1-\xi_1\,]\,\Delta\mathsf{Y}_\xi\ , & \text{if } \dot{\xi}_1 < 0 \Leftrightarrow \dot{\xi}_2 > 0 \end{cases} \tag{2.73}$$

is introduced as a hardening-type function. This specific choice for the dissipation function $\zeta$ renders the evolution of the related state variables rate-independent. Furthermore, a time discretisation scheme needs to be applied prior to solving (2.35) which is achieved via forward differences, cf. Section 2.1.3, of the form

$$\dot{\bullet} \approx [\,\bullet_{n+1} - \bullet_n\,]/\Delta t\ . \tag{2.74}$$

With this at hand, quantity $\mathfrak{D}$ (as introduced in Section 2.1.3) reads

$$\mathfrak{D} = \frac{1}{\Delta t}\left[\sum_{i=1}^{2} \mathsf{Y}_\xi(\xi_{1,n+1})\,|\xi_{i,n+1} - \xi_{i,n}|\right] V_{\mathcal{B}}\ , \tag{2.75}$$

where the hardening-type yield limit is now given as

$$\mathsf{Y}_\xi(\xi_{1,n+1}) := \begin{cases} \mathsf{Y}_\xi^0 + \xi_{1,n+1}\,\Delta\mathsf{Y}_\xi \ , & \text{if } \xi_{1,n+1} > \xi_{1,n} \Leftrightarrow \xi_{2,n+1} < \xi_{2,n} \\ \mathsf{Y}_\xi^0 + [\,1 - \xi_{1,n+1}\,]\,\Delta\mathsf{Y}_\xi \ , & \text{if } \xi_{1,n+1} < \xi_{1,n} \Leftrightarrow \xi_{2,n+1} > \xi_{2,n} \end{cases} \tag{2.76}$$

in its time-discretised form.

Using the incremental variational approach discussed in Section 2.1.3, the solution of the minimisation problem (2.35) does not only explicitly yield the current values for the internal state variables. It moreover, in a kind of implicit manner, yields the (partially) relaxed energy density with respect to first-order laminates via the sub-problem

$$R_1\psi^{\text{mat}} := \inf_{\boldsymbol{a}} \left\{\psi^{\text{mat}}\right\} \ , \tag{2.77}$$

with $\psi^{\text{mat}}$ specified in (2.69). Here, this sub-problem can be carried out analytically which yields the optimal strain jump (projected onto $\hat{\boldsymbol{n}}_{12}^{\text{tw}}$)

$$\boldsymbol{a}^*(\boldsymbol{p}\backslash\boldsymbol{a}) := \arg\inf_{\boldsymbol{a}} \left\{\psi^{\text{mat}}\right\} = -\left[\,\hat{\boldsymbol{n}}_{12}^{\text{tw}}\cdot\mathsf{E}\cdot\hat{\boldsymbol{n}}_{12}^{\text{tw}}\,\right]^{-1}\cdot\left[\,\hat{\boldsymbol{n}}_{12}^{\text{tw}}\cdot\mathsf{E} : [\,\boldsymbol{\varepsilon}_2^{\text{tr}} - \boldsymbol{\varepsilon}_1^{\text{tr}}\,]\right] \ . \tag{2.78}$$

The effective material behaviour in terms of stresses is given by

$$\boldsymbol{\sigma} := \partial_{\boldsymbol{\varepsilon}}\psi^{\text{mat}} = \mathsf{E} : [\,\boldsymbol{\varepsilon} - \boldsymbol{\varepsilon}^{\text{tr}}\,] \tag{2.79}$$

with the averaged transformation strains

$$\boldsymbol{\varepsilon}^{\text{tr}} := \sum_{i=1}^{2} \xi_i\,\boldsymbol{\varepsilon}_i^{\text{tr}} \ . \tag{2.80}$$

In order to reproduce the material response obtained via experiments on single crystal Ni$_2$MnGa specimens, see, for instance, [71, 76, 111], the effect of prescribed constant stresses has to be taken into account, cf. $\overline{\boldsymbol{\sigma}}$ in (2.34). The strains which exactly yield the stress state to be prescribed are therfore still to be determined. Here, the linear relation (2.79) can be used to find

$$\boldsymbol{\varepsilon}(\boldsymbol{p}) = \mathsf{E}^{-1} : \overline{\boldsymbol{\sigma}} + \boldsymbol{\varepsilon}^{\text{tr}} \ , \tag{2.81}$$

which enters the energy function $\widetilde{\Pi}^{\text{hom}}$ in (2.34), including the stored energy density $\psi^{\text{mat}}$ (2.69). The inverse of the elasticity tensor is often also referred to as the compliance tensor $\mathsf{S} := \mathsf{E}^{-1}$, cf. [112].

In addition to the analytical solution for the optimal strain jump $\boldsymbol{a}$ as outlined in (2.78), the equality constraint $\xi_1 + \xi_2 = 1$ in (2.51) might be used to reduce the number of variables and constraints by, e.g., replacing $\xi_2 = 1 - \xi_1$. As shown in the appendix, see Section 2.5.1, the following relations between the magnetisation orientations among the domains of one martensite variant hold

$$\theta_2 \equiv -\theta_1 \ , \quad \theta_4 \equiv -\theta_3 \ . \tag{2.82}$$

This allows a further reduction of the number of variables and inequality constraints to be considered.

### 2.2.4 Summary of constitutive equations

This section summarises the essential problem to be solved. The values for the variables at time $t_{n+1}$, i.e.

$$\boldsymbol{p}_{n+1} := \{\xi_{1,n+1}, \xi_{2,n+1}, \eta_{1,n+1}, \eta_{2,n+1}, \theta_{1,n+1}, \theta_{2,n+1}, \theta_{3,n+1}, \theta_{4,n+1}, \boldsymbol{a}_{n+1}, \varphi_{n+1}\} \tag{2.83}$$

are determined via

$$\boldsymbol{p}_{n+1} = \arg\min \left\{ \widetilde{\Pi}^{\text{hom}}_{n+1}(\boldsymbol{p}_{n+1}) + \mathfrak{D}(\boldsymbol{p}_{n+1}, \boldsymbol{p}_n) \right\} \tag{2.84}$$

subject to

$$\begin{aligned} \xi_{i,n+1} \geq 0 \ , \quad \xi_{1,n+1} + \xi_{2,n+1} = 1 \ , \quad |\eta_{i,n+1}| \leq \xi_{i,n+1} \ , \quad \text{with } i = 1, 2 \ , \\ |\theta_{j,n+1}| \leq \pi/2 \ , \quad \text{with } j = 1, \ldots, 4 \ , \end{aligned} \tag{2.85}$$

where $\mathfrak{D}(\boldsymbol{p}_{n+1}, \boldsymbol{p}_n)$ is given by (2.75). With the analytical solution for $\boldsymbol{a}_{n+1}$, cf. (2.78), instead of $\widetilde{\Pi}^{\text{hom}}_{n+1}$, the partially relaxed energy-enthalpy function at time $t_{n+1}$ for the underlying case of homogeneous states might be used

$$\begin{aligned} \widetilde{\Pi}^{\text{hom,rel}}_{n+1} := \Big[ & R_1\psi^{\text{mat}}(\boldsymbol{p}_{n+1} \backslash \boldsymbol{a}_{n+1}) + \frac{\mu_0}{2}\, \boldsymbol{m}(\boldsymbol{p}_{n+1} \backslash \boldsymbol{a}_{n+1}) \cdot \boldsymbol{D} \cdot \boldsymbol{m}(\boldsymbol{p}_{n+1} \backslash \boldsymbol{a}_{n+1}) \\ & - \mu_0\, \overline{\boldsymbol{h}}_{n+1} \cdot \boldsymbol{m}(\boldsymbol{p}_{n+1} \backslash \boldsymbol{a}_{n+1}) - \overline{\boldsymbol{\sigma}}_{n+1} : \boldsymbol{\varepsilon}(\boldsymbol{p}_{n+1} \backslash \boldsymbol{a}_{n+1}) \Big] V_{\mathcal{B}} \end{aligned} \tag{2.86}$$

with $R_1\psi^{\text{mat}}(\boldsymbol{p}_{n+1} \backslash \boldsymbol{a}_{n+1})$ determined by (2.77), $\boldsymbol{\varepsilon}(\boldsymbol{p}_{n+1} \backslash \boldsymbol{a}_{n+1})$ is specified in (2.81), and $\boldsymbol{m}(\boldsymbol{p}_{n+1} \backslash \boldsymbol{a}_{n+1})$ is defined in (2.52). The quantities $\overline{\boldsymbol{h}}_{n+1}$ and $\overline{\boldsymbol{\sigma}}_{n+1}$ denote the prescribed values of the magnetic field and stresses at time $t_{n+1}$.

Standard solvers of nonlinear constrained minimisation can be utilised to find the solution of (2.84) subject to (2.85), cf. [13, 137]. For the numerical examples presented in the following section, the `GlobalSearch` and `MultiStart` functions of the MATLAB optimisation toolbox were employed. Further details regarding the numerical implementation are outlined in [112].

**Table 2.1:** Material parameters for $Ni_2MnGa$ (slightly off-stoichiometric composition with five-layered modulated tetragonal structure).

| Model parameter | Symbol | Value | Unit | Reference |
|---|---|---|---|---|
| Young's modulus | $E$ | 5000.0 | MPa | — |
| Poisson's ratio | $\nu$ | 0.3 | — | — |
| Saturation magnetisation | $m_s$ | 514.0 | kA/m | [76] |
| Anisotropy constant | $k_1$ | 0.167 | $MJ/m^3$ | [76] |
| Dissipation coefficient | $\mathsf{Y}_\xi^0$ | 0.03 | $MJ/m^3$ | — |
| Dissipation coefficient | $\Delta\mathsf{Y}_\xi$ | 0.003 | $MJ/m^3$ | — |
| Bain strain coefficient | $b_1$ | 0.0188 | | [204] |
| Bain strain coefficient | $b_2$ | - 0.0394 | — | [204] |
| Demagnetisation coefficient | $D_{11}$ | 0.2154 | — | — |

## 2.3 Numerical examples

In this section, the response of prismatic single-crystalline $Ni_2MnGa$ MSMA specimens to magneto-mechanical loading—which is the typical experimental scenario [111, 204]—is modelled with a focus on the martensitic variant reorientation or, in other words, the *variant switching* behaviour. The material constants and model parameters used for all simulations are listed in Table 2.1. For the considered prismatic specimen (length: 9 mm, width: 5 mm, height: 5 mm, cf. Heczko [71], Straka et al. [204]), the demagnetisation tensor has the form

$$\boldsymbol{D} = D_{11}\,\boldsymbol{e}_1 \otimes \boldsymbol{e}_1 + \frac{1 - D_{11}}{2}\,[\,\boldsymbol{e}_2 \otimes \boldsymbol{e}_2 + \boldsymbol{e}_3 \otimes \boldsymbol{e}_3\,]\ , \tag{2.87}$$

where the demagnetisation coefficient $D_{11}$ in Table 2.1 was calculated in advance using a magnetostatic finite element simulation.

### 2.3.1 Variant switching diagrams

The term *phase diagram* for MSMAs was introduced in [107, 108], see also DeSimone [39] and others, in analogy to the concept of phase diagrams in SMA modelling [124]. Unlike the critical stress-temperature surfaces for the austenite-martensite phase transformation in conventional SMAs, phase diagrams in MSMA visualise the initiation and termination of the *variant reorientation*, i.e. the stress and magnetic field-driven switching between different variants of the martensite phase. We consequently refer to them as *variant switching diagrams* in this publication.

The calculations underlying the results shown in this section are designed to determine critical states of the martensite reorientation processes, namely the initiation and the completion of variant switching in $Ni_2MnGa$ as functions of applied stresses and magnetic fields. To this end, a first set of numerical studies were performed under the loading conditions illustrated in Figure 2.3. Here, a single crystal specimen, initially entirely in the stress-favoured variant state, potentially switches to the magnetic field-favoured variant under the action of the applied magnetic field $\overline{\boldsymbol{h}} = \overline{h}_2(t)\,\boldsymbol{e}_2$ and the constant compressive bias stress $\overline{\boldsymbol{\sigma}} = \overline{\sigma}_{11}\,\boldsymbol{e}_1 \otimes \boldsymbol{e}_1$. See, e.g., [71, 202] for experimentally determined response curves under similar loading conditions.

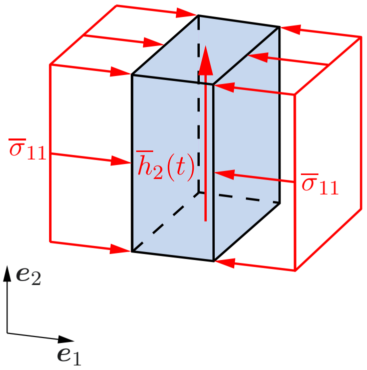

**Figure 2.3:** Illustration of the applied loading for the magnetic field-driven numerical studies under constant stress. Initial conditions: single variant 1 state ($\xi_1 = 1$) with zero net magnetisation ($\eta_1 = 0$).

Figure 2.4 shows the corresponding variant switching diagram. The indicated switching surfaces—here lines representing their traces in the two-dimensional plot—were obtained in the following manner: The load was increased in small loading steps and the critical state was detected when $\xi_2$—initially being zero—exceeded a specific tolerance value ($\text{tol} = 10^{-4}$). The various points determined in this manner were then used to define a regression curve (solid red line). The dashed red line analogously denotes the states where the reorientation into variant 2 is completed, i.e. a value of $\xi_2 > 1 - \text{tol}$ is reached for the first time. During unloading, the reverse reorientation process into variant 1 is indicated by the dashed blue line (initiation) and the solid blue line (completion). A total of five response regions can be distinguished in the switching diagram for different applied stress levels: (I) For low stress levels, a full reorientation process ($1 \rightarrow 2$) occurs, but the initially present martensite variant 1 will not form again during unloading. (II) While the behaviour during loading is essentially the same, reverse switching does occur when unloading at higher stress levels, however not completely. (III) The reorientation into the stress-favoured variant 1 is always completed during unloading at these now sufficiently large bias stress levels. (IV) The reorientation process is no longer completed during loading, since the mechanism of magnetisation rotation becomes energetically relatively less costly. However, the partially-switched material is always completely reoriented into variant 1 after unloading. (V) For compressive stress levels above the *blocking stress*, see Kiefer et al. [111], the variant switching process is never initiated.

**Remark 2** *Regression curves are used to smooth the nonlinear segments in the curves that represent the initiation and completion of the variant switching in Figure 2.4 and* *of all following martensite variant switching diagrams. The horizontal, respectively vertical, segments are not taken into account for the determination of the regression curves. Hence, the plotted curves may consist out of multiple segments.*

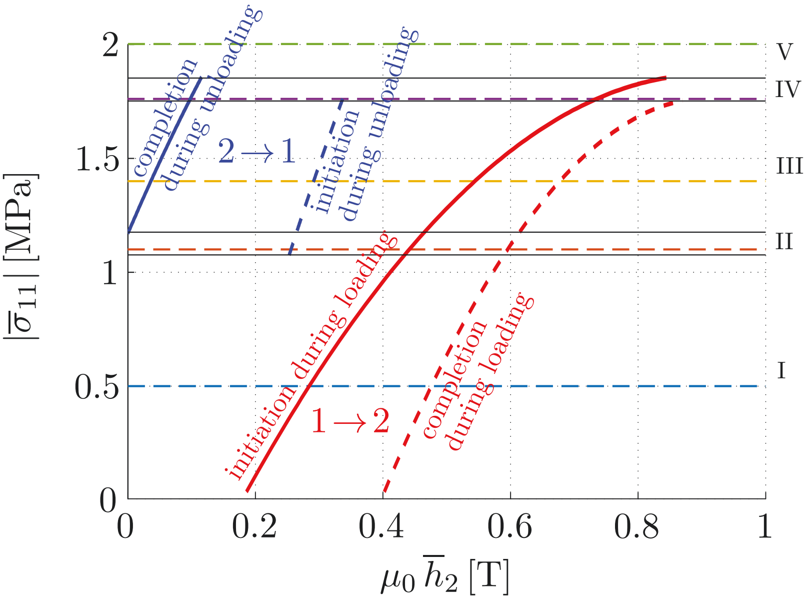

**Figure 2.4:** Martensite variant switching diagram. Compressive stresses $\overline{\sigma}_{11}$ are kept constant during several calculations with different prescribed values, while one loading/unloading half cycle is performed with respect to the magnetic field $\mu_0\,\overline{h}_2 \in [\,0\,\mathrm{T}, 1\,\mathrm{T}\,]$. The red lines indicate the critical states of variant reorientation during loading, whereas the blue lines indicate the same during unloading. The black solid horizontal lines separate five different regions characterised by complete, partial, or even fully-suppressed forward/reverse variant switching.

For each of the response regions (I)–(V) discussed above, characteristic strain and magnetisation curves are depicted in Figure 2.5. The corresponding stress levels have also been indicated in the switching diagram of Figure 2.4 by dashed horizontal lines of matching colour. The nonlinearity of both the predicted strains—which are shifted in the plot by a respective elastic and variant 1 Bain strain offset for better comparability—as well as the magnetisation responses clearly reflect the occurrence of the variant reorientation process. Moreover, their observed hysteretic nature solely stems from dissipative effects associated with the corresponding twin boundary motion. Similar variant switching diagrams were previously proposed in Kiefer and Lagoudas [110]. In this approach, however, variant switching, magnetisation rotation, and magnetic domain evolution could not occur simultaneously. The energy relaxation-based MSMA model presented here, on the other hand, is not limited by such restrictions.

The next set of results stems from similar calculations as mentioned before, except that the applied magnetic field $\overline{\boldsymbol{h}} = \overline{h}_2\,\boldsymbol{e}_2$ is now kept constant—at different levels for each calculation—and the applied stress $\overline{\boldsymbol{\sigma}} = \overline{\sigma}_{11}(t)\,\boldsymbol{e}_1 \otimes \boldsymbol{e}_1$ is varied in a loading-unloading

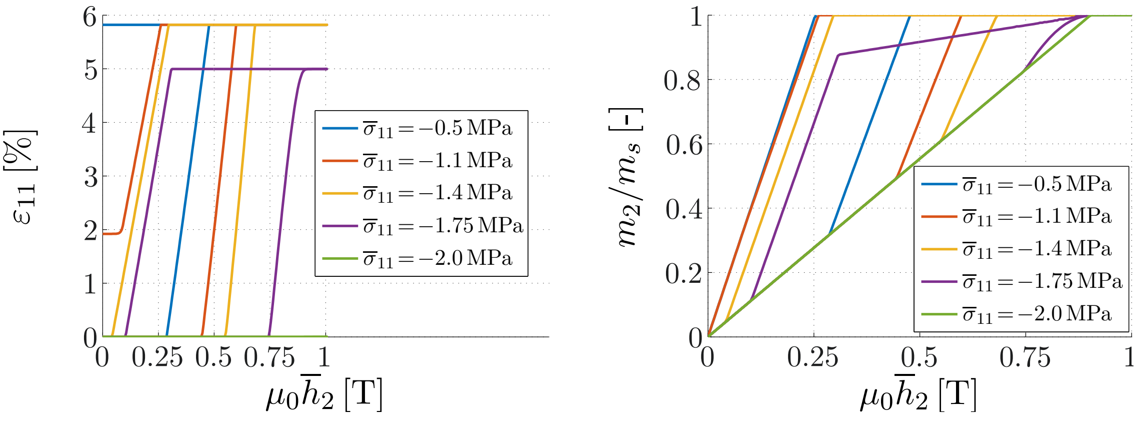

(a) (b)

**Figure 2.5:** Magnetic field-induced (a) strain and (b) magnetisation response curves exemplarily selected for each of the five response regions defined in Figure 2.4. The different behaviour patterns are due to complete or partial variant reorientation (during loading and/or unloading) as well as fully-suppressed variant switching for compressive stresses above the blocking stress.

half cycle between 0.0 and 10.0 MPa, see Figure 2.6 and, e.g., [71] for experimentally determined response curves under similar loading conditions. In this case, the initial state is that of the magnetic field-favoured variant. The variant switching diagram for this loading case is shown in Figure 2.7. The dashed blue line connects critical states at which the switching into the first variant starts ($\dot{\xi}_1 > 0$). The solid blue line indicates the states where this process is completed ($\xi_1 = 1$). During unloading, critical values for the potential reverse reorientation into variant 2 are illustrated by the solid red line (initiation) and the dashed red line (completion), respectively. Due to the lack of an alternative mechanism to reduce the strain energy, there is always a complete switching into the stress-favoured variant under compressive stress loading at constant magnetic bias fields. During unloading, however, three different response regions can be distinguished: (I) For low magnetic fields, no reverse reorientation occurs. (II) For higher levels of the applied magnetic field, martensite variant 2 begins to form, but is not fully regained. (III) The behaviour is similar to (II), except that the variant switching to the magnetic field-favoured variant 2 is always completed at these sufficiently large magnetic bias field levels. It is important to point out that the variant switching diagrams under magnetic field-driven (Figure 2.4) and stress-driven (Figure 2.7) loading in fact coincide. In other words, the critical surfaces perfectly match—albeit that not all such points can actually be reached under magnetic loading at constant stress.

For each of the response regions (I)–(III) mentioned above, i.e. corresponding stress-driven simulations at three distinct levels of the bias magnetic field, the representative strain—which are shifted in the plot by a respective elastic and variant 2 Bain strain offset for better comparability—and magnetisation responses are depicted in Figure 2.8.

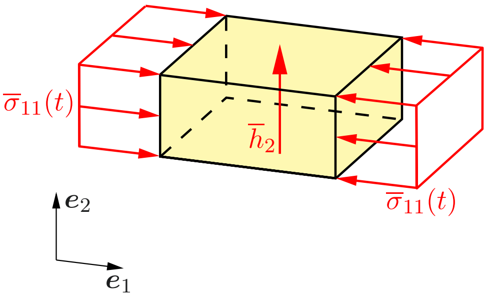

**Figure 2.6:** Illustration of the applied loading for the stress-driven numerical studies under constant magnetic field. Initial conditions: single variant 2 state ($\xi_2 = 1$) with zero net magnetisation ($\eta_2 = 0$).

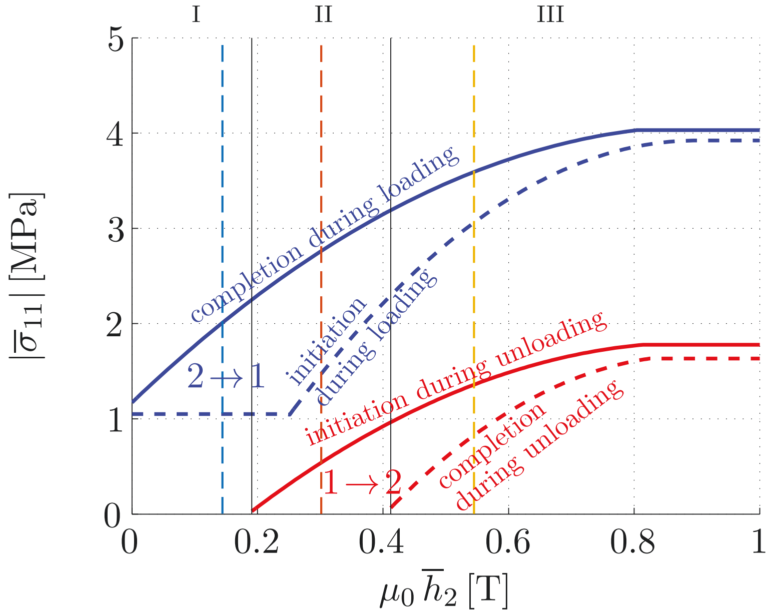

**Figure 2.7:** Martensite variant switching diagram. The magnetic field $\mu_0\,\overline{h}_2 \in [\,0\,\mathrm{T}, 1\,\mathrm{T}\,]$ is kept constant during several calculations with different prescribed values, while one loading/unloading half cycle is performed with respect to the compressive stress $\overline{\sigma}_{11}$. The black solid vertical lines separate three different regions characterised by complete, partial, or even fully-suppressed reverse variant switching during unloading.

The selected loading paths have again been indicated in the associated variant switching diagram (Figure 2.7). It should be pointed out that, although the initial condition is set to $\eta_2 = 0$, the initial net magnetisation of the specimen observed in the magnetisation curves of Figure 2.8 (b) is not zero. The calculations in the first step—at zero stress—correctly predict a reduction of the unfavourably-oriented domain type at low fields ($\mu_0\,\overline{h}_2 = 0.13\,\mathrm{T}$) and even their complete elimination at higher fields ($\mu_0\,\overline{h}_2 = 0.30\,\mathrm{T}$ and $0.55\,\mathrm{T}$), yielding not only a single variant, but also a single domain state to which the stress loading is subsequently applied.

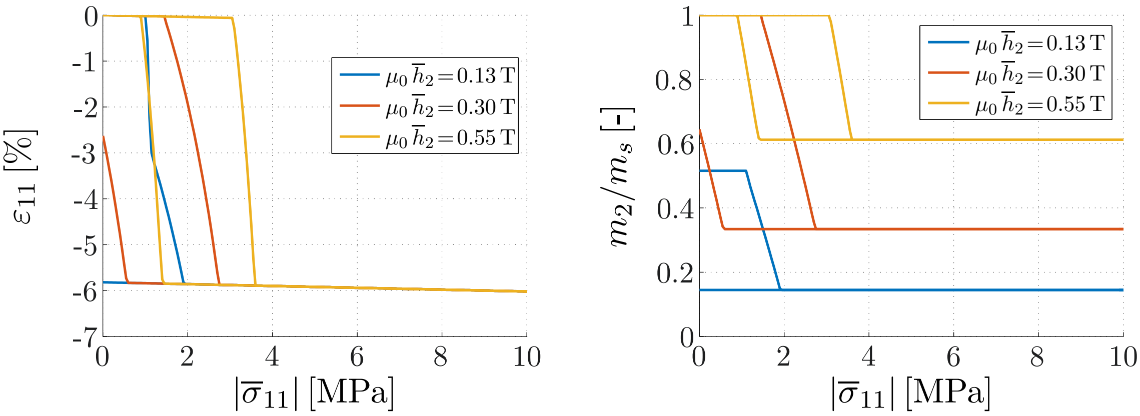

(a) (b)

**Figure 2.8:** Stress-induced (a) strain and (b) magnetisation response curves exemplarily selected for each of the three response regions defined in Figure 2.7. The different behaviour patterns indeed reflect complete, partial, or no variant reorientation during unloading.

The response with full recovery of the magnetic field-favoured variant (yellow curve) has been referred to as the *magnetic field-biased super-, magneto-, or pseudoelastic effect* [99, 110, 159, 201, 203] in the literature. Responses with partially or fully-suppressed reverse switching (orange and blue curves) have been termed *magnetic field-biased superplasticity* [201], or simply *magneto-plasticity* [99, 159]—although both labels are somewhat misleading, since, unlike plastic deformation, variant switching is a crystallographically reversible effect. This phenomenon is more comparable to the one-way shape memory effect [124], with the magnetic field playing the role of temperature as a means to recover the initial state that is not reached when unloading.

The loading conditions for the last example related to variant switching diagrams are illustrated in Figure 2.9. Here, one component of the applied magnetic field $\overline{\boldsymbol{h}} = \overline{h}_1(t)\,\boldsymbol{e}_1 + \overline{h}_2\,\boldsymbol{e}_2$ is varied over time, namely $\mu_0\,\overline{h}_1(t) \in [\,0\,\mathrm{T}, 1.75\,\mathrm{T}\,]$, while the other component is held fixed at different levels. Such loading effectively corresponds to a rotating applied magnetic field vector with varying magnitude—which might seem difficult to apply and interpret from a physical view. In practice, however, this can be realised with a variable magnetic field applied through an electromagnet or enveloping solenoid promoting one variant and a counteracting perpendicularly-arranged permanent magnet favouring the other. The assumed *zero-stress* conditions, on the other hand, are always an approximation—albeit usually quite reasonable—, since, in the experiment, one must (mechanically) prevent free rotation of the specimen under magnetic field application.

The predicted variant switching diagram for these load cases is shown in Figure 2.10. Again, blue lines indicate critical switching points, in terms of initiation (dashed line) and completion (solid line), from variant 2, preferred by the constant magnetic field $\overline{h}_2$, into variant 1, in this case favoured by the magnetic field $\overline{h}_1$. This switching under magnetic

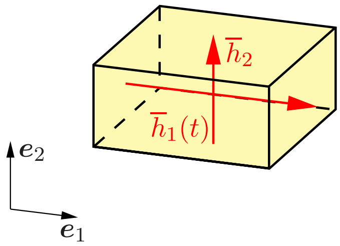

**Figure 2.9:** Illustration of the applied loading for the magnetic field-driven numerical studies under perpendicular magnetic bias field at zero stress. Initial conditions: single variant 2 state ($\xi_2 = 1$) with zero net magnetisation ($\eta_2 = 0$).

field loading is always completed for all bias field levels. The critical switching points during unloading are indicated by red lines for the initiation (solid line) and completion (dashed line) of the variant switching. Again, three different response regions may occur: (I) For low $\overline{h}_2$ levels, the energetic incentive to switch back is insufficient and no reverse reorientation occurs. (II) For higher bias field values, martensite variant 2 forms again, but will not be fully regained. (III) The behaviour is similar to (II), except that the reverse switching into the $\overline{h}_2$-favoured variant is completed.

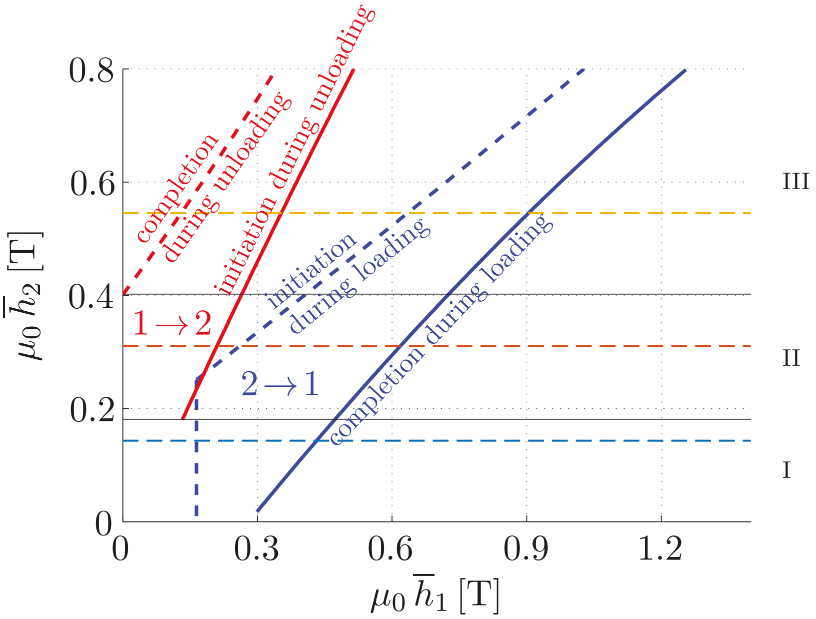

**Figure 2.10:** Martensite variant switching diagram. The magnetic field $\mu_0\overline{h}_2 \in [\,0\,\mathrm{T}, 0.8\,\mathrm{T}\,]$ is kept constant during several calculations with different prescribed values, while one loading/unloading half cycle is performed with respect to $\overline{h}_1$. The black solid horizontal lines distinguish three different regions, which are characterised by complete, partial, or no variant reorientation during unloading.

Predicted strains—which are shifted in the plot by a respective elastic and variant 2 Bain strain offset for better comparability—and magnetisation curves for three distinct bias field levels, each representing one of the characteristic response regions (I)–(III), are shown in Figure 2.11. Some interesting observations can be made by comparing these results to the corresponding curves of Figure 2.8. While the induced strain responses are qualitatively very comparable under stress and magnetic field loading—except for the slight slopes in the strain curves caused by elastic deformations in the former case—the magnetisation responses are actually quite different. They begin and end up at identical vertical axis intercepts, i.e. at the same magnetisation values at zero cyclic loading. Under $\overline{h}_1$ magnetic field loading—at constant $\overline{h}_2$—, however, the magnetisation curves show significant nonlinearity in the pre- and post-switching response stages. This effect is caused by the rotation of local magnetic moments away from the easy-axis in variant 2—and later analogously towards the easy-axis in variant 1—as the $\overline{h}_1$ field is increased at constant $\overline{h}_2$. The reverse is true for unloading. In the loading region, where the response is dominated by variant switching, the magnetisation curves are essentially linear. The magnetisation responses at the lowest bias field level ($\mu_0\,\overline{h}_2 = 0.13\,\mathrm{T}$) further suggests the activation of domain wall motion—see, for instance, the constant $m_2$ response in the direction of the $\overline{h}_2$ at low loading/unloading fields—, where the initial and final configuration are multi-domain settings. These allow the magnetisation to rotate in the $\overline{h}_1$ direction, while being constant in the $\overline{h}_2$ direction. To better understand the interplay of these mechanisms and their influence on the effective MSMA behaviour as predicted by the proposed model, the next section will take a closer look at the evolution of microstructures—in terms of their internal state variable representation—along selected loading paths.

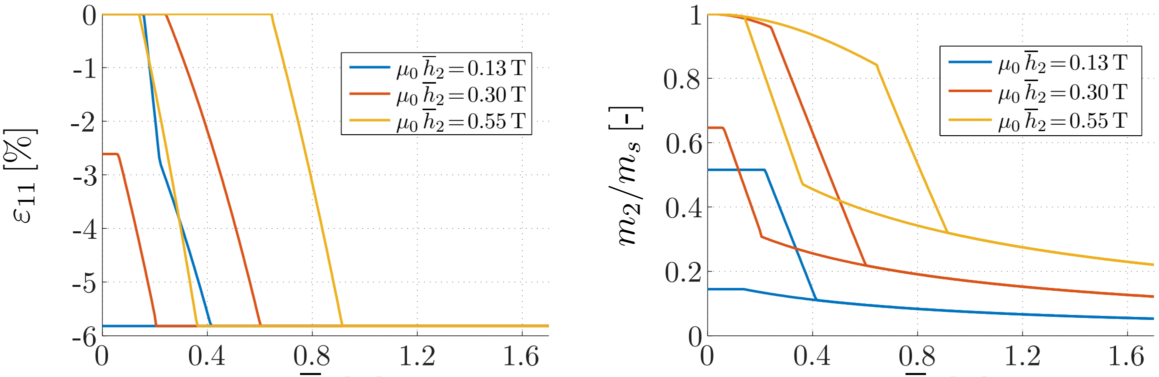

(a) (b)

**Figure 2.11:** Selected magnetic field induced (a) strain and (b) magnetisation response curves under constant magnetic field $\overline{h}_2$ and perpendicular magnetic field $\overline{h}_1(t)$ for each of the three different response regions defined in Figure 2.10. The different behaviour patterns are due to complete, partial, or fully-suppressed variant reorientation during unloading.

### 2.3.2 The connection of effective material responses to microstructure evolution

In this section, we return to selected results previously presented in Section 2.3.1, in order to more carefully interpret the effective responses in terms of the underlying microstructure evolution, as predicted by the energy relaxation-based model. All strain response curves are shifted in the plots by a respective elastic and Bain strain offset for better comparability.

As the first example, we again consider the response simulations for the load case of magnetic field-driven variant reorientation under constant bias stress (see Figure 2.5), particularly at the compressive stress levels of $\overline{\sigma}_{11} = -1.1\,\mathrm{MPa}$ and $-1.75\,\mathrm{MPa}$. Figure 2.12 shows these responses, this time for a full loading cycle, and is further enriched by microstructural sketches at selected loading stages, labelled ① to ⑥. As a natural consequence of our approach to not spatially resolve the microstructure, but to effectively represent it in terms of a set of microstructural variables, these sketches reflect the idealised microstructure only in the sense of variant, respectively domain, volume fractions and magnetisation vector orientations. For the sake of simplicity, the calculated twin boundary orientation—which, in fact, turned out to be constant at $\varphi = 45°$ regardless of the loading conditions—is not indicated in these sketches.

The microstructure evolves as follows: Starting in ① from a macroscopically unmagnetised single variant 1 state, the application of the magnetic field $\overline{h}_2$ firstly causes a rotation of the local magnetisation vectors. At a certain stage in ②, it becomes energetically less costly to switch into the second martensite variant, while the rotation of the magnetisation vectors in variant 1 still slightly increases, cf. ③. The second variant then grows at the expense of the first—this is interpretable as twin boundary motion—until it is either entirely eliminated and the largest possible magnetic field-induced strain is obtained under constant $\overline{\sigma}_{11} = -1.1\,\mathrm{MPa}$ or the magnetisation in the direction of the applied magnetic field saturates and the switching process stops under constant $\overline{\sigma}_{11} = -1.75\,\mathrm{MPa}$. The final configuration during loading is shown in ④. Upon unloading, the reverse switching is initiated at a much lower field than was needed to complete the forward process, which effectively results in hysteretic behaviour. The initial first $\sigma_{11}$-favoured martensite variant grows during unloading, wherein the volume fractions of both domains are equal, as shown in ⑤. At zero magnetic field loading under constant $\overline{\sigma}_{11} = -1.1\,\mathrm{MPa}$, see ⑥, one observes a state in which all variant/domain combinations are present. For this stress, however, while the overall magnetisation correctly averages to zero—thus minimising the demagnetisation field energy—the volume fractions are such that a remanent strain results. For the higher compression stress $\overline{\sigma}_{11} = -1.75\,\mathrm{MPa}$, the initial martensite variant is completely recovered in ⑥ and the configuration at zero magnetic field is identical to the initial configuration in ①.

Similarly, we again consider the case of stress-driven loading at constant magnetic bias field (see Figure 2.8), particularly $\mu_0\,\overline{h}_2 = 0.3\,\mathrm{T}$. Figure 2.13 shows the computed strain and magnetisation response curves and visualises associated microstructures for four dif-

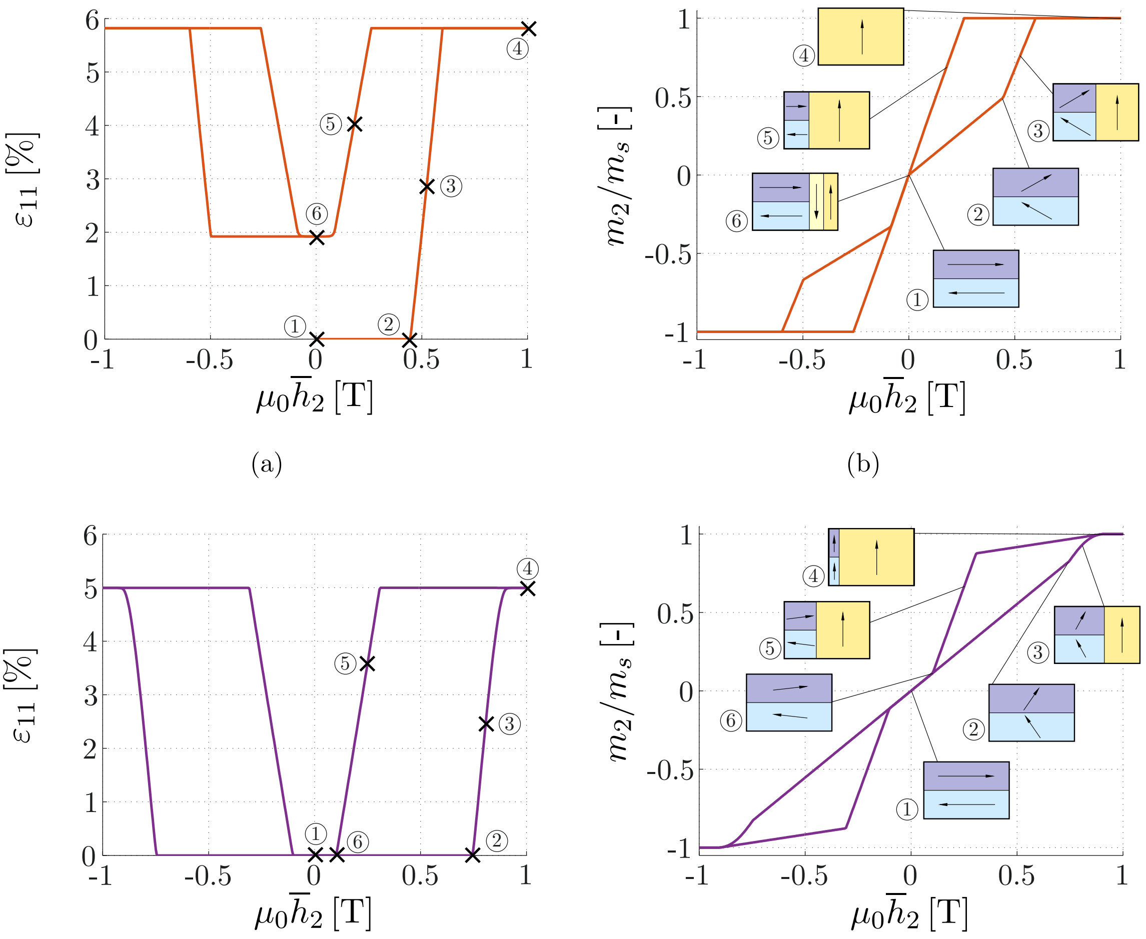

(a) (b)

(c) (d)

**Figure 2.12:** Predicted butterfly hysteresis curves, in terms of magnetic field-induced strain (left column) and magnetisation responses (right column) for two selected loading cases (cf. Figure 2.5). Graphs (a) and (b) show the response for the bias stress level of $\overline{\sigma}_{11} = -1.1\,\text{MPa}$, (c) and (d) those for $\overline{\sigma}_{11} = -1.75\,\text{MPa}$. The attached sketches reflect the state of the microstructure in terms of variant/domain volume fractions and local magnetisation orientations, for six characteristic loading stages. The twin boundary orientation of $\varphi = 45°$ is not visualised for the sake of simplicity. Sketched mechanism: magnetisation vector rotation, martensite variant switching, and domain wall motion.

ferent stages during the loading/unloading sequence. The microstructure evolves as follows: Starting from a single variant and in this case also single domain, i.e. magnetically-saturated state, the compressive stress loading causes slight elastic deformation but initially no changes in the magnetisation, as we have neglected conventional magnetostriction. After variant switching is initiated in ①, variant 1 shows domains in which the magnetisation vectors are slightly rotated towards the bias field direction, see ②. This interplay of mechanisms clearly has a nonlinear effect on the strain response. Once the variant reorientation process is completed in ③, the magnetisation again stays constant during further load increase. The domain volume fractions and the magnetisation rotations are such that they compensate each other in the $\boldsymbol{e}_1$-direction, in which no magnetic field is applied, and the magnetisation $m_1$ is equal to zero. During unloading, variant 1 partially switches back, see ④. But, at zero stress, neither a single variant nor a single domain state is reached for the given bias field level, so that both remanent straining as well as magnetisation are observed.

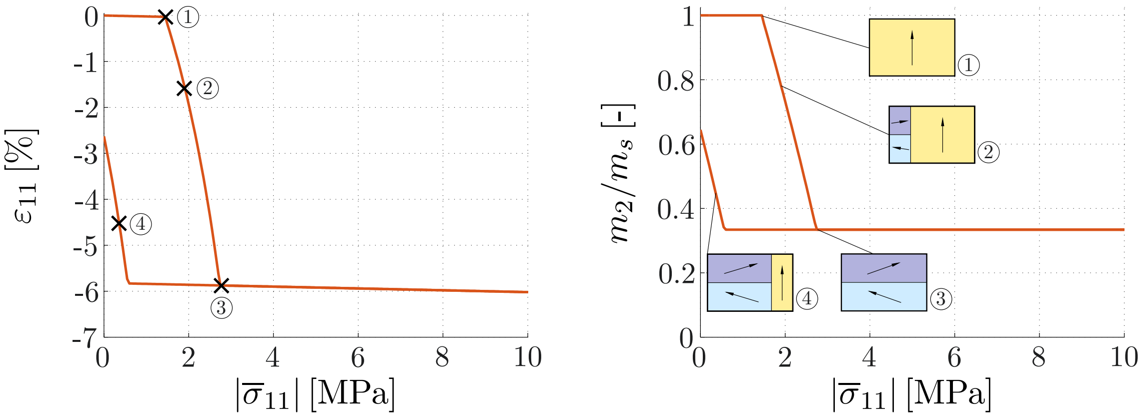

(a) (b)

**Figure 2.13:** Predicted hysteresis curves, in terms of compression stress-induced (a) strain and (b) magnetisation responses for the bias field level of $\mu_0\,\overline{h}_2 = 0.3\,\mathrm{T}$ (cf. Figure 2.8). The attached sketches reflect the state of the microstructure in terms of variant/domain volume fractions and local magnetisation orientations for four characteristic loading stages. Again, the twin boundary orientation of $\varphi = 45°$ is not visualised for the sake of simplicity. Sketched mechanism: magnetisation vector rotation and martensite variant switching.

Finally, we return to the load case of magnetic field-driven variant switching under the influence of a perpendicularly applied bias field of $\mu_0\,\overline{h}_2 = 0.3\,\mathrm{T}$ and stress-free conditions (see Figure 2.11). Figure 2.14 again shows the predicted hysteretic magnetic field-induced strain and magnetisation responses for a complete loading cycle, with seven selected loading stages highlighted in terms of their microstructural state. To better understand the full impact that the microstructure evolution has on the effective response, the strain and magnetisation components in the respective other field directions have now also been included.

The microstructure evolves as follows: Starting from a single 2nd martensite variant and magnetically-saturated single domain state in ①, the field application in the $\boldsymbol{e}_1$-direction causes a rotation away from the variant 2 easy-axis, see ②. While this effect has a linear influence on $m_1$, it clearly introduces nonlinearity in $m_2$. When variant switching is initiated in ②, variant 1 forms in a single domain state, since—unlike under stress loading—domains can now be favourably or unfavourably oriented (magnetised) with

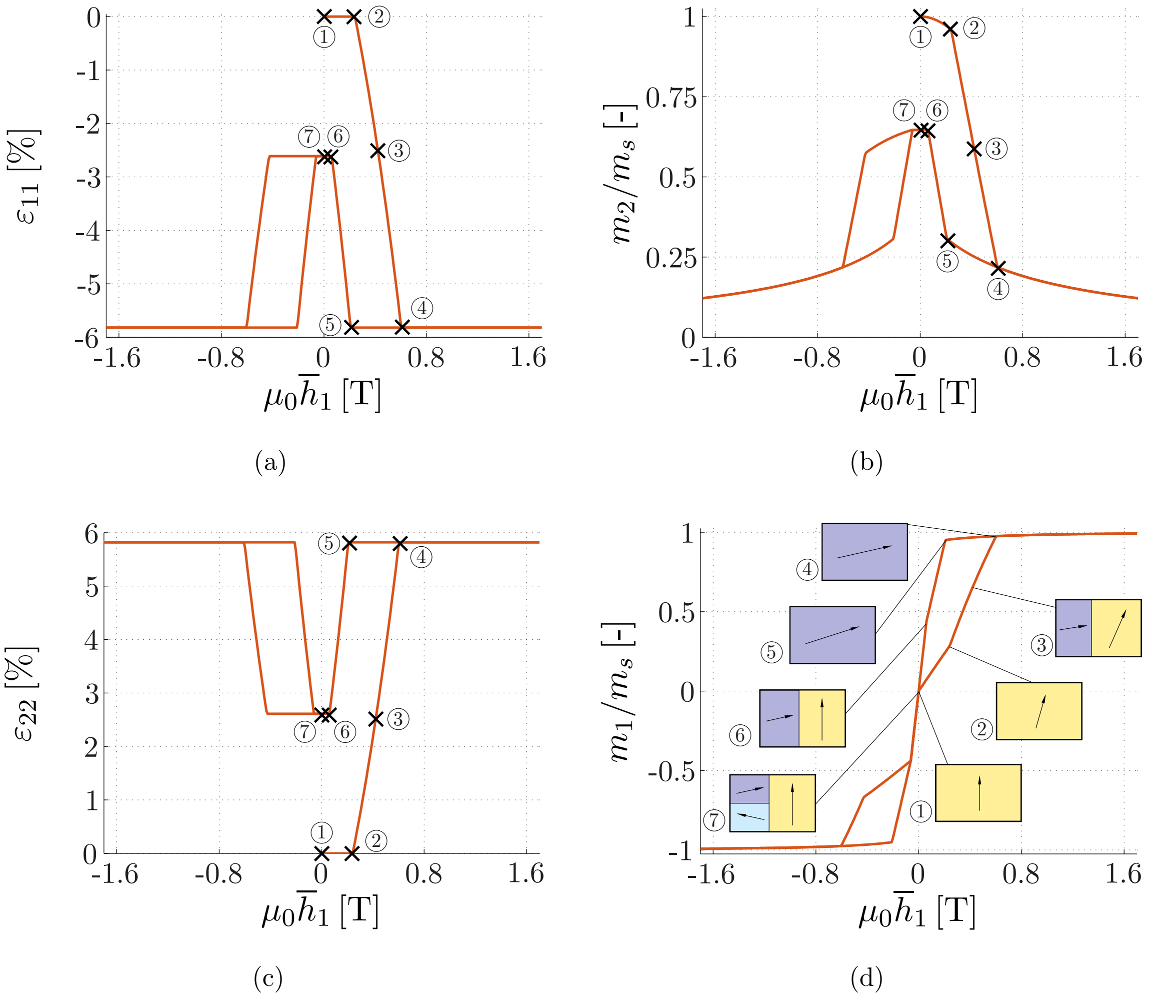

**Figure 2.14:** Predicted butterfly hysteresis curves, in terms of magnetic field-induced strain (left column) and magnetisation responses (right column) under a perpendicular bias field of $\mu_0\,\overline{h}_2 = 0.3\,\mathrm{T}$. Graphs (a) and (b) show the plots previously presented in Figure 2.11—here for a full loading cycle—which are now supplemented by the graphs (c) and (d) showing the corresponding responses in the respective other field directions. The attached sketches reflect the state of the microstructure in terms of variant/domain volume fractions and local magnetisation orientations, for seven characteristic loading stages. The twin boundary orientation of $\varphi = 45°$ is not visualised for the sake of simplicity. Sketched mechanism: magnetisation vector rotation, martensite variant switching, and domain wall motion.

respect to the applied field, see ③. Further load increase eventually again results in a single variant, single domain state in ④ with a slight rotation of the magnetisation vector towards the direction of the bias field. This rotation increases as the $h_1$-loading becomes less influential during unloading, see ⑤. It then becomes energetically preferential to initiate the reverse switching process in ⑤, which stops in ⑥. However, at zero $\overline{h}_1$ load in ⑦, remanent strains—reflecting a remaining variant mixture—and non-vanishing $m_2$

magnetisation are observed. In contrast, the value of $m_1$ at $\overline{h}_1 = 0$ is zero, due to the emergence of the second domain type in variant 1 at low applied $\overline{h}_1$ field levels.

### 2.3.3 The influence of the shape anisotropy and a closer look at the demagnetisation effect

The first example presented in this section dealing with numerical results is devoted to the investigation of the influence of specimen shape orientation, which corresponds to the well-known effect of *shape anisotropy* in magnetostatics. To study this phenomenon, the prismatic specimen under consideration—but not the single-crystalline material itself—is rotated through the angle $\beta$ in the $\boldsymbol{e}_1$-$\boldsymbol{e}_2$-plane. Consequently, the crystal orientation, including the magnetic easy-axes, and the loading directions are still assumed to be aligned with the respective coordinate axes. The demagnetisation tensor, however, is updated according to

$$\boldsymbol{D} := \boldsymbol{R} \cdot \boldsymbol{D}^{\text{ref}} \cdot \boldsymbol{R}^{\text{t}} \, , \tag{2.88}$$

where

$$\boldsymbol{R} := \cos(\beta) \, [\, \boldsymbol{e}_1 \otimes \boldsymbol{e}_1 + \boldsymbol{e}_2 \otimes \boldsymbol{e}_2 \,] + \sin(\beta) \, [\, -\boldsymbol{e}_1 \otimes \boldsymbol{e}_2 + \boldsymbol{e}_2 \otimes \boldsymbol{e}_1 \,] + \boldsymbol{e}_3 \otimes \boldsymbol{e}_3 \tag{2.89}$$

is a proper-orthogonal rotation operator—with the usual properties of $\boldsymbol{R}^{\text{t}} = \boldsymbol{R}^{-1}$ and $\det \boldsymbol{R} = 1$—and where $\boldsymbol{D}^{\text{ref}}$ denotes the reference demagnetisation tensor that was defined in (2.87).

The computed influence of selected specimen orientations ($\beta = \pm 30°$) on the magnetic field-induced strain—which are shifted in the plot by a respective elastic and variant 1 Bain strain offset for better comparability—and on the magnetisation hysteresis curves is presented in Figure 2.15. The rotation of the specimen with respect to the magnetic loading directions affects the coefficients of the demagnetisation tensor, according to (2.88), and consequently clearly influences the effective specimen response. This effect of the shape anisotropy is most easily observed in the $m_1$-response which, under the original specimen orientation ($\beta = 0$) is essentially negligible, but shows significant values in rotated settings. The sign of the prescribed rotation angle is only registered in the $m_1$ magnetisation behaviour, but not in the other response curves.

In the second and final example of this section, the influence of the demagnetisation field is analysed. In all previous examples, the response curves were presented as a function of the externally applied magnetic field, as often reported in experiments in the literature, cf. [71, 202, 211, 212]. Due to the demagnetisation effect, the total internal magnetic field is significantly lower than the externally applied magnetic field. Consequently, system responses were calculated instead of purely constitutive responses. For this final investigation, the prismatic specimen consists solely of the first or second martensite variant. A suitable compression stress is applied to maintain the single vari-

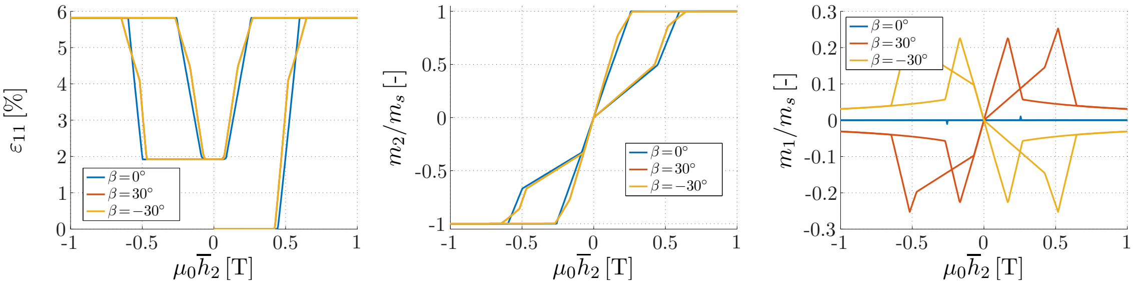

(a) (b) (c)

**Figure 2.15:** Predicted response in terms of (a) magnetic field-induced strains and (b) $m_2$, (c) $m_1$ magnetisation curves under a compressive bias stress of $\overline{\sigma}_{11} = -1.1\,\mathrm{MPa}$ (cf. Figures 2.5 and 2.12), here for a full loading cycle. The angle $\beta$ defines the rotation of the prismatic specimen (with 9:5:5 aspect ratios) in the $\boldsymbol{e}_1$-$\boldsymbol{e}_2$ plane.

ant configuration. The magnetic field-induced easy- and hard-axis response curves of both martensite variants are depicted in Figure 2.16. Obviously, specimens are magnetised easier along the longer edge. In a postprocessing routine, the total magnetic fields $h_i$ were calculated as the sum of the externally applied magnetic fields and the demagnetisation fields. The (constitutive) responses in easy- and hard-axis direction of both martensite variants as a function of the total magnetic field perfectly coincide, see Figure 2.16 and also the discussion in [147].

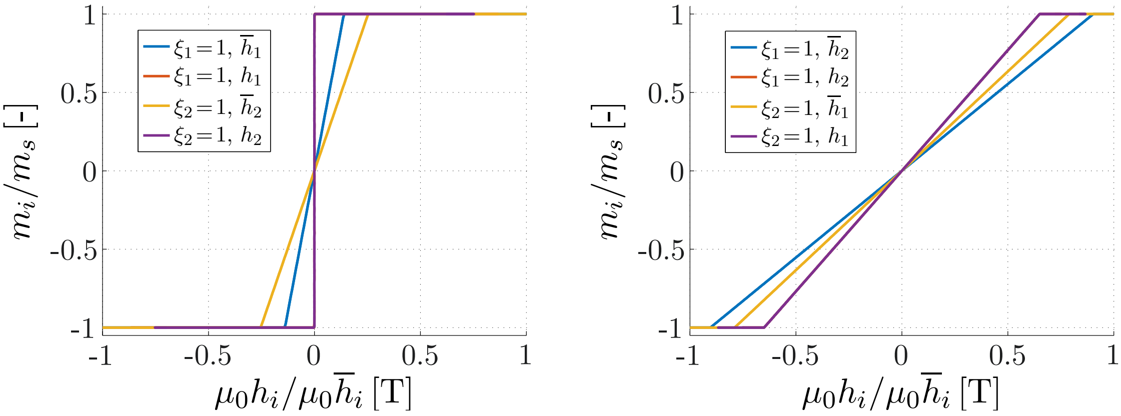

(a) (b)

**Figure 2.16:** Magnetic field-induced magnetisation response curves in the (a) easy- and (b) hard-axes directions of the prismatic specimen alternating consisting solely of the first ($\xi_1 = 1$) or second martensite variant ($\xi_2 = 1$). The system responses as functions of the externally applied magnetic fields $\overline{h}_i$ are compared to the constitutive responses as functions of the total magnetic fields $h_i$. The latter responses perfectly coincide for both configurations.

## 2.4 Summary and outlook

In this chapter, we have presented a general variational modelling framework for magnetisable multiphase solids, whose effective behaviour is governed by stress and magnetic field-driven microstructure evolution. This approach accounts for the non-local influence of the demagnetisation field on magnetic domain formation in a micromagnetics-inspired framework. The key ingredients to the total potential on which the global variational principle is based are the energy storage function and the dissipation potential. Under the homogeneous loading conditions—with prescribed stress and magnetic field—considered here, the simulation of constitutive and system responses reduces to a constrained minimisation problem with respect to the variables that parametrise the microstructure. In this context, the free energy density is incorporated in a partially-relaxed sense, i.e. an energy hull that effectively describes the energy of a phase mixture, when the unstable (non-quasiconvex) homogeneous material has decomposed into microstructure. In other words, only the individual potentials of the constituent phases must be specified, the effective (homogenised) potential naturally follows through appropriate mixture rules and energy relaxation concepts.

This very general approach was successfully applied to the simulation of magnetic shape memory alloy behaviour as a challenging model problem. Motivated by the characteristic microstructures of MSMAs—twinned martensite single crystals with laminate-like internal ferromagnetic domain structures—a rank-one relaxation scheme with respect to first-order laminates was specifically considered. In this model, the strongly interacting microscale mechanisms of variant switching, magnetisation rotation away from easy-axes, and magnetic domain evolution are all incorporated and allowed to evolve independently, but also to be active at the same time. Since the driving forces for the evolution of the internal state variables are energetic in nature, both magnetic field and stress-driven variant switching can be modelled. Several numerical examples were run to demonstrate that the model captures all of the key characteristics of MSMA behaviour, particularly its nonlinear, anisotropic, inelastic, and magnetomechanically-coupled nature. Typical response types, such as the field-induced magnetic shape memory effect or magnetic field-biased pseudo-elasticity and pseudo-plasticity, were successfully predicted. Switching diagrams were computed as particularly insightful tools to visually link variant switching processes to the effective strain and magnetisation response curves for essentially arbitrary loading paths. Finally, emphasis was placed on carefully explaining the connection between the predicted evolution of microstructure and the effective behaviour, as predicted by the model for selected loading cases. It is also important to emphasise that the model is able to make quantitatively-accurate predictions of MSMA response, with relatively few standard input parameters—e.g. elastic constants, saturation magnetisation, magnetocrystalline anisotropy constant, Bain strains, respectively unit cell dimensions.

The following chapters deal with the numerical implementation of the general variational framework, briefly described in Section 2.1, by means of the finite element method.

This allows the modelling of local and effective MSMA specimen responses for arbitrary geometries. In terms of future work, one natural extension of the presented MSMA model would be to include the third tetragonal variant—or a generalization to an $n$-variant setting for other crystal symmetry classes. This mainly applies to an adequate parametrisation of the magnetisation vectors in three-dimensional space, an adequate parametrisation of the interface normals between all occurring martensite variants, as well as suitable numerical homogenisation schemes for the energy densities, where, e.g., laminates of higher order may be considered. Likewise, a more subtle point deserves attention, namely the fact that the rank-one relaxation scheme applied here fulfils strain compatibility and the force balance at material interfaces (twin boundaries), but that no attention is paid to an analogous satisfaction of the magnetic jump conditions across domain walls. On-going work is concerned with establishing equivalent relaxation concepts for the magnetic, and eventually for the fully-coupled, cases.

## 2.5 Appendix

### 2.5.1 Dependencies among the domain magnetisations

As elaborated in Section 2.2, the set of variables describing the material's microstructure is given by

$$\boldsymbol{p} := \{\xi_1, \xi_2, \eta_1, \eta_2, \theta_1, \theta_2, \theta_3, \theta_4, \boldsymbol{a}, \varphi\} \ . \tag{2.90}$$

In this section, analytical relations between the angles $\theta_1$ and $\theta_2$ as well as $\theta_3$ and $\theta_4$ are derived. This allows us to reduce the number of internal state variables and related inequality constraints.

To this end, additional variables $\gamma_1$, $\gamma_2$ with $0 \leq \gamma_i \leq 1$ are introduced, which relate to the variant and domain volume fractions according to

$$\alpha_1 = \xi_1 \, \gamma_1, \ \ \alpha_2 = \xi_1 \, [\, 1 - \gamma_1 \,], \ \ \alpha_3 = \xi_2 \, \gamma_2, \ \text{ and } \alpha_4 = \xi_2 \, [\, 1 - \gamma_2 \,] \tag{2.91}$$

and which can be interpreted as relative magnetic domain volume fractions. The "compatibility" conditions with respect to the magnetisations in each domain $\boldsymbol{m}_j^{\text{dom}}$ and effective magnetisations $\boldsymbol{m}_i^*$ in each variant $i = 1, 2$ then read

$$\boldsymbol{m}_1^* = m_{1k} \, \boldsymbol{e}_k = \gamma_1 \, \boldsymbol{m}_1^{\text{dom}}(\theta_1) + [\, 1 - \gamma_1 \,] \, \boldsymbol{m}_2^{\text{dom}}(\theta_2) \quad \text{with} \quad \|\boldsymbol{m}_1^*\| \leq m_s \ , \tag{2.92}$$

$$\boldsymbol{m}_2^* = m_{2k} \, \boldsymbol{e}_k = \gamma_2 \, \boldsymbol{m}_3^{\text{dom}}(\theta_3) + [\, 1 - \gamma_2 \,] \, \boldsymbol{m}_4^{\text{dom}}(\theta_4) \quad \text{with} \quad \|\boldsymbol{m}_2^*\| \leq m_s \ . \tag{2.93}$$

Such a representation could also be used as an effective parametrisation of the underlying microstructure, where $\gamma_i$ or even the coordinates $m_{ik}$ themselves would act as internal state variables. Here, this formulation is, however, just used for further derivations. These relations are now inserted into the magnetocrystalline anisotropy energy (cf. (2.65), (2.68))

$$\psi^{\mathrm{an}} = \sum_{j=1}^{4} \alpha_j \, k_1 \, \sin^2(\theta_j) \ , \tag{2.94}$$

which for instance yields

$$\begin{aligned} \psi^{\mathrm{an}} = & \alpha_1 \, k_1 \left[ \frac{1}{\gamma_1 \, m_s} [ \quad m_{12} + [\, 1 - \gamma_1 \,] \, m_s \, \sin(\theta_2) \,] \right]^2 + \alpha_2 \, k_1 \, \sin^2(\theta_2) \\ + & \alpha_3 \, k_1 \left[ \frac{1}{\gamma_2 \, m_s} [ -m_{21} + [\, 1 - \gamma_2 \,] \, m_s \, \sin(\theta_4) \,] \right]^2 + \alpha_4 \, k_1 \, \sin^2(\theta_4) \ . \end{aligned} \tag{2.95}$$

The effective magnetisation in each variant $i$ essentially depends—for the underlying two-dimensional setting—on two coordinates $m_{i1}$ and $m_{i2}$. However, it is parametrised by three variables, namely $\gamma_1$, $\theta_1$, and $\theta_2$, respectively $\gamma_2$, $\theta_3$, and $\theta_4$. Hence, there need to be relations between the latter variables. In this line, $\theta_2$ and $\theta_4$ shall be eliminated and determined via minimisation of the magnetocrystalline anisotropy energy. The other energy contributions depending on the magnetisation can be disregarded due to the fact that the magnetisation state is considered prescribed here. In fact, one obtains

$$\theta_2 = \arg\min \{\psi^{\mathrm{an}}\} \ \Rightarrow \ \cos(\theta_2) = 0 \Leftrightarrow \theta_2 = \pm\frac{\pi}{2} \quad \vee \quad \sin(\theta_2) = -\frac{m_{12}}{m_s} \ , \tag{2.96}$$

$$\theta_4 = \arg\min \{\psi^{\mathrm{an}}\} \ \Rightarrow \ \cos(\theta_4) = 0 \Leftrightarrow \theta_4 = \pm\frac{\pi}{2} \quad \vee \quad \sin(\theta_4) = \frac{m_{21}}{m_s} \ , \tag{2.97}$$

In this context, the Hessian matrix reads

$$\begin{aligned} \mathcal{H} := \frac{2\,k_1}{m_s} \Bigg[ & \frac{\xi_1 \, [\, \gamma_1 - 1 \,]}{\gamma_1} [\, m_{12} \, \sin(\theta_2) - m_s \, \cos(2\,\theta_2) \,] \, \boldsymbol{e}_1 \otimes \boldsymbol{e}_1 \\ & - \frac{\xi_2 \, [\, \gamma_2 - 1 \,]}{\gamma_2} [\, m_{21} \, \sin(\theta_4) + m_s \, \cos(2\,\theta_4) \,] \, \boldsymbol{e}_2 \otimes \boldsymbol{e}_2 \Bigg] \ , \end{aligned} \tag{2.98}$$

where the respective non zero Eigenvalues $\lambda_i^{\mathcal{H}}$ for the different solutions are given by

$$\lambda_1^{\mathcal{H}}\big|_{\theta_2=\pi/2} = -\frac{2\,k_1}{m_s\,\gamma_1}\,\xi_1\,[\,1-\gamma_1\,]\;[\,m_{12}+m_s\,] \leq 0\;, \tag{2.99}$$

$$\lambda_2^{\mathcal{H}}\big|_{\theta_4=\pi/2} = \frac{2\,k_1}{m_s\,\gamma_2}\,\xi_2\,[\,1-\gamma_2\,]\;[\,m_{21}-m_s\,] \leq 0\;, \tag{2.100}$$

$$\lambda_1^{\mathcal{H}}\big|_{\theta_2=-\pi/2} = \frac{2\,k_1}{m_s\,\gamma_1}\,\xi_1\,[\,1-\gamma_1\,]\;[\,m_{12}-m_s\,] \leq 0\;, \tag{2.101}$$

$$\lambda_2^{\mathcal{H}}\big|_{\theta_4=-\pi/2} = -\frac{2\,k_1}{m_s\,\gamma_2}\,\xi_2\,[\,1-\gamma_2\,]\;[\,m_{21}+m_s\,] \leq 0\;, \tag{2.102}$$

and

$$\lambda_1^{\mathcal{H}}\big|_{\sin(\theta_2)=-m_{12}/m_s} = \frac{2\,k_1}{\gamma_1}\,\xi_1\,[\,1-\gamma_1\,]\;\cos^2(\theta_2) \geq 0\;, \tag{2.103}$$

$$\lambda_2^{\mathcal{H}}\big|_{\sin(\theta_4)=m_{21}/m_s} = \frac{2\,k_1}{\gamma_2}\,\xi_2\,[\,1-\gamma_2\,]\;\cos^2(\theta_4) \geq 0\;. \tag{2.104}$$

It is noted that

$$m_{ik}+m_s \geq 0\;, \quad m_{ik}-m_s \leq 0\;, \tag{2.105}$$

due to the fact that $\|\boldsymbol{m}_i^*\| \leq m_s$. Thus, the feasible solution is always given by

$$\sin(\theta_2) = -\frac{m_{12}}{m_s}\;, \quad \sin(\theta_4) = \frac{m_{21}}{m_s}\;. \tag{2.106}$$

Reinserting these results into (2.92), (2.93) yields

$$\sin(\theta_1) = \frac{m_{12}}{m_s} = -\sin(\theta_2) \equiv \sin(-\,\theta_2) \quad \Rightarrow \quad \theta_1 = -\,\theta_2\;, \tag{2.107}$$

$$\sin(\theta_3) = -\frac{m_{21}}{m_s} = -\sin(\theta_4) \equiv \sin(-\,\theta_4) \quad \Rightarrow \quad \theta_3 = -\,\theta_4\;. \tag{2.108}$$

## 2.5.2 Analysis of the martensite twin boundary orientation

The results presented in Section 2.3.2 have shown that the intermartensitic twin boundary orientation $\varphi = 45°$ remains constant for all considered loading cases. The following derivation will show that $\varphi = 45°$ in fact minimises the elastic strain energy density as part of (2.69).

In Section 2.2.2, the compatibility condition was derived w.r.t. the total strains of both martensite variants. The martensite variants may form kinematically compatible interfaces, even in the absence of elastic strains. The Hadamard condition implies a rank one connection in terms of the the strain jump $[\![\boldsymbol{\varepsilon}^{\mathrm{tr}}]\!]$, cf. (2.58), viz.

$$[\![\boldsymbol{\varepsilon}^{\mathrm{tr}}]\!] := \boldsymbol{\varepsilon}_1^{\mathrm{tr}} - \boldsymbol{\varepsilon}_2^{\mathrm{tr}} = [\, \boldsymbol{b} \otimes \hat{\boldsymbol{n}}_{12}^{\mathrm{tr}} \,]^{\mathrm{sym}} = \frac{1}{2}\, [\, \boldsymbol{b} \otimes \hat{\boldsymbol{n}}_{12}^{\mathrm{tr}} + \hat{\boldsymbol{n}}_{12}^{\mathrm{tr}} \otimes \boldsymbol{b} \,] \;, \tag{2.109}$$

wherein $\boldsymbol{b}$ is the strain jump and $\hat{\boldsymbol{n}}_{12}^{\mathrm{tr}}$ is the interface normal. The two solutions fulfilling the compatibility condition are

$$\boldsymbol{b} = \sqrt{2}\, [\, b_1 - b_2 \,]\, [\, \mp \boldsymbol{e}_1 + \boldsymbol{e}_2 \,] \;, \quad \hat{\boldsymbol{n}}_{12}^{\mathrm{tr}} = \frac{1}{\sqrt{2}}\, [\, \pm \boldsymbol{e}_1 + \boldsymbol{e}_2 \,] \;, \tag{2.110}$$

cf. [15], for the transformation strains introduced in (2.42). In previous work [112], the convex hull $C\psi^{\mathrm{mat}}$ of the elastic strain energy density was derived. With the transformation strain jump (2.109) at hand, the application of the convexification approach results in the elastic strains of both martensite variants $\boldsymbol{\varepsilon}_i^{\mathrm{el,C}}$, viz.

$$\boldsymbol{\varepsilon}_1^{\mathrm{el,C}} = \boldsymbol{\varepsilon} + \xi_2 [\, \boldsymbol{b} \otimes \hat{\boldsymbol{n}}_{12}^{\mathrm{tr}} \,]^{\mathrm{sym}} - \boldsymbol{\varepsilon}_1^{\mathrm{tr}} \;, \quad \boldsymbol{\varepsilon}_2^{\mathrm{el,C}} = \boldsymbol{\varepsilon} - \xi_1 [\, \boldsymbol{b} \otimes \hat{\boldsymbol{n}}_{12}^{\mathrm{tr}} \,]^{\mathrm{sym}} - \boldsymbol{\varepsilon}_2^{\mathrm{tr}} \;. \tag{2.111}$$

For the interface orientations in (2.110), the optimal strain jump in the context of the rank one convexification approach (2.78) are calculated as follows. The interface orientations in (2.110) are equivalent to $\varphi = \pm 45°$, cf. (2.63). Having the elasticity tensor for the isotropic case (2.70) at hand, the first part in (2.78) is

$$\hat{\boldsymbol{n}}_{12}^{\mathrm{tw}} \cdot \boldsymbol{\mathsf{E}} \cdot \hat{\boldsymbol{n}}_{12}^{\mathrm{tw}} = [\, \lambda + \mu \,]\, \hat{\boldsymbol{n}}_{12}^{\mathrm{tw}} \otimes \hat{\boldsymbol{n}}_{12}^{\mathrm{tw}} + \mu\, \boldsymbol{I} \tag{2.112}$$

and the analytical solution for its inverse ($\varphi = \pm 45°$) is

$$\left[\, \hat{\boldsymbol{n}}_{12}^{\mathrm{tw}} \cdot \boldsymbol{\mathsf{E}} \cdot \hat{\boldsymbol{n}}_{12}^{\mathrm{tw}} \,\right]^{-1} = \begin{bmatrix} \frac{\lambda + 3\mu}{4\mu^2 + 2\mu\lambda} & \frac{\mp [\lambda + \mu]}{4\mu^2 + 2\mu\lambda} & 0 \\ \frac{\mp [\lambda + \mu]}{4\mu^2 + 2\mu\lambda} & \frac{\lambda + 3\mu}{4\mu^2 + 2\mu\lambda} & 0 \\ 0 & 0 & \frac{1}{\mu} \end{bmatrix} \;. \tag{2.113}$$

The second part in (2.78) is

$$\hat{\boldsymbol{n}}_{12}^{\mathrm{tw}} \cdot \boldsymbol{\mathsf{E}} : [\, \boldsymbol{\varepsilon}_2^{\mathrm{tr}} - \boldsymbol{\varepsilon}_1^{\mathrm{tr}} \,] = \lambda\, \hat{\boldsymbol{n}}_{12}^{\mathrm{tw}}\, [\, \mathrm{tr}(\boldsymbol{\varepsilon}_2^{\mathrm{tr}}) - \mathrm{tr}(\boldsymbol{\varepsilon}_1^{\mathrm{tr}}) \,] + 2\, \mu\, \hat{\boldsymbol{n}}_{12}^{\mathrm{tw}} \cdot [\, \boldsymbol{\varepsilon}_2^{\mathrm{tr}} - \boldsymbol{\varepsilon}_1^{\mathrm{tr}} \,] \;. \tag{2.114}$$

Insertion of $\varphi = \pm 45°$ and $\mathrm{tr}(\boldsymbol{\varepsilon}_1^{\mathrm{tr}}) = \mathrm{tr}(\boldsymbol{\varepsilon}_2^{\mathrm{tr}})$ results in

$$\hat{\boldsymbol{n}}_{12}^{\mathrm{tw}} \cdot \boldsymbol{\mathsf{E}} : [\, \boldsymbol{\varepsilon}_2^{\mathrm{tr}} - \boldsymbol{\varepsilon}_1^{\mathrm{tr}} \,] = \sqrt{2}\, \mu\, [\, b_2 - b_1 \,][\, \mp \boldsymbol{e}_1 + \boldsymbol{e}_2 \,] \;. \tag{2.115}$$

Insertion of (2.113) and (2.115) into (2.78) results in

$$\boldsymbol{a} = \sqrt{2}\, [\, b_1 - b_2 \,]\, [\, \mp \boldsymbol{e}_1 + \boldsymbol{e}_2 \,] \;, \tag{2.116}$$

which is identical to strain jump $\boldsymbol{b}$ in (2.110). As a consequence, the elastic strains and the corresponding strain energy densities in the context of the rank one convexification approach and the convexification approach are identical for $\varphi = \pm 45°$. Since the convex hull is the lowest possible energy bound, see (2.41), the interface orientations $\varphi = \pm 45°$ in fact minimise the elastic strain energy density.

# 3 A micromagnetics-inspired FE-framework — spatial resolution of magnetic degrees of freedom

The material presented in this chapter is, in large parts, based on the ideas outlined in the recent work [21]. The chapter can be regarded as the first step in the finite element implementation of micromagnetics-inspired constitutive models, such as the model introduced in Chapter 2. The focus of this chapter lies on the simultaneous solution of the magnetostatic boundary value problem and the evolution equations for the microstructure-describing state variables.

Microstructure evolution in magnetic materials is typically a non-local effect, in the sense that the behaviour at a material point depends on the magnetostatic energy stored within the demagnetisation field in the entire domain. To account for this, we propose a finite element framework in which the internal state variables parametrising the magnetic and crystallographic microstructure are treated as global fields that optimise a global potential. Contrary to conventional micromagnetics, however, the microscale is not spatially resolved and exchange energy terms are neglected in this approach. The influence of microstructure evolution is incorporated in an effective manner which allows the computation of meso- and macroscale problems. This approach necessitates the development and implementation of novel mixed finite element formulations. It further requires the enforcement of inequality constraints at the global level. To handle the latter, we employ Fischer-Burmeister complementarity functions and introduce the associated Lagrange multipliers as additional nodal degrees of freedom. As a particular application of this general methodology, a recently established energy relaxation-based model for magnetic shape memory behaviour is implemented and tested. Special cases—including ellipsoidal specimen geometries—are used to verify magnetic field-induced magnetisation and strain responses obtained from finite element simulations compared to calculations based on the demagnetisation factor concept.

The chapter is structured as follows: Section 3.1 introduces the general variational setting of the non-local approach for the modelling of magnetic materials with evolving microstructures. In Section 3.2, the central governing equations of our constitutive model for magnetic shape memory alloys are briefly presented. It should be emphasised here that, strictly speaking, the classic distinction between local material model and global boundary value problems can no longer be made in the non-local setting. This notwithstanding, we will occasionally still refer to the constitutive model when specifying energy storage or dissipation terms associated with a particular material behaviour. Section 3.3 subsequently discusses the main aspects regarding the finite element implementation of the theoretical framework as well as particular algorithmic treatments, for instance the approach selected to enforce physical constraints. The aforementioned verification of the model is presented in Section 3.4 in terms of finite element analyses of the behaviour of circular, quadratic, ellipsoidal, and rectangular specimens. Finally, the central contributions of this work are summarised in Section 3.5, followed by an outlook on our ongoing and future research activities in this area. Further important details regarding the stored energy density are given in the appendix in Section 3.6.

## 3.1 Variational framework

Prior to the elaborate discussion on the variational framework, the general magnetic variables and some relations among them shall be introduced. The magnetic field strength $\boldsymbol{h} = \overline{\boldsymbol{h}} + \widetilde{\boldsymbol{h}}$ can be decomposed into a prescribed part $\overline{\boldsymbol{h}}$ and demagnetisation field $\widetilde{\boldsymbol{h}}$. The latter occurs due to the magnetisation $\boldsymbol{m}$ of a magnetisable body $\mathcal{B}$ placed within the magnetic field and also affects the medium surrounding the body, which is often referred to as free space. The magnetic field and the magnetisation both contribute to magnetic induction $\boldsymbol{b}$ which is decomposed in the same manner in this contribution as $\boldsymbol{h}$, viz. $\boldsymbol{b} = \overline{\boldsymbol{b}} + \widetilde{\boldsymbol{b}}$. As general relations, one has $\boldsymbol{b} = \mu_0 \, [\, \boldsymbol{h} + \boldsymbol{m} \,]$, with $\mu_0$ as the vacuum permeability of the free space. Accordingly, such relations can also be introduced separately for the applied part and the demagnetisation part, viz. $\overline{\boldsymbol{b}} = \mu_0 \, \overline{\boldsymbol{h}}$ and $\widetilde{\boldsymbol{b}} = \mu_0 \, [\, \widetilde{\boldsymbol{h}} + \boldsymbol{m} \,]$. This definition of $\widetilde{\boldsymbol{b}}$ is rather of conceptual nature—from a physical standpoint it may be more reasonable to relate $\widetilde{\boldsymbol{b}}$ only to $\widetilde{\boldsymbol{h}}$.

The micromagnetics-inspired total potential of a magnetostrictive material with configuration $\mathcal{B}$ embedded in $\mathbb{R}^3$ is introduced as a function of the global primary field variables, i.e. the displacement field $\boldsymbol{u}$, the scalar magnetic potential of the demagnetisation field $\widetilde{\phi}$, and a set of state variables $\boldsymbol{p}$ that describe the underlying microstructure, e.g. the magnetisation $\boldsymbol{m}(\boldsymbol{p})$, as

$$\varPi(\boldsymbol{u}, \widetilde{\phi}, \boldsymbol{p}) = \varPi^{\text{int}}(\boldsymbol{u}, \boldsymbol{p}) + \varPi^{\text{free}}(\widetilde{\phi}) + \varPi^{\text{ext}}(\boldsymbol{u}, \boldsymbol{p}) \; . \tag{3.1}$$

The internal potential $\varPi^{\text{int}}$ contains the stored energy density $\psi^{\text{mat}}$, the free energy potential $\varPi^{\text{free}}$ accounts for the stored energy density in the demagnetisation field, and the external potential $\mathit{\Pi}^{\text{ext}}$ covers mechanical loading via tractions $\overline{\boldsymbol{t}}$ and magnetic field loading $\overline{\boldsymbol{h}}$. Therefore, $\mathit{\Pi}$ can be specified according to

$$\mathit{\Pi}(\boldsymbol{u},\widetilde{\phi},\boldsymbol{p}) := \int\limits_{\mathcal{B}} \psi^{\text{mat}}(\boldsymbol{\varepsilon},\boldsymbol{p})\,\mathrm{d}v + \frac{\mu_0}{2}\int\limits_{\mathbb{R}^3} \|\widetilde{\boldsymbol{h}}\|^2\,\mathrm{d}v - \int\limits_{\partial\mathcal{B}_t} \overline{\boldsymbol{t}}\cdot\boldsymbol{u}\,\mathrm{d}a - \mu_0\int\limits_{\mathcal{B}} \overline{\boldsymbol{h}}\cdot\boldsymbol{m}(\boldsymbol{p})\,\mathrm{d}v\ , \tag{3.2}$$

with $\boldsymbol{\varepsilon} := \nabla^{\text{sym}}_{\boldsymbol{x}}\boldsymbol{u} = \frac{1}{2}\,[\,\nabla_{\boldsymbol{x}}\boldsymbol{u} + \nabla_{\boldsymbol{x}}\boldsymbol{u}^{\,\text{t}}\,]$ as strains and the demagnetisation field strength $\widetilde{\boldsymbol{h}} := -\nabla_{\boldsymbol{x}}\widetilde{\phi}$ . The latter relation automatically satisfies Ampere's law, i.e. $\text{curl}_{\boldsymbol{x}}(\widetilde{\boldsymbol{h}}) = \boldsymbol{0}$. The substitution, see [41, 88],

$$\int\limits_{\mathbb{R}^3} \|\nabla_{\boldsymbol{x}}\widetilde{\phi}\|^2\,\mathrm{d}v = \int\limits_{\mathbb{R}^3} \|\widetilde{\boldsymbol{h}}\|^2\,\mathrm{d}v = -\int\limits_{\mathcal{B}} \widetilde{\boldsymbol{h}}\cdot\boldsymbol{m}(\boldsymbol{p})\,\mathrm{d}v\ , \tag{3.3}$$

with $\|\bullet\| := \sqrt{\bullet\cdot\bullet}$, is used to gain an alternative representations of (3.2), namely

$$\widetilde{\mathit{\Pi}}(\boldsymbol{u},\widetilde{\phi},\boldsymbol{p}) := \int\limits_{\mathcal{B}} \psi^{\text{mat}}(\boldsymbol{\varepsilon},\boldsymbol{p})\,\mathrm{d}v - \frac{\mu_0}{2}\int\limits_{\mathbb{R}^3} \|\widetilde{\boldsymbol{h}}\|^2\,\mathrm{d}v - \int\limits_{\partial\mathcal{B}_t} \overline{\boldsymbol{t}}\cdot\boldsymbol{u}\,\mathrm{d}a - \mu_0\int\limits_{\mathcal{B}} \boldsymbol{h}\cdot\boldsymbol{m}(\boldsymbol{p})\,\mathrm{d}v\ . \tag{3.4}$$

The energy potential defined in (3.4) serves as a basis for the following derivations and for the specific finite element implementation.

The tractions $\overline{\boldsymbol{t}}$ applied at the Neumann boundary $\partial\mathcal{B}_t$ can be related to the stress distribution $\boldsymbol{\sigma}$ within the bulk of the body $\mathcal{B}$, i.e.

$$\begin{aligned}\int\limits_{\partial\mathcal{B}_t} \overline{\boldsymbol{t}}\cdot\boldsymbol{u}\,\mathrm{d}a &= \int\limits_{\partial\mathcal{B}_t} [\,\boldsymbol{\sigma}\cdot\boldsymbol{n}\,]\cdot\boldsymbol{u}\,\mathrm{d}a = \int\limits_{\mathcal{B}} \text{div}_{\boldsymbol{x}}(\boldsymbol{\sigma}^{\text{t}}\cdot\boldsymbol{u})\,\mathrm{d}v \\ &= \int\limits_{\mathcal{B}} \nabla^{\text{sym}}_{\boldsymbol{x}}\boldsymbol{u} : \boldsymbol{\sigma}\,\mathrm{d}v + \int\limits_{\mathcal{B}} \boldsymbol{u}\cdot\text{div}_{\boldsymbol{x}}\boldsymbol{\sigma}\,\mathrm{d}v = \int\limits_{\mathcal{B}} \boldsymbol{\varepsilon} : \boldsymbol{\sigma}\,\mathrm{d}v\ ,\end{aligned} \tag{3.5}$$

wherein additional body forces are assumed to vanish identically, such that $\text{div}_{\boldsymbol{x}}\boldsymbol{\sigma} = \boldsymbol{0}$. Here and in what follows, we consider elastic strains to be negligible, cf. [39, 41]. As a consequence, the displacement field $\boldsymbol{u}$ can be omitted and the total strains $\boldsymbol{\varepsilon}(\boldsymbol{p})$ are given by explicit relations depending on the state variables $\boldsymbol{p}$, see Section 3.2 for a detailed discussion. In this context, the stress states considered as this work proceeds are homogeneously distributed within $\mathcal{B}$ and are denoted $\overline{\boldsymbol{\sigma}}$.

With these assumptions at hand, the total potential (3.4) reads

$$\widetilde{\mathit{\Pi}}(\widetilde{\phi},\boldsymbol{p}) = \int\limits_{\mathcal{B}} \widetilde{\pi}\,\mathrm{d}v - \frac{\mu_0}{2}\int\limits_{\mathbb{R}^3} \|\widetilde{\boldsymbol{h}}\|^2\,\mathrm{d}v\ , \tag{3.6}$$

wherein the energy density $\widetilde{\pi}$ is defined as

$$\widetilde{\pi} := \psi^{\mathrm{mat}}(\boldsymbol{p}) - \boldsymbol{\varepsilon}(\boldsymbol{p}) : \overline{\boldsymbol{\sigma}} - \mu_0 \, \boldsymbol{h} \cdot \boldsymbol{m}(\boldsymbol{p}) \; . \tag{3.7}$$

Based on this global potential, the power-type potential

$$\mathcal{L} := \int\limits_t \left[ \dot{\widetilde{\mathit{\Pi}}} + \int\limits_{\mathcal{B}} \zeta(\dot{\boldsymbol{p}}) \, \mathrm{d}v \right] \mathrm{d}t \tag{3.8}$$

can be defined based on the approach suggested in, e.g., [23, 145, 178] and in line with, e.g., [8], which takes dissipative effects into account via the dissipation functional $\zeta(\dot{\boldsymbol{p}})$, cf. [17, 46, 235]. The magnetomechanical response is generally modelled to be governed by the global rate-type variational principle

$$\{\dot{\boldsymbol{u}}, \dot{\widetilde{\phi}}, \dot{\boldsymbol{p}}\} = \arg \left[ \inf_{\dot{\boldsymbol{u}}} \sup_{\dot{\widetilde{\phi}}} \inf_{\dot{\boldsymbol{p}}} \mathcal{L}(\dot{\boldsymbol{u}}, \dot{\widetilde{\phi}}, \dot{\boldsymbol{p}}) \right] \quad \text{subject to} \quad \boldsymbol{r}_{\mathrm{c}}(\boldsymbol{p}) \leq \boldsymbol{0} \; , \tag{3.9}$$

where the constraints $\boldsymbol{r}_{\mathrm{c}}(\boldsymbol{p}) \leq \boldsymbol{0}$ are introduced and will be specified later. Since the displacement field $\boldsymbol{u}$ was omitted, the global rate-type variational principle reduces to

$$\{\dot{\widetilde{\phi}}, \dot{\boldsymbol{p}}\} = \arg \left[ \sup_{\dot{\widetilde{\phi}}} \inf_{\dot{\boldsymbol{p}}} \mathcal{L}(\dot{\widetilde{\phi}}, \dot{\boldsymbol{p}}) \right] \quad \text{subject to} \quad \boldsymbol{r}_{\mathrm{c}}(\boldsymbol{p}) \leq \boldsymbol{0} \; . \tag{3.10}$$

Due to the assumption that the rates of the underlying state variables minimise this potential, it follows—in line with the Karush-Kuhn-Tucker (KKT) theorem—that the first variation of $\mathcal{L}$ needs to fulfil

$$\delta\mathcal{L} \doteq -\delta \left[ \int\limits_t \boldsymbol{\lambda} \cdot \dot{\boldsymbol{r}}_{\mathrm{c}} \, \mathrm{d}t \right] = -\delta \left[ \int\limits_t \boldsymbol{\lambda} \cdot \frac{\partial \boldsymbol{r}_{\mathrm{c}}}{\partial \boldsymbol{p}} \cdot \dot{\boldsymbol{p}} \, \mathrm{d}t \right] \; . \tag{3.11}$$

With

$$\dot{\widetilde{\mathit{\Pi}}} = \int\limits_{\mathcal{B}} \left[ \frac{\partial \widetilde{\pi}}{\partial \nabla_{\boldsymbol{x}} \widetilde{\phi}} \cdot \nabla_{\boldsymbol{x}} \dot{\widetilde{\phi}} + \frac{\partial \widetilde{\pi}}{\partial \boldsymbol{p}} \cdot \dot{\boldsymbol{p}} \right] \mathrm{d}v + \mu_0 \int\limits_{\mathbb{R}^3} \widetilde{\boldsymbol{h}} \cdot \nabla_{\boldsymbol{x}} \dot{\widetilde{\phi}} \, \mathrm{d}v \tag{3.12}$$

one obtains the stationarity condition of the power-type potential

$$
\begin{aligned}
\delta\mathcal{L} = \int\limits_t \left[ \int\limits_{\mathcal{B}} \left[ \frac{\partial \widetilde{\pi}}{\partial \nabla_{\boldsymbol{x}} \widetilde{\phi}} \cdot \nabla_{\boldsymbol{x}} \delta\dot{\widetilde{\phi}} + \frac{\partial \widetilde{\pi}}{\partial \boldsymbol{p}} \cdot \delta\dot{\boldsymbol{p}} + \frac{\partial \zeta}{\partial \dot{\boldsymbol{p}}} \cdot \delta\dot{\boldsymbol{p}} \right] \mathrm{d}v + \mu_0 \int\limits_{\mathbb{R}^3} \widetilde{\boldsymbol{h}} \cdot \nabla_{\boldsymbol{x}} \delta\dot{\widetilde{\phi}} \, \mathrm{d}v \right] \mathrm{d}t \\
\doteq - \int\limits_t \left[ \left[ \boldsymbol{\lambda} \cdot \frac{\partial \boldsymbol{r}_{\mathrm{c}}}{\partial \boldsymbol{p}} \right] \cdot \delta\dot{\boldsymbol{p}} \right] \mathrm{d}t \; . \qquad (3.13)
\end{aligned}
$$

One may then consider three individual stationarity conditions via

$$
\int\limits_t \left[ \int\limits_{\mathcal{B}} \left[ - \frac{\partial \widetilde{\pi}}{\partial \widetilde{\boldsymbol{h}}} + \mu_0 \, \widetilde{\boldsymbol{h}} \right] \cdot \nabla_{\boldsymbol{x}} \delta\dot{\widetilde{\phi}} \, \mathrm{d}v \right] \mathrm{d}t \doteq 0 \; , \qquad (3.14)
$$

$$
\int\limits_t \left[ \mu_0 \int\limits_{\mathbb{R}^3 \setminus \mathcal{B}} \widetilde{\boldsymbol{h}} \cdot \nabla_{\boldsymbol{x}} \delta\dot{\widetilde{\phi}} \, \mathrm{d}v \right] \mathrm{d}t \doteq 0 \; , \qquad (3.15)
$$

$$
\int\limits_t \left[ \int\limits_{\mathcal{B}} \left[ \frac{\partial \widetilde{\pi}}{\partial \boldsymbol{p}} + \frac{\partial \zeta}{\partial \dot{\boldsymbol{p}}} \right] \cdot \delta\dot{\boldsymbol{p}} \, \mathrm{d}v + \boldsymbol{\lambda} \cdot \frac{\partial \boldsymbol{r}_{\mathrm{c}}}{\partial \boldsymbol{p}} \cdot \delta\dot{\boldsymbol{p}} \right] \mathrm{d}t \doteq 0 \; , \qquad (3.16)
$$

which can be recast into

$$
\int\limits_{\mathcal{B}} \left[ - \frac{\partial \widetilde{\pi}}{\partial \widetilde{\boldsymbol{h}}} + \mu_0 \, \widetilde{\boldsymbol{h}} \right] \cdot \nabla_{\boldsymbol{x}} \delta\dot{\widetilde{\phi}} \, \mathrm{d}v \doteq 0 \; , \qquad (3.17)
$$

$$
\mu_0 \int\limits_{\mathbb{R}^3 \setminus \mathcal{B}} \widetilde{\boldsymbol{h}} \cdot \nabla_{\boldsymbol{x}} \delta\dot{\widetilde{\phi}} \, \mathrm{d}v \doteq 0 \; , \qquad (3.18)
$$

$$
\int\limits_{\mathcal{B}} \left[ \frac{\partial \widetilde{\pi}}{\partial \boldsymbol{p}} + \frac{\partial \zeta}{\partial \dot{\boldsymbol{p}}} \right] \cdot \delta\dot{\boldsymbol{p}} \, \mathrm{d}v + \boldsymbol{\lambda} \cdot \frac{\partial \boldsymbol{r}_{\mathrm{c}}}{\partial \boldsymbol{p}} \cdot \delta\dot{\boldsymbol{p}} \doteq 0 \; , \qquad (3.19)
$$

if (3.14) to (3.16) shall hold for any time $t$. The interpretation of $\delta\dot{\widetilde{\phi}}$ and $\delta\dot{\boldsymbol{p}}$ as test functions reveals the similarities between the first variation displayed via (3.17) to (3.19) and the weak form of the stationarity conditions. The corresponding strong forms (Euler-Lagrange equations) can be shown to follow as

$$
\begin{aligned}
\operatorname{div}_{\boldsymbol{x}} \widetilde{\boldsymbol{b}} &= 0 \quad \text{in } \mathcal{B} \;, && (3.20)\\
\operatorname{div}_{\boldsymbol{x}} \widetilde{\boldsymbol{h}} = -\,\Delta_{\boldsymbol{x}} \widetilde{\phi} &= 0 \quad \text{in } \mathbb{R}^3 \setminus \mathcal{B} \;, && (3.21)\\
[\![ \widetilde{\boldsymbol{b}} ]\!] \cdot \boldsymbol{n} &= 0 \quad \text{on } \partial\mathcal{B} \;, && (3.22)\\
\boldsymbol{0} \in \int_{\mathcal{B}} \left[ \frac{\partial \widetilde{\pi}}{\partial \boldsymbol{p}} + \frac{\partial \zeta}{\partial \dot{\boldsymbol{p}}} \right] \mathrm{d}v + \boldsymbol{\lambda} \cdot \frac{\partial \boldsymbol{r}_{\mathrm{c}}}{\partial \boldsymbol{p}} & \quad\;\; \text{in } \mathcal{B} \;, && (3.23)
\end{aligned}
$$

where (3.20) to (3.22) reflect Gauss's law of magnetism and where (3.23) is the Biot equation governing the evolution of the internal state variables. However, these relations are simply displayed here for the sake of completeness and physical insight. Equations (3.17) to (3.19) will further serve as the basis for the finite element implementation elaborated in Section 3.3. The occurring derivatives of the energy density $\widetilde{\pi}$ can be regarded as (negative) thermodynamically conjugate driving forces and specifically read

$$
-\frac{\partial \widetilde{\pi}}{\partial \widetilde{\boldsymbol{h}}} = \mu_0 \, \boldsymbol{m}(\boldsymbol{p}) \;, \tag{3.24}
$$

$$
\frac{\partial \widetilde{\pi}}{\partial \boldsymbol{p}} = \frac{\partial \psi^{\mathrm{mat}}(\boldsymbol{p})}{\partial \boldsymbol{p}} - \overline{\boldsymbol{\sigma}} : \frac{\partial \boldsymbol{\varepsilon}(\boldsymbol{p})}{\partial \boldsymbol{p}} - \mu_0 \, \boldsymbol{h} \cdot \frac{\partial \boldsymbol{m}(\boldsymbol{p})}{\partial \boldsymbol{p}} \;. \tag{3.25}
$$

With (3.24) at hand, (3.17) is recast into

$$
\mu_0 \int_{\mathcal{B}} \left[ \widetilde{\boldsymbol{h}} + \boldsymbol{m} \right] \cdot \nabla_{\boldsymbol{x}} \delta \dot{\widetilde{\phi}} \, \mathrm{d}v \doteq 0 \;. \tag{3.26}
$$

The combination of (3.26) and (3.18) yields

$$
\mu_0 \int_{\mathcal{B}} \left[ \widetilde{\boldsymbol{h}} + \boldsymbol{m} \right] \cdot \nabla_{\boldsymbol{x}} \delta \dot{\widetilde{\phi}} \, \mathrm{d}v + \mu_0 \int_{\mathbb{R}^3 \setminus \mathcal{B}} \widetilde{\boldsymbol{h}} \cdot \nabla_{\boldsymbol{x}} \delta \dot{\widetilde{\phi}} \, \mathrm{d}v = \int_{\mathbb{R}^3} \widetilde{\boldsymbol{b}} \cdot \nabla_{\boldsymbol{x}} \delta \dot{\widetilde{\phi}} \, \mathrm{d}v \doteq 0 \;, \tag{3.27}
$$

with the—above introduced—magnetic induction $\widetilde{\boldsymbol{b}} = \mu_0 \left[ \widetilde{\boldsymbol{h}} + \boldsymbol{m} \right]$ and $\boldsymbol{m} = \boldsymbol{0}$ in $\mathbb{R}^3 \setminus \mathcal{B}$.

## 3.2 Constitutive model

In this section, the constitutive model based on microstructural quantities related to the different crystallographic phases of the material is elaborated. For the considered two dimensional case, two (nearly) tetragonal (5M modulated) variants of martensite exist, see Figure 3.1, with the corresponding variant volume fractions $\xi_i$, where $\xi_2 = 1 - \xi_1$ due to the conservation of mass, provided that the mass densities of the respective phases are identical. The transformation or Bain strains of the two martensite variants (2D) are introduced as

$$\boldsymbol{\varepsilon}_1^{\mathrm{tr}} = b_2\, \boldsymbol{e}_1 \otimes \boldsymbol{e}_1 + b_1\, \boldsymbol{e}_2 \otimes \boldsymbol{e}_2 \quad \text{and} \quad \boldsymbol{\varepsilon}_2^{\mathrm{tr}} = b_1\, \boldsymbol{e}_1 \otimes \boldsymbol{e}_1 + b_2\, \boldsymbol{e}_2 \otimes \boldsymbol{e}_2 \ , \tag{3.28}$$

where $b_1$ and $b_2$ are the Bain strain coefficients, which have to be determined experimentally, and $\{\boldsymbol{e}_{1,2,3}\}$ is an orthonormal frame aligned with the crystallographic axes. The two martensite variants may form kinematically compatible interfaces, see, e.g., [60]. Since elastic strains are not considered in the present approach, the total (averaged) strain depends only on the transformation strains $\boldsymbol{\varepsilon}_i^{\mathrm{tr}}$ and the martensite volume fractions $\xi_i$, viz. a convex combination of the energy well states, cf. [41],

$$\boldsymbol{\varepsilon} := \xi_1\, \boldsymbol{\varepsilon}_1^{\mathrm{tr}} + \xi_2\, \boldsymbol{\varepsilon}_2^{\mathrm{tr}} \ . \tag{3.29}$$

In addition to the volume fraction of the first martensite variant $\xi_1$, further state variables are introduced to describe the magnetic state of the underlying microstructure. Here, the normalised effective magnetisations of the first and second martensite variant $\boldsymbol{m}_i^* = m_{i1}\, \boldsymbol{e}_1 + m_{i2}\, \boldsymbol{e}_2$ are used. The total magnetisation is calculated by averaging the contributions of the two martensite variants

$$\boldsymbol{m} := m_s\, [\, \xi_1\, \boldsymbol{m}_1^* + \xi_2\, \boldsymbol{m}_2^* \,] \ , \tag{3.30}$$

where $m_s$ is the saturation magnetisation which has to be determined experimentally. Usually, the value of $m_s$ is temperature-dependent, but due to the assumption of isothermal conditions, it is kept fixed during the simulations discussed as this work proceeds. The set of variables describing the microstructural state is consequently denoted as $\boldsymbol{p} = [\, \xi_1, m_{11}, m_{12}, m_{21}, m_{22} \,]^{\mathrm{t}}$. These variables are accompanied by the constraints

$$r_1 := -\,\xi_1 \leq 0 \ , \quad r_2 := \xi_1 - 1 \leq 0 \ , \quad r_3 := \|\boldsymbol{m}_1^*\| - 1 \ , \quad r_4 := \|\boldsymbol{m}_2^*\| - 1 \ , \tag{3.31}$$

so that $\boldsymbol{r}_{\mathrm{c}} = [\, r_1, r_2, r_3, r_4 \,]^{\mathrm{t}}$ and $\boldsymbol{\lambda} = [\, \lambda_1, \lambda_2, \lambda_3, \lambda_4 \,]^{\mathrm{t}}$ as the corresponding Lagrange multipliers, see Section 3.1.

Due to the fact that elastic strains and conventional magnetostriction are omitted, the stored energy density $\psi^{\mathrm{mat}}$ generally introduced in Section 3.1 reduces to

$$\psi^{\mathrm{mat}} = \psi^{\mathrm{an}} = k_1\, [\, \xi_1\, m_{12}^2 + \xi_2\, m_{21}^2 \,] \ , \tag{3.32}$$

where $\psi^{\mathrm{an}}$ denotes the magnetocrystalline anisotropy energy density that depends on the material parameter $k_1$ according to [116, 170]. This energy contribution accounts for the stored energy due to deviations of the magnetisation vectors from the respective magnetic easy-axes in both martensite variants.

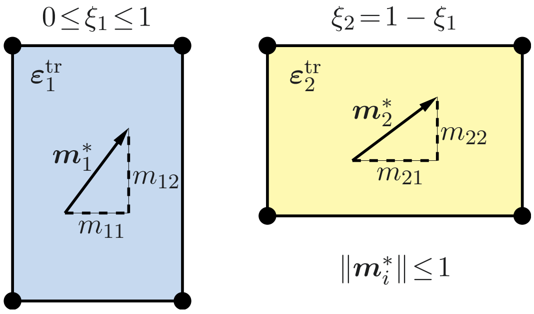

**Figure 3.1:** Parametrisation of the microstructure and constraints for the corresponding state variables. Martensite variants (transformation strains $\boldsymbol{\varepsilon}_i^{\text{tr}}$, variant volume fractions $\xi_i$) and effective magnetisations of the martensite variants ($\boldsymbol{m}_i^* = m_{i1}\,\boldsymbol{e}_1 + m_{i2}\,\boldsymbol{e}_2$).

To complete the constitutive framework, the dissipation function $\zeta$ is chosen as

$$\zeta(\dot{\xi}_1) := Y_\xi\,|\dot{\xi}_1| + \frac{\eta_\xi}{2}\,[\dot{\xi}_1]^2\ , \tag{3.33}$$

where $Y_\xi$ can be interpreted as a threshold and $\eta_\xi$ as a viscosity-type parameter. As for example discussed in [7], such dissipation functions result in evolution equations of viscoplastic type. As a consequence, the volume fraction $\xi_1$ is assumed to be the only state variable associated with dissipation. The reason for this lies in the fact that the dissipation related to the mechanism of domain wall motion (easy-axis magnetisation) and the deviation of the local magnetisation direction from the respective easy-axis (hard-axis magnetisation) is considered negligible according to experimental findings, see Figure 3.2, where the single variant response curves show almost no hysteretic behaviour.

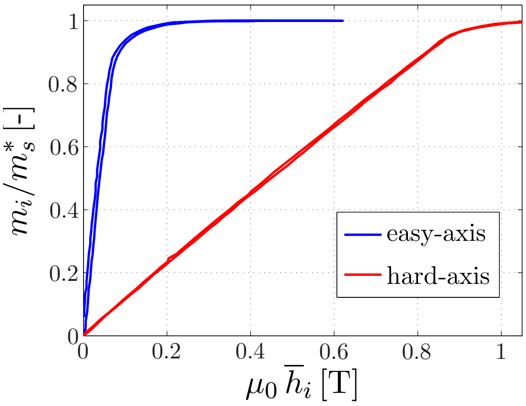

**Figure 3.2:** Measured easy- and hard-axis magnetic field-induced magnetisation response of a thin nearly square wafer consisting of a single martensite variant under the constant compression stress of 1.9 MPa in the easy-axis direction, cf. [211, 212].

The threshold parameter $Y_\xi$ is the absolute value of the corresponding driving force—also termed critical driving force—that must be overcome in order to initialise the martensite reorientation. The corresponding driving force $\mathcal{F}_{\xi_1}$ is generally defined as the negative gradient of (3.25) w.r.t. $\xi_1$ in $\mathcal{B}$ and for the specific constitutive model

$$\mathcal{F}_{\xi_1} = k_1\,[\,m_{21}^2 - m_{12}^2\,] + \overline{\boldsymbol{\sigma}} : [\,\boldsymbol{\varepsilon}_1^{\mathrm{tr}} - \boldsymbol{\varepsilon}_2^{\mathrm{tr}}\,] + \mu_0\, m_s\, \boldsymbol{h} \cdot [\,\boldsymbol{m}_1^* - \boldsymbol{m}_2^*\,]\ . \tag{3.34}$$

With the definition of the Macaulay brackets $\langle\bullet\rangle := 0.5\,[\,\bullet + |\bullet|\,]$, the explicit form of the evolution equation for $\xi_1$ is written in a compact form

$$\dot{\xi}_1 = \frac{1}{\eta_\xi}\,\mathrm{sign}\,(\mathcal{F}_{\xi_1})\,\langle|\mathcal{F}_{\xi_1}| - Y_\xi\rangle\ \ . \tag{3.35}$$

For the numerical implementation, rate $\dot{\xi}_1$ is discretised in time in time interval $\Delta\,t = t_{n+1} - t_n$ by the forward difference

$$\dot{\xi}_1 \approx \frac{\xi_1^{n+1} - \xi_1^n}{t_{n+1} - t_n}\ . \tag{3.36}$$

Since the evolutions of the effective magnetisations are not dissipative, their evolution equations are derived from the stationarity of (3.25) as part of (3.19) w.r.t. $m_{ij}$ in $\mathcal{B}$

$$\frac{\partial\psi^{\mathrm{mat}}(\boldsymbol{p})}{\partial m_{ij}} - \overline{\boldsymbol{\sigma}} : \frac{\partial\boldsymbol{\varepsilon}(\boldsymbol{p})}{\partial m_{ij}} - \mu_0\,\boldsymbol{h}\cdot\frac{\partial\boldsymbol{m}(\boldsymbol{p})}{\partial m_{ij}} = 0\ ,\quad \text{for}\quad i,j = 1,2\ . \tag{3.37}$$

The residual vector $\boldsymbol{r}^{\mathrm{evo}}$ containing the time discrete evolution equation for $\xi_1$ (3.35) and for all other state variables (3.37) is defined as

$$\boldsymbol{r}^{\mathrm{evo}} := \begin{bmatrix} \xi_1 - \xi_1^n - \dfrac{\Delta\,t}{\eta_\xi}\,\mathrm{sign}\,(\mathcal{F}_{\xi_1})\ \langle|\mathcal{F}_{\xi_1}| - Y_\xi\rangle \\ -\mu_0\,m_s\,\xi_1\,h_1 \\ 2\,k_1\,\xi_1\,m_{12} - \mu_0\,m_s\,\xi_1\,h_2 \\ 2\,k_1\,[1-\xi_1]\,m_{21} - \mu_0\,m_s\,[1-\xi_1]\,h_1 \\ -\mu_0\,m_s\,[1-\xi_1]\,h_2 \end{bmatrix}\ , \tag{3.38}$$

where all quantities are evaluated at time $t = t^{n+1}$ (backward Euler method), except for $\xi_1^n$, which is considered to be a known quantity.

**Remark 3** *The field variables $m_{11}, m_{12}, m_{21}$, and $m_{22}$ describe the effective magnetisation inside the first, respectively second, martensite variant. They are directly related to other variables describing the microstructure, also used in previous works [39, 112], viz. the angles measuring the deviations from the magnetic easy-axes $\theta_j$, the net magneti-*

*sations $\eta_i$, the relative domain volume fractions of the corresponding martensite variants $\gamma_i$, and the absolute domain volume fractions $\alpha_j$ by*

$$\begin{aligned}
&\theta_1 = -\,\theta_2 = \arcsin(m_{12}) \;, && \theta_3 = -\,\theta_4 = -\arcsin(m_{21}) \;, \\
&\eta_1 = \xi_1 \, \frac{m_{11}}{\cos(\theta_1)} \;, && \eta_2 = \xi_2 \, \frac{m_{22}}{\cos(\theta_3)} \;, \\
&\gamma_1 = 0.5 \left[ \frac{m_{11}}{\cos(\theta_1)} + 1 \right] \;, && \gamma_2 = 0.5 \left[ \frac{m_{22}}{\cos(\theta_3)} + 1 \right] \;, \quad \textit{for } \cos(\theta_j) \neq 0 \;, \\
&\alpha_{2i-1} = 0.5 \, [\, \xi_i + \eta_i \,] = \xi_i \, \gamma_i \;, && \alpha_{2i} = 0.5 \, [\, \xi_i - \eta_i \,] = \xi_i \, [\, 1 - \gamma_i \,] \;, \quad \textit{with } i = 1, 2 \;.
\end{aligned} \tag{3.39}$$

*The magnetic compatibility within one martensite variant is fulfilled across the* 180° *domain interface with its normal perpendicular to the magnetic easy-axes inside each martensite variant for the angles $\theta_1 = -\,\theta_2$, respectively $\theta_3 = -\,\theta_4$ . In addition, the magnetocrystalline anisotropy energy is minimised for this combination of angles, see Section 3.6 for details. For $\cos(\theta_j) = 0$, the magnetisation inside the corresponding martensite variant is fully aligned with one of the magnetic hard-axes. Consequently, the magnetisation vectors in both domains point in the same direction. In such a case, the relative domain volume fractions $\gamma_i$ and the net magnetisations $\eta_i$ may take arbitrary values satisfying the constraints stated above, without having an influence on the effective material response. The previously used microstructure and the corresponding state variables are schematically sketched in Figure 3.3.*

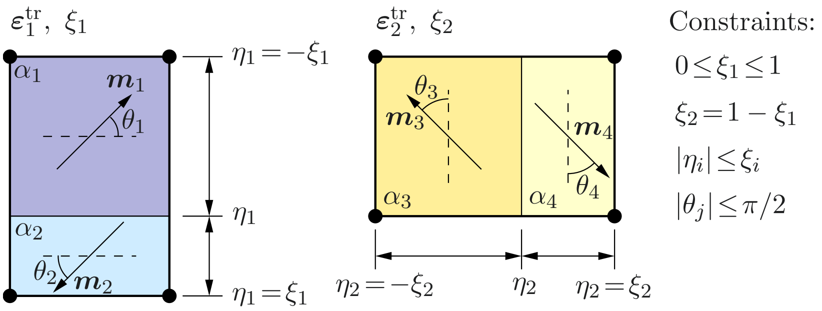
$\varepsilon_1^{\mathrm{tr}}$, $\xi_1$
$\alpha_1$
$\boldsymbol{m}_1$
$\theta_1$
$\alpha_2$
$\theta_2$
$\boldsymbol{m}_2$
$\eta_1 = -\xi_1$
$\eta_1$
$\eta_1 = \xi_1$
$\varepsilon_2^{\mathrm{tr}}$, $\xi_2$
$\theta_3$
$\boldsymbol{m}_3$
$\boldsymbol{m}_4$
$\theta_4$
$\alpha_3$
$\alpha_4$
$\eta_2 = -\xi_2$
$\eta_2$
$\eta_2 = \xi_2$
Constraints:
$0 \leq \xi_1 \leq 1$
$\xi_2 = 1 - \xi_1$
$|\eta_i| \leq \xi_i$
$|\theta_j| \leq \pi/2$

**Figure 3.3:** Previously used parametrisation of the microstructure and constraints for the corresponding state variables. Martensite variants (transformation strains $\boldsymbol{\varepsilon}_i^{\mathrm{tr}}$, variant volume fractions $\xi_i$), magnetic domains (net magnetisations $\eta_i$), and magnetisation vectors ($\boldsymbol{m}_j(\theta_j)$ with $\theta_j$ as the deviations from the easy-axes). Absolute domain volume fractions $\alpha_j$ as dependent variables.

## 3.3 Finite element discretisation

In this section, the general finite element-based implementation and different aspects concerning the algorithmic treatment are discussed, where the two-dimensional case is considered. In general, two different regions are considered separately, viz. the magnetisable body $\mathcal{B}$ and the surrounding free space $\mathbb{R}^2 \backslash \mathcal{B}$. Concerning the latter, it is convenient to define a sufficiently large free space box $\varOmega \subset \mathbb{R}^2$, with $\widetilde{\phi} = 0$ on $\partial \varOmega$. The different regions are spatially discretised via

$$\mathcal{B} \approx \bigcup_{e=1}^{n_{\text{el}}^{\mathcal{B}}} \mathcal{B}^e \,, \quad \varOmega \backslash \mathcal{B} \approx \bigcup_{e=n_{\text{el}}^{\mathcal{B}}+1}^{n_{\text{el}}^{\mathcal{B}}+n_{\text{el}}^{\varOmega\backslash\mathcal{B}}} \mathcal{B}^e \,, \tag{3.40}$$

where $n_{\text{el}}^{\bullet}$ denotes the total number of finite elements $\mathcal{B}^e$ used to geometrically approximate the respective region $\bullet \in \{\mathcal{B}, \varOmega \backslash \mathcal{B}\}$. As shown in Figure 3.4 in terms of the underlying master element, the different field variables are discretised by using interpolation polynomials of different order: For the spatial discretisation of $\widetilde{\phi}$, an eight-node quadratic serendipity element is used, see [43]. Therefore, the number of nodes used to discretise $\widetilde{\phi}$ within the respective finite element is $n_{\text{en}}^{\widetilde{\phi}} = 8$. In contrast, a bilinear four-node element is used for the variables $\boldsymbol{p}$ and $\boldsymbol{\lambda}$ resulting in $n_{\text{en}}^{\boldsymbol{p}} = n_{\text{en}}^{\boldsymbol{\lambda}} = 4$. This choice is due to the fact that only the gradient of $\widetilde{\phi}$ appears in the underlying equations in contrast to $\boldsymbol{p}$, which solely appears as a global field itself. Accordingly, $\widetilde{\phi}$ is interpolated by using polynomials of higher order compared to the discretisation of $\boldsymbol{p}$. The field $\boldsymbol{p}$ and the corresponding $\boldsymbol{\lambda}$ are solely resolved in the $n_{\text{el}}^{\mathcal{B}}$ elements of the body, while field $\widetilde{\phi}$ is resolved in all elements, cf. Section 3.1.

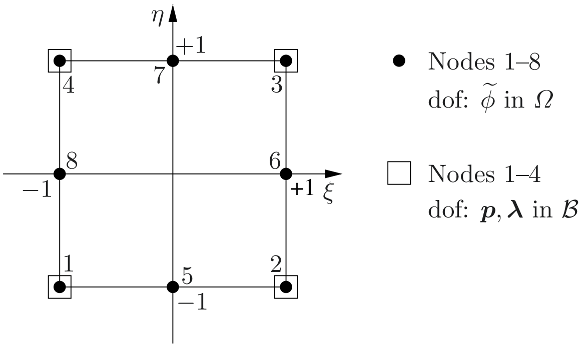
$\eta$
+1
4
7
3
8
6
−1
+1
$\xi$
1
5
2
−1
● Nodes 1–8
dof: $\widetilde{\phi}$ in $\varOmega$
□ Nodes 1–4
dof: $\boldsymbol{p}, \boldsymbol{\lambda}$ in $\mathcal{B}$

**Figure 3.4:** Mixed bilinear (nodes 1–4) and incomplete quadratic serendipity element (nodes 1–8) in the $\xi, \eta$-space. While discrete values of $\widetilde{\phi}$ exist at all nodes, discrete values of the variables $\boldsymbol{p}$ and $\boldsymbol{\lambda}$ exist only at the nodes 1–4 marked with a box. The variables $\boldsymbol{p}$ and $\boldsymbol{\lambda}$ are only resolved in $\mathcal{B}$ and on $\partial\mathcal{B}$. The corresponding shape functions are listed in, e.g., [43].

In the following, the finite element-based derivation of the governing equations is presented, where $\widetilde{\phi}$, $\boldsymbol{p}$, and the Karush-Kuhn-Tucker parameters $\boldsymbol{\lambda}$ denote the global variables. First, the individual variations $\delta\dot{\widetilde{\phi}}$ and $\delta\dot{\boldsymbol{p}}$ are spatially discretised using the above introduced mixed element formulation w.r.t. the element $e$ according to

$$\delta\dot{\widetilde{\phi}}^{e} \approx \sum_{A=1}^{n_{\mathrm{en}}^{\widetilde{\phi}}} \delta\dot{\widetilde{\phi}}^{eA}\, N_{\widetilde{\phi}}^{A} \;, \quad \delta\dot{\boldsymbol{p}}^{e} \approx \sum_{C=1}^{n_{\mathrm{en}}^{\boldsymbol{p}}} \delta\dot{\boldsymbol{p}}^{eC}\, N_{\boldsymbol{p}}^{C} \;, \tag{3.41}$$

where $\delta\dot{\widetilde{\phi}}^{eA}$, $\delta\dot{\boldsymbol{p}}^{eC}$ denote the discrete values of the respective variations and where $N_{\widetilde{\phi}}^{A}$, $N_{\boldsymbol{p}}^{C}$ reflect the respective shape functions. The gradient of $\delta\dot{\widetilde{\phi}}$ is thus given by

$$\nabla_{\boldsymbol{x}}\delta\dot{\widetilde{\phi}}^{e} = \sum_{A=1}^{n_{\mathrm{en}}^{\widetilde{\phi}}} \delta\dot{\widetilde{\phi}}^{eA}\, \nabla_{\boldsymbol{x}} N_{\widetilde{\phi}}^{A} \;. \tag{3.42}$$

With these approximations at hand, (3.27) and (3.19) can be recast into

$$\sum_{e=1}^{n_{\mathrm{el}}^{\mathcal{B}}+n_{\mathrm{el}}^{\varOmega\backslash\mathcal{B}}} \sum_{A=1}^{n_{\mathrm{en}}^{\widetilde{\phi}}} \delta\dot{\widetilde{\phi}}^{eA} \int_{\mathcal{B}^e} \nabla_{\boldsymbol{x}} N_{\widetilde{\phi}}^{A} \cdot \widetilde{\boldsymbol{b}}\, \mathrm{d}v = 0 \;, \tag{3.43}$$

$$\sum_{e=1}^{n_{\mathrm{el}}^{\mathcal{B}}} \sum_{C=1}^{n_{\mathrm{en}}^{\boldsymbol{p}}} \delta\dot{\boldsymbol{p}}^{eC} \cdot \int_{\mathcal{B}^e} N_{\boldsymbol{p}}^{C}\, \boldsymbol{r}^{\mathrm{evo}}\, \mathrm{d}v - \sum_{E=1}^{n_{\mathrm{np}}^{\mathcal{B}\boldsymbol{p}}} \delta\dot{\boldsymbol{p}}^{E} \cdot \left[\boldsymbol{\lambda}^{E} \cdot \frac{\partial \boldsymbol{r}_{\mathrm{c}}}{\partial \boldsymbol{p}}\right] = 0 \;, \tag{3.44}$$

with $n_{\mathrm{np}}^{\mathcal{B}\boldsymbol{p}}$ as the number of node points used for the discretisation of $\boldsymbol{p}$ in $\mathcal{B}$ and the residual concerning the evolution of the state variables $\boldsymbol{r}^{\mathrm{evo}}$ as defined in (3.38). It is noteworthy that the Karush-Kuhn-Tucker parameters $\boldsymbol{\lambda}$ are treated differently from $\widetilde{\phi}$ and $\boldsymbol{p}$. Due to the choice of bilinear shape functions for the state variables $\boldsymbol{p}$, the compliance of the constraints at all nodes is identical to satisfying the constraints everywhere else, cf. [11]. As a consequence, no interpolation of $\boldsymbol{\lambda}$ is required and thus the set $\boldsymbol{\lambda}^{E}$ can be introduced as discrete values at node $E$ without defining a global field. Referring to (3.44), the term in brackets can be specified according to

$$\boldsymbol{\lambda}^{E} \cdot \frac{\partial \boldsymbol{r}_{\mathrm{c}}}{\partial \boldsymbol{p}} = \begin{bmatrix} -\lambda_1^E + \lambda_2^E \\ \lambda_3^E\, m_{11}/\|\boldsymbol{m}_1^*\| \\ \lambda_3^E\, m_{12}/\|\boldsymbol{m}_1^*\| \\ \lambda_4^E\, m_{21}/\|\boldsymbol{m}_2^*\| \\ \lambda_4^E\, m_{22}/\|\boldsymbol{m}_2^*\| \end{bmatrix} \;. \tag{3.45}$$

The actual field variables are spatially discretised using the same sets of shape functions

$$\widetilde{\phi}^e \approx \sum_{A=1}^{n_{\text{en}}^{\widetilde{\phi}}} \widetilde{\phi}^{eA}\, N_{\widetilde{\phi}}^{A} \;\Rightarrow\; \widetilde{\boldsymbol{h}}^e = -\nabla_{\boldsymbol{x}}\widetilde{\phi}^e = -\sum_{A=1}^{n_{\text{en}}^{\widetilde{\phi}}} \widetilde{\phi}^{eA}\, \nabla_{\boldsymbol{x}} N_{\widetilde{\phi}}^{A} \;, \tag{3.46}$$

$$\boldsymbol{p}^e \approx \sum_{C=1}^{n_{\text{en}}^{\boldsymbol{p}}} \boldsymbol{p}^{eC}\, N_{\boldsymbol{p}}^{C} \;. \tag{3.47}$$

Furthermore, the additional Karush-Kuhn-Tucker conditions, i.e.

$$r_i \leq 0 \;, \quad \lambda_i \geq 0 \;, \quad r_i\, \lambda_i = 0 \quad \text{with} \quad i = 1, \ldots, 4 \;, \tag{3.48}$$

need to be taken into account. In line with, e.g., [7, 51, 189], the Fischer-Burmeister nonlinear complementarity problem functions

$$g_i := \sqrt{[r_i]^2 + [\lambda_i]^2} + r_i - \lambda_i = 0 \quad \text{with} \quad i = 1, \ldots, 4 \tag{3.49}$$

are used to substitute (3.48). According to the discretisation of $\boldsymbol{\lambda}$, these equations are solved at every node referring to $\mathcal{B}$ and the underlying four-node elements, where

$$\boldsymbol{g}(\boldsymbol{p}, \boldsymbol{\lambda}) := [\, g_1, g_2, g_3, g_4\,]^{\text{t}} \tag{3.50}$$

is introduced, cf. [11]. With all the above relations at hand, the final system of equations is assembled using assembly operators $\boldsymbol{\mathsf{A}}$ by

$$\boldsymbol{r} := \mathop{\boldsymbol{\mathsf{A}}}_{e=1}^{n_{\text{el}}^{\mathcal{B}}} \begin{bmatrix} r_{\widetilde{\phi}}^{A} \\ \boldsymbol{r}_{\boldsymbol{p}}^{C} \\ \boldsymbol{0} \end{bmatrix} + \mathop{\boldsymbol{\mathsf{A}}}_{e=n_{\text{el}}^{\mathcal{B}}+1}^{n_{\text{el}}^{\mathcal{B}}+n_{\text{el}}^{\Omega\setminus\mathcal{B}}} \begin{bmatrix} r_{\widetilde{\phi}}^{A} \\ \boldsymbol{0} \\ \boldsymbol{0} \end{bmatrix} + \mathop{\boldsymbol{\mathsf{A}}}_{E=1}^{n_{\text{np}}^{\mathcal{B}\boldsymbol{p}}} \begin{bmatrix} 0 \\ \boldsymbol{r}_{\boldsymbol{p}}^{E} \\ \boldsymbol{r}_{\boldsymbol{\lambda}}^{E} \end{bmatrix} = \mathop{\boldsymbol{\mathsf{A}}}_{e=1}^{n_{\text{el}}^{\mathcal{B}}+n_{\text{el}}^{\Omega\setminus\mathcal{B}}} \begin{bmatrix} r_{\widetilde{\phi}}^{A} \\ \{\boldsymbol{r}_{\boldsymbol{p}}^{C}\} \\ \boldsymbol{0} \end{bmatrix} + \mathop{\boldsymbol{\mathsf{A}}}_{E=1}^{n_{\text{np}}^{\mathcal{B}\boldsymbol{p}}} \begin{bmatrix} 0 \\ \boldsymbol{r}_{\boldsymbol{p}}^{E} \\ \boldsymbol{r}_{\boldsymbol{\lambda}}^{E} \end{bmatrix} \;, \tag{3.51}$$

wherein $\{\bullet\}$ marks entries that contribute only to the $e=1,\dots,n_{\mathrm{el}}^{\mathcal{B}}$ elements, to allow a compact notation of (3.51) and the following equations. The individual residuals occurring in (3.51) are defined as follows

$$r_{\widetilde{\phi}}^{A} := \int\limits_{\mathcal{B}^e} \nabla_{\boldsymbol{x}} N_{\widetilde{\phi}}^{A} \cdot \widetilde{\boldsymbol{b}}\,\mathrm{d}v \;, \tag{3.52}$$

$$\boldsymbol{r}_{\boldsymbol{p}}^{C} := \int\limits_{\mathcal{B}^e} N_{\boldsymbol{p}}^{C}\, \boldsymbol{r}^{\mathrm{evo}}\,\mathrm{d}v \;, \tag{3.53}$$

$$\boldsymbol{r}_{\boldsymbol{p}}^{E} := \left[\, \boldsymbol{\lambda}^{E} \cdot \frac{\partial \boldsymbol{r}_{\mathrm{c}}(\boldsymbol{p}^{E})}{\partial \boldsymbol{p}^{E}} \,\right] \;, \tag{3.54}$$

$$\boldsymbol{r}_{\boldsymbol{\lambda}}^{E} := \boldsymbol{g}(\boldsymbol{p}^{E}, \boldsymbol{\lambda}^{E}) \;. \tag{3.55}$$

In this contribution, the corresponding nonlinear system of equations is solved by using a Newton-Raphson scheme. Therefore, the linearisations (first-order Taylor expansions) of the individual contributions of (3.51) are required. Having introduced the elementwise approximations for $\widetilde{\phi}$, $\boldsymbol{p}$, and $\nabla_{\boldsymbol{x}}\widetilde{\phi}$, which depend on the nodal values at the nodes $A$ and $C$, and the Lagrange multipliers $\boldsymbol{\lambda}$ at nodes $E$, the node-specific increments of the linearisations are defined as follows. Firstly, the non-zero increments of $r_{\widetilde{\phi}}^{A}$ and $\boldsymbol{r}_{\boldsymbol{p}}^{C}$ w.r.t. the variables at node $B$, respectively $D$, are considered via

$$\begin{aligned}
\Delta\, r_{\widetilde{\phi}}^{A} &= \sum_{B=1}^{n_{\mathrm{en}}^{\widetilde{\phi}}} \frac{\mathrm{d} r_{\widetilde{\phi}}^{A}}{\mathrm{d}\widetilde{\phi}^{B}}\, \Delta\, \widetilde{\phi}^{B} + \left\{ \sum_{D=1}^{n_{\mathrm{en}}^{\boldsymbol{p}}} \frac{\mathrm{d} r_{\widetilde{\phi}}^{A}}{\mathrm{d}\boldsymbol{p}^{D}} \cdot \Delta\, \boldsymbol{p}^{D} \right\} \;, \\
\Delta\, \boldsymbol{r}_{\boldsymbol{p}}^{C} &= \sum_{B=1}^{n_{\mathrm{en}}^{\widetilde{\phi}}} \frac{\mathrm{d} \boldsymbol{r}_{\boldsymbol{p}}^{C}}{\mathrm{d}\widetilde{\phi}^{B}}\, \Delta\, \widetilde{\phi}^{B} + \sum_{D=1}^{n_{\mathrm{en}}^{\boldsymbol{p}}} \frac{\mathrm{d} \boldsymbol{r}_{\boldsymbol{p}}^{C}}{\mathrm{d}\boldsymbol{p}^{D}} \cdot \Delta\, \boldsymbol{p}^{D} \;,
\end{aligned} \tag{3.56}$$

where $\Delta\,\widetilde{\phi}^{B}$ and $\Delta\,\boldsymbol{p}^{D}$ are the increments of the nodal degrees of freedom at node $B$ and $D$. Secondly, the non-zero increments of $\boldsymbol{r}_{\boldsymbol{p}}^{E}$ and $\boldsymbol{r}_{\boldsymbol{\lambda}}^{E}$ at node $E$ w.r.t. the variables at the same node are considered

$$\begin{aligned}
\Delta\, \boldsymbol{r}_{\boldsymbol{p}}^{E} &= \frac{\mathrm{d}\boldsymbol{r}_{\boldsymbol{p}}^{E}}{\mathrm{d}\boldsymbol{p}^{E}} \cdot \Delta\, \boldsymbol{p}^{E} + \frac{\mathrm{d}\boldsymbol{r}_{\boldsymbol{p}}^{E}}{\mathrm{d}\boldsymbol{\lambda}^{E}} \cdot \Delta\, \boldsymbol{\lambda}^{E} \;, \\
\Delta\, \boldsymbol{r}_{\boldsymbol{\lambda}}^{E} &= \frac{\mathrm{d}\boldsymbol{r}_{\boldsymbol{\lambda}}^{E}}{\mathrm{d}\boldsymbol{p}^{E}} \cdot \Delta\, \boldsymbol{p}^{E} + \frac{\mathrm{d}\boldsymbol{r}_{\boldsymbol{\lambda}}^{E}}{\mathrm{d}\boldsymbol{\lambda}^{E}} \cdot \Delta\, \boldsymbol{\lambda}^{E} \;,
\end{aligned} \tag{3.57}$$

where $\Delta\,\boldsymbol{p}^{E}$ and $\Delta\,\boldsymbol{\lambda}^{E}$ are the increments of the nodal degrees of freedom at node $E$.

The terms in front of the nodal increments in (3.56) and (3.57) are defined as the stiffness matrices. In this contribution, the total derivatives are replaced by partial derivatives, since no implicit dependencies exist. The individual stiffness matrices are defined as follows

$$K^{AB}_{\widetilde{\phi}\widetilde{\phi}} := \frac{\mathrm{d}r^A_{\widetilde{\phi}}}{\mathrm{d}\widetilde{\phi}^B} = \mu_0 \int\limits_{\mathcal{B}^e} -\nabla_{\boldsymbol{x}} N^A_{\widetilde{\phi}} \cdot \nabla_{\boldsymbol{x}} N^B_{\widetilde{\phi}} \,\mathrm{d}v \;, \tag{3.58}$$

$$\boldsymbol{K}^{AD}_{\widetilde{\phi}\boldsymbol{p}} := \frac{\mathrm{d}r^A_{\widetilde{\phi}}}{\mathrm{d}\boldsymbol{p}^D} = \mu_0 \int\limits_{\mathcal{B}^e} \nabla_{\boldsymbol{x}} N^A_{\widetilde{\phi}} \cdot \frac{\partial \boldsymbol{m}}{\partial \boldsymbol{p}}\, N^D_{\boldsymbol{p}} \,\mathrm{d}v \;, \tag{3.59}$$

$$\boldsymbol{K}^{CB}_{\boldsymbol{p}\widetilde{\phi}} := \frac{\mathrm{d}\boldsymbol{r}^C_{\boldsymbol{p}}}{\mathrm{d}\widetilde{\phi}^B} = \int\limits_{\mathcal{B}^e} -N^C_{\boldsymbol{p}}\, \frac{\partial \boldsymbol{r}^{\mathrm{evo}}}{\partial \widetilde{\boldsymbol{h}}} \cdot \nabla_{\boldsymbol{x}} N^B_{\widetilde{\phi}} \,\mathrm{d}v \;, \tag{3.60}$$

$$\boldsymbol{K}^{CD}_{\boldsymbol{p}\boldsymbol{p}} := \frac{\mathrm{d}\boldsymbol{r}^C_{\boldsymbol{p}}}{\mathrm{d}\boldsymbol{p}^D} = \int\limits_{\mathcal{B}^e} N^C_{\boldsymbol{p}}\, \frac{\partial \boldsymbol{r}^{\mathrm{evo}}}{\partial \boldsymbol{p}}\, N^D_{\boldsymbol{p}} \,\mathrm{d}v \;, \tag{3.61}$$

$$\boldsymbol{K}^{EE}_{\boldsymbol{p}\boldsymbol{p}} := \frac{\mathrm{d}\boldsymbol{r}^E_{\boldsymbol{p}}}{\mathrm{d}\boldsymbol{p}^E} = \boldsymbol{\lambda}^E \cdot \frac{\partial^2 \boldsymbol{r}_{\mathrm{c}}(\boldsymbol{p}^E)}{\partial {\boldsymbol{p}^E}^2} \;, \tag{3.62}$$

$$\boldsymbol{K}^{EE}_{\boldsymbol{p}\boldsymbol{\lambda}} := \frac{\mathrm{d}\boldsymbol{r}^E_{\boldsymbol{p}}}{\mathrm{d}\boldsymbol{\lambda}^E} = \left[ \frac{\partial \boldsymbol{r}_{\mathrm{c}}(\boldsymbol{p}^E)}{\partial \boldsymbol{p}^E} \right]^{\mathrm{t}} \;, \tag{3.63}$$

$$\boldsymbol{K}^{EE}_{\boldsymbol{\lambda}\boldsymbol{p}} := \frac{\mathrm{d}\boldsymbol{r}^E_{\boldsymbol{\lambda}}}{\mathrm{d}\boldsymbol{p}^E} = \frac{\partial \boldsymbol{g}(\boldsymbol{p}^E, \boldsymbol{\lambda}^E)}{\partial \boldsymbol{p}^E} \;, \tag{3.64}$$

$$\boldsymbol{K}^{EE}_{\boldsymbol{\lambda}\boldsymbol{\lambda}} := \frac{\mathrm{d}\boldsymbol{r}^E_{\boldsymbol{\lambda}}}{\mathrm{d}\boldsymbol{\lambda}^E} = \frac{\partial \boldsymbol{g}(\boldsymbol{p}^E, \boldsymbol{\lambda}^E)}{\partial \boldsymbol{\lambda}^E} \;, \tag{3.65}$$

with

$$\frac{\partial g_i(\boldsymbol{p}^E, \lambda^E_i)}{\partial \boldsymbol{p}^E} = \frac{\partial r_i(\boldsymbol{p}^E)}{\partial \boldsymbol{p}^E} \cdot \left[ \frac{r_i(\boldsymbol{p}^E)}{\sqrt{[\, r_i(\boldsymbol{p}^E)\,]^2 + [\,\lambda^E_i\,]^2}} + 1 \right] \;, \tag{3.66}$$

$$\frac{\partial g_i(\boldsymbol{p}^E, \lambda^E_i)}{\partial \lambda^E_i} = \frac{\lambda^E_i}{\sqrt{[\, r_i(\boldsymbol{p}^E)\,]^2 + [\,\lambda^E_i\,]^2}} - 1 \;, \tag{3.67}$$

and $i = 1, \ldots, 4$. The total global stiffness matrix of the system is obtained by the following assembly operations

$$\boldsymbol{K} := \mathop{\mathsf{A}}_{e=1}^{n_{\mathrm{el}}^{\mathcal{B}}+n_{\mathrm{el}}^{\Omega\setminus\mathcal{B}}} \begin{bmatrix} K^{AB}_{\widetilde{\phi}\widetilde{\phi}} & \left\{\boldsymbol{K}^{AD}_{\widetilde{\phi}\boldsymbol{p}}\right\} & 0 \\ \left\{\boldsymbol{K}^{CB}_{\boldsymbol{p}\widetilde{\phi}}\right\} & \left\{\boldsymbol{K}^{CD}_{\boldsymbol{p}\boldsymbol{p}}\right\} & 0 \\ \boldsymbol{0} & \boldsymbol{0} & 0 \end{bmatrix} + \mathop{\mathsf{A}}_{E=1}^{n_{\mathrm{np}}^{\mathcal{B}\boldsymbol{p}}} \begin{bmatrix} 0 & \boldsymbol{0} & \boldsymbol{0} \\ \boldsymbol{0} & \boldsymbol{K}^{EE}_{\boldsymbol{p}\boldsymbol{p}} & \boldsymbol{K}^{EE}_{\boldsymbol{p}\boldsymbol{\lambda}} \\ \boldsymbol{0} & \boldsymbol{K}^{EE}_{\boldsymbol{\lambda}\boldsymbol{p}} & \boldsymbol{K}^{EE}_{\boldsymbol{\lambda}\boldsymbol{\lambda}} \end{bmatrix} . \tag{3.68}$$

The nodal increments occurring in (3.56) and (3.57) are formally assembled in a global vector of the nodal increments in analogy to (3.51) and (3.68), i.e.

$$\Delta\boldsymbol{d} := \mathop{\mathsf{A}}_{e=1}^{n_{\mathrm{el}}^{\mathcal{B}}+n_{\mathrm{el}}^{\Omega\setminus\mathcal{B}}} \begin{bmatrix} \Delta\,\widetilde{\phi}^{B} \\ \left\{\Delta\,\boldsymbol{p}^{D}\right\} \\ \boldsymbol{0} \end{bmatrix} + \mathop{\mathsf{A}}_{E=1}^{n_{\mathrm{np}}^{\mathcal{B}\boldsymbol{p}}} \begin{bmatrix} 0 \\ \Delta\,\boldsymbol{p}^{E} \\ \Delta\,\boldsymbol{\lambda}^{E} \end{bmatrix} . \tag{3.69}$$

The newly introduced quantity $\Delta\boldsymbol{d}$ is used in the compact representation of the update of the nodal degrees of freedom during the global iteration. The global system of equations

$$\boldsymbol{r}^{l} + \boldsymbol{K}^{l} \cdot \Delta\boldsymbol{d} = \boldsymbol{0} \ , \quad \text{with} \quad \Delta\boldsymbol{d} = \boldsymbol{d}^{l+1} - \boldsymbol{d}^{l} \ , \tag{3.70}$$

where $l$ is the iteration counter, is solved for $\Delta\boldsymbol{d}$ during each iteration step until $\|\boldsymbol{r}\| \leq \mathrm{tol}$, where a convenient choice for the tolerance is $\mathrm{tol} = 10^{-8}$.

## 3.4 Numerical examples

In this section, several numerical examples show the capability of the finite element model and the advantages over calculations performed using a demagnetisation tensor to capture the demagnetisation effect. All finite element simulations are two dimensional. Total strains in the form of (3.29) are two-dimensional and, moreover, any strain contributions to the stored energy density are neglected, see (3.32). This renders both the strain state as well as the stress state to be two-dimensional for the subsequently discussed numerical examples. The magnetic quantities are resolved in the plane, which corresponds to specimens with infinite size in the $\boldsymbol{e}_3$-direction. The response behaviour patterns under magnetomechanical loading of four different specimens embedded in a free space box are investigated. A circular, a quadratic, an ellipsoidal, and a rectangular specimen are used, where the axes, respectively edges, are aligned with the coordinate system. The aspect ratios of the ellipsoidal and the rectangular specimen are $5/3$. Area-averaged responses of finite element simulations are compared to response behaviour patterns of calculations performed in a driver routine, where the demagnetisation effect is captured by using a demagnetisation tensor. The demagnetisation coefficients were calculated in advance in magnetostatic finite element simulations, where a homogeneous magnetisation state was prescribed and the demagnetisation field was computed. The body-averaged demagnetisation factors $D_{11}$ and $D_{22}$ were calculated as a function of the area-averaged demagnetisation field $\widetilde{h}_1^{\mathrm{ave}}$, or respectively $\widetilde{h}_2^{\mathrm{ave}}$, and the prescribed magnetisation $m_i$, i.e.

$$D_{11} = -\frac{\widetilde{h}_1^{\mathrm{ave}}}{m_1} \quad \text{and} \quad D_{22} = -\frac{\widetilde{h}_2^{\mathrm{ave}}}{m_2} \,. \tag{3.71}$$

The averaged demagnetisation field perpendicular to the $\widetilde{h}_i^{\mathrm{ave}}$ is zero, since the coordinate system and the principal axes of the specimens coincide in this two-dimensional example. The material and model parameters as well as the calculated demagnetisation factors used for the simulations presented below are listed in Table 3.1. Concerning the magnetic field, homogeneous Dirichlet boundary conditions $\widetilde{\phi}=0$ are applied at the boundary $\partial\Omega$ of the free space box $\Omega$.

**Table 3.1:** Material constants and model parameters for $\mathrm{Ni}_{49.7}\mathrm{Mn}_{29.1}\mathrm{Ga}_{21.2}$.

| Model parameter | Symbol | Value | Unit | Reference |
|---|---:|---:|---:|---:|
| Bain strain coefficients | $b_1$ | 0.0188 | [-] | [204] |
| | $b_2$ | − 0.0394 | [-] | [204] |
| Anisotropy constant | $k_1$ | 0.167 | MJ/m$^3$ | [71, 76] |
| Saturation magnetisation | $m_{\mathrm{s}}$ | 514.0 | kA/m | [76, 106] |
| Reorientation threshold | $Y_\xi$ | 0.03 | MJ/m$^3$ | - |
| Viscosity | $\eta_\xi$ | 0.005 | 1/[kPa s] | - |
| Demagn. coeff. circle ($D_{11} = D_{22}$) | $D_{11}$ | 0.4824 | [-] | - |
| Demagn. coeff. square ($D_{11} = D_{22}$) | $D_{11}$ | 0.4746 | [-] | - |
| Demagn. coeff. ellipse short edge | $D_{11}$ | 0.6085 | [-] | - |
| Demagn. coeff. ellipse long edge | $D_{22}$ | 0.3586 | [-] | - |
| Demagn. coeff. rectangle short edge | $D_{11}$ | 0.5854 | [-] | - |
| Demagn. coeff. rectangle long edge | $D_{22}$ | 0.3660 | [-] | - |

The first example considers the magnetisation response in easy- and hard-axis direction of a circular and a quadratic specimen essentially consisting of a single martensite variant ($\xi_2=0.99$). A constant compression stress of $\overline{\sigma}_{22}=-3.0\,\mathrm{MPa}$ is applied in order to maintain the initial configuration during a half cycle of $\overline{h}_i$ magnetic field loading. Figure 3.5 shows the area-averaged magnetisation response of a circular and a quadratic specimen, where the edges of the latter are oriented in horizontal and vertical direction. The responses calculated with a driver routine utilising demagnetisation factors of the ideal circle, so that $D_{11} = D_{22} = 0.5$, as well as calculated values, see Table 3.1, are plotted for comparison. The latter ones coincide with the area-averaged responses of the circular specimen and serve as a first verification of the finite element implementation. Although theoretically unconditionally valid for ellipsoidal geometries, the spatial distribution of the underlying state variables may not turn out to be perfectly homogeneous in the simulations. Therefore, averaged quantities are used for comparison in particular. While the quadratic specimen shows a nonlinear response for both loading cases—which is also observable in experiments, see Figure 3.2 for comparison—all other response curves are linear. The hard-axis magnetisation does not saturate for the maximum applied magnetic field of 1T. Since the mechanisms of domain wall motion (easy-axis) and magnetisation rotation (hard-axis) were introduced to be non-dissipative, the response curves for the unloading case are identical to the loading case, i.e. no hysteresis occurs.

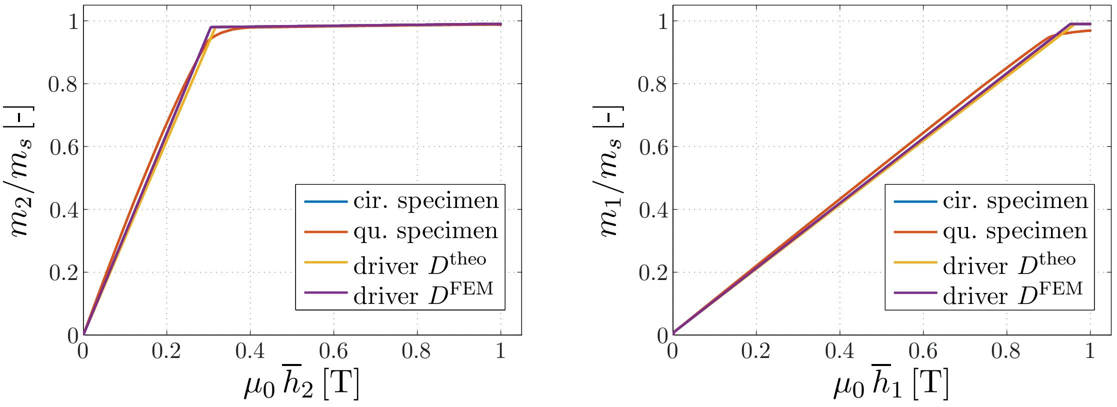

(a) (b)

**Figure 3.5:** Magnetic field-induced magnetisation response in (a) easy- and (b) hard-axis direction under the constant compression stress $\overline{\sigma}_{22} = -3.0\,\text{MPa}$. Both figures show the area-averaged magnetisation response of a circular (cir.) and a quadratic (qu.) specimen embedded in a free space box compared to the response calculated using a driver routine, with a theoretical ($D_{11} = D_{22} = 0.5$) and a calculated ($D_{11} = D_{22} = 0.4824$) demagnetisation tensor of the circular specimen.

As a further verification of the finite element implementation, the magnetisation response curves in easy- and hard-axis directions of different specimens of single variant martensite are analysed. While the response of ellipsoidal specimens is identical to the response calculated with a driver routine using the demagnetisation factors given in Table 3.1, see Figure 3.6 (a) and (b) for the body-averaged response curves of ellipsoidal bodies, the response of rectangular specimens is nonlinear and differs from the driver routines, even though the demagnetisation factors were calculated using the same meshes. The reason for this effect is that the demagnetisation factor concept assumes spatially homogeneous magnetisations, whereas their actual distributions are inhomogeneous in non-ellipsoidal specimens—with derivations particularly large in the corner regions—as correctly predicted by the full-field finite element solutions. Figure 3.6 shows (c) the easy- and (d) the hard-axis magnetisation response curves of the rectangular and the square specimen. The short, or respectively the long, edges of the rectangular specimen coincide with the applied magnetic field loading direction. The shape anisotropy is clearly observable, where specimens are more easily magnetised along longer edges.

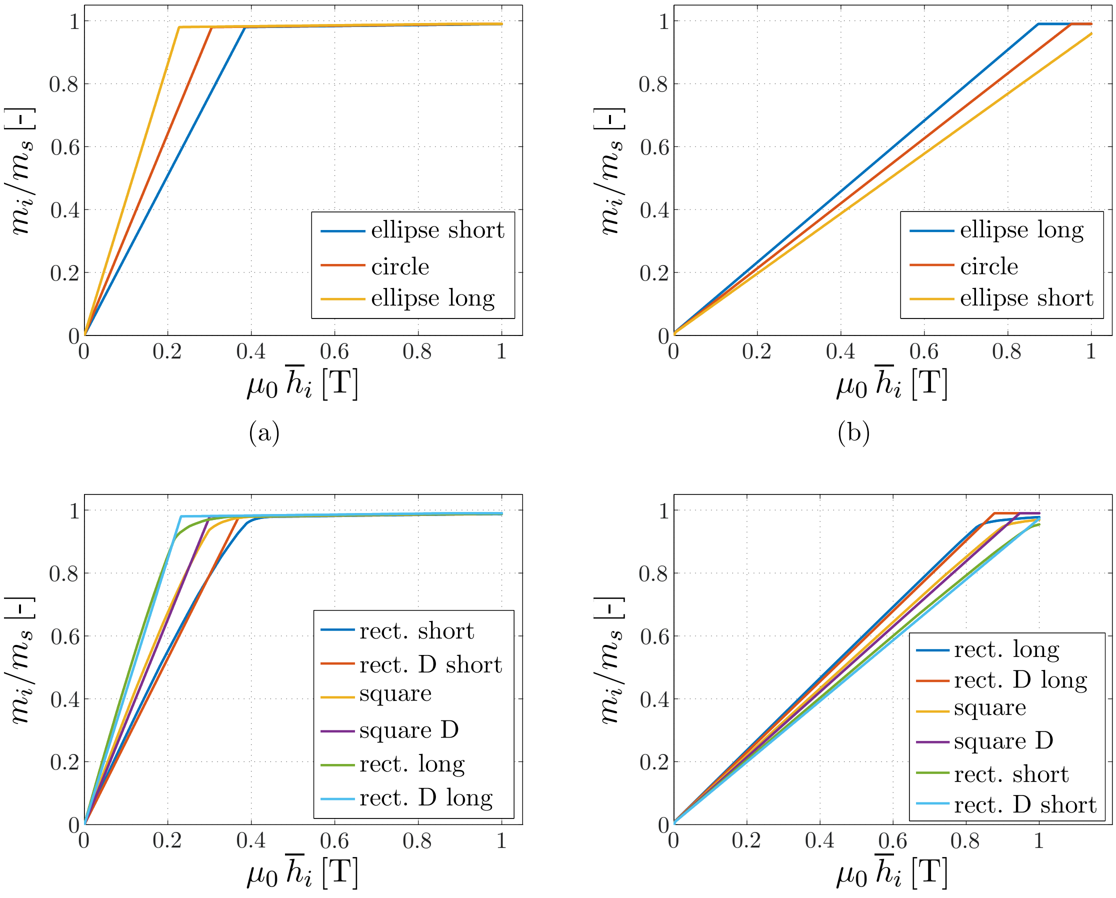

(a) (b)

(c) (d)

**Figure 3.6:** Magnetic field-induced magnetisation response in (a), (c) easy- and (b), (d) hard-axis direction under the constant compression stress $\overline{\sigma} = -3.0\,\mathrm{MPa}$ applied to maintain the initial single martensite variant. All figures show the area-averaged magnetisation response of (a), (b) a circle and an ellipse and (c), (d) a square and a rectangle, all embedded into a free space box (loading applied along the short and long edge of the ellipse and the rectangle). In (c) and (d), the responses are compared to the response calculated using a driver routine. The demagnetisation factors are given in Table 3.1.

The previous examples had in common that only the mechanisms of domain wall motion and rotation of the magnetisation vectors, associated with magnetisations along the easy- and the hard-axis directions in each martensite variant, were active. The mechanism of martensite variant reorientation which is essential for the response behaviour of MSMAs was suppressed by a sufficient high compression stress. In the following example, a square specimen is subjected to a constant compression stress of $\overline{\sigma}_{22} = -1.0\,\mathrm{MPa}$, which is below the blocking stress and favours the initial configuration ($\xi_2 = 0.99$), while a perpendicular cyclic $\overline{h}_1$ magnetic field loading is applied, favouring the first martensite variant. Responses of MSMA specimens experimentally measured under similar loading conditions are used for comparison, see Figure 3.7. In Figure 3.8, the simulated body-averaged (a) strain, where the initial value is shifted to zero, and (b) normalised magnetisation response of the square specimen are plotted and compared to simulations of a driver routine utilising a demagnetisation tensor, given in Table 3.1. In addition, the body-averaged underlying microstructure in terms of martensite volume fractions, magnetic domain volume fractions and the orientations of the magnetisation vectors is schematically sketched for selected loads. Here, "area-averaged microstructure" means the area-averaged values of the underlying microstructural state variables and its associated graphical representation. Starting with zero magnetisation in the single variant state ①, a nearly linear magnetisation response is observable, while the strain remains mostly zero as the main mechanism is magnetisation rotation towards the hard-axis. At a certain point ②, the onset of martensite variant reorientation is visible in the strain response, and the increasing slope of the magnetisation response is associated with easy-axis magnetisation (domain wall motion) in the forming first martensite variant. At state ③, large areas of the body have completely switched into the first martensite variant and the slope in both response curves decreases clearly for increasing external field loading, until a nearly homogeneous state is achieved in ④. For decreasing magnetic field, the onset of the martensite variant reorientation into the initial second martensite variant is delayed due to the threshold for the variant reorientation in the dissipative response, which yields the clearly visible hysteresis loop. From ⑤ onwards, both response curves are again nearly linear. For zero magnetic field, the initial configuration is recovered. Interestingly, the response calculated using a demagnetisation tensor approximates the body-averaged response quite well, except for states of high magnetisation from ③–⑤. The second half of the cycle is very similar to the first and therefore not discussed in detail. Figures 3.9, 3.10 and 3.11 show the corresponding spatial distributions of $\xi_1$, $m_1$, and $m_2$, in addition to iso-lines of the magnetic potential $\widetilde{\phi}$—not to be confused with the field lines of $\widetilde{\boldsymbol{h}}$—for the selected loading points marked in Figure 3.8. In addition to these spatial distributions, Figure 3.12 shows the homogeneous distribution of $\xi_1$, $m_1$, and $m_2$ in the circular specimen and iso-lines of the magnetic potential $\widetilde{\phi}$ during the martensite reorientation process under identical boundary conditions.

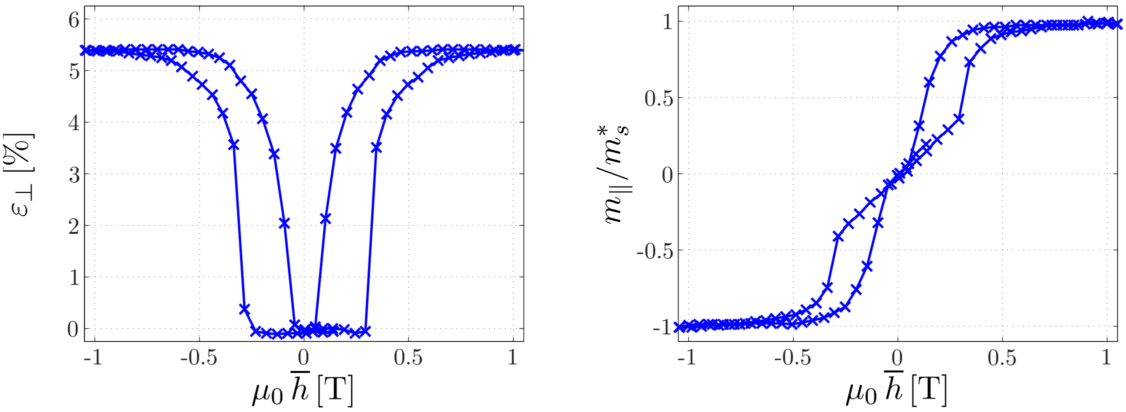

(a) (b)

**Figure 3.7:** Experimentally measured magnetic field-induced (a) strain and (b) magnetisation response under the constant compression stress $\overline{\sigma} = -1.0\,\mathrm{MPa}$ and perpendicular $\overline{h}$ cyclic magnetic field loading as reported by Straka and Heczko [202].

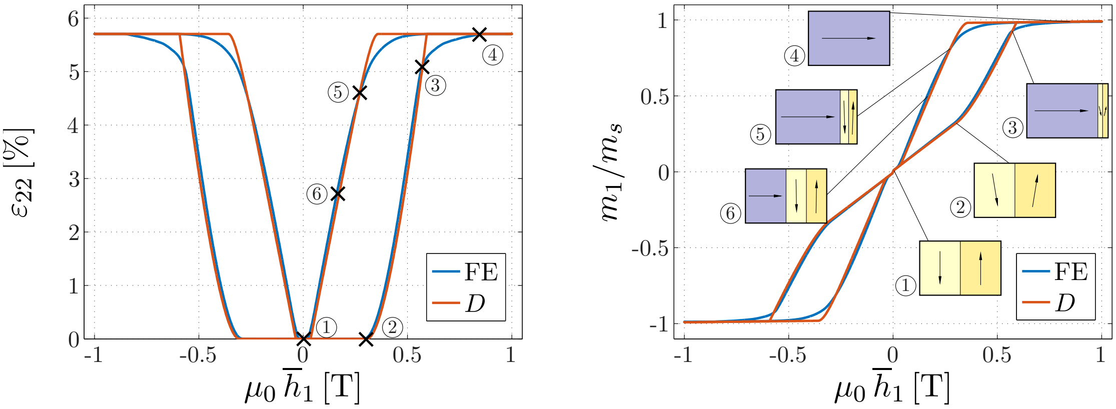

(a) (b)

**Figure 3.8:** Simulated body-averaged magnetic field-induced (a) strain and (b) magnetisation response under the constant compression stress $\overline{\sigma}_{22} = -1.0\,\mathrm{MPa}$ and perpendicular cyclic $\overline{h}_1$ magnetic field loading of a square specimen embedded in a free space box. The response calculations utilising a demagnetisation tensor, given in Table 3.1, are plotted for comparison. The evolution of the body-averaged microstructure is sketched for selected loading states.

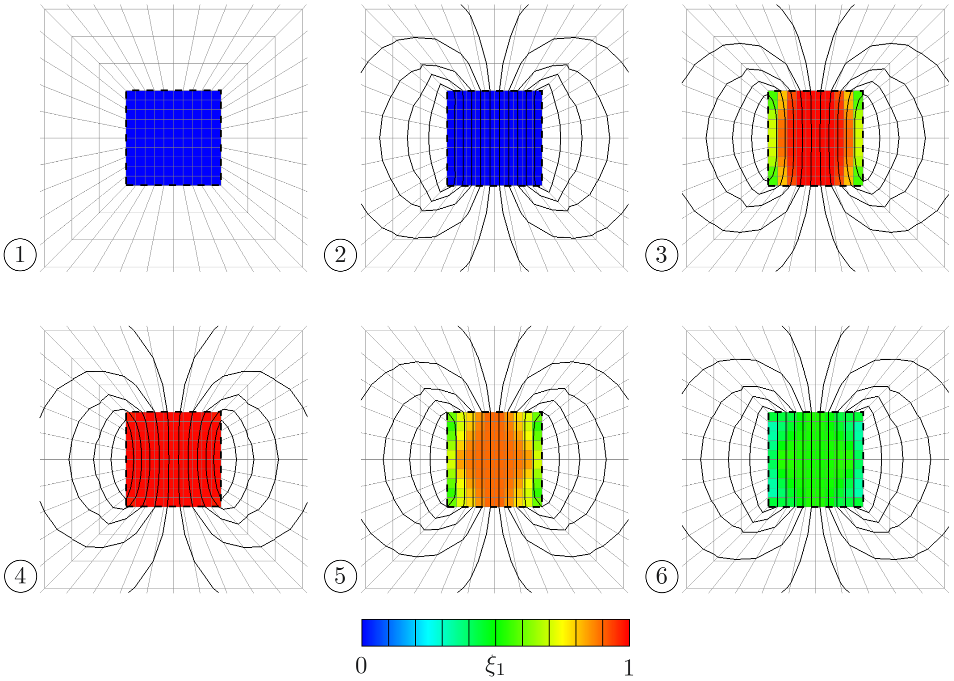

**Figure 3.9:** Spatial distribution of the variant volume fraction $\xi_1$ for selected load steps marked in Figure 3.8. In addition, iso-lines of the magnetic potential $\widetilde{\phi}$ are plotted in black.

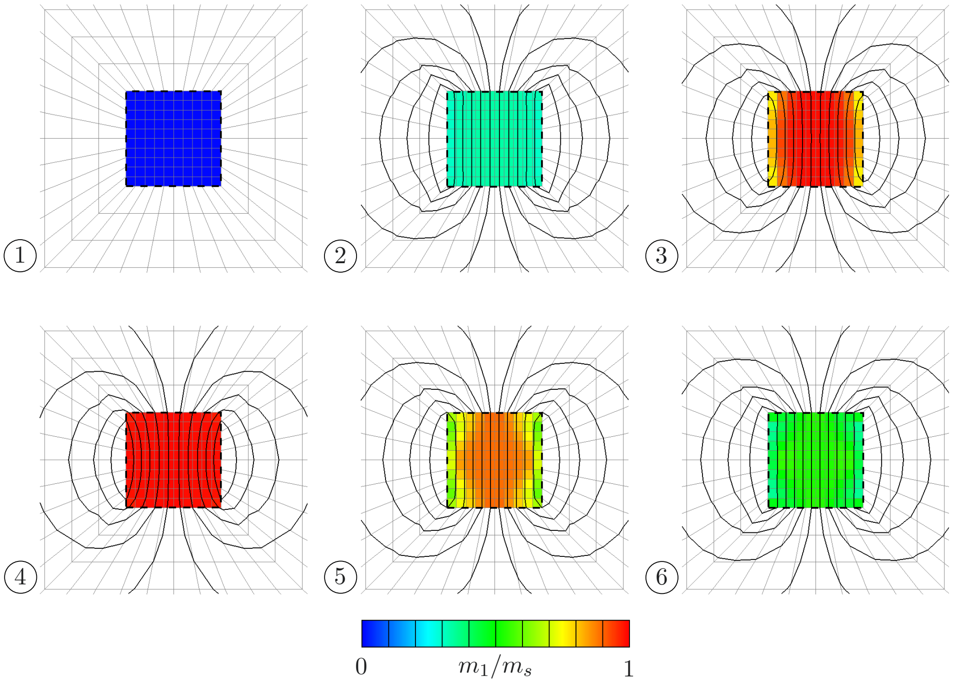

**Figure 3.10:** Spatial distribution of the magnetisation $m_1$ in the direction of the applied $\overline{h}_1$ magnetic field for selected load steps marked in Figure 3.8. In addition, iso-lines of the magnetic potential $\widetilde{\phi}$ are plotted in black.

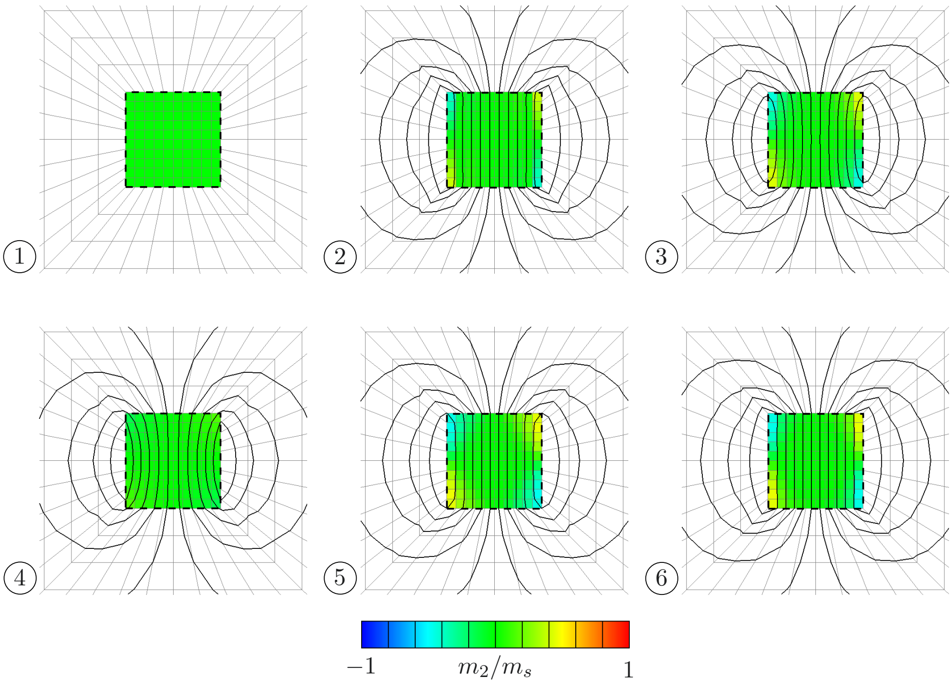

**Figure 3.11:** Spatial distribution of the magnetisation $m_2$ perpendicular to the applied $\overline{h}_1$ magnetic field for selected load steps marked in Figure 3.8. In addition, iso-lines of the magnetic potential $\widetilde{\phi}$ are plotted in black.

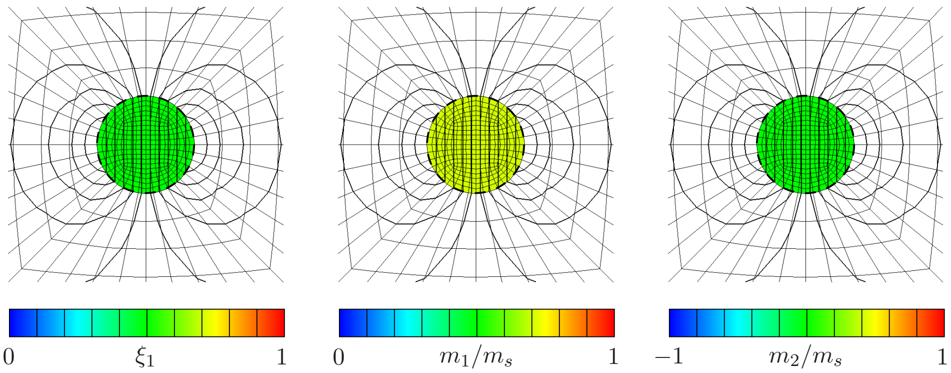

**Figure 3.12:** Spatially homogeneous distribution of the variant volume fraction $\xi_1$ and the magnetisations $m_1$ and $m_2$ for a circular body during the martensite reorientation under the constant compression stress $\underset{\sim}{\overline{\sigma}}_{22} = -1.0\,\text{MPa}$ and cyclic $\overline{h}_1$ magnetic field loading. In addition, iso-lines of the magnetic potential $\widetilde{\phi}$ are plotted in black.

**Remark 4** *Initially, the same elements were used for the discretisation of body $\mathcal{B}$ and surrounding free space $\Omega \setminus \mathcal{B}$. Magnetic potential $\widetilde{\phi}$ and state variables $\boldsymbol{p}$ were spatially discretised using the same set of shape functions. In a first approach, the magnetic potential of the demagnetisation field $\widetilde{\phi}$, the magnetisation of the first martensite variant $\boldsymbol{m}_1^*$ (constraint $r := m_s \,\|\boldsymbol{m}_1^*\| - m_s$), and one KKT-parameter $\lambda$ were used as the global degrees of freedom. Neglecting dissipative contributions and considering stress free states, the evolution of state variables $\boldsymbol{m}_1^*$ under $\overline{\boldsymbol{h}}$ magnetic field loading was analysed for a purely phenomenological stored energy density, cf.[49],*

$$\psi^{\text{phen}} = \frac{\mu_0}{2\,\chi}\,\boldsymbol{m}\cdot\boldsymbol{m}\ , \tag{3.72}$$

*wherein $\chi$ is the magnetic susceptibility and $\boldsymbol{m} = m_s\,\boldsymbol{m}_1^*$. Two distinct susceptibilities were used for the body ($\chi_{\mathcal{B}} = 100$) and the free space ($\chi_{\Omega\setminus\mathcal{B}} = 0.01$). For unsaturated states, the magnetisation is highly inhomogeneous inside the body, see Figure 3.13 (a). For saturated states, however, the magnetisation is mainly homogeneous inside the body, except for the outer element row, see Figure 3.13 (b). The outer edge does not saturate due to the neighbouring slightly paramagnetic free space. By using two distinct element routines for the body and the surrounding free space, where the magnetisation is only resolved in $\mathcal{B}$, the free space behaves like a perfect vacuum ($\chi_{\Omega\setminus\mathcal{B}}=0$) and the magnetisation response is homogeneous inside the circular body during all loading conditions, see Figure 3.13 (c). Figure 3.14 shows a comparison of the body-averaged magnetisation response using identical and different elements, wherein the non-saturating outer element row is clearly visible in the effective body-averaged response curve.*

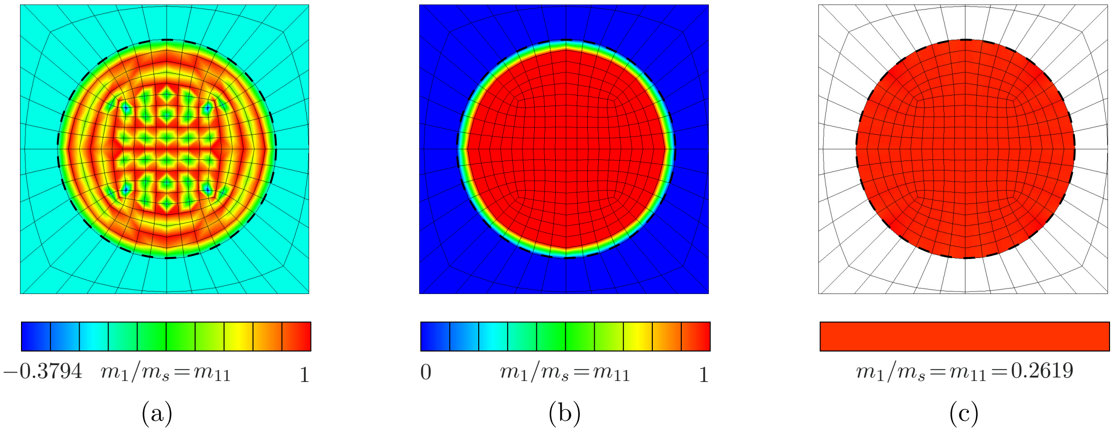

**Figure 3.13:** Phenomenological model: magnetisation distribution inside a circular body. Inhomogeneous response due to the use of the same elements for the body and the surrounding free space for (a) an intermediate and (b) a saturated state. (c) Homogeneous response due to the use of different elements for the body and the surrounding free space during all loading conditions. Interpolated nodal values in (a) and (b). Element-averaged values in (c).

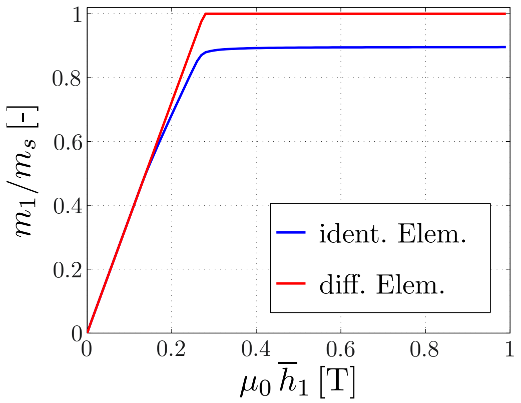

(a)

**Figure 3.14:** Phenomenological model: Effective body-averaged magnetisation response in the direction of the applied magnetic field using identical (blue) and different (red) elements for the body and the surrounding free space. See Figure 3.13 for selected spatial distributions.

*Secondly, the magnetocrystalline anisotropy energy density* $\psi^{\mathrm{an}}$*, as introduced in Section 3.2, was used as the total stored energy density for a single variant of martensite* $(\xi_1 = 1)$*. Figure 3.15 shows one selected magnetisation distribution inside the circular body under* $\overline{h}_2$ *magnetic field loading in the hard-axis direction. A high oscillation of the magnetisation in the easy-axis direction is observable, see Figure 3.15 (a). This behaviour is prevented by using shape functions of a higher polynomial degree for the magnetic potential of demagnetisation field* $\widetilde{\phi}$ *in comparison to the polynomial degree of the shape functions used for the state variables, see the discussion in Section 3.3.*

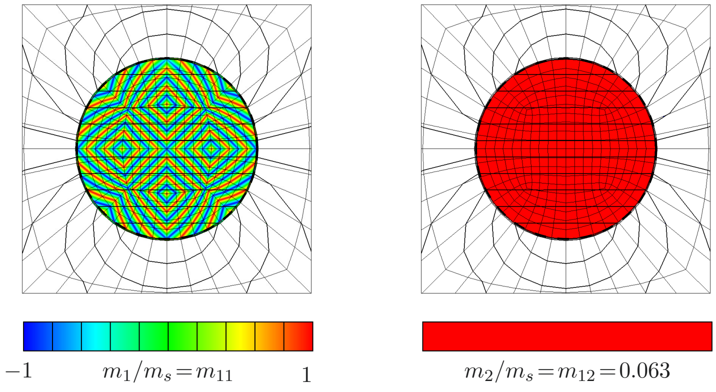

(a) (b)

**Figure 3.15:** Single variant of martensite: magnetisation distribution inside a circular body in (a) easy- and (b) hard-axis direction under $\overline{h}_2$ magnetic field (hard-axis) loading. Interpolated nodal values in (a). Element-averaged values in (b). In addition, iso-lines of the magnetic potential $\widetilde{\phi}$ are plotted in black. All spatially resolved field variables are discretised using the same set of shape functions.

## 3.5 Summary and outlook

This chapter presented a micromagnetics-inspired finite element framework for the modelling and simulation of the material and structural behaviour of MSMA specimens. This framework is micromechanically-motivated since crystallographic information is taken into account, which is reflected in the consideration of different martensite variants associated with the respective Bain strains and directions of spontaneous magnetisation. Due to the non-local nature of the magnetostatic problem, the state variables $\boldsymbol{p}$ which carry this crystallographic information, have to be introduced as global degrees of freedom, just as the scalar magnetic potential $\widetilde{\phi}$. Furthermore, the consideration of unavoidable constraints with respect to $\boldsymbol{p}$ necessitates the introduction of Karush-Kuhn-Tucker parameters at the global level or, in other words, as additional degrees of freedom. The fulfilment of the KKT-type inequality constraints is accomplished by nonlinear Fischer-Burmeister complementarity functions, which are introduced as additional algebraic equations at each node. Dissipative effects arising from the martensite reorientation processes are captured via a dissipation functional, where the resulting evolution equations of elasto-viscoplastic-type are obtained in a variationally-consistent manner as Biot equations. The presented results show the capabilities of the finite element framework regarding the prediction of the effective behaviour of arbitrarily-shaped two-dimensional specimens, where, for instance, the demagnetisation field and the magnetisation are inhomogeneously distributed in space. The results achieved for square-shaped specimens turn out be in good agreement with experimental findings. The framework has been verified in terms of calculations for circular specimens, where the results obtained via the novel finite element framework coincide with analytical solutions obtained by using the concept of demagnetisation tensors.

In the following chapter, the presented framework shall be enhanced in terms of the additional consideration of mechanical degrees of freedom, i.e. the displacement field. Thus, the variational framework will be equivalent to solving the mechanical equilibrium equations simultaneously to Maxwell's equations. Furthermore, elastic strain contributions will be taken into account within the material model, where energy relaxation principles w.r.t. the energy of the phase mixture will be discussed and employed. In future work, another important milestone will be the extension to three-dimensional problems as well as the application of the framework to other magnetostrictive material classes, for instance Terfenol-D, Galfenol, and cobalt ferrite.

## 3.6 Appendix

In previous works, see, e.g., [112], the magnetic state of the underlying two-dimensional microstructure was parametrised by using the net magnetisations $\eta_i$ of both martensite variants, the deviations of the magnetisation vectors from the magnetic easy-axes characterised by the angles $\theta_j$ in each of the four magnetic domains, and the martensite variant volume fractions $\xi_i$. Results of numerical simulations suggested that the deviations of the magnetisation vectors within one martensite variant are not independent, since the optimal deviations were $\theta_2 = -\,\theta_1$ and $\theta_4 = -\,\theta_3$. This relation can be shown analytically, allowing a reparametrisation of the underlying microstruture by simultaneously decreasing the number of constraints. In the following derivation, only the first variant of martensite is considered, i.e. $\xi_1 = 1$. The second martensite variant may be treated analogously.

In the first step, the effective magnetisation of the first martensite variant $\boldsymbol{m}_1^*$ is defined as

$$\boldsymbol{m}_1^* = \gamma_1 \left[ \cos(\theta_1)\, \boldsymbol{e}_1 + \sin(\theta_1)\, \boldsymbol{e}_2 \right] + \left[ 1 - \gamma_1 \right] \left[ -\cos(\theta_2)\, \boldsymbol{e}_1 - \sin(\theta_2)\, \boldsymbol{e}_2 \right] , \tag{3.73}$$

wherein $\gamma_i = 0.5 \left[ \eta_i / \xi_i + 1 \right]$ denotes the relative magnetic domain volume fraction of the $i$-th martensite variant. The constraints for the variables are $0 \leq \gamma_i \leq 1$ and $-\pi/2 \leq \theta_j \leq \pi/2$. The magnetisation vectors are introduced for each domain of one martensite variant, whereas in the modelling framework described in Section 3.2 an effective magnetisation vector for the whole variant is used. This approach is interpretable as the introduction of a plane spanned by the magnetisations of the two domains $\boldsymbol{m}_j$, where several combinations of those and the domain volume fraction $\gamma_1$ yield the same effective magnetisation $\boldsymbol{m}_1^*$. It is assumed that angle $\theta_2$ minimises the anisotropy energy density. In the following, $\gamma_1 \neq 0$ and $\gamma_1 \neq 1$ shall hold, i.e. both domains exist, and $\theta_j \neq \pm\,\pi/2$. The anisotropy energy density of the first martensite variant ($\xi_1 = 1$, $\eta_1$ replaced by $\gamma_1$) $\psi_1^{\mathrm{an}} = \gamma_1 \sin^2(\theta_1) + \left[ 1 - \gamma_1 \right] \sin^2(\theta_2)$ is reformulated using (3.73) via

$$\frac{\psi_1^{\mathrm{an}}}{k_1} = \frac{m_{12}^2 + 2\, m_{12} \left[ 1 - \gamma_1 \right] \sin(\theta_2) + \left[ 1 - \gamma_1 \right] \sin^2(\theta_2)}{\gamma_1} . \tag{3.74}$$

The partial derivative of (3.74) w.r.t. $\theta_2$ results in

$$\frac{1}{k_1} \frac{\partial \psi_1^{\mathrm{an}}}{\partial \theta_2} = \frac{2 \left[ 1 - \gamma_1 \right]}{\gamma_1} \cos(\theta_2) \left[ m_{12} + \sin(\theta_2) \right] . \tag{3.75}$$

The necessary condition for a minimum w.r.t. $\theta_2$ states $\partial_{\theta_2} \psi_1^{\mathrm{an}} = 0$, which, under the assumptions mentioned above, is always satisfied for $m_{12} = -\sin(\theta_2)$ or $\cos(\theta_2) = 0$. The second partial derivative of (3.74) w.r.t. $\theta_2$, i.e.

$$\frac{1}{k_1} \frac{\partial^2 \psi_1^{\mathrm{an}}}{\partial \theta_2^2} = \frac{2 \left[ 1 - \gamma_1 \right]}{\gamma_1} \left[ \cos^2(\theta_2) - \sin(\theta_2) \left[ m_{12} + \sin(\theta_2) \right] \right] \tag{3.76}$$

is used to check the sufficient condition for a minimum, respectively maximum. Insertion of $m_{12} = -\sin(\theta_2)$ into (3.76) yields

$$k_1 \frac{2 \left[ 1 - \gamma_1 \right]}{\gamma_1} \cos^2(\theta_2) > 0 , \quad \text{for} \quad \cos(\theta_2) \neq 0 , \tag{3.77}$$

viz. the sufficient condition for a minimum. The insertion of $\cos(\theta_2) = 0$ into (3.76) yields

$$k_1 \, \frac{2\,[\,1-\gamma_1\,]}{\gamma_1} \, \big[-\sin^2(\theta_2) - \sin(\theta_2)\, m_{12}\,\big] < 0 \ , \quad \text{for} \quad -1 < m_{12} < 1 \ , \tag{3.78}$$

viz. the sufficient condition for a maximum. Since (3.73) must be fulfilled, the cases $\cos(\theta_2) = 0, m_{12} = -1$, and $m_{12} = 1$ yield either $\theta_2 = -\,\theta_1$ or $\gamma_1 = 0$, respectively $\gamma_1 = 1$, which were excluded in the assumptions mentioned above. As a consequence, the anisotropy related energy density is minimised for a given effective magnetisation $\boldsymbol{m}_1^*$ with $\theta_2 = -\,\theta_1$. The derivation for the second martensite variant follows by analogy and yields $\theta_4 = -\,\theta_3$. The number of state variables can therefore be reduced by two: Instead of $[\,\eta_1, \eta_2, \theta_1, \theta_2, \theta_3, \theta_4\,]^{\mathrm{t}}$, the new set of variables $[\,m_{11}, m_{12}, m_{21}, m_{22}\,]^{\mathrm{t}}$ is used to describe the magnetic state in the finite element implementation, where, in addition, the number of inequality constraints is reduced from fourteen to four.

# 4 A micromagnetics-inspired FE-framework — spatial resolution of mechanical and magnetic degrees of freedom

The chapter can be regarded as the second step in the finite element implementation of micromagnetics-inspired constitutive models, such as the model introduced in Chapter 2. It is generally based on the ideas presented in Chapter 3, but extends the formulation by incorporating the displacement field as a further field variable that is spatially resolved. The focus of this chapter lies on the simultaneous solution of the fully coupled mechanical and magnetic boundary value problems as well as on the evolution equations for the microstructure-describing state variables.

As demonstrated in Chapter 3, the non-local demagnetisation field effects the evolution of the microstructure at any point of the magnetic material. The finite element framework proposed in this and in the previous chapters account for this by treating the internal state variables that parametrise the magnetic and crystallographic microstructure as global field variables in addition to the other primary field variables. The present framework is considered to be inspired by the micromagnetics theory, but exchange energy terms are neglected and the microscale is spatially not resolved. The underlying microstructure and its evolution is incorporated in an effective manner. The present approach necessitates the development of a novel mixed element formulation. Additional inequality constraints arise due to physical bounds of the state variables that must be enforced at the global level. Fischer-Burmeister complementarity functions are employed and the associated Lagrange multipliers are incorporated as additional nodal degrees of freedom. An energy relaxation-based model for $Ni_2MnGa$ MSMAs based on previous works is presented and implemented in the general framework. Many numerical examples demonstrate the capabilities of the finite element implementation.

The chapter is structured as follows: the general variational framework for the considered three-field problem is summarised in Section 4.1. In addition to the introduction of multiple parametrisations of the microstructure and the constitutive model for $Ni_2MnGa$, the rate-dependent evolution equations for the state variables are derived in Section 4.2. The finite element implementation and the algorithmic treatment are discussed in detail in Section 4.3. Section 4.4 is dedicated to numerical examples. The implementation is verified by comparison to results obtained by the application of the concept of demagnetisation factors. The response behaviour of several specimen geometries is analysed and, to some extent, compared to experimental findings. The chapter is briefly summarised, followed by an outlook on possible future work in Section 4.5. The different parametrisations are connected in the appendix at the end of the chapter in Section 4.6. In addition, the constitutive driver is detailed, and the shape functions as well as the stiffness matrix contributions are listed.

## 4.1 Variational framework

In this contribution, we consider a magnetostrictive material with configuration $\mathcal{B}$, which is embedded in $\mathbb{R}^3$. The spatial positions are denoted $\boldsymbol{x}$. The state of the material and the surrounding free space is characterised in the time interval $\mathcal{I} \subset \mathbb{R}_{\geq 0}$ using the global primary field variables

$$\boldsymbol{u} : \begin{cases} \mathcal{B} \times \mathcal{I} \to \mathbb{R}^3 \\ (\boldsymbol{x}, t) \mapsto \boldsymbol{u}(\boldsymbol{x}, t) \end{cases} , \quad \widetilde{\phi} : \begin{cases} \mathbb{R}^3 \times \mathcal{I} \to \mathbb{R} \\ (\boldsymbol{x}, t) \mapsto \widetilde{\phi}(\boldsymbol{x}, t) \end{cases} , \quad \boldsymbol{p} : \begin{cases} \mathcal{B} \times \mathcal{I} \to \mathbb{R}^{n_p} \\ (\boldsymbol{x}, t) \mapsto \boldsymbol{p}(\boldsymbol{x}, t) \end{cases} , \tag{4.1}$$

wherein $\boldsymbol{u}(\boldsymbol{x})$ is the displacement field, $\widetilde{\phi}(\boldsymbol{x})$ is the scalar magnetic potential of the demagnetisation field, and where $\boldsymbol{p}(\boldsymbol{x})$ is the vector containing the $n_p$ state variables, which characterise the underlying microstructure, e.g. the magnetisation $\boldsymbol{m}(\boldsymbol{p})$, cf. [10, 21, 146]. Figure 4.1 shows a schematic representation of a magnetostrictive material $\mathcal{B}$ embedded in a finite size free space box $\varOmega$, the mechanical, respectively magnetic, boundary value problems, and the spatial resolution of the state variables. See below for details regarding the free space box. Due to the gradient type relations

$$\boldsymbol{f} := \nabla_{\boldsymbol{x}} \boldsymbol{u} \ , \quad \boldsymbol{\varepsilon} := \nabla_{\boldsymbol{x}}^{\text{sym}} \boldsymbol{u} = \frac{1}{2} \left[ \nabla_{\boldsymbol{x}} \boldsymbol{u} + [\nabla_{\boldsymbol{x}} \boldsymbol{u}]^{\text{t}} \right] , \quad \widetilde{\boldsymbol{h}} := -\nabla_{\boldsymbol{x}} \widetilde{\phi} \ , \tag{4.2}$$

wherein $\boldsymbol{\varepsilon}$ is the infinitesimal strain tensor and $\widetilde{\boldsymbol{h}}$ is the magnetic field strength of the demagnetisation field, respectively the demagnetisation (self-)field, the deformation compatibility $\text{curl}_{\boldsymbol{x}} \boldsymbol{f} = \boldsymbol{0}$ and Ampere's law in the absence of free currents $\text{curl}_{\boldsymbol{x}} \widetilde{\boldsymbol{h}} = \boldsymbol{0}$ can be satisfied a priori. The demagnetisation field $\widetilde{\boldsymbol{h}}$ builds up as the magnetostrictive body magnetises due to the application of a prescribed superimposed spatially homogeneous magnetic field strength $\overline{\boldsymbol{h}}$. The total magnetic field strength is consequently denoted as $\boldsymbol{h} = \overline{\boldsymbol{h}} + \widetilde{\boldsymbol{h}}$. The magnetic induction is calculated by using the relation $\boldsymbol{b} = \mu_0 [\boldsymbol{h} + \boldsymbol{m}]$, wherein $\mu_0$ is the vacuum permeability. In analogy to the magnetic field $\boldsymbol{h}$, the magnetic induction is decomposed into $\boldsymbol{b} = \overline{\boldsymbol{b}} + \widetilde{\boldsymbol{b}}$, wherein the spatially homogeneous part $\overline{\boldsymbol{b}} = \mu_0 \overline{\boldsymbol{h}}$

is due to the applied magnetic field and wherein $\widetilde{\boldsymbol{b}} = \mu_0 \, [\, \widetilde{\boldsymbol{h}} + \widetilde{\boldsymbol{m}} \,]$ is the demagnetisation part. The latter definition is more of a conceptual nature, cf. [21], and allows a compact notation of the following derivations. Since the state variables are only resolved in $\boldsymbol{x} \in \mathcal{B}$, the magnetisation $\boldsymbol{m}(\boldsymbol{p})$ and magnetic induction $\widetilde{\boldsymbol{b}}$, as dependent quantities, are consequently $\boldsymbol{m} = \boldsymbol{0}$ and $\widetilde{\boldsymbol{b}} = \mu_0 \, \widetilde{\boldsymbol{h}}$ in $\mathbb{R}^3 \backslash \mathcal{B}$. Since the demagnetisation field is known to decrease rather rapidly with distance from the magnetisable body, cf. [114], it is common practice to consider a finite size free space box $\Omega \subset \mathbb{R}^3$ in numerical simulations, as depicted in Figure 4.1 (middle). If purely homogeneous Dirichlet conditions for the magnetic potential $\widetilde{\phi} = 0$ are applied on the boundary of the free space box $\partial \Omega$, it is possible to show that

$$\int\limits_{\Omega} \widetilde{\boldsymbol{h}} \, \mathrm{d}v = - \int\limits_{\Omega} \nabla_{\boldsymbol{x}} \widetilde{\phi} \, \mathrm{d}v = - \int\limits_{\partial\Omega} \widetilde{\phi} \, \boldsymbol{n}_{\Omega} \, \mathrm{d}a = \boldsymbol{0} \ , \tag{4.3}$$

see [146]. In consequence, calculating the volume-averaged magnetic field

$$\langle \boldsymbol{h} \rangle := \frac{1}{V_{\Omega}} \int\limits_{\Omega} \boldsymbol{h} \, \mathrm{d}v = \frac{1}{V_{\Omega}} \int\limits_{\Omega} \left[ \overline{\boldsymbol{h}} + \widetilde{\boldsymbol{h}} \right] \, \mathrm{d}v = \overline{\boldsymbol{h}} \ , \tag{4.4}$$

shows that the applied magnetic field $\overline{\boldsymbol{h}}$ can be interpreted as the volume-averaged magnetic field.

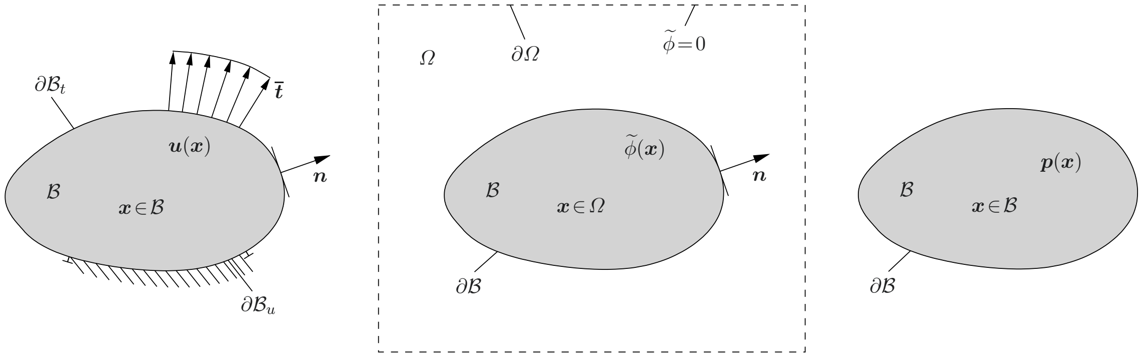

$\partial\mathcal{B}_t$
$\bar{\boldsymbol{t}}$
$\boldsymbol{u}(\boldsymbol{x})$
$\mathcal{B}$
$\boldsymbol{x} \in \mathcal{B}$
$\boldsymbol{n}$
$\partial\mathcal{B}_u$
$\Omega$
$\partial\Omega$
$\widetilde{\phi} = 0$
$\widetilde{\phi}(\boldsymbol{x})$
$\mathcal{B}$
$\boldsymbol{x} \in \Omega$
$\boldsymbol{n}$
$\partial\mathcal{B}$
$\mathcal{B}$
$\boldsymbol{p}(\boldsymbol{x})$
$\boldsymbol{x} \in \mathcal{B}$
$\partial\mathcal{B}$

**Figure 4.1:** Schematic representation of a magnetostrictive material $\mathcal{B}$ embedded into a sufficiently large finite size free space box $\Omega$, which serves as an approximation of $\mathbb{R}^3$ in the simulations, and the corresponding (left) mechanical boundary value problem, (middle) magnetostatic boundary value problem, and (right) spatial distribution of the state variables. In addition, a superimposed spatial homogeneous magnetic field $\overline{\boldsymbol{h}}$ acts on the magnetisation $\boldsymbol{m}(\boldsymbol{p})$, cf. [48, 146].

Conceptionally in line with [146], see also [18, 19, 42], the micromagnetics-inspired total potential of the system is introduced as

$$\Pi(\boldsymbol{u}, \widetilde{\phi}, \boldsymbol{p}) = \Pi^{\mathrm{int}}(\boldsymbol{u}, \boldsymbol{p}) + \Pi^{\mathrm{free}}(\widetilde{\phi}) + \Pi^{\mathrm{ext}}(\boldsymbol{u}, \boldsymbol{p}) \ , \tag{4.5}$$

wherein $\varPi^{\text{int}}$ accounts for the stored energy density $\psi^{\text{mat}}$ in the magnetisable body, $\varPi^{\text{free}}$ accounts for the energy stored in the demagnetisation self-field in the body and the surrounding free space, and where $\varPi^{\text{ext}}$ accounts for the externally applied tractions $\overline{\boldsymbol{t}}$ and the applied spatially homogeneous magnetic field $\overline{\boldsymbol{h}}$. To be precise, the total potential is assumed to be

$$\varPi(\boldsymbol{u},\widetilde{\phi},\boldsymbol{p}) := \int_{\mathcal{B}} \psi^{\text{mat}}(\boldsymbol{\varepsilon},\boldsymbol{p})\,\mathrm{d}v + \frac{\mu_0}{2}\int_{\mathbb{R}^3}\|\widetilde{\boldsymbol{h}}\|^2\mathrm{d}v - \int_{\partial\mathcal{B}_t}\overline{\boldsymbol{t}}\cdot\boldsymbol{u}\,\mathrm{d}a - \mu_0\int_{\mathcal{B}}\overline{\boldsymbol{h}}\cdot\boldsymbol{m}(\boldsymbol{p})\,\mathrm{d}v\;, \tag{4.6}$$

wherein the latter term is also known as the Zeeman energy, which favours an alignment of the magnetisation with the externally applied magnetic field, cf. [48, 97, 146]. In contrast to classic micromagnetics approaches, see, e.g., [18, 42, 146], the magnetisation depends on a set of state variables $\boldsymbol{p}$ and is not directly introduced as an order parameter field. In addition, the exchange energy contributions that penalise gradients of the magnetisation are neglected. This is in line with, e.g., [38, 41], and known as the assumption of a large body limit. The evolution of the microstructure will be taken into account in an effective sense and not all details are resolved, e.g. the number of domains and the size of the domain walls. With the magnetic potential $\widetilde{\phi}$ vanishing at infinity, the substitution, see [41, 87, 88],

$$\int_{\mathbb{R}^3}\|\nabla_{\boldsymbol{x}}\widetilde{\phi}\|^2\,\mathrm{d}v = \int_{\mathbb{R}^3}\|\widetilde{\boldsymbol{h}}\|^2\,\mathrm{d}v = -\int_{\mathcal{B}}\widetilde{\boldsymbol{h}}\cdot\boldsymbol{m}(\boldsymbol{p})\,\mathrm{d}v\;, \tag{4.7}$$

wherein $\|\bullet\| := \sqrt{\bullet\cdot\bullet}$, is used to gain two alternative representations of (4.6), namely

$$\widetilde{\varPi}(\boldsymbol{u},\widetilde{\phi},\boldsymbol{p}) := \int_{\mathcal{B}} \psi^{\text{mat}}(\boldsymbol{\varepsilon},\boldsymbol{p})\mathrm{d}v - \frac{\mu_0}{2}\int_{\mathbb{R}^3}\|\widetilde{\boldsymbol{h}}\|^2\mathrm{d}v - \int_{\partial\mathcal{B}_t}\overline{\boldsymbol{t}}\cdot\boldsymbol{u}\mathrm{d}a - \mu_0\int_{\mathcal{B}}\left[\overline{\boldsymbol{h}}+\widetilde{\boldsymbol{h}}\right]\cdot\boldsymbol{m}(\boldsymbol{p})\mathrm{d}v\;, \tag{4.8}$$

which is in line with [146], and

$$\widehat{\varPi}(\boldsymbol{u},\widetilde{\phi},\boldsymbol{p}) := \int_{\mathcal{B}} \psi^{\text{mat}}(\boldsymbol{\varepsilon},\boldsymbol{p})\mathrm{d}v - \frac{\mu_0}{2}\int_{\mathcal{B}}\widetilde{\boldsymbol{h}}\cdot\boldsymbol{m}(\boldsymbol{p})\mathrm{d}v - \int_{\partial\mathcal{B}_t}\overline{\boldsymbol{t}}\cdot\boldsymbol{u}\mathrm{d}a - \mu_0\int_{\mathcal{B}}\overline{\boldsymbol{h}}\cdot\boldsymbol{m}(\boldsymbol{p})\mathrm{d}v\;, \tag{4.9}$$

which is in line with [19].

The potential $\widetilde{\varPi}$ defined in (4.8) serves as a basis for our finite element implementation. The alternative form of (4.8)

$$\widetilde{\varPi}(\boldsymbol{u},\widetilde{\phi},\boldsymbol{p}) = \int_{\mathcal{B}}\widetilde{\pi}(\boldsymbol{u},\boldsymbol{p})\,\mathrm{d}v - \frac{\mu_0}{2}\int_{\mathbb{R}^3}\|\widetilde{\boldsymbol{h}}\|^2\,\mathrm{d}v - \int_{\partial\mathcal{B}_t}\overline{\boldsymbol{t}}\cdot\boldsymbol{u}\,\mathrm{d}a\;, \tag{4.10}$$

wherein the energy density $\widetilde{\pi}$ is defined as

$$\widetilde{\pi}(\boldsymbol{u},\boldsymbol{p}) := \psi^{\mathrm{mat}}(\boldsymbol{\varepsilon},\boldsymbol{p}) - \mu_0 \left[\overline{\boldsymbol{h}} + \widetilde{\boldsymbol{h}}\right] \cdot \boldsymbol{m}(\boldsymbol{p}) \ , \tag{4.11}$$

is introduced for a compact representation of the following derivations, cf. [21]. Conceptionally in line with [49], the magnetomechanical response is then modelled to be governed by the global variational principle

$$\{\boldsymbol{u},\widetilde{\phi},\boldsymbol{p}\} = \arg\left[\inf_{\boldsymbol{u}} \sup_{\widetilde{\phi}} \inf_{\boldsymbol{p}} \widetilde{\Pi}(\boldsymbol{u},\widetilde{\phi},\boldsymbol{p})\right] \quad \text{subject to} \quad \boldsymbol{r}_{\mathrm{c}}(\boldsymbol{p}) \leq \boldsymbol{0} \ , \tag{4.12}$$

wherein vector $\boldsymbol{r}_{\mathrm{c}}(\boldsymbol{p})$ is a collection of all physical inequality constraints $r_i \leq 0$ for the state variables $\boldsymbol{p}$ and will be specified later. Based on the energy potential (4.10), the power-type potential, cf. [8, 10, 21, 23, 145, 178],

$$\mathcal{L} := \int_t \left[\dot{\widetilde{\Pi}} + \int_{\mathcal{B}} \zeta(\dot{\boldsymbol{p}}) \,\mathrm{d}v\right] \mathrm{d}t \ , \tag{4.13}$$

is defined, where dissipative effects are taken into account by the newly introduced dissipation functional $\zeta(\dot{\boldsymbol{p}})$, see [17, 46, 66, 177, 235], using the concept of standard dissipative materials. In this time dependent setting, the magnetomechanical response is then modelled to be governed by the global rate-type variational principle

$$\{\dot{\boldsymbol{u}},\dot{\widetilde{\phi}},\dot{\boldsymbol{p}}\} = \arg\left[\inf_{\dot{\boldsymbol{u}}} \sup_{\dot{\widetilde{\phi}}} \inf_{\dot{\boldsymbol{p}}} \mathcal{L}(\dot{\boldsymbol{u}},\dot{\widetilde{\phi}},\dot{\boldsymbol{p}})\right] \quad \text{subject to} \quad \boldsymbol{r}_{\mathrm{c}}(\boldsymbol{p}) \leq \boldsymbol{0} \ , \tag{4.14}$$

wherein, in analogy to (4.12), vector $\boldsymbol{r}_{\mathrm{c}}(\boldsymbol{p})$ is a collection of all physical inequality constraints $r_i \leq 0$ for the state variables $\boldsymbol{p}$ and will be specified later. Due to the assumption that the rates of the state variables minimise the potential $\mathcal{L}$, see (4.14), the stationarity condition, according to the Karush-Kuhn-Tucker theorem, cf. [21], reads,

$$\delta\mathcal{L} \doteq -\,\delta\left[\int_t \boldsymbol{\lambda} \cdot \dot{\boldsymbol{r}}_{\mathrm{c}} \,\mathrm{d}t\right] = -\,\delta\left[\int_t \boldsymbol{\lambda} \cdot \frac{\partial \boldsymbol{r}_{\mathrm{c}}}{\partial \boldsymbol{p}} \cdot \dot{\boldsymbol{p}} \,\mathrm{d}t\right] \ , \tag{4.15}$$

wherein the Karush-Kuhn-Tucker parameters, often also denoted as Lagrange-multipliers, are collected in vector $\boldsymbol{\lambda}$. The numerical treatment of the arising Karush-Kuhn-Tucker conditions is outlined in Section 4.3. The following derivation is in analogy to the author's previous work, see [21]. The non-zero contributions of the energy functional (4.10) in (4.13) are

$$\dot{\widetilde{\mathit{\Pi}}} = \int_{\mathcal{B}} \left[ \frac{\partial\widetilde{\pi}}{\partial\boldsymbol{\varepsilon}} : \nabla_{\boldsymbol{x}}\dot{\boldsymbol{u}} + \frac{\partial\widetilde{\pi}}{\partial\nabla_{\boldsymbol{x}}\widetilde{\phi}} \cdot \nabla_{\boldsymbol{x}}\dot{\widetilde{\phi}} + \frac{\partial\widetilde{\pi}}{\partial\boldsymbol{p}} \cdot \dot{\boldsymbol{p}} \right] \mathrm{d}v + \mu_0 \int_{\mathbb{R}^3} \widetilde{\boldsymbol{h}} \cdot \nabla_{\boldsymbol{x}}\dot{\widetilde{\phi}}\,\mathrm{d}v - \int_{\partial\mathcal{B}_t} \bar{\boldsymbol{t}} \cdot \dot{\boldsymbol{u}}\,\mathrm{d}a \, . \tag{4.16}$$

With (4.16) at hand, the variation of (4.13) combined with (4.15) yields the stationarity condition

$$\begin{aligned} \delta\mathcal{L} = \int_t \Bigg[ \int_{\mathcal{B}} \left[ \frac{\partial\widetilde{\pi}}{\partial\boldsymbol{\varepsilon}} : \nabla_{\boldsymbol{x}}\delta\dot{\boldsymbol{u}} + \frac{\partial\widetilde{\pi}}{\partial\nabla_{\boldsymbol{x}}\widetilde{\phi}} \cdot \nabla_{\boldsymbol{x}}\delta\dot{\widetilde{\phi}} + \frac{\partial\widetilde{\pi}}{\partial\boldsymbol{p}} \cdot \delta\dot{\boldsymbol{p}} + \frac{\partial\zeta}{\partial\dot{\boldsymbol{p}}} \cdot \delta\dot{\boldsymbol{p}} \right] \mathrm{d}v \\ + \mu_0 \int_{\mathbb{R}^3} \widetilde{\boldsymbol{h}} \cdot \nabla_{\boldsymbol{x}}\delta\dot{\widetilde{\phi}}\,\mathrm{d}v - \int_{\partial\mathcal{B}_t} \bar{\boldsymbol{t}} \cdot \delta\dot{\boldsymbol{u}}\,\mathrm{d}a \Bigg] \mathrm{d}t \doteq - \int_t \left[ \left[ \boldsymbol{\lambda} \cdot \frac{\partial\boldsymbol{r}_{\mathrm{c}}}{\partial\boldsymbol{p}} \right] \cdot \delta\dot{\boldsymbol{p}} \right] \mathrm{d}t \, . \end{aligned} \tag{4.17}$$

The four individual stationarity conditions of (4.17) for the primary fields are

$$\int_t \left[ \int_{\mathcal{B}} \frac{\partial\widetilde{\pi}}{\partial\boldsymbol{\varepsilon}} : \nabla_{\boldsymbol{x}}\delta\dot{\boldsymbol{u}}\,\mathrm{d}v - \int_{\partial\mathcal{B}_t} \bar{\boldsymbol{t}} \cdot \delta\dot{\boldsymbol{u}}\,\mathrm{d}a \right] \mathrm{d}t \doteq 0 \, , \tag{4.18}$$

$$\int_t \left[ \int_{\mathcal{B}} \left[ -\frac{\partial\widetilde{\pi}}{\partial\widetilde{\boldsymbol{h}}} + \mu_0\,\widetilde{\boldsymbol{h}} \right] \cdot \nabla_{\boldsymbol{x}}\delta\dot{\widetilde{\phi}}\,\mathrm{d}v \right] \mathrm{d}t \doteq 0 \, , \tag{4.19}$$

$$\int_t \left[ \mu_0 \int_{\mathbb{R}^3\backslash\mathcal{B}} \widetilde{\boldsymbol{h}} \cdot \nabla_{\boldsymbol{x}}\delta\dot{\widetilde{\phi}}\,\mathrm{d}v \right] \mathrm{d}t \doteq 0 \, , \tag{4.20}$$

$$\int_t \left[ \int_{\mathcal{B}} \left[ \frac{\partial\widetilde{\pi}}{\partial\boldsymbol{p}} + \frac{\partial\zeta}{\partial\dot{\boldsymbol{p}}} \right] \cdot \delta\dot{\boldsymbol{p}}\,\mathrm{d}v + \boldsymbol{\lambda} \cdot \frac{\partial\boldsymbol{r}_{\mathrm{c}}}{\partial\boldsymbol{p}} \cdot \delta\dot{\boldsymbol{p}} \right] \mathrm{d}t \doteq 0 \, . \tag{4.21}$$

Since (4.18) to (4.21) shall hold for any time $t$, they are recast into

$$\int\limits_{\mathcal{B}} \frac{\partial \widetilde{\pi}}{\partial \boldsymbol{\varepsilon}} : \nabla_{\boldsymbol{x}} \delta \dot{\boldsymbol{u}} \,\mathrm{d}v - \int\limits_{\partial \mathcal{B}_t} \bar{\boldsymbol{t}} \cdot \delta \dot{\boldsymbol{u}} \,\mathrm{d}a \doteq 0 \ , \tag{4.22}$$

$$\int\limits_{\mathcal{B}} \left[ -\frac{\partial \widetilde{\pi}}{\partial \widetilde{\boldsymbol{h}}} + \mu_0 \, \widetilde{\boldsymbol{h}} \right] \cdot \nabla_{\boldsymbol{x}} \delta \dot{\widetilde{\phi}} \,\mathrm{d}v \doteq 0 \ , \tag{4.23}$$

$$\mu_0 \int\limits_{\mathbb{R}^3 \backslash \mathcal{B}} \widetilde{\boldsymbol{h}} \cdot \nabla_{\boldsymbol{x}} \delta \dot{\widetilde{\phi}} \,\mathrm{d}v \doteq 0 \ , \tag{4.24}$$

$$\int\limits_{\mathcal{B}} \left[ \frac{\partial \widetilde{\pi}}{\partial \boldsymbol{p}} + \frac{\partial \zeta}{\partial \dot{\boldsymbol{p}}} \right] \cdot \delta \dot{\boldsymbol{p}} \,\mathrm{d}v + \boldsymbol{\lambda} \cdot \frac{\partial \boldsymbol{r}_{\mathrm{c}}}{\partial \boldsymbol{p}} \cdot \delta \dot{\boldsymbol{p}} \doteq 0 \ . \tag{4.25}$$

The Euler-Lagrange equations of the rate type variational principle may be derived by applying integration by parts and generalised divergence theorems to (4.22), (4.23), (4.24), and (4.25), see also [10, 21]. They are displayed here for the sake of completeness. For arbitrary but admissible variations, they are

$$\delta_{\boldsymbol{u}} \mathcal{L} : \quad \mathrm{div}_{\boldsymbol{x}} \boldsymbol{\sigma} = \boldsymbol{0} \quad \text{in } \mathcal{B} \ , \quad \boldsymbol{\sigma} \cdot \boldsymbol{n} = \bar{\boldsymbol{t}} \quad \text{on } \partial \mathcal{B}_t \ , \tag{4.26}$$

$$\begin{aligned} \delta_{\widetilde{\phi}} \mathcal{L} : \quad & \mathrm{div}_{\boldsymbol{x}} \widetilde{\boldsymbol{b}} = 0 \quad \text{in } \mathcal{B} \ , \quad \mathrm{div}_{\boldsymbol{x}} \widetilde{\boldsymbol{h}} = -\Delta_{\boldsymbol{x}} \widetilde{\phi} = 0 \quad \text{in } \mathbb{R}^3 \backslash \mathcal{B} \ , \\ & [\![ \widetilde{\boldsymbol{b}} ]\!] \cdot \boldsymbol{n} = 0 \quad \text{on } \partial \mathcal{B} \ , \end{aligned} \tag{4.27}$$

$$\delta_{\boldsymbol{p}} \mathcal{L} : \quad \boldsymbol{0} \in \int\limits_{\mathcal{B}} \left[ \frac{\partial \widetilde{\pi}}{\partial \boldsymbol{p}} + \frac{\partial \zeta}{\partial \dot{\boldsymbol{p}}} \right] \mathrm{d}v + \boldsymbol{\lambda} \cdot \frac{\partial \boldsymbol{r}_{\mathrm{c}}}{\partial \boldsymbol{p}} \quad \text{in } \mathcal{B} \ , \tag{4.28}$$

wherein the constitutive relation $\boldsymbol{\sigma} := \partial_{\boldsymbol{\varepsilon}} \psi^{\mathrm{mat}}(\boldsymbol{\varepsilon}, \boldsymbol{p})$ for the stress has been introduced. The Euler-Lagrange equations are interpretable as follows. The terms in equation (4.26) are the balance of linear momentum and the Neumann-type boundary conditions. From the variation w.r.t. the magnetic potential in (4.27), Gauss's law of magnetism is derived, wherein the Laplace operator $\Delta_{\boldsymbol{x}}$ and the jump condition $[\![\widetilde{\boldsymbol{b}}]\!] = \widetilde{\boldsymbol{b}}_+ - \widetilde{\boldsymbol{b}}_-$, i.e. the jump in $\widetilde{\boldsymbol{b}}$ between the sides $\partial \mathcal{B}_+$ and $\partial \mathcal{B}_-$ of the interface $\partial \mathcal{B}$, were used. Equation (4.28) is the Biot equation governing the evolution of the state variables. In the following, equations (4.22)–(4.25) will serve as a basis for the finite element implementation. The derivatives of the energy potential may be interpreted as the negative thermodynamically conjugate driving forces

$$\frac{\partial\widetilde{\pi}}{\partial\boldsymbol{\varepsilon}} = \frac{\partial\psi^{\text{mat}}}{\partial\boldsymbol{\varepsilon}} = \boldsymbol{\sigma} \ , \tag{4.29}$$

$$-\frac{\partial\widetilde{\pi}}{\partial\widetilde{\boldsymbol{h}}} = \mu_0\,\boldsymbol{m}(\boldsymbol{p}) \ , \tag{4.30}$$

$$\frac{\partial\widetilde{\pi}}{\partial\boldsymbol{p}} = \frac{\partial\psi^{\text{mat}}(\boldsymbol{p})}{\partial\boldsymbol{p}} - \mu_0\left[\overline{\boldsymbol{h}} + \widetilde{\boldsymbol{h}}\right]\cdot\frac{\partial\boldsymbol{m}(\boldsymbol{p})}{\partial\boldsymbol{p}} = \frac{\partial\psi^{\text{mat}}(\boldsymbol{p})}{\partial\boldsymbol{p}} - \mu_0\,\boldsymbol{h}\cdot\frac{\partial\boldsymbol{m}(\boldsymbol{p})}{\partial\boldsymbol{p}} \ . \tag{4.31}$$

Insertion of (4.30) into (4.23) yields

$$\mu_0\int_{\mathcal{B}}\left[\widetilde{\boldsymbol{h}} + \boldsymbol{m}(\boldsymbol{p})\right]\cdot\nabla_{\boldsymbol{x}}\delta\dot{\widetilde{\phi}}\,\mathrm{d}v \doteq 0 \ . \tag{4.32}$$

Combining (4.32) and (4.24) results in

$$\mu_0\int_{\mathcal{B}}\left[\widetilde{\boldsymbol{h}} + \boldsymbol{m}(\boldsymbol{p})\right]\cdot\nabla_{\boldsymbol{x}}\delta\dot{\widetilde{\phi}}\,\mathrm{d}v + \mu_0\int_{\mathbb{R}^3\backslash\mathcal{B}}\widetilde{\boldsymbol{h}}\cdot\nabla_{\boldsymbol{x}}\delta\dot{\widetilde{\phi}}\,\mathrm{d}v = \int_{\mathbb{R}^3}\widetilde{\boldsymbol{b}}\cdot\nabla_{\boldsymbol{x}}\delta\dot{\widetilde{\phi}}\,\mathrm{d}v \ , \tag{4.33}$$

where the above introduced magnetic induction $\widetilde{\boldsymbol{b}} = \mu_0\,[\,\widetilde{\boldsymbol{h}} + \boldsymbol{m}\,]$ and $\boldsymbol{m} = \boldsymbol{0}$ for $\boldsymbol{x} \in \mathbb{R}^3\backslash\mathcal{B}$ was used. The individual contributions depend on the chosen constitutive model and will be specified in the subsequent sections.

## 4.2 Constitutive model

After having introduced the global variational framework, the set of state variables $\boldsymbol{p}$ describing the underlying microstructure, the free energy density $\psi^{\text{mat}}(\boldsymbol{\varepsilon}, \boldsymbol{p})$, as well as the dissipation potential $\zeta(\dot{\boldsymbol{p}})$ associated with the evolution of the state variables need to be specified.

In this contribution, for the two dimensional case, two variants of nearly tetragonal (5M modulated) martensite are considered. The corresponding variant volume fractions are introduced as $\xi_1$, with $0 \leq \xi_1 \leq 1$, and $\xi_2 = 1 - \xi_1$, where the constraint of volume preservation, assuming mass conservation in terms of negligible density changes and identical densities of both variants, is directly incorporated, i.e. $\xi_1 + \xi_2 = 1$. The associated transformation or Bain strains of the two martensite variants are

$$\boldsymbol{\varepsilon}_1^{\text{tr}} = b_2\,\boldsymbol{e}_1\otimes\boldsymbol{e}_1 + b_1\,\boldsymbol{e}_2\otimes\boldsymbol{e}_2 + b_1\,\boldsymbol{e}_3\otimes\boldsymbol{e}_3 \ , \quad \boldsymbol{\varepsilon}_2^{\text{tr}} = b_1\,\boldsymbol{e}_1\otimes\boldsymbol{e}_1 + b_2\,\boldsymbol{e}_2\otimes\boldsymbol{e}_2 + b_1\,\boldsymbol{e}_3\otimes\boldsymbol{e}_3 \ , \tag{4.34}$$

with the Bain strain coefficients $b_1$ and $b_2$ and $\{\boldsymbol{e}_{1,2,3}\}$ as an orthonormal frame aligned with the crystallographic axes. The coefficients are directly related to the lattice constants of the cubic austenite parent phase $a_0 = 0.584\,\text{nm}$ and the martensite product phase $a = 0.595\,\text{nm}$ and $c = 0.561\,\text{nm}$, see [204], by $b_1 = [\,a - a_0\,]/a_0$ and $b_2 = [\,c - a_0\,]/a_0$. The transformation strains are related to the transformation matrix $\boldsymbol{U}_i$ by $\boldsymbol{\varepsilon}_i^{\text{tr}} = \boldsymbol{U}_i - \boldsymbol{I}$. It is worth noting that the shape memory effect only occurrs in materials where $\text{tr}(\boldsymbol{\varepsilon}_i^{\text{tr}}) \approx 0$ and that the considered martensite variants may form compatible twins that fulfil the strain compatibility condition in the small strain setting, see [15, 112, 218], viz.

$$\boldsymbol{\varepsilon}_1^{\text{tr}} - \boldsymbol{\varepsilon}_2^{\text{tr}} = \left[\,\boldsymbol{a}_{12} \otimes \boldsymbol{n}_{12}^{\text{tw}}\,\right]^{\text{sym}} = \frac{1}{2}\left[\,\boldsymbol{a}_{12} \otimes \boldsymbol{n}_{12}^{\text{tw}} + \boldsymbol{n}_{12}^{\text{tw}} \otimes \boldsymbol{a}_{12}\,\right] \ , \tag{4.35}$$

with the strain jump $\boldsymbol{a}_{12}$ and the interface normal $\boldsymbol{n}_{12}^{\text{tw}}$. The two solutions fulfilling (4.35) for the transformation strains introduced in (4.34) are

$$\boldsymbol{a}_{12} = \sqrt{2}\,[\,b_1 - b_2\,]\,[\,\mp\boldsymbol{e}_1 + \boldsymbol{e}_2\,] \ , \quad \boldsymbol{n}_{12}^{\text{tw}} = \frac{1}{\sqrt{2}}\,[\,\pm\boldsymbol{e}_1 + \boldsymbol{e}_2\,] \ . \tag{4.36}$$

Figure 4.2 illustrates one possible arrangement of the two martensite variants, coloured in blue and yellow, for the first of the two possible twin interfaces.

In the present modelling approach, the spatial distribution of the two martensite variants and the occurring interfaces are not resolved in full detail. Instead, the material behaviour and the assumed underlying microstructure are taken into account in an effective or homogenised sense. The underlying microstructure is assumed to consist of a single martensite variant or a mixture of both variants with different transformation strains, introduced in (4.34). The effective or homogenised strain of the phase mixture $\boldsymbol{\varepsilon}$ on the macroscale is assumed to be the weighted average of the total strains of the two martensite variants $\boldsymbol{\varepsilon}_i$, cf. [112], viz.

$$\boldsymbol{\varepsilon} := \xi_1\,\boldsymbol{\varepsilon}_1 + \xi_2\,\boldsymbol{\varepsilon}_2 \ , \tag{4.37}$$

where the $\boldsymbol{\varepsilon}_i$ need not be identical. The difference of the strains of both martensite variants is defined as the strain jump $[\![\boldsymbol{\varepsilon}]\!] := \boldsymbol{\varepsilon}_1 - \boldsymbol{\varepsilon}_2$. The strains $\boldsymbol{\varepsilon}_i$ are assumed to be additively decomposable into elastic $\boldsymbol{\varepsilon}_i^{\text{el}}$ and transformation parts $\boldsymbol{\varepsilon}_i^{\text{tr}}$, viz. $\boldsymbol{\varepsilon}_i = \boldsymbol{\varepsilon}_i^{\text{el}} + \boldsymbol{\varepsilon}_i^{\text{tr}}$. With this decomposition at hand, the insertion of the strain jump in (4.37) yields the elastic strains of the two martensite variants

$$\boldsymbol{\varepsilon}_1^{\text{el}} = \boldsymbol{\varepsilon} + \xi_2\,[\![\boldsymbol{\varepsilon}]\!] - \boldsymbol{\varepsilon}_1^{\text{tr}} \ , \quad \boldsymbol{\varepsilon}_2^{\text{el}} = \boldsymbol{\varepsilon} - \xi_1\,[\![\boldsymbol{\varepsilon}]\!] - \boldsymbol{\varepsilon}_2^{\text{tr}} \ . \tag{4.38}$$

They account for the energy storage due to reversible deviations from the energy well states. In this contribution, the elastic strain energy density $\psi_i^{\text{el}}$ of the $i$-th martensite variant is defined as

$$\psi_i^{\text{el}}(\boldsymbol{\varepsilon}_i^{\text{el}}) := \frac{1}{2}\,\boldsymbol{\varepsilon}_i^{\text{el}} : \mathbf{E}_i : \boldsymbol{\varepsilon}_i^{\text{el}} \ , \quad \text{with} \quad i = 1, 2 \ , \tag{4.39}$$

wherein $\mathbf{E}_i$ is a fourth-order elasticity tensor. For the sake of simplicity, the elasticity tensors of the two martensite variants are assumed to be identical, i.e. $\mathbf{E} = \mathbf{E}_1 = \mathbf{E}_2$, and isotropic, viz.

$$\mathbf{E} \mathrel{\widehat{=}} \big[\,\lambda^{\text{lam}}\,\delta_{ij}\,\delta_{kl} + \mu^{\text{lam}}\,[\delta_{ik}\,\delta_{jl} + \delta_{il}\,\delta_{jk}]\,\big]\ \boldsymbol{e}_i \otimes \boldsymbol{e}_j \otimes \boldsymbol{e}_k \otimes \boldsymbol{e}_l \ , \tag{4.40}$$

with the Lamé constants $\lambda^{\text{lam}}$ and $\mu^{\text{lam}}$, which are related to the Young's modulus $E$ and the Poisson's ratio $\nu$ through $\lambda^{\text{lam}} = [\,E\,\nu\,]/[\,[\,1+\nu\,]\,[\,1-2\,\nu\,]\,]$ and $\mu^{\text{lam}} = E/[\,2\,[\,1+\nu\,]\,]$. The total elastic strain energy density—applying a standard mixture rule—is defined as the average of the strain energy densities of the martensite variants, cf. [112],

$$\psi^{\,\text{el}} := \sum_{i=1}^{2} \xi_i\,\psi_i^{\text{el}} \ . \tag{4.41}$$

The strain jump $[\![\boldsymbol{\varepsilon}]\!]$ occurring in the elastic strains (4.38) is assumed to be determinable by the constrained minimisation of (4.41)

$$\psi^{\,\text{rel}}(\boldsymbol{\varepsilon}, \xi_i) := \inf_{[\![\boldsymbol{\varepsilon}]\!]}\ \psi^{\,\text{el}}(\boldsymbol{\varepsilon}, [\![\boldsymbol{\varepsilon}]\!], \xi_i) \quad \text{subject to } [\![\boldsymbol{\varepsilon}]\!] \text{ being admissible} \ , \tag{4.42}$$

where $\psi^{\,\text{rel}}$ is the so called relaxed energy density. In the context of numerical homogenisation, the admissible space of the strain jump is restricted, see [114, 156] for comparison, viz.

$$[\![\boldsymbol{\varepsilon}]\!] \in \left\{ \begin{array}{cl} \mathbf{0} & \text{Taylor/Voigt} \\ \{[\,\boldsymbol{a} \otimes \boldsymbol{n}^{\text{tw}}]^{\text{sym}} \mid \boldsymbol{a} \in \mathbb{R}^3\} & \text{partial rank-one} \\ \mathbb{R}^{3\times 3}_{\text{sym}} & \text{Reuss/Sachs} \end{array} \right. \ . \tag{4.43}$$

The Taylor/Voigt assumption, viz. identical strains, yields the upper bound of the total strain energy density. In this contribution, the strain jump $[\![\boldsymbol{\varepsilon}]\!]$ shall not be restricted which is identical to the Reuss/Sachs assumption and yields the lower bound of the strain energy density of the mixture, where the stresses in both martensite variants are identical, see below. However, kinematic compatibility of the total strains at the twin interface between the two variants is not enforced and hence not guaranteed, which would be the case for the jump being a rank-one tensor, with the strain jump $\boldsymbol{a}$ projected onto the interface normal $\boldsymbol{n}^{\text{tw}}$, see the compatibility of the transformation strains in (4.35) for comparison. Using the constitutive relation $\boldsymbol{\sigma} := \partial_{\boldsymbol{\varepsilon}} \psi^{\text{el}}$, the necessary condition states

$$\frac{\partial \psi^{\text{el}}}{\partial [\![\boldsymbol{\varepsilon}]\!]} = \xi_1 \, \xi_2 \, \mathsf{E} : [\, \boldsymbol{\varepsilon}_1^{\text{el}} - \boldsymbol{\varepsilon}_2^{\text{el}} \,] = \xi_1 \, \xi_2 \, [\, \boldsymbol{\sigma}_1 - \boldsymbol{\sigma}_2 \,] = \mathbf{0} \; , \quad \text{for} \quad [\![\boldsymbol{\varepsilon}]\!] \in \mathbb{R}^{3\times3}_{\text{sym}} \; , \tag{4.44}$$

which is satisfied for equal stresses and—for the assumptions stated above—equal elastic strains in both martensite variants. Insertion into (4.38) yields the optimal strain jump $[\![\boldsymbol{\varepsilon}]\!] = \boldsymbol{\varepsilon}_1^{\text{tr}} - \boldsymbol{\varepsilon}_2^{\text{tr}}$ and equal elastic strains

$$\boldsymbol{\varepsilon}_1^{\text{el}} = \boldsymbol{\varepsilon}_2^{\text{el}} = \boldsymbol{\varepsilon} - \sum_{i=1}^{2} \xi_i \, \boldsymbol{\varepsilon}_i^{\text{tr}} \; . \tag{4.45}$$

With (4.45) at hand, insertion into (4.41) yields the convex energy hull, cf. [94, 112],

$$C\psi^{\text{el}} = \frac{1}{2} \left[ \boldsymbol{\varepsilon} - \sum_{i=1}^{2} \xi_i \, \boldsymbol{\varepsilon}_i^{\text{tr}} \right] : \mathsf{E} : \left[ \boldsymbol{\varepsilon} - \sum_{i=1}^{2} \xi_i \, \boldsymbol{\varepsilon}_i^{\text{tr}} \right] \; , \tag{4.46}$$

which depends only on the macroscopic strain $\boldsymbol{\varepsilon}$ and the variant volume fraction $\xi_1$ ($\xi_2 = 1 - \xi_1$). The macroscopic stress is calculated by

$$\boldsymbol{\sigma} = \frac{\partial C\psi^{\text{el}}}{\partial \boldsymbol{\varepsilon}} = \mathsf{E} : \left[ \boldsymbol{\varepsilon} - \sum_{i=1}^{2} \xi_i \, \boldsymbol{\varepsilon}_i^{\text{tr}} \right] \; , \tag{4.47}$$

see (4.44) for comparison.

In order to fully characterise the underlying microstructure, the magnetic state needs to be specified. Each of the above introduced martensite variants has two opposingly oriented magnetic easy-axes directions aligned with the short $c$ edge of the tetragonal unit cell. The volumes, respectively areas, of equal magnetisation are defined as the magnetic domains with the absolute domain volume fractions $\alpha_j$, where $0 \leq \alpha_j \leq 1$. They are related to the variant volume fractions $\xi_i$ and the so-called net magnetisations within each martensite variant $\eta_i$, with $-\xi_i \leq \eta_i \leq \xi_i$, cf. [213], by

$$\alpha_{2i-1} = \frac{1}{2} \, [\, \xi_i + \eta_i \,] \quad \text{and} \quad \alpha_{2i} = \frac{1}{2} \, [\, \xi_i - \eta_i \,] \; , \quad \text{with} \quad i = 1, 2 \; . \tag{4.48}$$

The inverse relation yields

$$\xi_i = \alpha_{2i-1} + \alpha_{2i} \quad \text{and} \quad \eta_i = \alpha_{2i-1} - \alpha_{2i} \; , \quad \text{with} \quad i = 1, 2 \; . \tag{4.49}$$

The domains within each martensite variant are separated by 180° interfaces with the interface normals $\boldsymbol{n}_i^{\text{dom}}$

$$\boldsymbol{n}_1^{\text{dom}} = \boldsymbol{e}_2 \quad \text{and} \quad \boldsymbol{n}_2^{\text{dom}} = \boldsymbol{e}_1 \ , \tag{4.50}$$

which are assumed to remain constant during all loading conditions. The magnetisation vectors in each domain are not fixed to point in the easy-axes directions and may rotate away, which is associated with some finite magnetocrystalline anisotropy energy and captured by the rotation angles $\theta_j$, which are, in order to allow a distinction of the individual domains, restricted to $-\pi/2 \le \theta_j \le \pi/2$. The magnetisations within the four domains $\boldsymbol{m}_j$ are defined as, cf. [108, 112],

$$\begin{aligned}
\boldsymbol{m}_1 &:= \phantom{-} m_s \left[ \cos(\theta_1)\, \boldsymbol{e}_1 + \sin(\theta_1)\, \boldsymbol{e}_2 \right] \ , \\
\boldsymbol{m}_2 &:= - m_s \left[ \cos(\theta_2)\, \boldsymbol{e}_1 + \sin(\theta_2)\, \boldsymbol{e}_2 \right] \ , \\
\boldsymbol{m}_3 &:= - m_s \left[ \sin(\theta_3)\, \boldsymbol{e}_1 - \cos(\theta_3)\, \boldsymbol{e}_2 \right] \ , \\
\boldsymbol{m}_4 &:= \phantom{-} m_s \left[ \sin(\theta_4)\, \boldsymbol{e}_1 - \cos(\theta_4)\, \boldsymbol{e}_2 \right] \ ,
\end{aligned} \tag{4.51}$$

with the saturation magnetisation $m_s$ describing the lengths of the magnetisation vectors. It is usually a temperature dependent material parameter, but kept constant due to the assumption of isothermal conditions. The effective or homogenised magnetisation $\boldsymbol{m}$ is calculated as the weighted average of the magnetisations inside the individual domains by

$$\boldsymbol{m} := \sum_{j=1}^{4} \alpha_j(\xi_i, \eta_i)\, \boldsymbol{m}_j(\theta_j) \ . \tag{4.52}$$

One possible arrangement of the domains $\alpha_j$, each with a corresponding domain magnetisation $\boldsymbol{m}_j$, and the domain interface normals $\boldsymbol{n}_i^{\text{dom}}$ is illustrated in Figure 4.2. In addition to the twin compatibility of the tetragonal martensite variants, the magnetic compatibility, cf. [39, 41],—here specified for the domain interfaces within each martensite variant—is given as

$$\left[ \boldsymbol{m}_{2i-1} - \boldsymbol{m}_{2i} \right] \cdot \boldsymbol{n}_i^{\text{dom}} = 0 \ , \quad \text{with} \quad i = 1, 2 \ . \tag{4.53}$$

It is fulfilled for the energy well states, i.e. if no deviation from the easy-axes occurs, within each martensite variant and across the twin interface for domain one and three, respectively two and four.

The magnetic compatibility condition may be violated at the expense of some excess magnetostatic energy, see [41]. In this contribution, we neither enforce the magnetic compatibility at the domain interfaces nor across the twin interface for arbitrary rotation angles $\theta_j$. However, it is possible to show that satisfying (4.53) minimises the

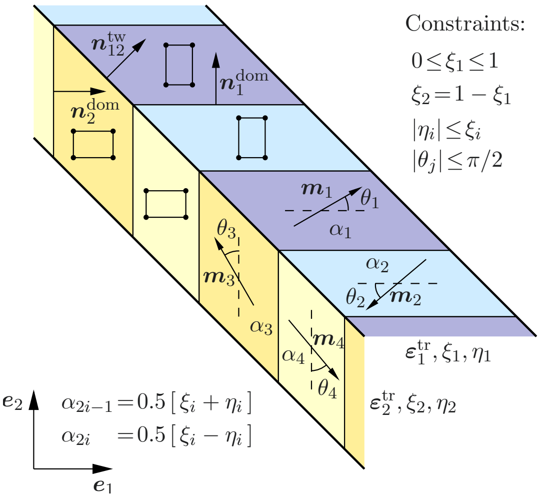
Constraints:
$0\le\xi_1\le1$
$\xi_2=1-\xi_1$
$|\eta_i|\le\xi_i$
$|\theta_j|\le\pi/2$
$\boldsymbol{n}_{12}^{\mathrm{tw}}$
$\boldsymbol{n}_1^{\mathrm{dom}}$
$\boldsymbol{n}_2^{\mathrm{dom}}$
$\boldsymbol{m}_1$
$\theta_1$
$\alpha_1$
$\alpha_2$
$\theta_2$
$\boldsymbol{m}_2$
$\theta_3$
$\boldsymbol{m}_3$
$\alpha_3$
$\boldsymbol{m}_4$
$\alpha_4$
$\theta_4$
$\boldsymbol{\varepsilon}_1^{\mathrm{tr}}, \xi_1, \eta_1$
$\boldsymbol{\varepsilon}_2^{\mathrm{tr}}, \xi_2, \eta_2$
$\boldsymbol{e}_2$
$\boldsymbol{e}_1$
$\alpha_{2i-1}=0.5\,[\,\xi_i+\eta_i\,]$
$\alpha_{2i}\quad=0.5\,[\,\xi_i-\eta_i\,]$

**Figure 4.2:** Initial parametrisation of the microstructure and constraints for the state variables. Martensite variants (transformation strains $\boldsymbol{\varepsilon}_i^{\mathrm{tr}}$, variant volume fractions $\xi_i$), magnetic domains (net magnetisations $\eta_i$), and magnetisation vectors ($\boldsymbol{m}_j(\theta_j)$ with $\theta_j$ as the deviation from the respective easy-axis). Absolute domain volume fractions $\alpha_j$ as dependent variables. In addition, one possible twin interface normal $\boldsymbol{n}_{12}^{\mathrm{tw}}$ (compatibility of the transformation strains) and the domain interface normals $\boldsymbol{n}_i^{\mathrm{dom}}$ (compatibility of the easy-axes magnetisations) are sketched. Adopted from [112]. See [60, 205] for experimentally observed twinned martensite patterns with internal domains.

magnetocrystalline anisotropy energy density within each martensite variant, see the derivation below and the appendix in Section 4.6.1. The magnetocrystalline anisotropy energy density within each domain for the considered case of uniaxial symmetry of the tetragonal martensite variants is, cf. [115, 170],

$$\psi_j^{\mathrm{an}}(\theta_j) = \sum_{n=1}^{N} k_n \, \sin^{2n}(\theta_j) \ , \quad \text{with} \quad j = 1, \ldots, 4 \ , \tag{4.54}$$

with the anisotropy constants $k_n$ and the $\theta_j$ introduced in (4.51). Since the magnetisation curves of 5M modulated martensite are nearly perfectly linear, cf. [73, 169, 200, 211], only the term of lowest order is important and consequently $N=1$, see also [116, 170]. The effective magnetocrystalline anisotropy energy density is calculated by applying a standard mixture rule

$$\psi^{\mathrm{an}} := \sum_{j=1}^{4} \alpha_j(\xi_i, \eta_i) \, \psi_j^{\mathrm{an}}(\theta_j) = k_1 \sum_{i=1}^{4} \alpha_j(\xi_i, \eta_i) \, \sin^2(\theta_j) \ . \tag{4.55}$$

In summary, the state of the underlying microstructure is determined by seven state variables $\boldsymbol{p}^\star = [\,\xi_1, \eta_1, \eta_2, \theta_1, \theta_2, \theta_3, \theta_4\,]^{\mathrm{t}}$, each constrained to lie in a specific interval with lower and upper bounds, written in terms of inequality constraints $r_c^\star \leq 0$

$$\begin{aligned}
&r_1^\star := -\xi_1 \ , \quad r_2^\star := \xi_1 - 1 \ , \quad r_{3,5}^\star := -\eta_i - \xi_i \ , \quad r_{4,6}^\star := \eta_i - \xi_i \ , \\
&r_{7,9,11,13}^\star := -\theta_j - \frac{\pi}{2} \ , \quad r_{8,10,12,14}^\star := \theta_j - \frac{\pi}{2} \ .
\end{aligned} \tag{4.56}$$

As mentioned above, it is possible to show that fulfilling (4.53) minimises the magnetocrystalline anisotropy (4.55) within each of the two martensite variants. In addition, the number of variables that describe the state of the underlying microstructure may be reduced by two and the number of corresponding inequality constraints may be reduced by ten. Firstly, the net magnetisations $\eta_i$ are replaced by the relative domain volume fractions $\gamma_i$, using the relation $\gamma_i = 0.5\,[\,\eta_i/\xi_i + 1\,]$, with $0 \leq \gamma_i \leq 1$, cf. [108, 110]. Secondly, effective normalised magnetisations $\boldsymbol{m}_i^* = m_{i1}\,\boldsymbol{e}_1 + m_{i2}\,\boldsymbol{e}_2$ of each martensite variant, with $\|\boldsymbol{m}_i^*\| \leq 1$ are introduced, cf. [21]. The former are used to replace the absolute domain volume fractions in (4.52) and the latter characterise the magnetic state of the two martensite variants, parametrised with $\gamma_i$ and the domain magnetisations $\boldsymbol{m}_i$, as introduced in (4.51), by

$$\begin{aligned}
\boldsymbol{m} &= \xi_1\,[\,\gamma_1\,\boldsymbol{m}_1 + [\,1-\gamma_1\,]\,\boldsymbol{m}_2\,] + \xi_2\,[\,\gamma_2\,\boldsymbol{m}_3 + [\,1-\gamma_2\,]\,\boldsymbol{m}_4\,] \\
&\equiv m_s\,[\,\xi_1\,\boldsymbol{m}_1^* + \xi_2\,\boldsymbol{m}_2^*\,] = m_s\,\boldsymbol{m}^* \ .
\end{aligned} \tag{4.57}$$

This relation is not unique, since three variables, namely the relative domain volume fraction $\gamma_i$ and the two angles $\theta_{2i-1}$ and $\theta_{2i}$, characterise the effective magnetisation within the $i$-th martensite variant parametrised with the two variables $m_{i1}$ and $m_{i2}$. It turned out that the magnetocrystalline anisotropy energy (4.55), with the alternative representation

$$\frac{\psi^{\mathrm{an}}}{k_1} = \xi_1\,[\,\gamma_1\,\sin^2(\theta_1) + [\,1-\gamma_1\,]\,\sin^2(\theta_2)\,] + \xi_2\,[\,\gamma_2\,\sin^2(\theta_3) + [\,1-\gamma_2\,]\,\sin^2(\theta_4)\,] \ , \tag{4.58}$$

is minimised for $\theta_{2i} = -\,\theta_{2i-1}$ within the $i$-th martensite variant at constant magnetisation, see the appendix in Section 4.6.1 for details. In addition, the magnetic compatibility condition across the 180° domain interfaces (4.53) is satisfied for $\theta_{2i} = -\,\theta_{2i-1}$. As already mentioned above, the number of variables may be reduced by two for optimal angles $\theta_2$ and $\theta_4$. From now on, the effective magnetisations are used to describe the magnetic state of the underlying microstructure. The new set of state variables is $\boldsymbol{p} = [\,\xi_1, m_{11}, m_{12}, m_{21}, m_{22}\,]^{\mathrm{t}}$, with four corresponding inequality constraints $r_i \leq 0$

$$r_1 := -\xi_1 \ , \quad r_2 := \xi_1 - 1 \ , \quad r_{3,4} := \|\boldsymbol{m}_i^*\| - 1 = \sqrt{\boldsymbol{m}_i^* \cdot \boldsymbol{m}_i^*} - 1 \ . \tag{4.59}$$

The constraints are collected in vector $\boldsymbol{r}_\mathrm{c}$, defined as

$$\boldsymbol{r}_\mathrm{c} := [\, r_1, r_2, r_3, r_4 \,]^\mathrm{t} \ . \tag{4.60}$$

Figure 4.3 illustrates the parametrisation with the newly introduced effective normalised magnetisations $\boldsymbol{m}_i^*$ of both martensite variants.

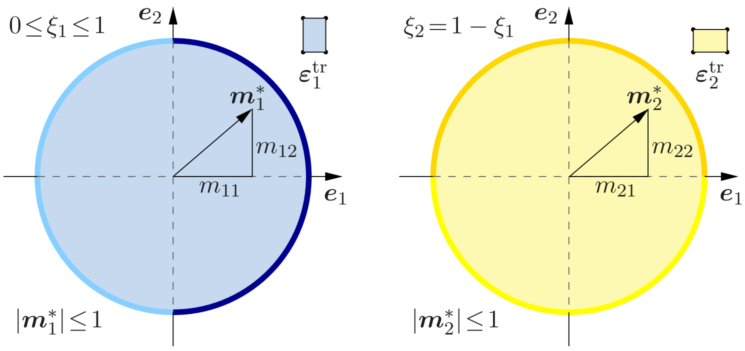
$0 \le \xi_1 \le 1$
$\boldsymbol{e}_2$
$\boldsymbol{\varepsilon}_1^\mathrm{tr}$
$\boldsymbol{m}_1^*$
$m_{12}$
$m_{11}$
$\boldsymbol{e}_1$
$|\boldsymbol{m}_1^*| \le 1$
$\xi_2 = 1 - \xi_1$
$\boldsymbol{e}_2$
$\boldsymbol{\varepsilon}_2^\mathrm{tr}$
$\boldsymbol{m}_2^*$
$m_{22}$
$m_{21}$
$\boldsymbol{e}_1$
$|\boldsymbol{m}_2^*| \le 1$

**Figure 4.3:** Parametrisation of the microstructure and constraints for the state variables. Martensite variants (transformation strains $\boldsymbol{\varepsilon}_i^\mathrm{tr}$, variant volume fractions $\xi_i$) and effective magnetisations of the martensite variants ($\boldsymbol{m}_i^* = m_{i1}\, \boldsymbol{e}_1 + m_{i2}\, \boldsymbol{e}_2$), see also [21].

**Remark 5** *Due to numerical reasons, slightly modified versions $r_c^*$ of the constraints $r_c$ are used for the numerical implementation. The admissible range of the volume fraction $\xi_1$ and the $\boldsymbol{m}_i^*$ is slightly reduced and a small value $\epsilon$ is added in the latter constraints to avoid a division by zero in the derivatives of $r_{3/4}$ w.r.t. $\boldsymbol{m}_i^*$, viz.*

$$r_1^* := -\xi_1 + \xi_\mathrm{tol} \ , \quad r_2^* := \xi_1 - 1 + \xi_\mathrm{tol} \ , \quad r_{3/4}^* := \sqrt{\boldsymbol{m}_i^* \cdot \boldsymbol{m}_i^* + \epsilon} - [\, 1 - m_\mathrm{tol}^* \,] \ . \tag{4.61}$$

*Convenient choices for the tolerance values are $\epsilon = 10^{-12}$ and $\xi_\mathrm{tol} = m_\mathrm{tol}^* = 10^{-3}$. The modified constraints are collected in the vector $\boldsymbol{r}_\mathrm{c}^*$, defined as*

$$\boldsymbol{r}_\mathrm{c}^* := [\, r_1^*, r_2^*, r_3^*, r_4^* \,]^\mathrm{t} \ . \tag{4.62}$$

**Remark 6** *The variables of the new set $\boldsymbol{p}$ are directly related to the initial variables $\boldsymbol{p}^\star$, as also used in previous works [10, 112, 114], see also [21], viz.*

$$\begin{aligned}
&\theta_1 = -\,\theta_2 = \arcsin(m_{12}) \ , && \theta_3 = -\,\theta_4 = -\ \arcsin(m_{21}) \ , \\
&\eta_1 = \xi_1 \, \frac{m_{11}}{\cos(\theta_1)} \ , && \eta_2 = \xi_2 \, \frac{m_{22}}{\cos(\theta_3)} \ , \\
&\gamma_1 = 0.5 \left[ \frac{m_{11}}{\cos(\theta_1)} + 1 \right] \ , && \gamma_2 = 0.5 \left[ \frac{m_{22}}{\cos(\theta_3)} + 1 \right] \ , \quad \textit{for } \cos(\theta_j) \neq 0 \ , \\
&\alpha_{2i-1} = 0.5\, [\, \xi_i + \eta_i \,] = \xi_i \, \gamma_i \ , && \alpha_{2i} = 0.5\, [\, \xi_i - \eta_i \,] = \xi_i \, [\, 1 - \gamma_i \,] \ , \quad \textit{with } i = 1, 2 \ .
\end{aligned} \tag{4.63}$$

*The excluded values* $\cos(\theta_j)=0$ *are equivalent to a full alignment of the corresponding magnetisation with the hard-axis direction. In such a case, both magnetisation and anisotropy energy density are independent of the the associated relative domain volume fraction* $\gamma_i$ *or net magnetisation* $\eta_i$*. Consequently, they may take arbitrary values that satisfy the constraints stated above.*

Insertion of (4.63) in (4.55) or (4.58) results in the compact form of the magnetocrystalline anisotropy energy density

$$\psi^{\,\mathrm{an}} = k_1\,[\,\xi_1\, m_{12}^2 + \xi_2\, m_{21}^2\,] = k_1\,[\,\xi_1\, m_{12}^2 + [\,1-\xi_1\,]\, m_{21}^2\,]\ . \tag{4.64}$$

The averaged magnetisation $\boldsymbol{m}$, see (4.57), is characterised by four variables for optimal angles $\theta_2 = -\,\theta_1$ and $\theta_4 = -\,\theta_3$, viz.

$$\begin{aligned}\boldsymbol{m} &= m_s\,\boldsymbol{m}^* = m_s\,[\,\xi_1\,\boldsymbol{m}_1^* + \xi_2\,\boldsymbol{m}_2^*\,]\\ &= m_s\,[[\,\xi_1\, m_{11} + \xi_2\, m_{21}\,]\,\boldsymbol{e}_1 + [\,\xi_1\, m_{12} + \xi_2\, m_{22}\,]\,\boldsymbol{e}_2]\ .\end{aligned} \tag{4.65}$$

The total stored energy density is the sum of the strain energy density (4.46), which depends only on the state variable $\xi_1$ that occurs in $\boldsymbol{p}^\star$ as well as $\boldsymbol{p}$, and on the magnetocrystalline anisotropy energy density (4.64)

$$\psi^{\mathrm{mat}}(\boldsymbol{\varepsilon},\boldsymbol{p}) = C\psi^{\,\mathrm{el}}(\boldsymbol{\varepsilon},\boldsymbol{p}) + \psi^{\,\mathrm{an}}(\boldsymbol{p})\ . \tag{4.66}$$

So far, the parametrisation of the underlying microstructure $\boldsymbol{p}$, the stored energy density, and the constraints were introduced. Experiments suggest that the mechanism of martensite variant reorientation (evolution of $\xi_1$) is associated with a significant amount of dissipation, since the stress and magnetic field induced strain and magnetisation response curves show a clearly visible hysteretic behaviour, see [71, 202] and the response curves taken from [200] in Figures 4.17 and 4.20. In other experiments, the mechanisms of domain wall motion (evolution of $\gamma_i$ or $m_{11}/m_{22}$ at constant $m_{12}/m_{21}$) and rotation of the magnetisation vectors (evolution of $m_{12}/m_{21}$), hence the easy- and the hard-axis magnetisation curves, were in fact isolated and only relatively low dissipation occurred, see the response curves taken from [211, 212] in Figure 4.8. In previous works by [10, 21, 112, 114], only the evolution of the martensite volume fractions were considered to be dissipative. In this contribution, however, the evolutions of all other state variables are also considered to be dissipative. In addition to the possibility of an even better approximation of experimental curves, the convergence of the global Newton-Raphson method improves, since the evolution of the state variables, especially $m_{11}/m_{22}$, is smoothed and erratic changes no longer occur. In the following, the time discrete evolution equations for all state variables of the set $\boldsymbol{p}$ are derived in analogy to [21].

In a first step, the vector containing all driving forces $\boldsymbol{\mathcal{F}}$, which are conjugate to the rates of the state variables $\dot{\boldsymbol{p}}$, are derived as the negative gradient $-\,\partial_{\boldsymbol{p}}\widetilde{\pi}$ in $\mathcal{B}$, cf. (4.31),

$$\boldsymbol{\mathcal{F}} := -\,\frac{\partial\psi^{\mathrm{mat}}}{\partial\boldsymbol{p}} + \mu_0\,\left[\,\overline{\boldsymbol{h}} + \widetilde{\boldsymbol{h}}\,\right]\cdot\frac{\partial\boldsymbol{m}}{\partial\boldsymbol{p}} = -\,\frac{\partial C\psi^{\,\mathrm{el}}}{\partial\boldsymbol{p}} - \frac{\partial\psi^{\,\mathrm{an}}}{\partial\boldsymbol{p}} + \mu_0\,m_s\,\boldsymbol{h}\cdot\frac{\partial\boldsymbol{m}^*}{\partial\boldsymbol{p}}\;. \tag{4.67}$$

With the individual contributions

$$\frac{\partial C\psi^{\,\mathrm{el}}}{\partial\boldsymbol{p}} = \begin{bmatrix}\boldsymbol{\sigma}:[\,\boldsymbol{\varepsilon}_2^{\mathrm{tr}} - \boldsymbol{\varepsilon}_1^{\mathrm{tr}}\,]\\ 0\\ 0\\ 0\\ 0\end{bmatrix}^{\mathrm{t}}, \quad \frac{\partial\psi^{\,\mathrm{an}}}{\partial\boldsymbol{p}} = k_1\begin{bmatrix}m_{12}^2 - m_{21}^2\\ 0\\ 2\,\xi_1\,m_{12}\\ 2\,\xi_2\,m_{21}\\ 0\end{bmatrix}^{\mathrm{t}},$$

$$\frac{\partial\boldsymbol{m}^*}{\partial\boldsymbol{p}} = \begin{bmatrix}[\,m_{11} - m_{21}\,] & \xi_1 & 0 & \xi_2 & 0\\ [\,m_{12} - m_{22}\,] & 0 & \xi_1 & 0 & \xi_2\end{bmatrix}, \tag{4.68}$$

the driving force vector (4.67) reads

$$\boldsymbol{\mathcal{F}} = \begin{bmatrix}\boldsymbol{\sigma}:[\,\boldsymbol{\varepsilon}_1^{\mathrm{tr}} - \boldsymbol{\varepsilon}_2^{\mathrm{tr}}\,] + k_1\,[\,m_{21}^2 - m_{12}^2\,] + \mu_0\,m_s\,\boldsymbol{h}\cdot[\,\boldsymbol{m}_1^* - \boldsymbol{m}_2^*\,]\\ \mu_0\,m_s\,h_1\,\xi_1\\ -2\,k_1\,\xi_1\,m_{12} + \mu_0\,m_s\,h_2\,\xi_1\\ -2\,k_1\,\xi_2\,m_{21} + \mu_0\,m_s\,h_1\,\xi_2\\ \mu_0\,m_s\,h_2\,\xi_2\end{bmatrix}^{\mathrm{t}}. \tag{4.69}$$

In the non-dissipative case where state variable $p_i$ is determined by minimising the total potential—neglecting contributions due to the constraints—, the necessary condition states $-\mathcal{F}_i = 0$. The evolution of the martensite volume fraction is triggered by mechanical as well as magnetic field loading, and all other variables evolve only due to magnetic field loading, see (4.69). The contributions due to the constraints (4.60), respectively (4.62), as outlined in (4.25), are often part of the so-called enhanced driving forces, cf. [44, 45]. In our finite element implementation, however, the contributions are only taken into account at discrete nodes of the finite element mesh and are not part of the volume integrals, as also suggested in (4.25), see Section 4.3 for details.

The second step is the choice of suitable dissipation functionals to derive thermodynamically consistent evolution equations, see, e.g., [81]. Here, we restrict ourselves to viscous rate-dependent evolution without and with a threshold, where no additional consistency conditions occur. It is expected that a rate dependent evolution is a suitable approximation of the real material behaviour, since otherwise instantaneous changes of the microstructure could evolve with infinite speed. In addition, an increase in the numerical robustness is expected.

The non-smooth dissipation potential of Perzyna type for viscous rate-dependent evolution with a threshold, respectively yield limit, that must be overcome by the driving force, cf. modelling of plasticity and [7], is defined as

$$\zeta_i(\dot{p}_i) := Y_i\,|\dot{p}_i| + \frac{\eta_i}{2}\,\dot{p}_i^2 \ , \tag{4.70}$$

where $Y_i > 0$ can be interpreted as a threshold and $\eta_i > 0$ as a viscosity parameter. For $\eta_i \to 0$, the rate-independent case is approximated. The threshold may be set to zero and consequently any driving force, except for $\mathcal{F}_i = 0$, will trigger an evolution of the corresponding state variable. The total dissipation functional is defined as follows

$$\zeta(\dot{\boldsymbol{p}}) := \sum_{i=1}^{5} \zeta_i(\dot{p}_i) = \sum_{i=1}^{5} \left[ Y_i\,|\dot{p}_i| + \frac{\eta_i}{2}\,\dot{p}_i^2 \right] \ . \tag{4.71}$$

With (4.69) defined in (4.67) and (4.70) at hand, the explicit evolution equations—neglecting the contributions due to the constraints—are derived from (4.25) in $\mathcal{B}$, see [81], as

$$\dot{p}_i = \frac{1}{\eta_i}\,\mathrm{sign}\,(\mathcal{F}_i)\,\langle|\mathcal{F}_i| - Y_i\rangle \ , \tag{4.72}$$

where Macaulay brackets, defined as $\langle\bullet\rangle := 0.5[\,\bullet + |\bullet|\,]$, are used for a compact notation. For the numerical implementation, the rate of the $i$-th variable of $\boldsymbol{p}$ is approximated assuming constant rates in the time interval $\Delta\,t = t_{n+1} - t_n$ by

$$\dot{p}_i \approx \frac{p_i^{n+1} - p_i^n}{\Delta\,t} = \frac{p_i^{n+1} - p_i^n}{t_{n+1} - t_n} \ , \tag{4.73}$$

with a known initial state $p_i^n$. Using the approximation of the rates (4.73), the evolution equation (4.72) shall be solved using the backward Euler method, viz.

$$p_i^{n+1} - p_i^n - \frac{\Delta\,t}{\eta_i}\,\mathrm{sign}\left(\mathcal{F}_i^{n+1}\right)\,\left\langle\left|\mathcal{F}_i^{n+1}\right| - Y_i\right\rangle = 0 \ . \tag{4.74}$$

After having introduced the dissipation potential and after deriving the corresponding evolution equation in general, the specific forms of the evolution equations for the state variables $\boldsymbol{p}$ are specified. The individual driving forces are collected in the driving force vector, as specified in (4.69). The threshold for the evolution of the martensite variant volume fraction is introduced as $Y_\xi$ and for the effective magnetisations as $Y_m = 0$.

Analogously, the viscosities $\eta_\xi$ and $\eta_m$ are introduced. The vector containing all residuals of the time discrete evolution equations is defined as

$$\boldsymbol{r}^{\text{evo}} := \begin{bmatrix} \xi_1^{n+1} - \xi_1^n - \frac{\Delta t}{\eta_\xi} \operatorname{sign}\left(\mathcal{F}_1^{n+1}\right) \left\langle \left|\mathcal{F}_1^{n+1}\right| - Y_\xi \right\rangle \\ m_{11}^{n+1} - m_{11}^n - \frac{\Delta t}{\eta_m} \mathcal{F}_2^{n+1}/\xi_1 \\ m_{12}^{n+1} - m_{12}^n - \frac{\Delta t}{\eta_m} \mathcal{F}_3^{n+1}/\xi_1 \\ m_{21}^{n+1} - m_{21}^n - \frac{\Delta t}{\eta_m} \mathcal{F}_4^{n+1}/\xi_2 \\ m_{22}^{n+1} - m_{22}^n - \frac{\Delta t}{\eta_m} \mathcal{F}_5^{n+1}/\xi_2 \end{bmatrix} , \tag{4.75}$$

where the driving forces for the evolution of the effective magnetisations were normalised by the corresponding martensite variant volume fraction of the corresponding martensite variant, since the evolution of the effective magnetisation within one martensite variant is assumed to be independent of the corresponding martensite variant volume fraction. For the sake of completeness, it should be mentioned that it is also possible to introduce a dual dissipation functional $\zeta^*$ and to interpret the evolution equation as the solution of a penalty type approach with a reversible domain in the context of the classic principle of maximum dissipation, see [148].

## 4.3 Implementation and algorithmic treatment

This section deals with the finite element implementation of the equations stemming from the micromagnetics inspired power-type potential (4.13) introduced in Section 4.1 and the constitutive model introduced in Section 4.2. Details regarding the algorithmic implementation and the numerical treatment of the inequality constraints are discussed. The derivation follows mostly standard finite element procedures, see, e.g., [86, 227] and [113]. It is based on previous work of the authors, see [21].

In this contribution, we focus on the two dimensional plane case, where the surrounding free space $\mathbb{R}^2$ is approximated by a sufficiently large finite size free space box $\mathit{\Omega} \subset \mathbb{R}^2$. As introduced in the energy potential (4.10) and the dissipation functionals as part of the power-type potential (4.13), two different regions, namely the areas of the magnetostrictive body $\mathcal{B}$ and the surrounding free space box $\mathit{\Omega}\backslash\mathcal{B}$, are considered. The areas are geometrically approximated using $n_{\text{el}}^{\mathcal{B}}$ elements $\mathcal{B}^e$ for the body and $n_{\text{el}}^{\mathit{\Omega}\backslash\mathcal{B}}$ elements $\mathcal{B}^e$ for the surrounding free space box

$$\mathcal{B} \approx \bigcup_{e=1}^{n_{\text{el}}^{\mathcal{B}}} \mathcal{B}^e , \quad \mathit{\Omega}\backslash\mathcal{B} \approx \bigcup_{e=n_{\text{el}}^{\mathcal{B}}+1}^{n_{\text{el}}^{\mathcal{B}}+n_{\text{el}}^{\mathit{\Omega}\backslash\mathcal{B}}} \mathcal{B}^e . \tag{4.76}$$

The displacement field $\boldsymbol{u}$ and the magnetic potential of the demagnetisation field $\widetilde{\phi}$ are spatially discretised using eight-node quadratic serendipity elements, see, e.g., [43], with

$n_{\text{en}}^{\boldsymbol{u}} = n_{\text{en}}^{\widetilde{\phi}} = 8$. The state variables, however, are spatially discretised using four-node bilinear elements, with $n_{\text{en}}^{\boldsymbol{p}} = 4$. This choice results from the fact that the displacement field $\boldsymbol{u}$ and the magnetic potential $\widetilde{\phi}$ shall be spatially discretised using shape functions of a higher polynomial degree than the polynomial degree of the shape functions used for the spatial discretisation of the state variables $\boldsymbol{p}$, since the gradients of the first two occur in the underlying equations, viz. the strain $\boldsymbol{\varepsilon}$ and demagnetisation field $\widetilde{\boldsymbol{h}}$, and since the state variables $\boldsymbol{p}$ appear solely as a global field itself. In contrast to all of these spatial discretisations, the KKT-parameters $\boldsymbol{\lambda}$ are only resolved at $n_{\text{np}}^{\mathcal{B}\boldsymbol{p}}$ discrete nodes of the finite element mesh—in particular the nodes where discrete values of the state variables $\boldsymbol{p}$ exist—and are not spatially discretised. This is motivated by the fact that by fulfilling the inequality constraints $\boldsymbol{r}_{\text{c}}(\boldsymbol{p}) \leq \boldsymbol{0}$ at all of these nodes, the inequality constraints are fulfilled everywhere inside the elements of the body, due to the choice of bilinear shape functions for the state variables $\boldsymbol{p}$, cf. [11]. The master elements in their local $\xi, \eta$-coordinate systems used for the discretisation of the body and the surrounding free space are shown in Figure 4.4. The shape functions and their gradients of the eight-node serendipity element and the four-node bilinear element are listed in Table 4.6 in the appendix, see Section 4.6.3.

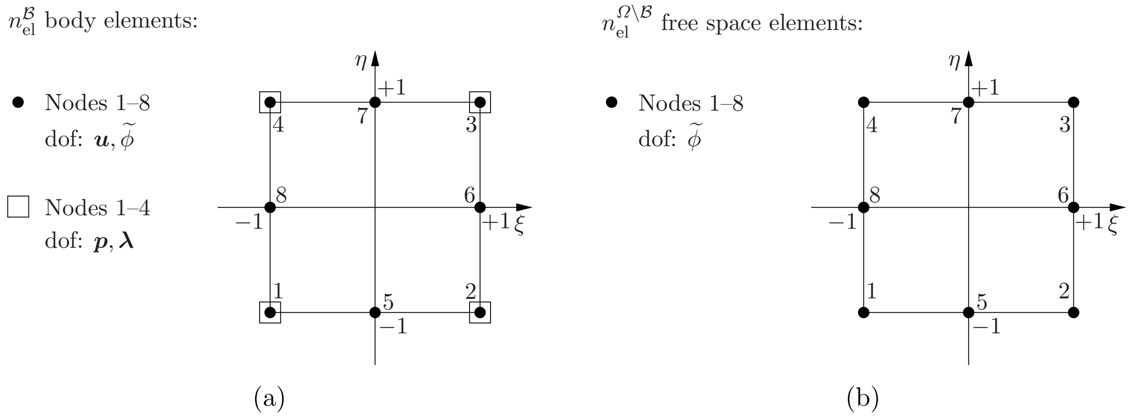
$n_{\text{el}}^{\mathcal{B}}$ body elements:
● Nodes 1–8
dof: $\boldsymbol{u}, \widetilde{\phi}$
☐ Nodes 1–4
dof: $\boldsymbol{p}, \boldsymbol{\lambda}$
$\eta$
+1
4
7
3
8
6
−1
+1 $\xi$
1
5
2
−1
$n_{\text{el}}^{\Omega\setminus\mathcal{B}}$ free space elements:
● Nodes 1–8
dof: $\widetilde{\phi}$
$\eta$
+1
4
7
3
8
6
−1
+1 $\xi$
1
5
2
−1

(a) (b)

**Figure 4.4:** (a) Mixed bilinear (nodes 1–4) and incomplete quadratic serendipity element (nodes 1–8) in the $\xi, \eta$-space used for the discretisation of the body $\mathcal{B}$. While discrete values of $\boldsymbol{u}$ and $\widetilde{\phi}$ exist at all nodes, discrete values of the variables $\boldsymbol{p}$ and $\boldsymbol{\lambda}$ exist only at nodes 1–4 marked with a box. (b) Incomplete quadratic serendipity element in the $\xi, \eta$-space used for the discretisation of the free space $\Omega \setminus \mathcal{B}$. Only the magnetic potential of the demagnetisation field $\widetilde{\phi}$ is resolved. See also [21] and [43].

**Remark 7** *Due to the use of mixed elements for the discretisation of the body, the areas in the considered two dimensional setting of the eight- and the four-node elements need not be identical, e.g. for elements used for the approximation of round parts of the geometry. To avoid overloading the notation, we do not distinguish between the areas of the eight- and the four-node elements. For a less coarse discretisation, their areas are approximately equal which is especially the case for the total area of the body.*

In the following, the governing equations of the finite element implementation are derived. Firstly, the three individual variations $\delta\dot{\boldsymbol{u}}, \delta\dot{\widetilde{\phi}}$, and $\delta\dot{\boldsymbol{p}}$ are spatially discretised using the above introduced mixed element formulation with $n_{\text{en}}^{\boldsymbol{u}} = n_{\text{en}}^{\widetilde{\phi}} = 8$ and $n_{\text{en}}^{\boldsymbol{p}} = 4$ nodes, w.r.t. element $e$

$$\delta\dot{\boldsymbol{u}}^e = \sum_{A=1}^{n_{\text{en}}^{\boldsymbol{u}}} \delta\dot{\boldsymbol{u}}^{eA}\, N_{\boldsymbol{u}}^A \ , \quad \delta\dot{\widetilde{\phi}}^e = \sum_{C=1}^{n_{\text{en}}^{\widetilde{\phi}}} \delta\dot{\widetilde{\phi}}^{eC}\, N_{\widetilde{\phi}}^C \ , \quad \delta\dot{\boldsymbol{p}}^e = \sum_{E=1}^{n_{\text{en}}^{\boldsymbol{p}}} \delta\dot{\boldsymbol{p}}^{eE}\, N_{\boldsymbol{p}}^E \ , \tag{4.77}$$

wherein $\delta\dot{\boldsymbol{u}}^{eA}, \delta\dot{\widetilde{\phi}}^{eC}$, and $\delta\dot{\boldsymbol{p}}^{eE}$ are discrete values of the variations and where $N_{\boldsymbol{u}}^A, N_{\widetilde{\phi}}^C$, and $N_{\boldsymbol{p}}^E$ are the shape functions used for the spatial discretisation of the variations within element $e$. Only the gradients of the first two variations $\delta\dot{\boldsymbol{u}}^e$ and $\delta\dot{\widetilde{\phi}}^e$ are calculated, since the gradient of the variation $\delta\dot{\boldsymbol{p}}$ does not occur in the governing equations, viz.

$$\nabla_{\boldsymbol{x}}\delta\dot{\boldsymbol{u}}^e = \sum_{A=1}^{n_{\text{en}}^{\boldsymbol{u}}} \delta\dot{\boldsymbol{u}}^{eA} \otimes \nabla_{\boldsymbol{x}} N_{\boldsymbol{u}}^A \ , \quad \nabla_{\boldsymbol{x}}\delta\dot{\widetilde{\phi}}^e = \sum_{C=1}^{n_{\text{en}}^{\widetilde{\phi}}} \delta\dot{\widetilde{\phi}}^{eC}\, \nabla_{\boldsymbol{x}} N_{\widetilde{\phi}}^C \ , \tag{4.78}$$

wherein $\nabla_{\boldsymbol{x}} N_{\boldsymbol{u}}^A$ and $\nabla_{\boldsymbol{x}} N_{\widetilde{\phi}}^C$ are the gradients of the shape functions.

With the spatial discretisation of the regions (4.76) and the spatial discretisation of the variations (4.77), respectively their gradients (4.78), at hand, (4.22), (4.33), and (4.25) are recast, by additionally using (4.29) and the vector containing the time discrete evolution equations (4.75), into

$$\sum_{e=1}^{n_{\text{el}}^{\mathcal{B}}} \sum_{A=1}^{n_{\text{en}}^{\boldsymbol{u}}} \delta\dot{\boldsymbol{u}}^{eA} \cdot \left[ \int\limits_{\mathcal{B}^e} \boldsymbol{\sigma} \cdot \nabla_{\boldsymbol{x}} N_{\boldsymbol{u}}^A \,\mathrm{d}v - \int\limits_{\mathcal{B}_t^e} N_{\boldsymbol{u}}^A\, \bar{\boldsymbol{t}} \,\mathrm{d}a \right] = 0 \ , \tag{4.79}$$

$$\sum_{e=1}^{n_{\text{el}}^{\mathcal{B}} + n_{\text{el}}^{\Omega\setminus\mathcal{B}}} \sum_{C=1}^{n_{\text{en}}^{\widetilde{\phi}}} \delta\dot{\widetilde{\phi}}^{eC} \int\limits_{\mathcal{B}^e} \nabla_{\boldsymbol{x}} N_{\widetilde{\phi}}^C \cdot \widetilde{\boldsymbol{b}} \,\mathrm{d}v = 0 \ , \tag{4.80}$$

$$\sum_{e=1}^{n_{\text{el}}^{\mathcal{B}}} \sum_{E=1}^{n_{\text{en}}^{\boldsymbol{p}}} \delta\dot{\boldsymbol{p}}^{eE} \cdot \int\limits_{\mathcal{B}^e} N_{\boldsymbol{p}}^E\, \boldsymbol{r}^{\text{evo}} \,\mathrm{d}v + \sum_{G=1}^{n_{\text{np}}^{\mathcal{B}\boldsymbol{p}}} \delta\dot{\boldsymbol{p}}^G \cdot \left[ \boldsymbol{\lambda}^G \cdot \frac{\partial \boldsymbol{r}_{\text{c}}(\boldsymbol{p}^G)}{\partial \boldsymbol{p}^G} \right] = 0 \ , \tag{4.81}$$

wherein

$$\boldsymbol{\lambda}^G \cdot \frac{\partial \boldsymbol{r}_{\rm c}(\boldsymbol{p}^G)}{\partial \boldsymbol{p}^G} = \begin{bmatrix} -\lambda_1^G + \lambda_2^G \\ \lambda_3^G \, m_{11}/\|\boldsymbol{m}_1^*\| \\ \lambda_3^G \, m_{12}/\|\boldsymbol{m}_1^*\| \\ \lambda_4^G \, m_{21}/\|\boldsymbol{m}_2^*\| \\ \lambda_4^G \, m_{22}/\|\boldsymbol{m}_2^*\| \end{bmatrix} . \tag{4.82}$$

**Remark 8** *The latter term in (4.81) accounts for the discrete contributions due to the constraints* $\boldsymbol{r}_{\rm c} \le \boldsymbol{0}$ *at all* $n_{\rm np}^{\mathcal{B}\boldsymbol{p}}$ *discrete nodes of the body* $\mathcal{B}$*. It is worth mentioning that the variations and the primary fields themselves are spatially approximated by using the same sets of shape functions. Consequently, discrete values of the variation* $\delta\dot{\boldsymbol{p}}^G$ *exist at exactly the same nodes as discrete values of the state variables* $\boldsymbol{p}^G$ *and the corresponding KKT-parameters* $\boldsymbol{\lambda}^G$*.*

The next step is the spatial discretisation of the primary fields and their gradients. Using the above introduced mixed element formulation with $n_{\rm en}^{\boldsymbol{u}} = n_{\rm en}^{\widetilde{\phi}} = 8$, respectively $n_{\rm en}^{\boldsymbol{p}} = 4$, nodes and the same sets of shape functions, the spatial discretisations w.r.t. element $e$ are

$$\boldsymbol{u}^e \approx \sum_{A=1}^{n_{\rm en}^{\boldsymbol{u}}} \boldsymbol{u}^{eA} \, N_{\boldsymbol{u}}^A \, , \qquad \widetilde{\phi}^e \approx \sum_{C=1}^{n_{\rm en}^{\widetilde{\phi}}} \widetilde{\phi}^{eC} \, N_{\widetilde{\phi}}^C \, , \qquad \boldsymbol{p}^e \approx \sum_{E=1}^{n_{\rm en}^{\boldsymbol{p}}} \boldsymbol{p}^{eE} \, N_{\boldsymbol{p}}^E \, ,$$

$$\nabla_{\boldsymbol{x}} \boldsymbol{u}^e = \sum_{A=1}^{n_{\rm en}^{\boldsymbol{u}}} \boldsymbol{u}^{eA} \otimes \nabla_{\boldsymbol{x}} N_{\boldsymbol{u}}^A \, , \quad \nabla_{\boldsymbol{x}} \widetilde{\phi}^e = \sum_{C=1}^{n_{\rm en}^{\widetilde{\phi}}} \widetilde{\phi}^{eC} \, \nabla_{\boldsymbol{x}} N_{\widetilde{\phi}}^C \, , \tag{4.83}$$

wherein $\boldsymbol{u}^{eA}, \widetilde{\phi}^{eC}$, and $\boldsymbol{p}^{eE}$ are discrete values of the primary fields. As introduced in (4.2), the spatial discretisation of the strain and the magnetic field are calculated by

$$\boldsymbol{f}^e = \sum_{A=1}^{n_{\rm en}^{\boldsymbol{u}}} \boldsymbol{u}^{eA} \otimes \nabla_{\boldsymbol{x}} N_{\boldsymbol{u}}^A \, , \quad \boldsymbol{\varepsilon}^e = \frac{1}{2} \left[ \boldsymbol{f}^e + [\, \boldsymbol{f}^e \,]^{\rm t} \right] \, , \quad \widetilde{\boldsymbol{h}}^e = - \sum_{C=1}^{n_{\rm en}^{\widetilde{\phi}}} \widetilde{\phi}^{eC} \, \nabla_{\boldsymbol{x}} N_{\widetilde{\phi}}^C \, . \tag{4.84}$$

As already stated above, the KKT-parameters $\boldsymbol{\lambda}^G$ that account for the compliance of the inequality constraints $r_i(\boldsymbol{p}^G) \le 0$, are introduced at all discrete nodes $n_{\rm np}^{\mathcal{B}\boldsymbol{p}}$ and are not spatially discretised. The Karush-Kuhn-Tucker conditions

$$r_i \le 0 \, , \quad \lambda_i^G \ge 0 \, , \quad \text{and} \quad \lambda_i^G \, r_i = 0 \, , \quad \text{with} \quad i = 1, \ldots, 4 \tag{4.85}$$

need to additionally be taken into account at all of the $n_{\mathrm{np}}^{\mathcal{B}\boldsymbol{p}}$ discrete nodes. In line with [7, 51, 189], the Fischer-Burmeister nonlinear complementarity problem (NCP) functions

$$g_i := \sqrt{[\,r_i\,]^2 + [\,\lambda_i^G\,]^2} + r_i - \lambda_i^G \;, \tag{4.86}$$

are used, where $g_i = 0$ is equivalent to satisfying the three KKT-conditions stated in (4.85). The function $g_i$ is plotted in Figure 4.5.

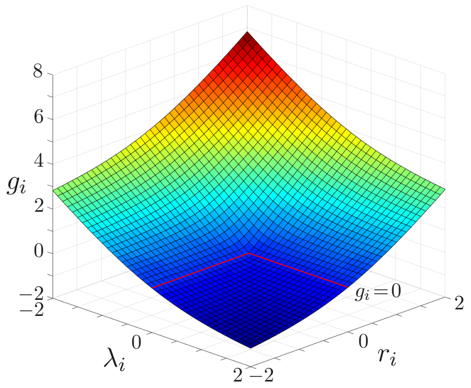

**Figure 4.5:** Representation of the Fischer-Burmeister function $g_i$ (4.86), adopted from [6].

**Remark 9** *The derivation of the Fischer-Burmeister functions $g_i$ is, e.g., detailed in [6] and summarised here. Starting with*

$$\lambda_i\, r_i = 0 \;, \tag{4.87}$$

*a multiplication with "$-2$" and addition of "$\lambda_i^2\!+\!r_i^2$" yields*

$$\lambda_i^2 - 2\,\lambda_i\, r_i + r_i^2 = \lambda_i^2 + r_i^2 \;. \tag{4.88}$$

*With (4.85) and the binomial theorem at hand, (4.88) is recast into*

$$\lambda_i - r_i = \sqrt{\lambda_i^2 + r_i^2} \;, \tag{4.89}$$

*respectively*

$$\sqrt{r_i^2 + \lambda_i^2} + r_i - \lambda_i = 0 \;, \tag{4.90}$$

*which is equal to $g_i\!=\!0$ in (4.86).*

The Fischer-Burmeister NCP functions $g_i = 0$ are solved at every one of the $n_{\mathrm{np}}^{\mathcal{B}\boldsymbol{p}}$ nodes of the body. The vector containing all Fischer-Burmeister NCP functions for node $G$ is defined as, cf. [11],

$$\boldsymbol{g}(\boldsymbol{p}^G, \boldsymbol{\lambda}^G) := [\, g_1, g_2, g_3, g_4 \,]^{\mathrm{t}} \; . \tag{4.91}$$

**Remark 10** *Due to numerical reasons, as already stated in Remark 5 in Section 4.2, slightly modified versions (4.61) of the constraints (4.59) are used. In addition, due to the possibility of a division by zero in the derivatives of the Fischer-Burmeister function (4.86), a small value $\epsilon$ is added to the square root and consequently the modified versions*

$$g_i^* = \sqrt{[\, r_i^* \,]^2 + [\, \lambda_i^G \,]^2 + \epsilon} + r_i^* - \lambda_i^G \; , \tag{4.92}$$

*where a convenient choice is $\epsilon = 10^{-12}$, are used for the numerical implementation.*

All of these quantities are assumed to exist at time $t = t_{n+1}$. In order to not overload the notation, the quantities at this time are not separately marked with an $n+1$. The state variables at time $t = t_n$, occurring in the time discrete evolution equations—see Section 4.2 for details—are known and thus constants.

The necessary condition for the stationarity of the system, fulfilling the constraints $r_i \leq 0$, states that (4.79), (4.80), and (4.81) must be zero for all admissible variations, satisfying the Dirichlet boundary conditions which are at the least used to prevent rigid body motions and to prescribe the magnetic potential $\widetilde{\phi} = 0$ on the surface $\partial\Omega$ of the free space box. This allows the definition of element-wise as well as discrete residuals. At first, the contributions due to the volume and surface integrals of element $e$ at node $A, C$, and $E$ are defined as

$$\begin{aligned} \boldsymbol{r}_{\boldsymbol{u}}^A &:= \int_{\mathcal{B}^e} \boldsymbol{\sigma} \cdot \nabla_{\boldsymbol{x}} N_{\boldsymbol{u}}^A \, \mathrm{d}v - \int_{\partial\mathcal{B}_t^e} N_{\boldsymbol{u}}^A \, \overline{\boldsymbol{t}} \, \mathrm{d}a \; , \\ r_{\widetilde{\phi}}^C &:= \int_{\mathcal{B}^e} \nabla_{\boldsymbol{x}} N_{\widetilde{\phi}}^C \cdot \widetilde{\boldsymbol{b}} \, \mathrm{d}v \; , \quad \boldsymbol{r}_{\boldsymbol{p}}^E := \int_{\mathcal{B}^e} N_{\boldsymbol{p}}^E \, \boldsymbol{r}^{\mathrm{evo}} \, \mathrm{d}v \; , \end{aligned} \tag{4.93}$$

wherein

$$\boldsymbol{f}_{\boldsymbol{u},\mathrm{int}}^{\mathcal{B}A} = \int_{\mathcal{B}^e} \boldsymbol{\sigma} \cdot \nabla_{\boldsymbol{x}} N_{\boldsymbol{u}}^A \, \mathrm{d}v \quad \text{and} \quad f_{\widetilde{\phi},\mathrm{int}}^{\mathcal{B}C} = \int_{\mathcal{B}^e} \nabla_{\boldsymbol{x}} N_{\widetilde{\phi}}^C \cdot \widetilde{\boldsymbol{b}} \, \mathrm{d}v \tag{4.94}$$

might be interpreted as internal force (vectors) corresponding to node $A$ and $C$ of element $e$. In addition, the second term in (4.93)

$$\boldsymbol{f}^{\mathcal{B}A}_{\boldsymbol{u},\mathrm{sur}} = \int\limits_{\partial\mathcal{B}^e_t} N^A_{\boldsymbol{u}}\,\bar{\boldsymbol{t}}\,\mathrm{d}a \tag{4.95}$$

might be interpreted as the surface force vector corresponding to node $A$ of element $e$. Secondly, the contributions due to the constraints at node $G$ of the $n^{\mathcal{B}\boldsymbol{p}}_{\mathrm{np}}$ discrete nodes are defined as

$$\boldsymbol{r}^G_{\boldsymbol{p}} := \boldsymbol{\lambda}^G \cdot \frac{\partial \boldsymbol{r}_{\mathrm{c}}(\boldsymbol{p}^G)}{\partial \boldsymbol{p}^G} \quad \text{and} \quad \boldsymbol{r}^G_{\boldsymbol{\lambda}} := \boldsymbol{g}(\boldsymbol{p}^G, \boldsymbol{\lambda}^G)\ , \tag{4.96}$$

wherein the first term was specified in (4.82) and wherein the second term is the vector containing the Fischer-Burmeister equations introduced in (4.91). The total residual vector of the system $\boldsymbol{r}$ is defined as the assembly of the contributions over all elements $e$ (4.93) and over all discrete nodes $G$ (4.96), viz.

$$\boldsymbol{r} := \mathop{\mathsf{A}}_{e=1}^{n^{\mathcal{B}}_{\mathrm{el}}} \begin{bmatrix} \boldsymbol{r}^A_{\boldsymbol{u}} \\ r^C_{\widetilde{\phi}} \\ \boldsymbol{r}^E_{\boldsymbol{p}} \\ \boldsymbol{0} \end{bmatrix} + \mathop{\mathsf{A}}_{e=n^{\mathcal{B}}_{\mathrm{el}}+1}^{n^{\mathcal{B}}_{\mathrm{el}}+n^{\Omega\backslash\mathcal{B}}_{\mathrm{el}}} \begin{bmatrix} \boldsymbol{0} \\ r^C_{\widetilde{\phi}} \\ \boldsymbol{0} \\ \boldsymbol{0} \end{bmatrix} + \mathop{\mathsf{A}}_{G=1}^{n^{\mathcal{B}\boldsymbol{p}}_{\mathrm{np}}} \begin{bmatrix} \boldsymbol{0} \\ 0 \\ \boldsymbol{r}^G_{\boldsymbol{p}} \\ \boldsymbol{r}^G_{\boldsymbol{\lambda}} \end{bmatrix} = \mathop{\mathsf{A}}_{e=1}^{n^{\mathcal{B}}_{\mathrm{el}}+n^{\Omega\backslash\mathcal{B}}_{\mathrm{el}}} \begin{bmatrix} \{\boldsymbol{r}^A_{\boldsymbol{u}}\} \\ r^C_{\widetilde{\phi}} \\ \{\boldsymbol{r}^E_{\boldsymbol{p}}\} \\ \boldsymbol{0} \end{bmatrix} + \mathop{\mathsf{A}}_{G=1}^{n^{\mathcal{B}\boldsymbol{p}}_{\mathrm{np}}} \begin{bmatrix} \boldsymbol{0} \\ 0 \\ \boldsymbol{r}^G_{\boldsymbol{p}} \\ \boldsymbol{r}^G_{\boldsymbol{\lambda}} \end{bmatrix}\ , \tag{4.97}$$

wherein the curly brackets $\{\bullet\}$ mark entries that contribute only to the $e = 1, \dots, n^{\mathcal{B}}_{\mathrm{el}}$ elements of the magnetisable body, to allow a compact notation of (4.97) and of the following equations. The necessary conditions for the stationarity of the system state that the global residual vector (4.97) is identical to zero ($\boldsymbol{r} = \boldsymbol{0}$), i.e. its norm $\|\boldsymbol{r}\| = 0$. In this contribution, the corresponding nonlinear system of equations is solved using a Newton-Raphson scheme. Therefore, the linearisations (first-order Taylor expansions) of the individual contributions of (4.97) are required. Having introduced the element-wise approximations for $\boldsymbol{u}, \widetilde{\phi}$, and $\boldsymbol{p}$ and their gradients (4.83)—depending on the discrete values at the $n^{\boldsymbol{u}}_{\mathrm{en}}, n^{\widetilde{\phi}}_{\mathrm{en}}$, and $n^{\boldsymbol{p}}_{\mathrm{en}}$ element nodes—in addition to the KKT-multipliers at the $n^{\mathcal{B}\boldsymbol{p}}_{\mathrm{np}}$ discrete nodes, the node-specific increments of the linearisations are defined as follows. Firstly, the non-zero increments of $\boldsymbol{r}_{\boldsymbol{u}}^{A}, r_{\widetilde{\phi}}^{C}$, and $\boldsymbol{r}_{\boldsymbol{p}}^{E}$ at node $A, C$, and $E$ w.r.t. the variables at node $B, D$, and $F$ are considered

$$
\begin{aligned}
\Delta\, \boldsymbol{r}_{\boldsymbol{u}}^{A} &= \sum_{B=1}^{n_{\text{en}}^{\boldsymbol{u}}} \frac{\mathrm{d}\boldsymbol{r}_{\boldsymbol{u}}^{A}}{\mathrm{d}\boldsymbol{u}^{B}} \cdot \Delta\, \boldsymbol{u}^{B} && && +\sum_{F=1}^{n_{\text{en}}^{\boldsymbol{p}}} \frac{\mathrm{d}\boldsymbol{r}_{\boldsymbol{u}}^{A}}{\mathrm{d}\boldsymbol{p}^{F}} \cdot \Delta\, \boldsymbol{p}^{F} \ , \\
\Delta\, r_{\widetilde{\phi}}^{C} &= && \sum_{D=1}^{n_{\text{en}}^{\widetilde{\phi}}} \frac{\mathrm{d} r_{\widetilde{\phi}}^{C}}{\mathrm{d}\widetilde{\phi}^{D}} \cdot \Delta\, \widetilde{\phi}^{D} && \left\{ +\sum_{F=1}^{n_{\text{en}}^{\boldsymbol{p}}} \frac{\mathrm{d} r_{\widetilde{\phi}}^{C}}{\mathrm{d}\boldsymbol{p}^{F}} \cdot \Delta\, \boldsymbol{p}^{F} \right\} \ , \\
\Delta\, \boldsymbol{r}_{\boldsymbol{p}}^{E} &= \sum_{B=1}^{n_{\text{en}}^{\boldsymbol{u}}} \frac{\mathrm{d}\boldsymbol{r}_{\boldsymbol{p}}^{E}}{\mathrm{d}\boldsymbol{u}^{B}} \cdot \Delta\, \boldsymbol{u}^{B} && + \sum_{D=1}^{n_{\text{en}}^{\widetilde{\phi}}} \frac{\mathrm{d}\boldsymbol{r}_{\boldsymbol{p}}^{E}}{\mathrm{d}\widetilde{\phi}^{D}} \cdot \Delta\, \widetilde{\phi}^{D} && +\sum_{F=1}^{n_{\text{en}}^{\boldsymbol{p}}} \frac{\mathrm{d}\boldsymbol{r}_{\boldsymbol{p}}^{E}}{\mathrm{d}\boldsymbol{p}^{F}} \cdot \Delta\, \boldsymbol{p}^{F} \ ,
\end{aligned}
\tag{4.98}
$$

where $\Delta\, \boldsymbol{u}^{B}, \Delta\, \widetilde{\phi}^{D}$ and $\Delta\, \boldsymbol{p}^{F}$ are the increments of the nodal degrees of freedom at nodes $B, D$, and $F$. For other constitutive models, a direct coupling between the displacement field $\boldsymbol{u}$ and the magnetic potential $\widetilde{\phi}$ might occur, resulting in additional non-zero contributions in (4.98). Secondly, the non-zero increments of $\boldsymbol{r}_{\boldsymbol{p}}^{G}$ and $\boldsymbol{r}_{\boldsymbol{\lambda}}^{G}$ at node $G$ w.r.t. the variables at the same node $G$ are considered

$$
\Delta\, \boldsymbol{r}_{\boldsymbol{p}}^{G} = \frac{\mathrm{d}\boldsymbol{r}_{\boldsymbol{p}}^{G}}{\mathrm{d}\boldsymbol{p}^{G}} \cdot \Delta\, \boldsymbol{p}^{G} + \frac{\mathrm{d}\boldsymbol{r}_{\boldsymbol{p}}^{G}}{\mathrm{d}\boldsymbol{\lambda}^{G}} \cdot \Delta\, \boldsymbol{\lambda}^{G} \ , \quad \Delta\, \boldsymbol{r}_{\boldsymbol{\lambda}}^{G} = \frac{\mathrm{d}\boldsymbol{r}_{\boldsymbol{\lambda}}^{G}}{\mathrm{d}\boldsymbol{p}^{G}} \cdot \Delta\, \boldsymbol{p}^{G} + \frac{\mathrm{d}\boldsymbol{r}_{\boldsymbol{\lambda}}^{G}}{\mathrm{d}\boldsymbol{\lambda}^{G}} \cdot \Delta\, \boldsymbol{\lambda}^{G} \ , \tag{4.99}
$$

where $\Delta\, \boldsymbol{p}^{G}$ and $\Delta\, \boldsymbol{\lambda}^{G}$ are the increments of the nodal degrees of freedom at node $G$. The terms in (4.98) and (4.99) in front of the nodal increments are defined as the stiffness matrices. In this contribution, the total derivatives are replaced by partial derivatives, since no implicit dependencies exist. The individual stiffness matrices are defined as follows

$$\boldsymbol{K}_{\boldsymbol{uu}}^{AB} := \frac{\mathrm{d}\boldsymbol{r}_{\boldsymbol{u}}^{A}}{\mathrm{d}\boldsymbol{u}^{B}} = \int\limits_{\mathcal{B}^e} \nabla_{\boldsymbol{x}} N_{\boldsymbol{u}}^{A} \cdot \frac{\partial \boldsymbol{\sigma}}{\partial \boldsymbol{\varepsilon}} \cdot \nabla_{\boldsymbol{x}} N_{\boldsymbol{u}}^{B} \, \mathrm{d}v \ , \tag{4.100}$$

$$\boldsymbol{K}_{\boldsymbol{up}}^{AF} := \frac{\mathrm{d}\boldsymbol{r}_{\boldsymbol{u}}^{A}}{\mathrm{d}\boldsymbol{p}^{F}} = \int\limits_{\mathcal{B}^e} \nabla_{\boldsymbol{x}} N_{\boldsymbol{u}}^{A} \cdot \frac{\partial \boldsymbol{\sigma}}{\partial \boldsymbol{p}} \, N_{\boldsymbol{p}}^{F} \, \mathrm{d}v \ , \tag{4.101}$$

$$K_{\widetilde{\phi}\widetilde{\phi}}^{CD} := \frac{\mathrm{d}r_{\widetilde{\phi}}^{C}}{\mathrm{d}\widetilde{\phi}^{D}} = \int\limits_{\mathcal{B}^e} -\mu_0 \, \nabla_{\boldsymbol{x}} N_{\widetilde{\phi}}^{C} \cdot \nabla_{\boldsymbol{x}} N_{\widetilde{\phi}}^{D} \, \mathrm{d}v \ , \tag{4.102}$$

$$\boldsymbol{K}_{\widetilde{\phi}\boldsymbol{p}}^{CF} := \frac{\mathrm{d}r_{\widetilde{\phi}}^{C}}{\mathrm{d}\boldsymbol{p}^{F}} = \int\limits_{\mathcal{B}^e} \mu_0 \, \nabla_{\boldsymbol{x}} N_{\widetilde{\phi}}^{C} \cdot \frac{\partial \boldsymbol{m}}{\partial \boldsymbol{p}} \, N_{\boldsymbol{p}}^{F} \, \mathrm{d}v \ , \tag{4.103}$$

$$\boldsymbol{K}_{\boldsymbol{pu}}^{EB} := \frac{\mathrm{d}\boldsymbol{r}_{\boldsymbol{p}}^{E}}{\mathrm{d}\boldsymbol{u}^{B}} = \int\limits_{\mathcal{B}^e} N_{\boldsymbol{p}}^{E} \, \frac{\partial \boldsymbol{r}^{\mathrm{evo}}}{\partial \boldsymbol{\varepsilon}} \cdot \nabla_{\boldsymbol{x}} N_{\boldsymbol{u}}^{B} \, \mathrm{d}v \ , \tag{4.104}$$

$$\boldsymbol{K}_{\boldsymbol{p}\widetilde{\phi}}^{ED} := \frac{\mathrm{d}\boldsymbol{r}_{\boldsymbol{p}}^{E}}{\mathrm{d}\widetilde{\phi}^{D}} = \int\limits_{\mathcal{B}^e} -N_{\boldsymbol{p}}^{E} \, \frac{\partial \boldsymbol{r}^{\mathrm{evo}}}{\partial \widetilde{\boldsymbol{h}}} \cdot \nabla_{\boldsymbol{x}} N_{\widetilde{\phi}}^{D} \, \mathrm{d}v \ , \tag{4.105}$$

$$\boldsymbol{K}_{\boldsymbol{pp}}^{EF} := \frac{\mathrm{d}\boldsymbol{r}_{\boldsymbol{p}}^{E}}{\mathrm{d}\boldsymbol{p}^{F}} = \int\limits_{\mathcal{B}^e} N_{\boldsymbol{p}}^{E} \, \frac{\partial \boldsymbol{r}^{\mathrm{evo}}}{\partial \boldsymbol{p}} \, N_{\boldsymbol{p}}^{F} \, \mathrm{d}v \ , \tag{4.106}$$

$$\boldsymbol{K}_{\boldsymbol{pp}}^{GG} := \frac{\mathrm{d}\boldsymbol{r}_{\boldsymbol{p}}^{G}}{\mathrm{d}\boldsymbol{p}^{G}} = \boldsymbol{\lambda}^{G} \cdot \frac{\partial^2 \boldsymbol{r}_{\mathrm{c}}(\boldsymbol{p}^{G})}{\partial {\boldsymbol{p}^{G}}^{2}} \ , \tag{4.107}$$

$$\boldsymbol{K}_{\boldsymbol{p\lambda}}^{GG} := \frac{\mathrm{d}\boldsymbol{r}_{\boldsymbol{p}}^{G}}{\mathrm{d}\boldsymbol{\lambda}^{G}} = \left[ \frac{\partial \boldsymbol{r}_{\mathrm{c}}(\boldsymbol{p}^{G})}{\partial \boldsymbol{p}^{G}} \right]^{\mathrm{t}} \ , \tag{4.108}$$

$$\boldsymbol{K}_{\boldsymbol{\lambda p}}^{GG} := \frac{\mathrm{d}\boldsymbol{r}_{\boldsymbol{\lambda}}^{G}}{\mathrm{d}\boldsymbol{p}^{G}} = \frac{\partial \boldsymbol{g}(\boldsymbol{p}^{G}, \boldsymbol{\lambda}^{G})}{\partial \boldsymbol{p}^{G}} \ , \tag{4.109}$$

$$\boldsymbol{K}_{\boldsymbol{\lambda\lambda}}^{GG} := \frac{\mathrm{d}\boldsymbol{r}_{\boldsymbol{\lambda}}^{G}}{\mathrm{d}\boldsymbol{\lambda}^{G}} = \frac{\partial \boldsymbol{g}(\boldsymbol{p}^{G}, \boldsymbol{\lambda}^{G})}{\partial \boldsymbol{\lambda}^{G}} \ , \tag{4.110}$$

with the $i=1,\dots,4$ entries in $\boldsymbol{K}^{GG}_{\boldsymbol{\lambda p}}$ and $\boldsymbol{K}^{GG}_{\boldsymbol{\lambda\lambda}}$

$$\frac{\partial g_i(\boldsymbol{p}^G,\lambda_i^G)}{\partial \boldsymbol{p}^G} = \frac{\partial r_i(\boldsymbol{p}^G)}{\partial \boldsymbol{p}^G} \left[ \frac{r_i(\boldsymbol{p}^G)}{\sqrt{[\,r_i(\boldsymbol{p}^G)\,]^2 + [\,\lambda_i^G\,]^2}} + 1 \right] , \tag{4.111}$$

$$\frac{\partial g_i(\boldsymbol{p}^G,\lambda_i^G)}{\partial \lambda_i^G} = \frac{\lambda_i^G}{\sqrt{[\,r_i(\boldsymbol{p}^G)\,]^2 + [\,\lambda_i^G\,]^2}} - 1 \,. \tag{4.112}$$

The individual stiffness matrices are specified in the appendix in Section 4.6.4. The total global stiffness matrix of the system is obtained by the following assembly operations

$$\boldsymbol{K} := \mathop{\mathsf{A}}_{e=1}^{n_{\mathrm{el}}^{\mathcal{B}}+n_{\mathrm{el}}^{\Omega\backslash\mathcal{B}}} \begin{bmatrix} \{\boldsymbol{K}^{AB}_{\boldsymbol{uu}}\} & \boldsymbol{0} & \{\boldsymbol{K}^{AF}_{\boldsymbol{up}}\} & \boldsymbol{0} \\ \boldsymbol{0} & K^{CD}_{\widetilde{\phi}\widetilde{\phi}} & \left\{\boldsymbol{K}^{CF}_{\widetilde{\phi}\boldsymbol{p}}\right\} & \boldsymbol{0} \\ \{\boldsymbol{K}^{EB}_{\boldsymbol{pu}}\} & \left\{\boldsymbol{K}^{ED}_{\boldsymbol{p}\widetilde{\phi}}\right\} & \{\boldsymbol{K}^{EF}_{\boldsymbol{pp}}\} & \boldsymbol{0} \\ \boldsymbol{0} & \boldsymbol{0} & \boldsymbol{0} & \boldsymbol{0} \end{bmatrix} + \mathop{\mathsf{A}}_{G=1}^{n_{\mathrm{np}}^{\mathcal{B}\boldsymbol{p}}} \begin{bmatrix} \boldsymbol{0} & \boldsymbol{0} & \boldsymbol{0} & \boldsymbol{0} \\ \boldsymbol{0} & 0 & \boldsymbol{0} & \boldsymbol{0} \\ \boldsymbol{0} & \boldsymbol{0} & \boldsymbol{K}^{GG}_{\boldsymbol{pp}} & \boldsymbol{K}^{GG}_{\boldsymbol{p\lambda}} \\ \boldsymbol{0} & \boldsymbol{0} & \boldsymbol{K}^{GG}_{\boldsymbol{\lambda p}} & \boldsymbol{K}^{GG}_{\boldsymbol{\lambda\lambda}} \end{bmatrix} , \tag{4.113}$$

wherein the first assembly operator accounts for the contributions of the volume integrals defined in (4.98), i.e. a summation over all elements $e$, and wherein the second assembly operator accounts for the contributions due the inequality constraints at the $n_{\mathrm{np}}^{\mathcal{B}\boldsymbol{p}}$ nodes $G$ defined in (4.99).

**Remark 11** *As indicated in the definition of the global residual vector (4.97) and the stiffness matrix (4.113), two different assembly routines are used in the finite element implementation. The first assembly operator accounts for the contributions evaluated in the distinct element routines for the* $n_{\mathrm{el}}^{\mathcal{B}}$ *elements of the body and the* $n_{\mathrm{el}}^{\Omega\backslash\mathcal{B}}$ *elements of the surrounding free space box. Therein, the contributions due to the volume integrals are evaluated by using a numerical integration scheme. The surface integrals, accounting for the prescribed tractions* $\bar{\boldsymbol{t}}$ *on the surface of the body* $\partial\mathcal{B}_t$*, see (4.93) and (4.95), are usually calculated in a preprocessing routine and later added to the global residual vector. After having assembled the contributions due to the volume integrals of all elements, the global residual vector* $\boldsymbol{r}$ *and the stiffness matrix* $\boldsymbol{K}$ *are modified and the contributions* $\boldsymbol{r}^G_{\boldsymbol{p}}$ *and* $\boldsymbol{K}^{GG}_{\boldsymbol{pp}}$ *are added to the already existing entries of the* $n_{\mathrm{np}}^{\mathcal{B}\boldsymbol{p}}$ *nodes. All other contributions arising from the constraints are directly stored in the residual vector and stiffness matrix. It is convenient to reserve memory for these contributions by adding temporary entries in the element routine of all body elements.*

The nodal increments occurring in (4.98) and (4.99) are formally assembled in a global vector of the nodal increments in analogy to (4.97) and (4.113), hence

$$\Delta\,\boldsymbol{d} := \mathop{\mathsf{A}}_{e=1}^{n_{\mathrm{el}}^{\mathcal{B}}+n_{\mathrm{el}}^{\Omega\setminus\mathcal{B}}} \begin{bmatrix} \{\Delta\,\boldsymbol{u}^{B}\} \\ \Delta\,\widetilde{\phi}^{D} \\ \{\Delta\,\boldsymbol{p}^{F}\} \\ \boldsymbol{0} \end{bmatrix} + \mathop{\mathsf{A}}_{G=1}^{n_{\mathrm{np}}^{\mathcal{B}\boldsymbol{p}}} \begin{bmatrix} \boldsymbol{0} \\ 0 \\ \Delta\,\boldsymbol{p}^{G} \\ \Delta\,\boldsymbol{\lambda}^{G} \end{bmatrix} . \tag{4.114}$$

The newly introduced quantity $\Delta\,\boldsymbol{d}$ is used in the compact notation for the update of all nodal degrees of freedom during the global iteration. The global system of equations

$$^{k}\boldsymbol{r} + {}^{k}\boldsymbol{K}\cdot\Delta\,\boldsymbol{d} = \boldsymbol{0} \ , \quad \text{with} \quad \Delta\,\boldsymbol{d} = {}^{k+1}\boldsymbol{d} - {}^{k}\boldsymbol{d} \ , \tag{4.115}$$

where $k$ is the iteration counter, is solved for $\Delta\,\boldsymbol{d}$ during each iteration step until $\|\boldsymbol{r}\| \leq \mathrm{tol}$, where a convenient choice for the tolerance is $\mathrm{tol}=10^{-8}$. The finite element scheme is depicted in Table 4.1. The mixed element routine used for elements of the body is shown in Table 4.2.

**Remark 12** *A discretised system consist usually of $n_{\mathrm{np}}$ number of node points with $n_{\mathrm{df}}$ degrees of freedom per node. The total number of degrees of freedom is consequently $n_{\mathrm{np}}\cdot n_{\mathrm{df}}$. The "natural" order of all degrees of freedom of the discretised system in the vector containing all global degrees of freedom would be*

$$\boldsymbol{d}=[\,\boldsymbol{u}_1^{\mathrm{t}}, \widetilde{\phi}_1, \boldsymbol{p}_1^{\mathrm{t}}, \boldsymbol{\lambda}_1^{\mathrm{t}}, \boldsymbol{u}_2^{\mathrm{t}}, \widetilde{\phi}_2, \boldsymbol{p}_2^{\mathrm{t}}, \boldsymbol{\lambda}_2^{\mathrm{t}}, \cdots , \boldsymbol{u}_{n_{np}}^{\mathrm{t}}, \widetilde{\phi}_{n_{np}}\ \boldsymbol{p}_{n_{np}}^{\mathrm{t}}\ \boldsymbol{\lambda}_{n_{np}}^{\mathrm{t}}\,]^{\mathrm{t}} \ .$$

*Since $\boldsymbol{u}$, $\boldsymbol{p}$, and $\boldsymbol{\lambda}$ are not resolved in elements of the free space region, and since $\boldsymbol{p}$ and the associated Lagrange multipliers $\boldsymbol{\lambda}$ are only resolved at $n_{\mathrm{np}}^{\mathcal{B}\boldsymbol{p}}$ nodes of the discretised body $\mathcal{B}$, this order is no longer directly applicable. A straightforward way to keep this order of the nodes is the assumption of $n_{\mathrm{df}}$ degrees of freedom per node. At the beginning of a finite element simulation, all nodes that belong only to the free space elements are identified. In addition, the nodes 5–8 of all body elements are identified as well. The degrees of freedom $1,2$ (displacement field) and $4$–$n_{\mathrm{df}}$ (state variables and KKT-parameters) of all nodes that belong solely to the free space, as well as the degrees of freedom $4$–$n_{\mathrm{df}}$ of the nodes 5–8 of the body elements are not involved in the calculation of the nodal increments during the global Newton-Raphson iteration, since their residual and stiffness matrix contributions are identical to zero.*

**Table 4.1:** Finite element scheme.

0. *Preprocessing:*

   Specify Dirichlet boundary conditions, viz. prevention of rigid body motions (optional: additional supports) and $\widetilde{\phi} = 0$ on $\partial\Omega$, and calculate the nodal contributions of the surface traction integrals (4.95) for the desired mechanical loading curve.

1. *Initialisation:*

   Set load counter $n = 0$, choose admissible initial configuration $\boldsymbol{p}_0$ satisfying the constraints, initialise the Lagrange multipliers $\lambda_i = 5 \cdot 10^{-13}$, and identify global degrees of freedom that are not taken into account in the simulation, see Remark 12.

2. *Load stepping:*

   Read Dirichlet and Neumann boundary conditions, the latter in terms of nodal contributions of the applied surface tractions $\overline{\boldsymbol{t}}_{n+1}$, and specify the superimposed magnetic field $\overline{\boldsymbol{h}}_{n+1}$. Set iteration counter $k = 0$ and set initial values for the primary field variables and Lagrange multipliers, viz. ${}^{k}\boldsymbol{d}_{n+1} = \boldsymbol{d}_n$, cf. (4.114).

3. *Assembly of the global residual vector* $\boldsymbol{r}$ *and the global stiffness matrix* $\boldsymbol{K}$*:*

   – Loop over the $n_{\text{el}}^{\mathcal{B}}$ body elements, numerical integration of (4.93)
     and the integrals (4.100) – (4.106) as detailed in Table 4.2

   – Loop over the $n_{\text{el}}^{\Omega\setminus\mathcal{B}}$ free space elements, numerical integration of $r^{C}_{\widetilde{\phi}}$ in (4.93)
     and the integral (4.102)

   – Assembly of the $e$ element-wise contributions as outlined in (4.97) and (4.113),
     (take the nodal contributions due to the Neumann boundary conditions into account)

   – Loop over all $n_{\text{np}}^{\mathcal{B}\boldsymbol{p}}$ nodes, calculation of (4.96) and (4.107) to (4.110)
     and assembly of the $G$ discrete contributions as outlined in (4.97) and (4.113)

4. *Newton update:*

   Check for convergence by calculating $\|{}^{k}\boldsymbol{r}\|$:

   – if $\|{}^{k}\boldsymbol{r}\| \leq \text{tol}$, with e.g. $\text{tol} = 10^{-8}$, go to 5.

   – otherwise, update the discrete nodal values as outlined in (4.115)

   $$ {}^{k+1}\boldsymbol{d}_{n+1} = {}^{k}\boldsymbol{d}_{n+1} - {}^{k}\boldsymbol{K}^{-1} \cdot {}^{k}\boldsymbol{r} \ , $$

   with the global vector of all nodal values $\boldsymbol{d}$, cf. (4.114).

   Set the iteration counter $k \Leftarrow k + 1$ and return to 3.

5. *Postprocessing:*

   Calculate all relevant body area-averaged quantities of the current step, save history data $\boldsymbol{p}_{n+1} = {}^{k}\boldsymbol{p}_{n+1}$ (occurring in the evolution equations), write output file for external postprocessing, set step counter $n \Leftarrow n + 1$ and return to 2.

**Table 4.2:** Schematic representation of the mixed element routine used for elements of the body $\mathcal{B}$.

- Summation over all $n_{\text{qp}}$ quadrature points $\sum\limits_{q=1}^{n_{\text{qp}}}$
    - Read the shape functions $N$, calculate their gradients $\nabla_{\boldsymbol{x}} N$ and the volume $\mathrm{d}v$
    - Calculate $\boldsymbol{\varepsilon}, \widetilde{\boldsymbol{h}}$ and $\boldsymbol{p}$
    - Material routine: calculate $\boldsymbol{\sigma}, \widetilde{\boldsymbol{b}}, \boldsymbol{r}^{\text{evo}}$ and the corresponding gradients
    - Store quantities for postprocessing
    - Serendipity element $\sum\limits_{A=C=1}^{n_{\text{en}}^{\boldsymbol{u}}=n_{\text{en}}^{\widetilde{\phi}}=8}$
        - Calculate and store $\boldsymbol{f}^{\mathcal{B}A}_{\boldsymbol{u},\text{int}}$ and $f^{\mathcal{B}C}_{\widetilde{\phi},\text{int}}$ as detailed in (4.93) and (4.94)
        - Serendipity element $\sum\limits_{B=D=1}^{n_{\text{en}}^{\boldsymbol{u}}=n_{\text{en}}^{\widetilde{\phi}}=8}$
            - Calculate and store $\boldsymbol{K}^{AB}_{\boldsymbol{uu}}$ and $K^{CD}_{\widetilde{\phi}\widetilde{\phi}}$ as detailed in (4.100) and (4.102)
        - Bilinear element $\sum\limits_{F=1}^{n_{\text{en}}^{\boldsymbol{p}}=4}$
            - Calculate and store $\boldsymbol{K}^{AF}_{\boldsymbol{up}}$ and $\boldsymbol{K}^{CF}_{\widetilde{\phi}\boldsymbol{p}}$ as detailed in (4.101) and (4.103)
    - Bilinear element $\sum\limits_{E=1}^{n_{\text{en}}^{\boldsymbol{p}}=4}$
        - Calculate and store $\boldsymbol{r}^{E}_{\boldsymbol{p}}$ as detailed in (4.93)
        - Serendipity element $\sum\limits_{B=D=1}^{n_{\text{en}}^{\boldsymbol{u}}=n_{\text{en}}^{\widetilde{\phi}}=8}$
            - Calculate and store $\boldsymbol{K}^{EB}_{\boldsymbol{pu}}$ and $\boldsymbol{K}^{ED}_{\boldsymbol{p}\widetilde{\phi}}$ as detailed in (4.104) and (4.105)
        - Bilinear element $\sum\limits_{F=1}^{n_{\text{en}}^{\boldsymbol{p}}=4}$
            - Calculate and store $\boldsymbol{K}^{EF}_{\boldsymbol{pp}}$ as detailed in (4.106)
- Reserve memory for the constraints $\sum\limits_{G=1}^{n_{\text{en}}^{\boldsymbol{p}}=4}$
    - Store dummies for $\boldsymbol{r}^{G}_{\boldsymbol{\lambda}}, \boldsymbol{K}^{GG}_{\boldsymbol{p\lambda}}, \boldsymbol{K}^{GG}_{\boldsymbol{\lambda p}}$ and $\boldsymbol{K}^{GG}_{\boldsymbol{\lambda\lambda}}$

## 4.4 Numerical examples

In this section, several numerical examples demonstrate the capabilities of the finite element simulations where inhomogeneous distributions of all quantities might occur, and show the advantages over calculations performed by using a demagnetisation tensor to capture the shape dependent demagnetisation effect, where solely macroscopically homogeneous states inside the bodies are considered. As introduced in Section 4.3, the finite element simulations are two dimensional and plane strain conditions are prescribed. As a consequence, the total strain $\varepsilon_{33}$ is equal to the transformation strain, viz. $\varepsilon_{33} = b_1$, since $\varepsilon_{33}^{\mathrm{el}} = 0$, see (4.34) and (4.45). The resolution of the magnetic quantities in the plane corresponds to specimens with infinite size in the $\boldsymbol{e}_3$-direction. The response behaviour of five differently shaped specimens is investigated, each embedded in a free space box, under magnetomechanical loading. To be precise, a circular, an ellipsoidal, a quadratic, a rectangular, and an I-shaped specimen are analysed, where the respective symmetry axes are aligned with the coordinate system. The aspect ratios of the major- to the minor-axis of the ellipsoidal specimen, respectively the long to the short edge of the rectangular specimen, are 5/3. The body area-averaged responses of finite element simulations are partially compared to calculations performed using a demagnetisation tensor in a constitutive driver routine, see the appendix in Section 4.6.2 for details regarding the constitutive driver. Even though the finite element simulations of ellipsoidal specimens show a spatially homogeneous response inside the area of the body, we consider body area-averaged response curves to minimise the influence of numerical errors. Some of the response curves are enhanced by sketches representing the body area-averaged microstructure in terms of martensite volume fractions, domain volume fractions, and the orientations of the magnetisation vectors inside the domains at selected load steps. The associated state variables are area-averaged quantities. The spatial distributions of multiple quantities are enhanced by iso-lines of the magnetic potential of the demagnetisation field $\widetilde{\phi}$, not to be confused with the demagnetisation field $\widetilde{\boldsymbol{h}} = -\nabla_{\boldsymbol{x}} \widetilde{\phi}$ itself. The demagnetisation factors of the specimen geometries used in the finite element simulations were calculated in magnetostatic finite element simulations using exactly the same meshes. For a prescribed homogeneous magnetisation $m_i$, the body area-averaged demagnetisation fields $\langle \widetilde{h}_i \rangle$ were computed and the body-averaged demagnetisation factors $\langle D_{ii} \rangle$ are calculated by

$$\langle D_{ii} \rangle = -\frac{\langle \widetilde{h}_i \rangle}{m_i} , \tag{4.116}$$

see [65] and the discussion therein and also [36, 155, 170, 188] for analytically determined demagnetisation tensors. Due to the symmetries of the considered specimens, the body area-averaged demagnetisation field perpendicular to the $\langle \widetilde{h}_i \rangle$ is zero. In the following, the body area-averaged quantities are not marked with $\langle \bullet \rangle$ for aesthetic reasons. The material constants and model parameters for $\mathrm{Ni}_{49.7}\mathrm{Mn}_{29.1}\mathrm{Ga}_{21.2}$ are listed in Table 4.3. The calculated demagnetisation factors for the meshes used in the finite element simulations are listed in Table 4.4.

**Table 4.3:** Material constants and model parameters for $Ni_{49.7}Mn_{29.1}Ga_{21.2}$.

| Material constant/model parameter | Symbol | Value | Unit | Reference |
|---|---|---|---|---|
| Young's modulus | $E$ | 5.0 | GPa | - |
| Poisson's ratio | $\nu$ | 0.3 | [-] | - |
| Bain strain coefficients | $b_1$ | 0.0188 | [-] | [204] |
|  | $b_2$ | $-0.0394$ | [-] | [204] |
| Vacuum permeability | $\mu_0$ | $4\,\pi\,10^{-7}$ | $N/A^2$ | - |
| Anisotropy constant | $k_1$ | 0.167 | $MJ/m^3$ | [71, 76] |
| Saturation magnetisation | $m_s$ | 514.0 | kA/m | [76, 106] |
| Martensite reorientation threshold | $Y_\xi$ | 0.03 | $MJ/m^3$ | - |
| Martensite reorientation viscosity | $\eta_\xi$ | 0.00125 | 1/[ kPa s ] | - |
| Magnetic evolution viscosity | $\eta_m$ | 0.0001 | 1/[ kPa s ] | - |

**Table 4.4:** Calculated demagnetisation factors for the considered specimen geometries.

| Specimen geometry | Demagnetisation factor | Value |
|---|---|---|
| Circle | $D_{11} = D_{22}$ | 0.4824 |
| Ellipse: minor-axis | $D_{11}$ | 0.6085 |
| Ellipse: major-axis | $D_{22}$ | 0.3586 |
| Square | $D_{11} = D_{22}$ | 0.4746 |
| Rectangle: short edge | $D_{11}$ | 0.5854 |
| Rectangle: long edge | $D_{22}$ | 0.3660 |
| I-profile | $D_{11}$ | 0.4664 |
| I-profile | $D_{22}$ | 0.4953 |

### 4.4.1 Magnetic field-induced easy- and hard-axis magnetisation response

In the first example, the easy- and hard-axis magnetisation response curves of the circular and the quadratic specimen consisting of a single variant of martensite ($\xi_2 = 0.999$) are considered. Prescribed tractions $\bar{t}_2$ are applied resulting in a constant compression stress $\bar{\sigma}_{22} = -\,5.0\,\text{MPa}$, which suppresses the martensite reorientation process and maintains the initial single variant of martensite. Half a cycle of magnetic field loading $\bar{h}_i$ is applied in the easy- and the hard-axis direction of both specimens, where the field is linearly increased from $\mu_0\,\overline{h}_i(t_0\!=\!0\,\text{ms})\!=\!0\,\text{T}$ to a maximum of $\mu_0\,\overline{h}_i(t_1\!=\!1\,\text{ms})\!=\!1\,\text{T}$ and linearly decreased back to the initial value at time $t_2 = 2\,\text{ms}$. The boundary value problems (BVPs) are schematically sketched in Figure 4.6 for (a), (b) the circle and (c), (d) the square under a magnetic field in their respective (a), (c) easy- and (b), (d) hard-axis directions. The corresponding body area-averaged easy- and hard-axis magnetisation

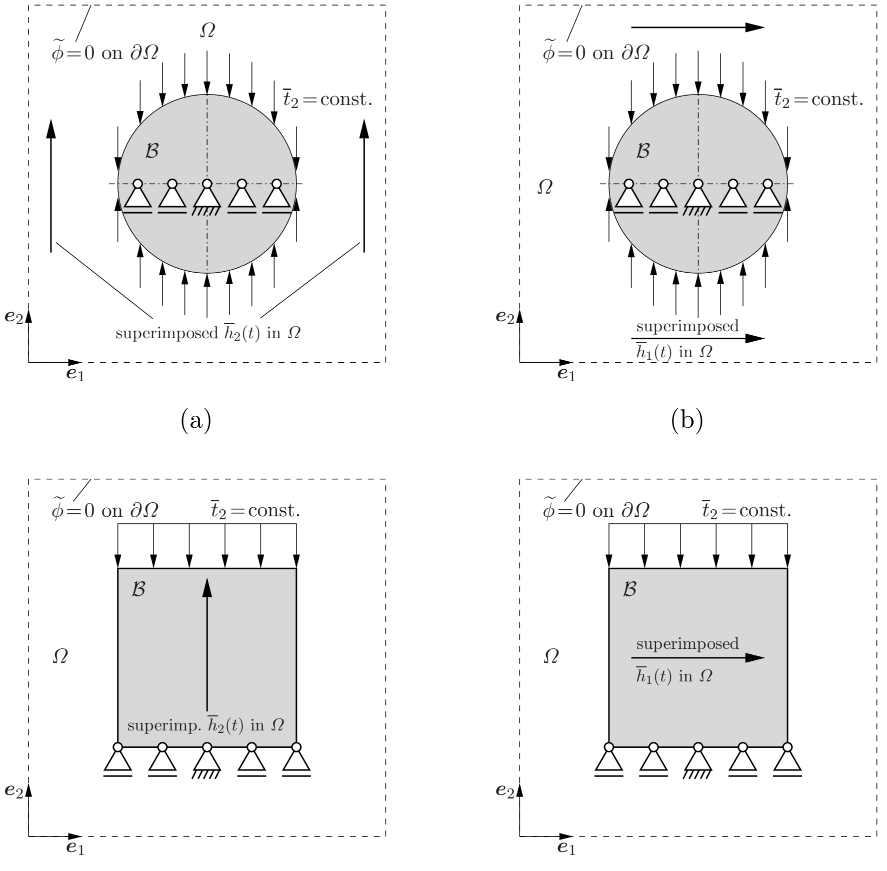
$\widetilde{\phi}=0$ on $\partial\Omega$
$\Omega$
$\overline{t}_2=$const.
$\mathcal{B}$
superimposed $\overline{h}_2(t)$ in $\Omega$
superimposed
$\overline{h}_1(t)$ in $\Omega$
superimp. $\overline{h}_2(t)$ in $\Omega$
$e_2$
$e_1$

(a) (b)

(c) (d)

**Figure 4.6:** Schematic representation of the magnetomechanical BVP of (a), (b) an ellipsoidal and (c), (d) a rectangular body $\mathcal{B}$ embedded into a finite size free space box $\Omega$. Prescribed loading in terms of tractions $\overline{t}_2 = \text{const.}$ favouring the initial second martensite variant ($\xi_2 = 0.999$) and superimposed spatially homogeneous magnetic fields $\overline{h}_i(t)$ in the (a), (c) vertical and (b), (d) horizontal direction.

curves are shown in Figure 4.7. The responses calculated by using a constitutive driver routine are plotted for comparison. For the circular specimen, they coincide perfectly with the response curves using the correct demagnetisation factor $D^{\text{FEM}}$, see Table 4.4, and serve as a first verification of the finite element implementation. The response curves calculated using the theoretical demagnetisation factors $D_{11}\!=\!D_{22}\!=\!0.5$ generally predict the same response behaviour. The slight deviation is possibly due to discretisation errors

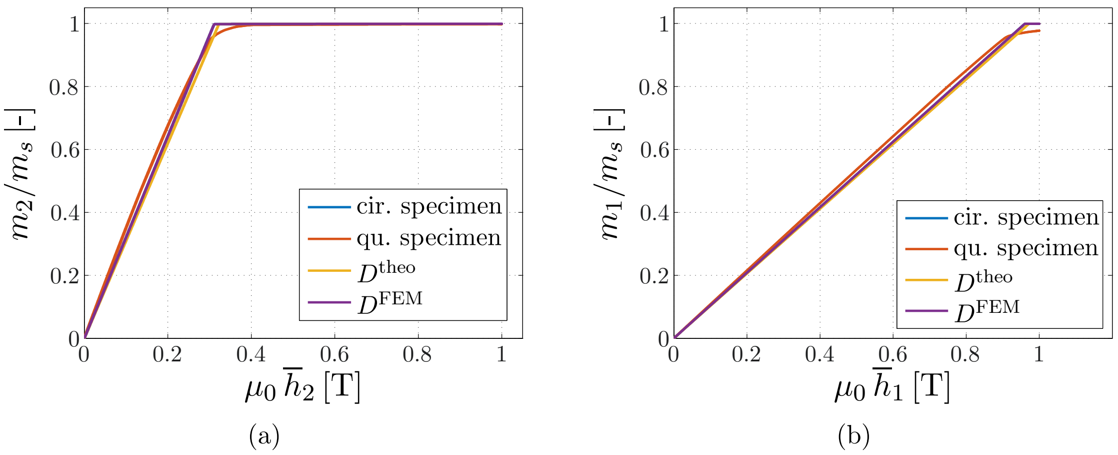

(a) (b)

**Figure 4.7:** Magnetic field-induced magnetisation response in (a) easy- and (b) hard-axis direction under constant compression stress $\overline{\sigma}_{22} = -5.0\,\text{MPa}$ to maintain the initial single martensite variant. The body area-averaged magnetisation responses of a circular (cir.) and a quadratic (qu.) specimen, both embedded into a free space box, are shown in comparison to calculations using a constitutive driver routine with the theoretical demagnetisation tensor $D^{\text{theo}}$ and the calculated one $D^{\text{FEM}}$ of the circular specimen.

or the size of the free space box. In contrast to these linear responses, the quadratic specimen clearly shows nonlinear responses which were also observed in experiments, see Figure 4.8 for comparison. In the finite element simulation of the quadratic specimen, the mechanisms of domain wall motion and rotation of the magnetisation vectors are not isolated. During the easy-axis magnetisation, the mechanism of magnetisation rotation occurs particularly in the corners of the quadratic specimen. During the hard-axis magnetisation, the mechanism of domain wall motion occurs likewise particularly in the

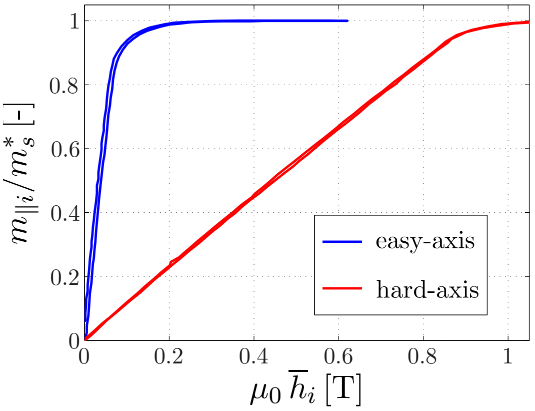

**Figure 4.8:** Measured easy- and hard-axis magnetic field-induced magnetisation response of a thin nearly square wafer consisting of a single martensite variant under compression stress of 1.9 MPa applied in the easy-axis direction taken from [211, 212].

corners of the specimen. For a maximum magnetic field of $\mu_0\,\overline{h}_i = 1\,\mathrm{T}$, the magnetisation in the hard-axis response curve of the quadratic specimen is still not saturated. Spatial distributions of the magnetisation in the direction of the magnetic field are shown in Figure 4.9 for (a), (b) the easy-axis and (c), (d) the hard-axis response. The occurring mechanisms of domain wall motion (easy-axis) and magnetisation rotation (hard-axis) were both introduced to be viscoelastic. Due to the low viscosity parameter, the response curves for the unloading case are in fact indistinguishable from the loading case.

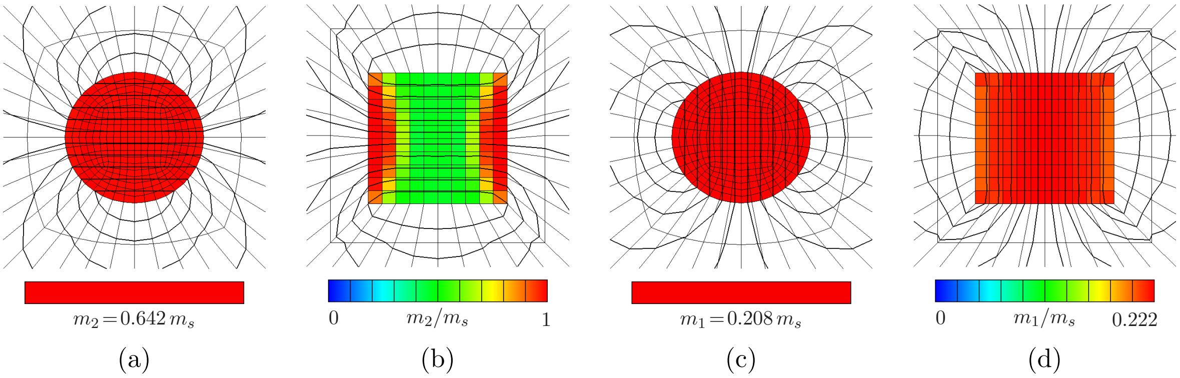

**Figure 4.9:** Easy-axis: selected spatial distributions of $m_2$ under $\mu_0\,\overline{h}_2 = 0.2\,\mathrm{T}$ of (a) a circle and (b) a square, see Figure 4.7 (a). Hard-axis: selected spatial distributions of $m_1$ under $\mu_0\,\overline{h}_1 = 0.2\,\mathrm{T}$ of (c) a circle and (d) a square, see Figure 4.7 (b). In addition, iso-lines of the magnetic potential $\widetilde{\phi}$ are shown in black.

In addition to the first example, the body area-averaged magnetisation responses of the ellipsoidal and the rectangular specimen are calculated analogously in terms of similar mechanical boundary conditions and magnetic field loading. They are compared to the response of the circular and the quadratic specimen in order to further verify the finite element implementation. In this case, the ellipsoidal and the rectangular specimen consists of the alternating first and second variants of martensite to investigate the shape dependency of the magnetisation response. Prescribed tractions $\overline{t}_i$ are applied resulting in a constant compression stress $\overline{\sigma}_{ii} = -\,5.0\,\mathrm{MPa}$ that suppresses the martensite reorientation process by keeping the variant volume fraction $\xi_i = 0.999$. Figure 4.10 shows the response curves of (a), (b) the ellipsoidal specimen and (c), (d) the rectangular specimen under a magnetic field applied in (a), (c) the easy- and (b), (d) the hard-axis directions. In addition, the response curves of the circular and quadratic specimen are plotted for comparison. The linear response behaviour of the ellipsoidal specimen coincides with the results of the calculations made by using a demagnetisation tensor. In contrast, the response behaviour of the rectangular specimen is clearly nonlinear, as previously observed in the response of the quadratic specimen. The linear response obtained by calculations utilising a demagnetisation tensor may be considered as a useful approximation until a certain saturation level is reached. Both figures clearly show the

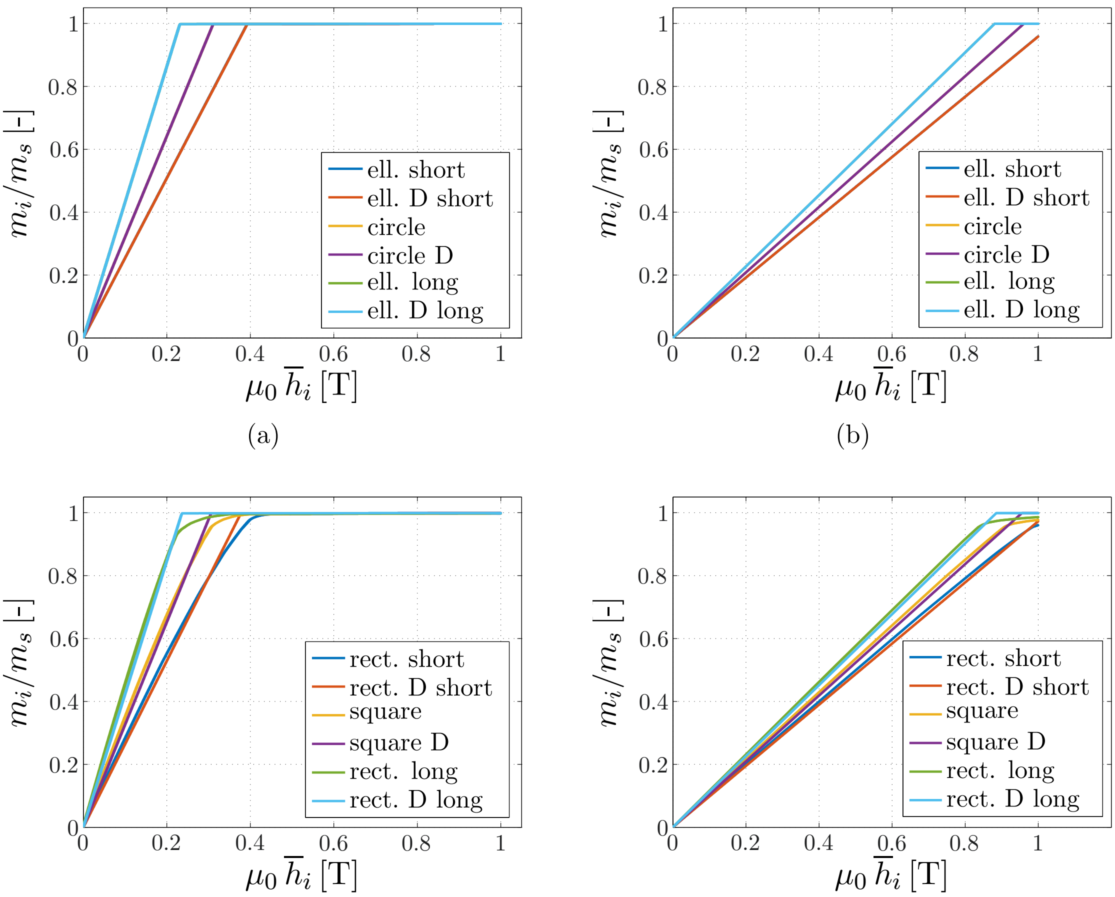

(a) (b)

(c) (d)

**Figure 4.10:** Body area-averaged magnetic field-induced magnetisation responses of (a), (b) an ellipsoid and a circle and (c), (d) a rectangle and a square, all embedded into free space boxes. The ellipsoid and the rectangle consist of the first, respectively second, alternating variants of martensite to study the shape dependency of the response. Magnetic fields are applied in (a), (c) the easy- and (b), (d) the hard-axes directions. Constant compression stresses $\overline{\sigma} = -5.0\,\mathrm{MPa}$ are applied to maintain the initial single martensite variant states. The area-averaged responses are shown in comparison to calculations using a constitutive driver routine (D), see Table 4.4 for the calculated demagnetisation tensors.

shape anisotropy, where a lower magnetic field is required to magnetise a specimen along the axis with the largest aspect ratio.

### 4.4.2 Magnetic field-induced martensite reorientation

In the first examples, the easy- and hard-axis magnetisation responses of differently shaped specimens were considered where the mechanisms of domain wall motion and rotation of the magnetisation vectors occurred. The third mechanism, the martensite variant reorientation, was suppressed by sufficiently large compression stresses applied in terms of tractions on the boundary of the specimens. It turns out that the latter mechanism is essential for the response behaviour of MSMAs under magnetomechanical loading, see [71, 202] and Figure 4.17, taken from [200], for experimentally determined response curves. In this example, a circular and a quadratic specimen are subjected to constant prescribed tractions $\overline{t}_2$ that favour the initial second martensite variant and result in a body area-averaged constant compression stress $\overline{\sigma}_{22} = -1.0\,\mathrm{MPa}$, which is below the blocking stress, see [111]. One period of a triangle wave shaped magnetic field loading $\overline{h}_1$ with a frequency of 250 Hz favouring the first martensite variant is applied perpendicular to the compression stress. The viscosity parameter for the martensite reorientation is set to $\eta^*_\xi = 4\,\eta_\xi$. The boundary value problems for both specimens are schematically sketched in Figures 4.6 (b) and (d). Figure 4.11 shows the body area-averaged magnetic field-induced (a) strain and (b) magnetisation response of the circular and the quadratic specimen in comparison to simulations of the constitutive driver routine. The initial strain is shifted to zero. The response of the circular specimen and the corresponding response of the constitutive driver routine coincide. Since the demagnetisation factors of the square specimen are similar to the circular specimen, see Table 4.4, the response curves are close to each other. In contrast, the response of the quadratic specimen clearly deviates for nearly saturated magnetisation states during

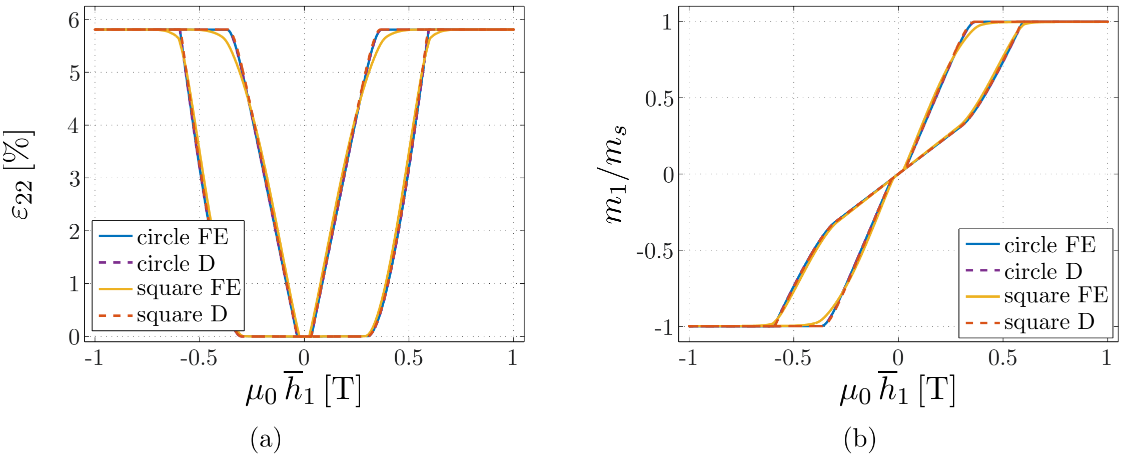

**Figure 4.11:** Magnetic field-induced (a) strain and (b) magnetisation response under constant compression stress $\overline{\sigma}_{22} = -1.0\,\mathrm{MPa}$ favouring the initial single martensite variant. The body area-averaged responses of a circular and a quadratic specimen embedded into a free space box (FE) are shown in comparison to calculations using a constitutive driver routine (D).

loading and, in particular, during unloading. All four responses have in common that the initial response is identical to the hard-axis response, which was discussed in more detail in the previous example. At a certain externally applied magnetic field, the mechanism of martensite variant reorientation into the magnetic field-favoured variant is activated, which is noticeable in the strain response curves and the slopes of the magnetisation response curves where the arising first martensite variant magnetises in its easy-axis direction. For larger magnetic fields, the martensite reorientation process is completed, observable in the strain response curves and in the saturation of the magnetisation. During unloading, the onset of the martensite reorientation into the stress-favoured initial martensite variant is delayed due to the threshold in the dissipation associated with the evolution of the martensite variant volume fraction. After a full reorientation into the initial variant, the strains are again zero and the magnetisation response curves coincide with the hard-axes response curves. The response behaviour during the second half of the loading cycle is similar to the first half and not discussed in detail.

The magnetic field-induced martensite reorientation process is analysed for the ellipsoidal and the rectangular specimen and compared to the response behaviour of the circular and the quadratic specimen. In this case, the ellipsoidal and the rectangular specimen consists initially of the first, respectively second, alternating variant of martensite to investigate—in analogy to the first example—the shape dependency of the magnetic field-induced strain and magnetisation response. Prescribed tractions $\overline{t}_i$ are applied and result in a body area-averaged constant compression stress $\overline{\sigma}_{ii} = -1.0\,\mathrm{MPa}$, that favours the initial martensite variant. The boundary conditions are set in analogy to the previous example. The corresponding boundary value problems are schematically sketched in Figure 4.6 (b) and (d) for the initially second martensite variant. The boundary conditions for the initially first martensite variant are set analogously. The triangle wave shaped magnetic field loading is applied with a frequency of 250 Hz and the viscosity of the martensite volume fraction is set to $\eta_\xi^* = 4\,\eta_\xi$. Figure 4.12 shows the body area-averaged response curves of (a), (b) the ellipsoidal specimen and (c), (d) the rectangular specimen in terms of (a), (c) the strain and (b), (d) the magnetisation responses. In addition, the response curves of the circular and quadratic specimen are plotted for comparison. The initial values of the strains are shifted to zero. All figures clearly show the shape anisotropy where lower magnetic fields are required to initialise and complete the magnetic field-induced martensite reorientation process and to reach a saturated state of the magnetisation in the direction of the axis with the largest aspect ratio. Selected spatial distributions of $\xi_1$ and the magnetisation $m_i/m_s$ in the direction of the applied magnetic field $\overline{h}_i$ are shown in Figure 4.13 for the ellipsoidal and rectangular specimen under vertical and horizontal magnetic field loading.

In addition to the investigation of the shape dependency of the magnetic field-induced martensite reorientation, the influence of the number of elements used for the discretisation of the body and the surrounding free space box, in terms of a mesh dependency study, is analysed. Since the distribution of the strain and the magnetisation are in fact homogeneous inside ellipsoidal bodies, the quadratic specimen, where inhomogeneous

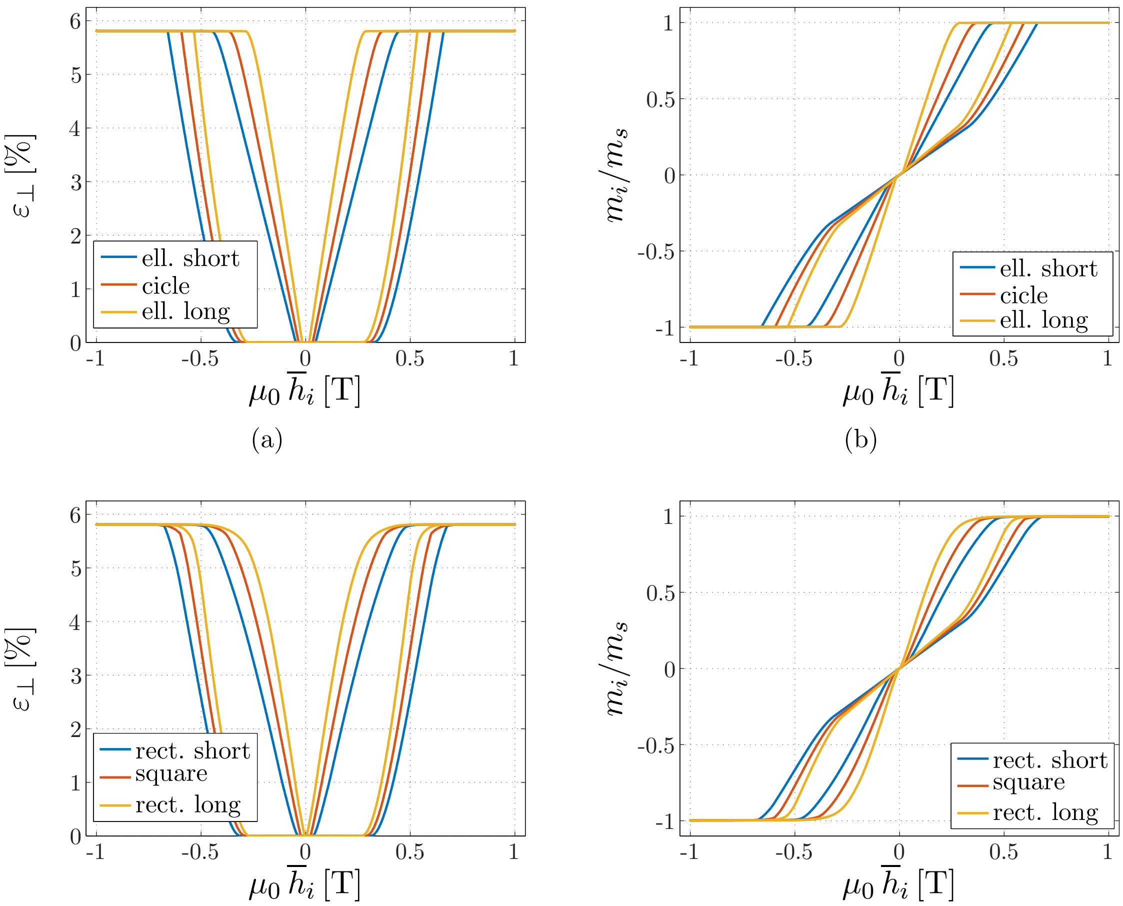

(a) (b)

(c) (d)

**Figure 4.12:** Body area-averaged magnetic field-induced (a), (c) strain and (b), (d) magnetisation response under constant compression stress $\overline{\sigma} = -1.0\,\mathrm{MPa}$ and perpendicular cyclic magnetic field $\overline{h}$ loading of (a), (b) an ellipsoid and a circle and (c), (d) a rectangle and a square, all embedded into free space boxes. The magnetic field is applied along the minor and major axis of the ellipsoid, respectively the short and long edge of the rectangle, to show the shape dependency of the response behaviour.

distributions occur, is used for this study. The number of elements is successively increased up to a factor of five in both spatial directions. Prescribed tractions $\overline{t}_2$ are applied resulting in a body area-averaged constant compression stress $\overline{\sigma}_{22} = -1.0\,\mathrm{MPa}$ favouring the initial second martensite variant. The boundary conditions are set in analogy to the previous examples. The boundary value problem is schematically sketched in Figure 4.6 (d). The triangle wave shaped magnetic field loading $\overline{h}_1$ is applied with a frequency of 250 Hz and the viscosity parameter of the martensite volume fraction evolution is set to $\eta_\xi^* = 4\,\eta_\xi$. Figure 4.14 shows the body area-averaged (a) strain and (b) magnetisation response curves where the initial values of the strain are shifted to zero. Both figures show that the body area-averaged responses of the quadratic specimen are qualitatively

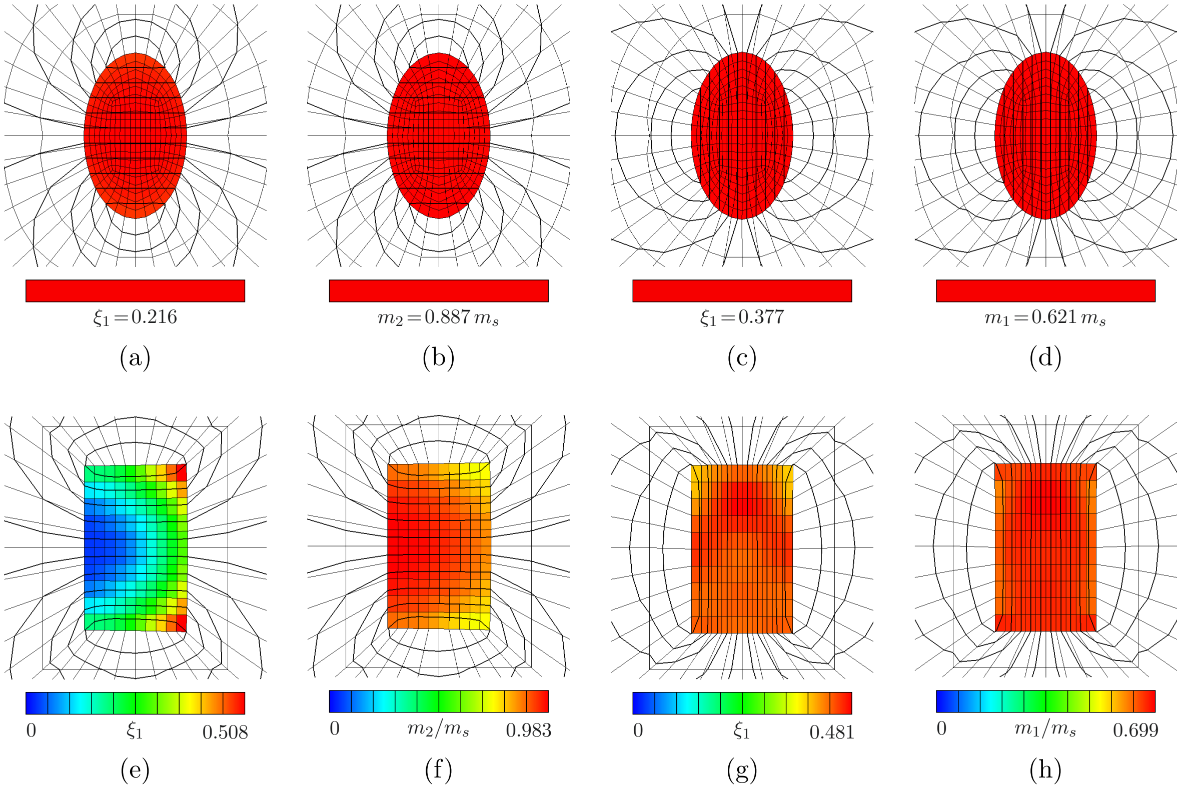

(a) (b) (c) (d)

(e) (f) (g) (h)

**Figure 4.13:** Selected spatial distributions of $\xi_1(\overline{h}_i)$ and $m_i(\overline{h}_i)$ under $\mu_0\,\overline{h}_i(t = 0.5\,\mathrm{ms}) = 0.499\,\mathrm{T}$ of (a), (b) the ellipsoid under $\overline{h}_2$ loading, (c), (d) the ellipsoid under $\overline{h}_1$ loading, (e), (f) the rectangle under $\overline{h}_2$ loading, and (g), (h) the rectangle under $\overline{h}_1$ loading, see Figure 4.12 for the body area-averaged response curves. In addition, iso-lines of the magnetic potential $\widetilde{\phi}$ are shown in black.

in very good agreement. A small visible deviation is observable in the strain response during the reorientation into the first martensite variant above $\varepsilon_{22} \approx 5.6\,\%$. The response curves calculated using very coarse meshes deviate noticeably from these response curves (not pictured). Selected spatial distributions of $\xi_1$ and the magnetisation $m_i/m_s$ in the direction of the applied magnetic field $\overline{h}_i$ loading are shown in Figure 4.15 for the three meshes considered in this study. In the following, the element sizes used for the discretisation of all other bodies are approximately the same as those used for the coarsest discretisation shown in this study, since the simulation results obtained are considered to be reasonable.

After having demonstrated that the finite element simulations are generally able to predict the mechanism of magnetic field-induced martensite reorientation and the shape dependency of this effect, the influence of the viscosity of the martensite reorientation $\eta_\xi$ as a material parameter, respectively a model parameter, is studied. The body area-averaged strain and magnetisation responses of the circular and the quadratic specimen are considered. Prescribed tractions $\overline{t}_2$ are applied resulting in a body area-averaged

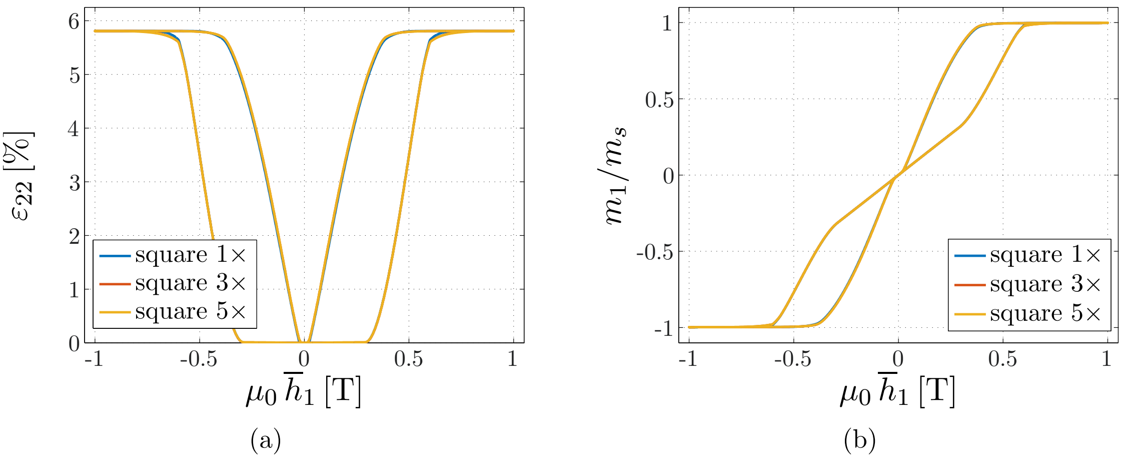

(a) (b)

**Figure 4.14:** Body area-averaged magnetic field-induced (a) strain and (b) magnetisation response under constant compression stress $\overline{\sigma}_{22} = -1.0\,\mathrm{MPa}$ and perpendicular cyclic magnetic field $\overline{h}_1$ loading of a quadratic body embedded in a free space box. The number of elements in each spatial direction is increased up to a factor of five to study the mesh dependency.

constant compression stress $\overline{\sigma}_{22} = -1.0\,\mathrm{MPa}$ favouring the initial second martensite variant. The boundary conditions are set in analogy to the previous examples. The boundary value problems are schematically sketched in Figures 4.6 (b) and (d). The triangle wave shaped magnetic field loading $\overline{h}_1$ is applied with a frequency of 250 Hz. The viscosity of the martensite reorientation is initially set to $\eta_\xi^* = 4\,\eta_\xi$, afterwards decreased to $\eta_\xi^* = 2\,\eta_\xi$, and finally set to $\eta_\xi^* = \eta_\xi$, which is the value listed in Table 4.3. Figure 4.16 shows the body area-averaged response curves of (a), (b) the circular specimen and (c), (d) the quadratic specimen in terms of (a), (c) the strain and (b), (d) the magnetisation responses for different viscosity parameters. The initial values of the strains are shifted to zero. The response curves of the circle clearly show that the onset of the martensite reorientation is independent of the chosen viscosity parameter, while the completion of the reorientation is delayed for larger viscosities. In addition, the slopes of the curves increase for decreasing $\eta_\xi^*$. These observations are generally applicable to the quadratic specimen, while the slopes increase even more for lower viscosities, in particular in the beginning of the initial reorientation for the lowest viscosity parameter. This, at least initially, almost vertical response behaviour is also observable in experiments, see Figure 4.17 for comparison. Even though experiments show that the magnetic field-induced martensite reorientation occurs at very high frequencies, as also prescribed in the simulations, the response is by no means rate-independent, cf. [77, 126]. In the following, the viscosity parameter $\eta_\xi^* = \eta_\xi$, as listed in Table 4.3, is used, due to the generally good approximation of the the response behaviour observed in experiments.

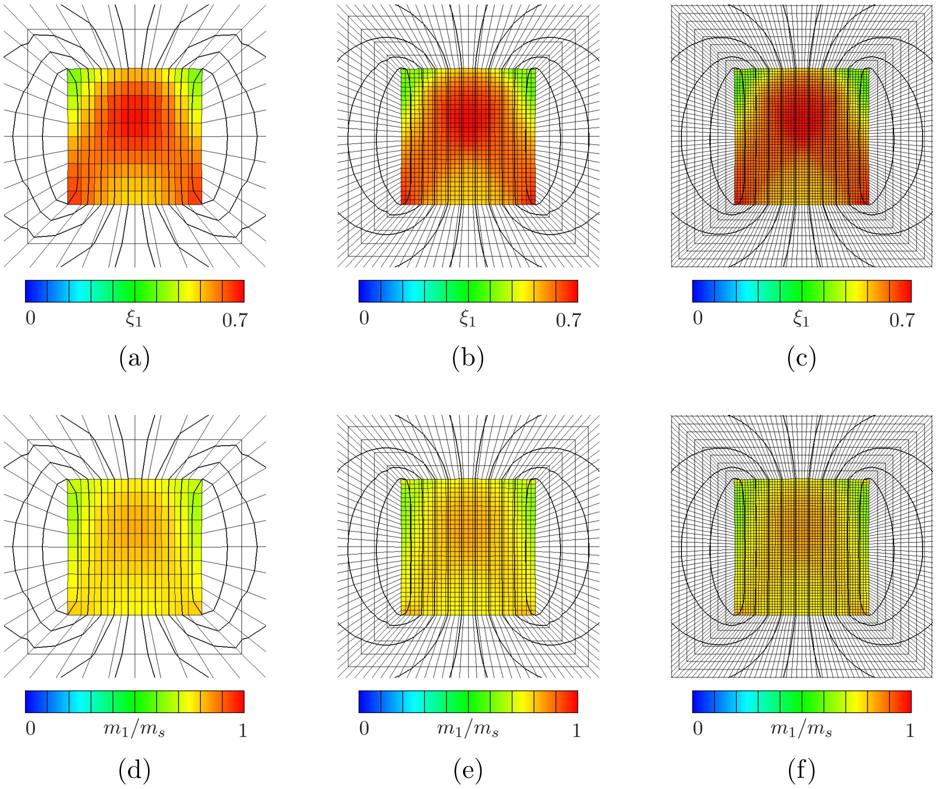

**Figure 4.15:** Selected spatial distributions of (a)–(c) $\xi_1$ and (d)–(f) $m_1/m_s$ under $\mu_0\,\overline{h}_1(t = 0.5\,\text{ms}) = 0.499\,\text{T}$ loading of (a), (d) the square specimen, (b), (e) the square specimen with three times elements in each spatial direction, and (c), (f) the square specimen with five times elements in each spatial direction, see Figure 4.14 for the body area-averaged response curves. In addition, iso-lines of the magnetic potential $\widetilde{\phi}$ are shown in black.

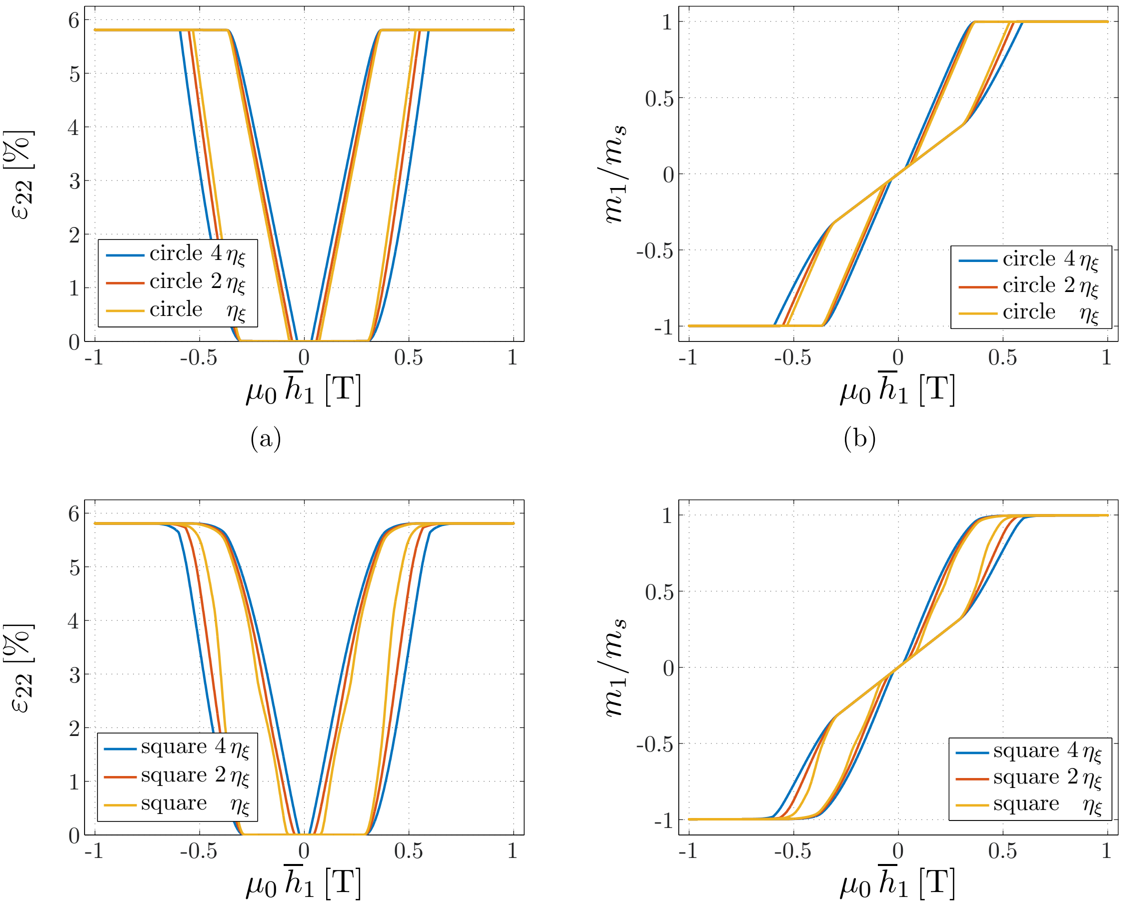

(a) (b) (c) (d)

**Figure 4.16:** Body area-averaged magnetic field-induced (a), (c) strain and (b), (d) magnetisation response under constant compression stress $\overline{\sigma}_{22} = -1.0\,\mathrm{MPa}$ and perpendicular cyclic magnetic field $\overline{h}_1$ loading of (a), (b) a circular and (c), (d) a quadratic specimen embedded in a free space box. The response behaviour is compared for multiple viscosities of the martensite variant reorientation.

### 4.4.3 Stress level dependency of the magnetic field-induced response behaviour

In this example, the stress level dependency of the magnetic field-induced martensite reorientation in terms of body area-averaged strain and magnetisation responses are analysed. Previously, two levels of body area-averaged compression stress have been considered, namely $\overline{\sigma} = -1.0\,\mathrm{MPa}$ and $\overline{\sigma} = -\,5.0\,\mathrm{MPa}$. The perpendicularly applied magnetic field loading $\overline{h}$ induced a complete reorientation into the magnetic field-favoured martensite variant at the lower compression stress. The initial variant was completely recovered during the removal of the magnetic field. For high compression stresses, the perpendicularly applied magnetic field could not induce a martensite variant reorientation due to the blocking stress effect. Experimental observations suggest that the strain and magnetisation response of specimens subject to a constant compression stress and a perpendicular cyclic magnetic field loading highly depends on the applied compression stress level, see [71, 202] and Figure 4.17, taken from [200]. Although the experimentally determined curves are not directly comparable to the simulations where plane boundary value problems are considered, many aspects of the experimental findings are captured by the finite element simulations as discussed below.

Figures 4.18 (a)–(d) show body area-averaged (a), (c) strain, where the initial values are shifted to zero, and (b), (d) magnetisation response curves of the rectangular specimen under multiple levels of constant compression stress $\overline{\sigma}_{11}$—applied in terms of tractions $\overline{t}_1$—favouring the initial martensite variant. In addition, one cycle of triangle wave shaped magnetic field loading $\overline{h}_2$ with a frequency of 250 Hz is applied perpendicular to the tractions along the long edge of the body. The boundary conditions are set in analogy to the boundary value problem sketched in Figure 4.6 (d). In the following, the response behaviour is compared to the response of the constitutive driver routine as well as experimental observations. All simulated response curves have in common that the magnetic field is able to initialise and complete the martensite reorientation process into the magnetic field-favoured second martensite variant. The onset of the reorientation process is delayed for higher compression stresses, observable in the experiments and the simulations. The body area-averaged response curves show a steeper response compared to the constitutive driver in all curves during the initial martensite reorientation, until a certain magnetic field is applied and until the slope of the area-averaged curves flattens noticeably, both is also observable in experiments. During unloading, the smoother response behaviour of the finite element simulations captures the response behaviour of experiments better than the simulated constitutive driver response. For low—or even zero—compression stress, a partial reorientation into the stress-favoured initial martensite variant is observable in the finite element simulations and the experiments, while the constitutive driver predicts zero reorientation for low compression stresses. Due to only partially or even completely suppressed reorientation during unloading, the corresponding response behaviour of the second half of the cycle differs from the initial first half of the loading cycle. All response curves have in common that the width of

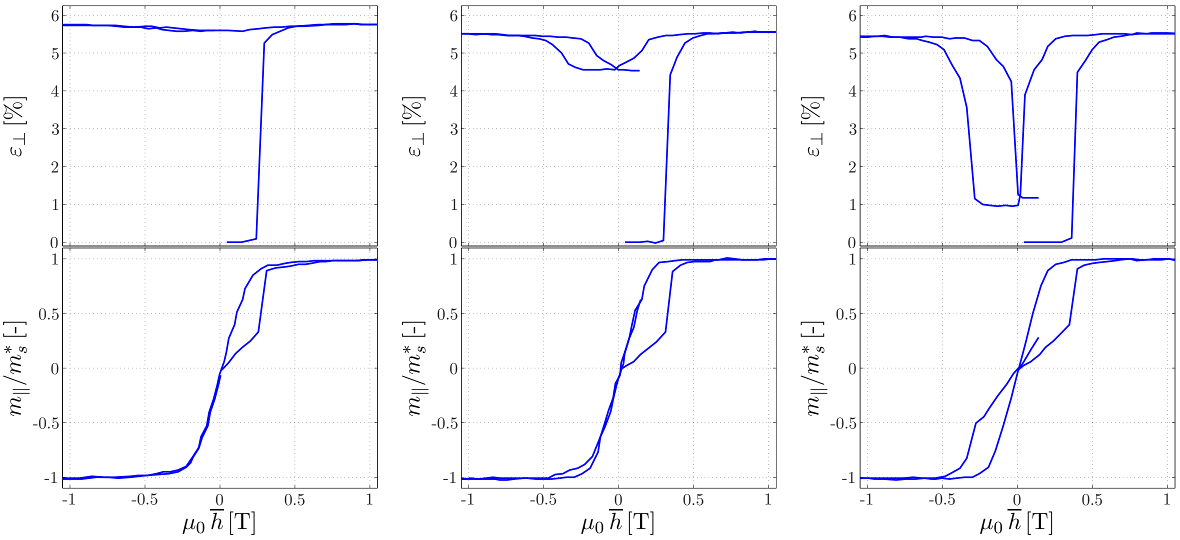

(a) 0.2 MPa (b) 0.6 MPa (c) 0.8 MPa

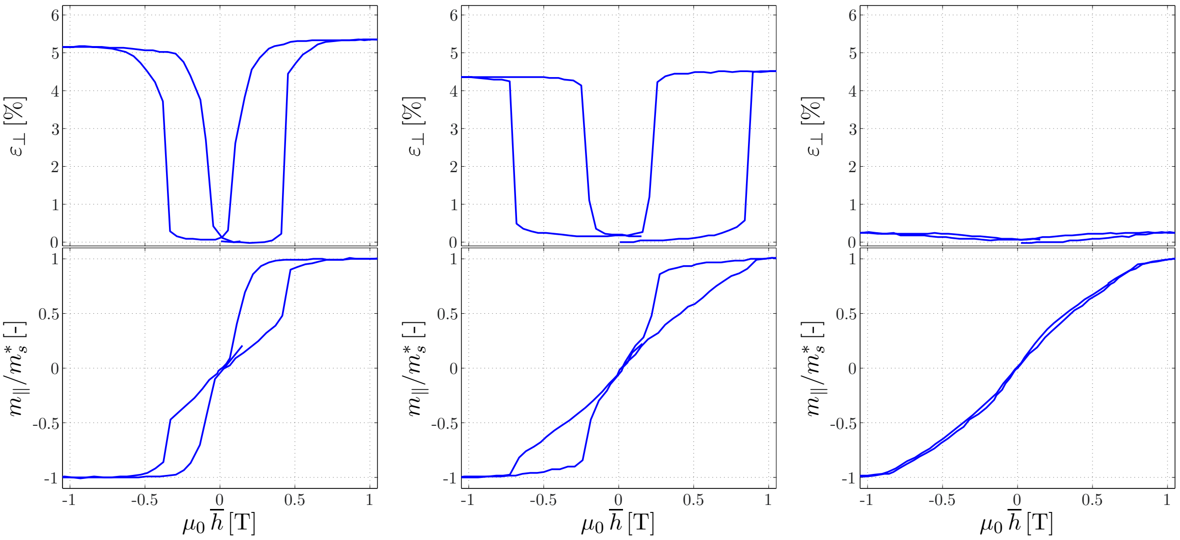

(d) 1.0 MPa (e) 1.8 MPa (f) 2.0 MPa

**Figure 4.17:** Experimentally measured magnetic field-induced variant reorientation under constant compression stress $\overline{\boldsymbol{\sigma}}$ and perpendicular cyclic magnetic field $\overline{\boldsymbol{h}}$ loading, taken from [200]. (a)–(f) show the strain $\varepsilon_\perp$ perpendicular to the magnetic field (at the top) and the normalised magnetisation response $m_\parallel/m_s^*$ in the direction of the magnetic field (at the bottom) at different levels of compression stress.

the magnetisation and, in particular, the strain response curve increases for increasing levels of compression stress. Although the simulations of the constitutive driver routine capture the response behaviour observed in experiments quite well, the finite element simulations approximate the real response behaviour even better. In addition to the presented response curves, the response under a fifth level of constant compression stress

$\overline{\sigma}_{11} = -\,0.5\,\mathrm{MPa}$ is considered. Figures 4.18 (e) and (f) show the body area-averaged response curves and some sketches of the body area-averaged underlying microstructure in terms of the martensite volume fractions, the domain volume fractions, and the orientations of the magnetisation vectors inside the domains at selected loading states. The corresponding spatial distribution of $\xi_1$ and $m_2/m_s$ is shown in Figure 4.19. Starting in ①, the magnetisation starts to rotate in the hard-axis direction. The onset of the martensite reorientation is initialised in ②. During further loading, the second martensite variant grows in the expense of the first, see ③ and ④ and during unloading, the initial martensite is partly recovered, see ⑤. In addition, the mechanism of domain wall motion in the second martensite variant is activated allowing a reduction of the magnetisation in the direction of the applied magnetic field. At the end of the first half of the loading cycle, all domains occur and a remanent strain is observable in ⑥. See also our previous work [10] and the discussion therein for comparison.

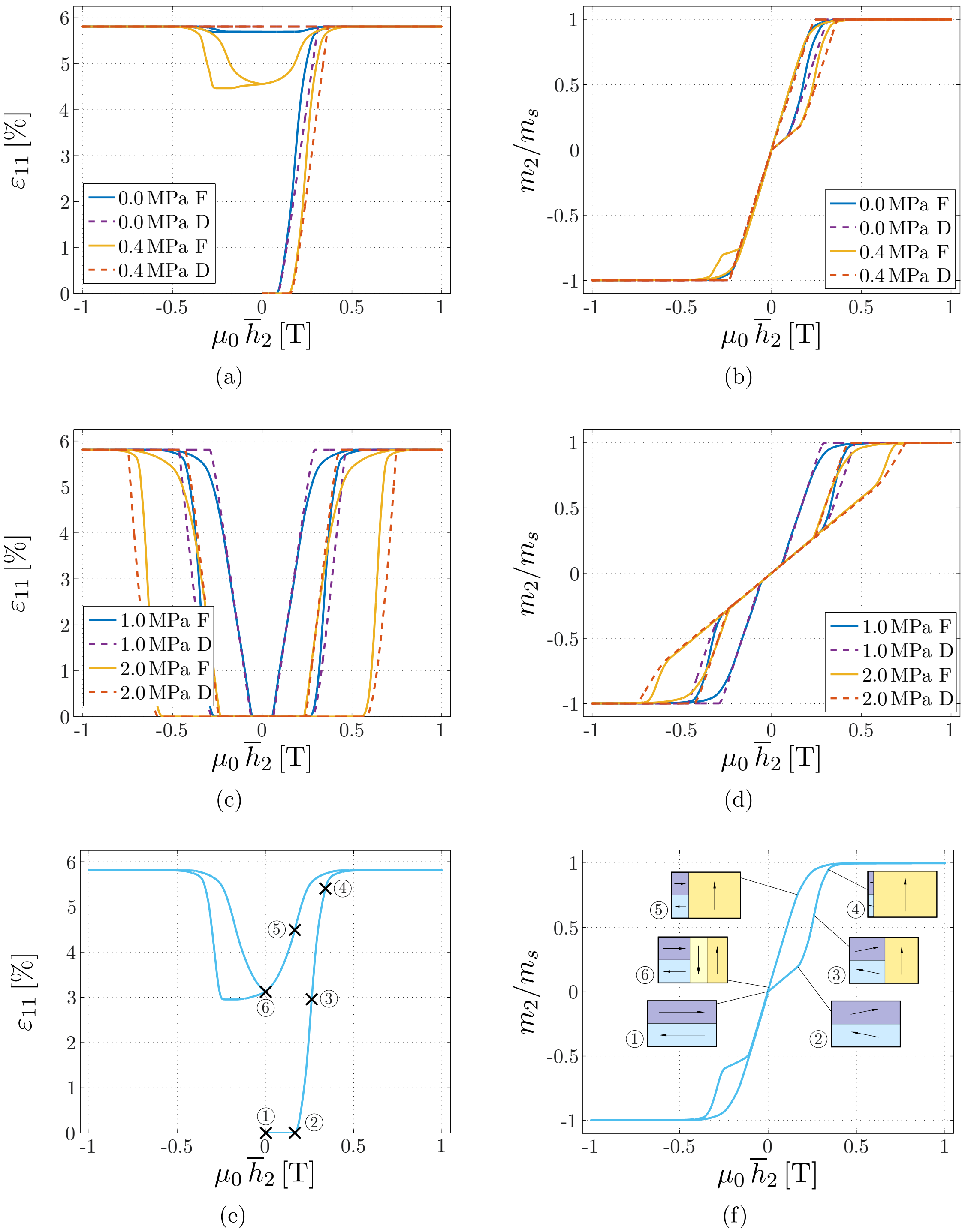

(a) (b) (c) (d) (e) (f)

**Figure 4.18:** Body area-averaged magnetic field-induced (a), (c), (e) strain and (b), (d), (f) magnetisation response under multiple levels of constant compression stress $\overline{\sigma}_{11}$ ($\overline{\sigma}_{11} = -0.5$ MPa for (e) and (f)) and perpendicular cyclic magnetic field $\overline{h}_2$ loading of the rectangular specimen (magnetic field applied along the long edge) embedded in a free space box. The responses of the finite element simulations (F) are compared to the response of a constitutive driver routine (D) in (a)–(d). The evolution of the body-averaged microstructure is sketched for selected loading states in (e) and (f). Sketched mechanism: magnetisation vector rotation, martensite variant switching, and domain wall motion.

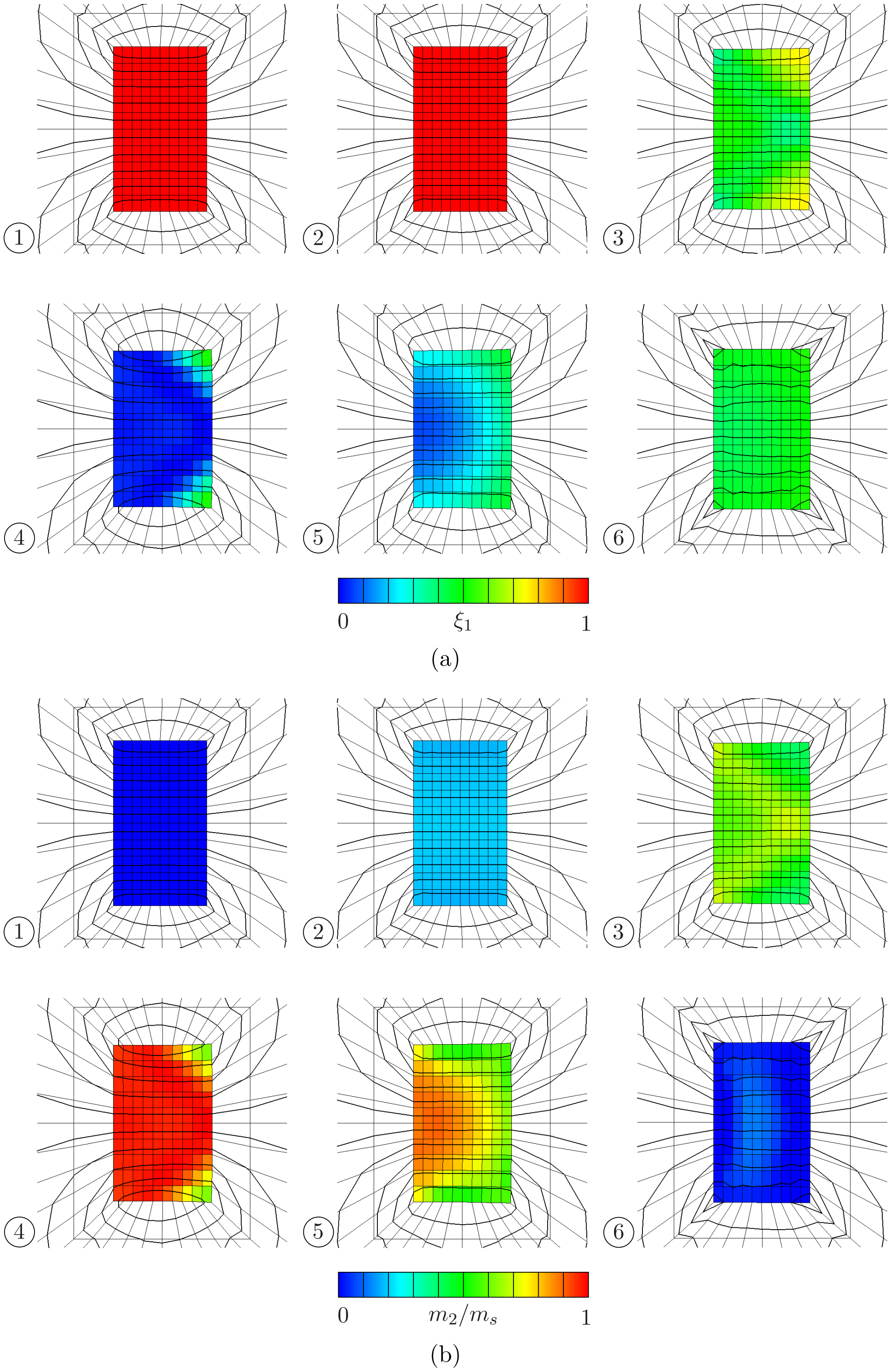

**Figure 4.19:** Spatial distributions of (a) $\xi_1$ and (b) $m_2/m_s$ for selected load steps marked in Figures 4.18 (e) and (f). In addition, iso-lines of the magnetic potential $\widetilde{\phi}$ are shown in black.

### 4.4.4 Stress-induced martensite reorientation under constant magnetic field

In contrast to all previous examples where constant tractions were applied on the boundaries of the specimens in addition to a parallel or to a perpendicular cyclic magnetic field, the response behaviour under multiple constant magnetic fields and cyclic perpendicularly applied tractions, resulting in a cyclic compression stress, is analysed in this example. Experimental observations suggest that an externally applied compression stress is always able to completely switch the configuration into the stress-favoured martensite variant, see [71] and Figure 4.20, taken from [200], for experimentally determined response curves. Depending on the amplitude of the perpendicularly applied constant magnetic field, the initial martensite variant is not at all, partially, or com-

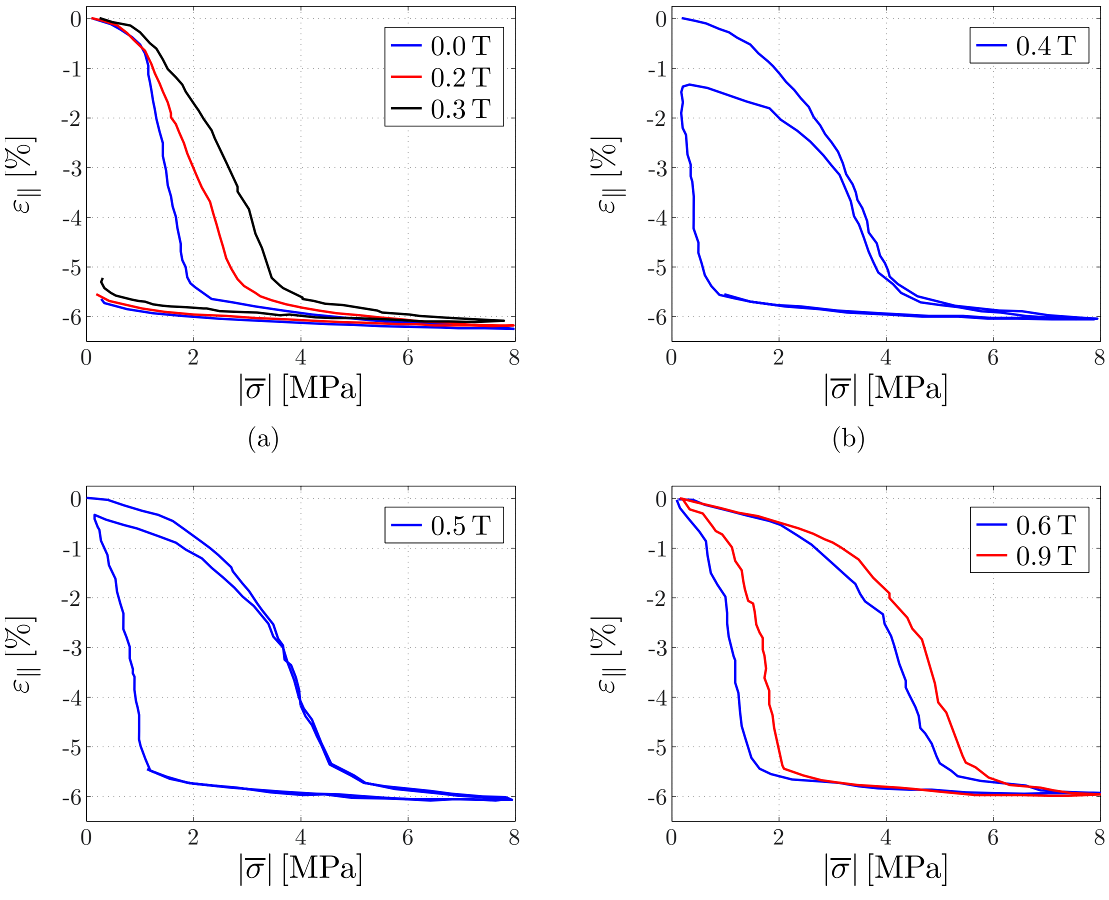

(a) (b) (c) (d)

**Figure 4.20:** Experimentally measured compressive stress-induced variant reorientation under constant magnetic field $\overline{\boldsymbol{h}}$ and perpendicular cyclic compression stress $\overline{\boldsymbol{\sigma}}$ loading, taken from [200]. (a)–(d) show the strain in the direction of the applied stress at multiple levels of constant magnetic fields.

pletely recovered during unloading. Although the experimentally determined curves are not directly comparable to the simulations where plane boundary value problems are considered, many aspects of the experimental findings are captured by the finite element simulations and the constitutive driver routine as discussed below.

A square specimen embedded into a free space box is used for the finite element simulations. The boundary value problem is schematically sketched in Figure 4.21. Multiple levels of constant magnetic field loading $\overline{h}_1$ favouring the initial first martensite variant are applied. The magnetic field is held constant without applying tractions until time $t_1 = 0.5\,\text{ms}$, allowing the state variables to evolve into a stationary state. Afterwards, the compression stress—applied as tractions $\overline{t}_2$ on the boundary—is linearly increased until reaching $\overline{\sigma}_{22} = -10.0\,\text{MPa}$ at time $t_2 = 1.5\,\text{ms}$, followed by a linear decrease to $\overline{\sigma}_{22} = 0.0\,\text{MPa}$ at time $t_3 = 2.5\,\text{ms}$. Figure 4.22 shows (a), (c) the strain where the initial values at time $t_1 = 0.5\,\text{ms}$ are shifted to zero, and (b), (d) the magnetisation responses under multiple levels of constant magnetic field loading. In the following, the body area-averaged responses are compared to the response of the constitutive driver routine as well as experimental observations. All simulated response curves have in common that the compression stress is able to initialise and complete the martensite reorientation process into the stress-favoured second martensite variant. The onset of the reorientation process is delayed for higher magnetic fields, observable in the experiments and the simulations. For zero magnetic field, the response behaviour of the finite element simulation and the constitutive driver routine coincide due to the absence of the demagnetisation field. For the smallest considered magnetic field $\mu_0\,\overline{h}_1 = 0.2\,\text{T}$, a partial reorientation into the second martensite variant occurs during the initial 0.5 s, visible in maximum value of the stress-induced strain response. Experiments and simulations have in common that the reorientation into the magnetic field-favoured variant occurs partially after exceeding

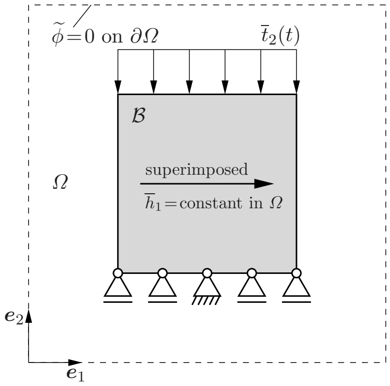

(a)

**Figure 4.21:** Schematic representation of the magnetomechanical BVP of a sqare body $\mathcal{B}$ embedded into a finite size free space box $\Omega$. Prescribed loading in terms of tractions $\overline{t}_2(t)$ favouring the second martensite variant and superimposed spatially homogeneous magnetic field $\overline{h}_1 = \text{const.}$ favouring the initial first martensite variant ($\xi_1 = 0.999$).

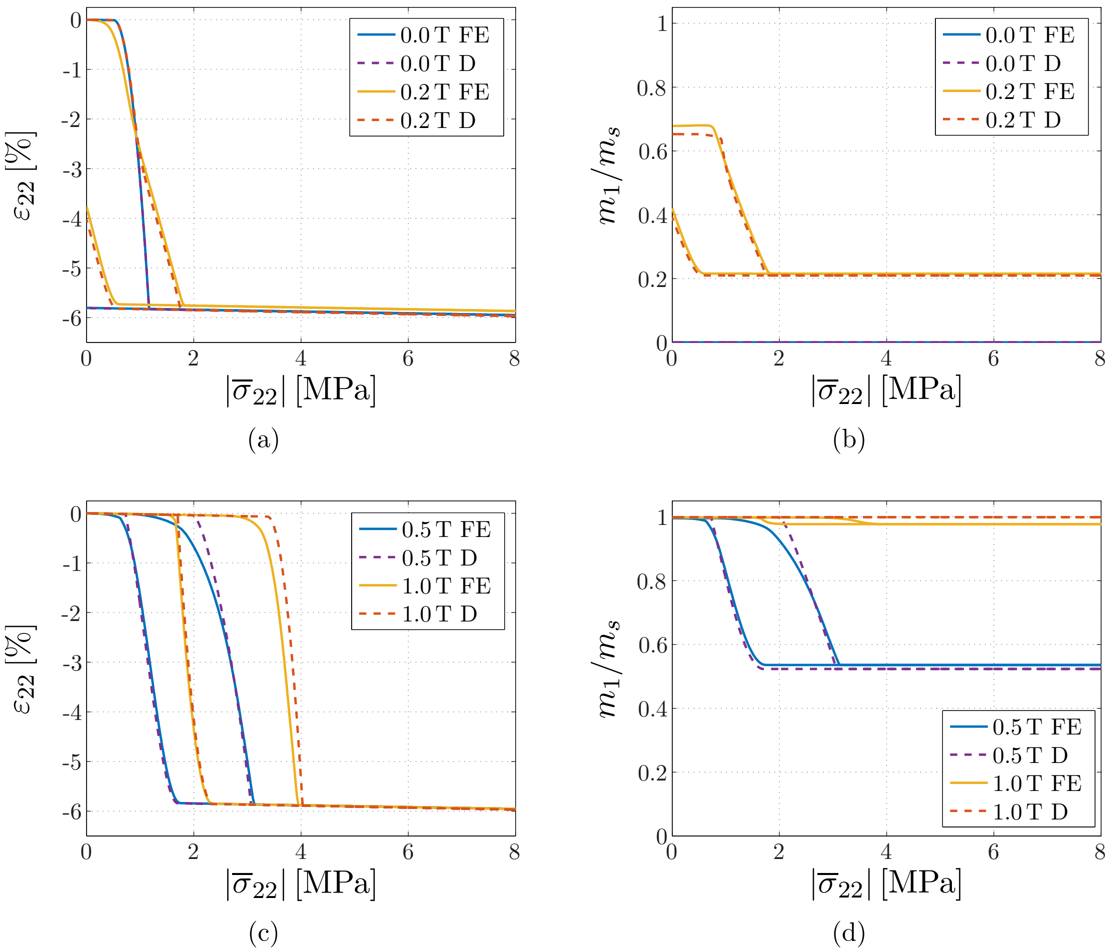

(a) (b)

(c) (d)

**Figure 4.22:** Body area-averaged stress-induced (a), (c) strain and (b), (d) magnetisation response under multiple levels of constant magnetic field $\overline{h}_1$ and perpendicular cyclic compression stress $\overline{\sigma}_{22}$ loading of the quadratic specimen embedded in a free space box. The response behaviour of the finite element simulations (FE) is compared to the response of a constitutive driver routine (D).

a critical magnetic field, or fully occurs for even larger critical magnetic fields during unloading. Generally, the constitutive driver routine captures the response behaviour quite well. The smooth onset of the martensite reorientation during the first half of the loading cycle is captured even better in the finite element simulation. Since no experimental data regarding the magnetisation response is available for the considered strain response curves, the body area-averaged magnetisation response curves are only compared to the response of the constitutive driver routine. Generally, the response curves are quite similar. For low magnetic fields, the magnetisation does not saturate in the direction of the applied field. For large magnetic fields, an initial saturated state is imposed that remains constant during the whole loading cycle for the largest magnetic fields only in the constitutive driver routine. In all other response curves the magnetisation drops off during the martensite variant reorientation, since the arising martensite variant magnetises in its hard-axis direction. In addition to the presented response curves, the response under a fifth level of constant magnetic field $\mu_0\,\overline{h}_1 = 0.3\,\mathrm{T}$ is considered. Figure 4.23 shows the body area-averaged response curves and some sketches of the body area-averaged underlying microstructure in terms of the martensite volume fractions, the domain volume fractions, and the orientations of the magnetisation vectors inside the domains at selected loading states. The corresponding spatial distribution of $\xi_1$ and $m_1/m_s$ is shown in Figure 4.24. During loading, a complete switching into the stress-favoured martensite variant is observable, see ① and ② for intermediate states. Elastic deformations are observable afterwards for increasing stress, whereas the magnetisation remains constant. In ③, the onset is initialised of the reverse switching into the first martensite variant which is only partly recovered at zero compression stress in ④ and a remanent strain occurs. From ③ to ④, the magnetisation increases, since the forming martensite variant is magnetised in its easy-axis direction. Simultaneously, the rotation of the magnetisation in the hard-axis direction of the second martensite variant decreases. See also our previous work [10] for comparison and for a detailed discussion concerning the similarities between magnetic field-induced MSMA response behaviour and temperature-induced shape memory alloy response behaviour.

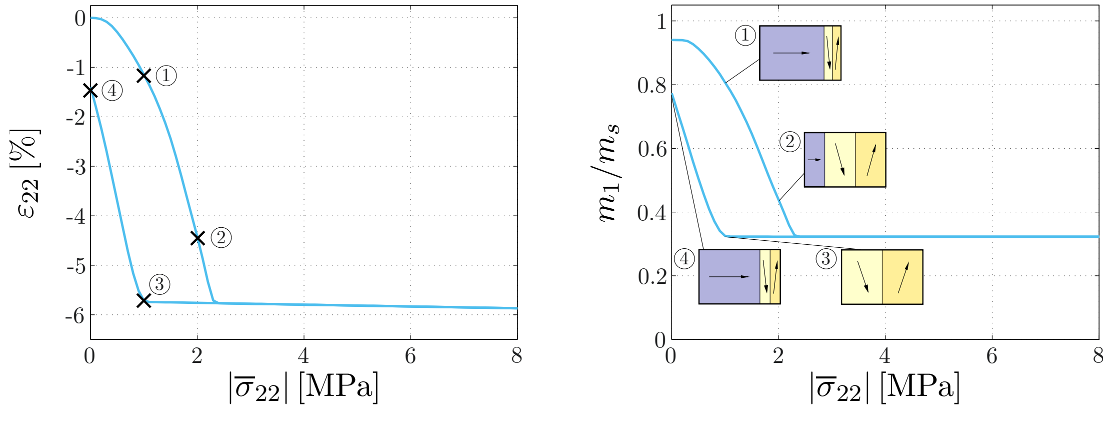

(a) (b)

**Figure 4.23:** Body area-averaged stress-induced (a) strain and (b) magnetisation response under constant magnetic field $\mu_0\,\overline{h}_1 = 0.3\,\mathrm{T}$ and perpendicular cyclic compression stress $\overline{\sigma}_{22}$ loading of the quadratic specimen embedded in a free space box. The evolution of the body-averaged microstructure is sketched for selected loading states. Sketched mechanism: magnetisation vector rotation and martensite variant switching.

## 4.4.5 Biaxial magnetic field-induced martensite reorientation

In the next example, a biaxial magnetic field is applied to the quadratic specimen. Multiple levels of constant magnetic field $\overline{h}_1$ are applied, thereby favouring the initial

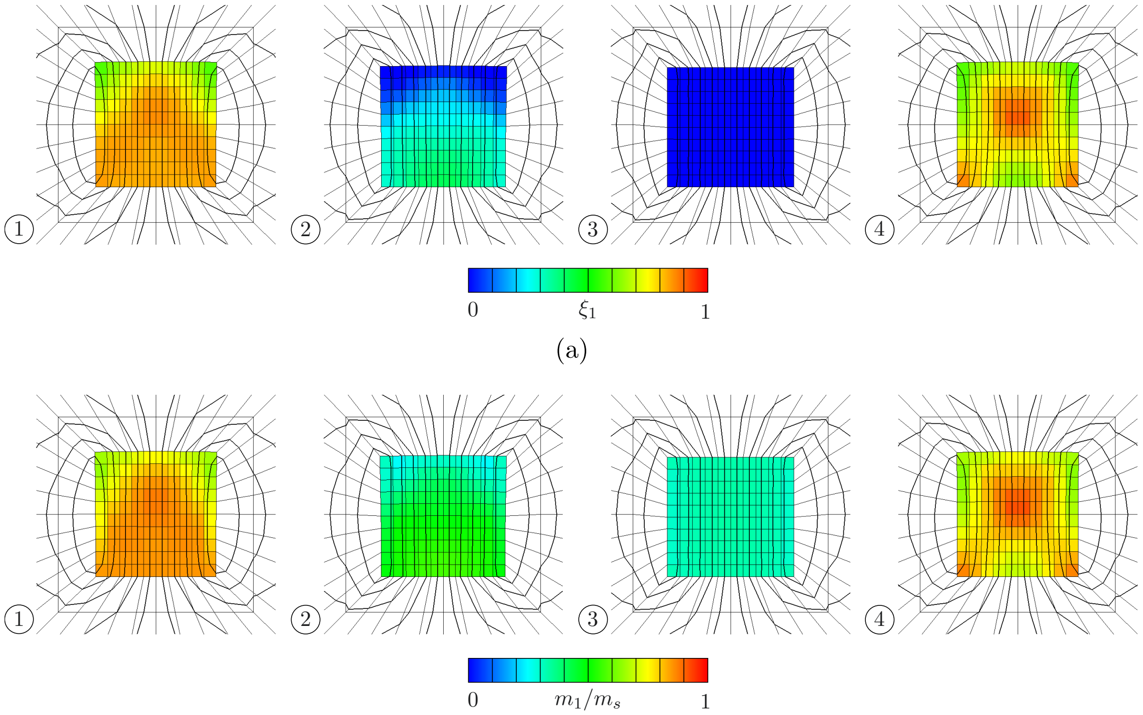

(a)

(b)

**Figure 4.24:** Spatial distributions of (a) $\xi_1$ and (b) $m_1/m_s$ for selected load steps marked in Figure 4.23. In addition, iso-lines of the magnetic potential $\widetilde{\phi}$ are shown in black.

first variant. During the initial 0.5 ms, the magnetic field in the perpendicular direction is set to zero, allowing the state variables to evolve into a stationary state. Afterwards, one period of a triangle wave shaped magnetic field loading $\overline{h}_2$ favouring the second martensite variant is applied perpendicularly to the other magnetic field with a frequency of 250 Hz. The response behaviour in terms of strain and magnetisation responses are investigated for multiple levels of constant $\overline{h}_1$ magnetic field loading. In principle, it would also be possible to superimpose a compression stress, applied in terms of tractions on the surface of the specimen. But, since the effect of a biaxial magnetic field on the response behaviour should be analysed on its own, only rigid body motions are suppressed and no tractions are applied on the surface of the body. The boundary value problem is schematically sketched in Figure 4.25.

Figure 4.26 shows (a), (c) the strain where the initial values at time $t_1 = 0.5$ ms are shifted to zero, and (b), (d) the magnetisation responses under multiple levels of constant magnetic field loading. In the following, body area-averaged response behaviour is compared to the responses of the constitutive driver routine. All simulated response curves have in common that the cyclic magnetic field is able to initialise and complete the martensite reorientation process into the cyclic magnetic field-favoured second martensite variant. The onset of the reorientation process is delayed for higher constant

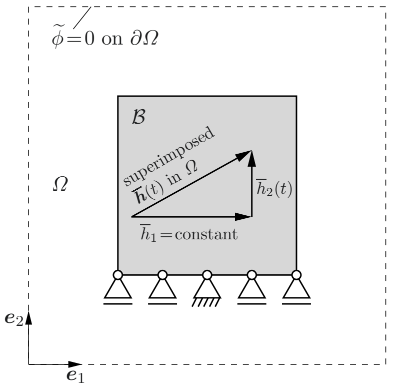
$\widetilde{\phi}=0$ on $\partial\Omega$
$\mathcal{B}$
superimposed
$\overline{\boldsymbol{h}}(t)$ in $\Omega$
$\overline{h}_2(t)$
$\overline{h}_1=$constant
$\Omega$
$\boldsymbol{e}_2$
$\boldsymbol{e}_1$

(a)

**Figure 4.25:** Schematic representation of the magnetomechanical BVP of a rectangular body $\mathcal{B}$ embedded into a finite size free space box $\Omega$. Prescribed loading in terms of a spatially homogeneous biaxial magnetic field $\overline{\boldsymbol{h}}(t)$ loading where the horizontal component $\overline{h}_1=$const. favours the initial first martensite variant, and where the vertical component $\overline{h}_2(t)$ favours the second martensite variant.

magnetic fields. For the smaller constant magnetic fields considered, only a partial reorientation into the initial martensite variant occurs during unloading. For larger constant magnetic fields, a complete reorientation into the initial first martensite variant is observable. The higher the constant applied magnetic field, the lower the magnetisation in the direction of the cyclic magnetic field. All response curves have in common that the width of the hysteresis in the magnetisation response curve and, in particular, the strain response curve increases for increasing levels of constant magnetic field. Generally, the response behaviour of the constitutive driver routine approximates the response behaviour of the finite element simulations quite well. The larger the constant magnetic field, the better the correlation of the corresponding response curves. Only for low constant magnetic fields, the strain response of both simulations obviously does not match. The response behaviour under biaxial magnetic field loading has, to some extent, certain similarities with the response behaviour under constant compression stress and cyclic perpendicular magnetic field loading, see Figures 4.18 for comparison. In addition to the presented response curves, the response under a fifth level of constant magnetic field $\mu_0\,\overline{h}_1=0.3\,\mathrm{T}$ is considered. Figure 4.27 shows the body area-averaged response curves and some sketches of the body area-averaged underlying microstructure in terms of the martensite volume fractions, the domain volume fractions, and the orientations of the magnetisation vectors inside the domains at selected loading states. The corresponding spatial distribution of $\xi_1$ is shown in Figure 4.28 and that of $m_i/m_s$ in Figure 4.29.

Starting from a single variant and single domain state in ①, the second martensite variant—consisting likewise of only one domain—grows at the expense of the other, see ②. In ③, switching is completed and a single domain configuration is observable where the magnetisation is slightly oriented in the direction of the constant magnetic bias field. During unloading, the initial configuration is only partially, but nearly completely re-

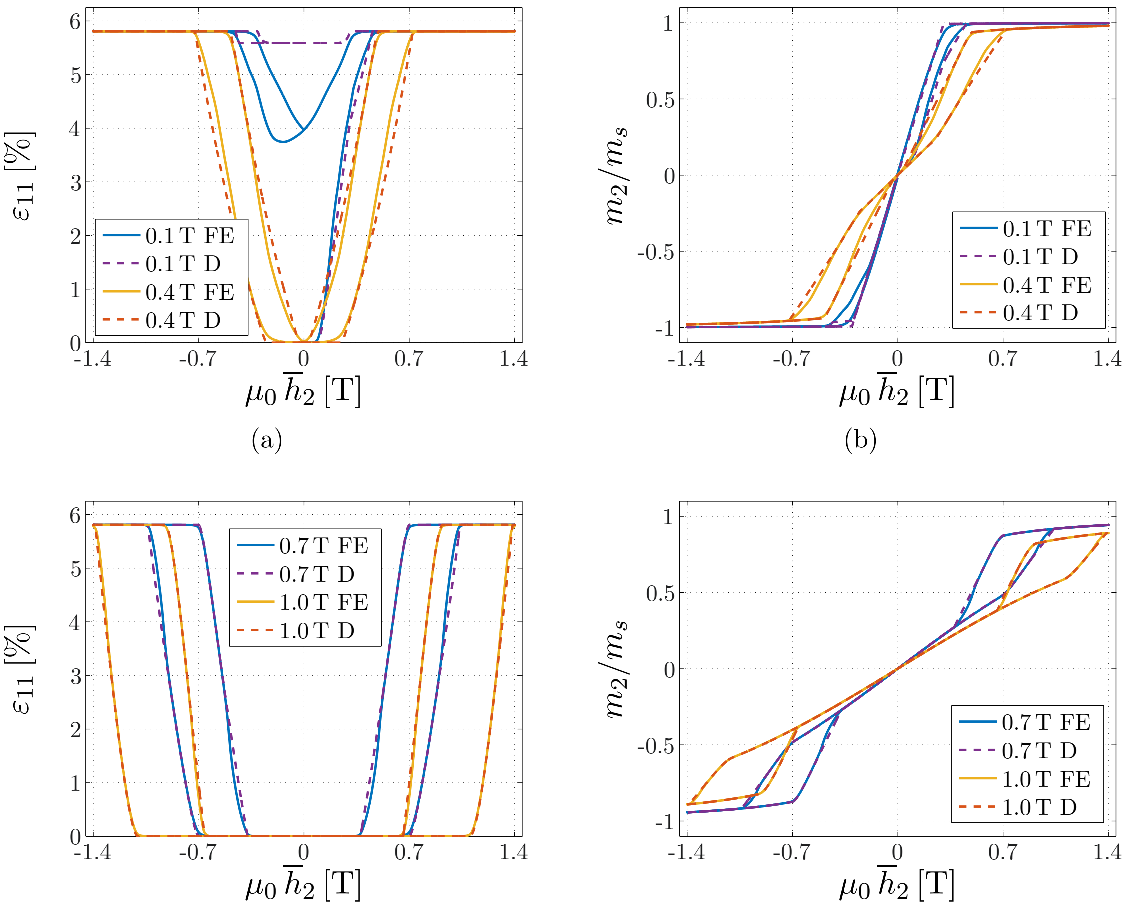

(a) (b)

(c) (d)

**Figure 4.26:** Body area-averaged magnetic field-induced (a), (c) strain and (b), (d) magnetisation response under multiple levels of constant magnetic field $\overline{h}_1$ and perpendicular cyclic magnetic field $\overline{h}_2$ loading of the quadratic specimen embedded in a free space box. The response behaviour of the finite element simulations (FE) is compared to the response of a constitutive driver routine (D).

covered, see ④ to ⑥, and a remanent strain is observable. See also our previous work [10] and the discussion therein for comparison.

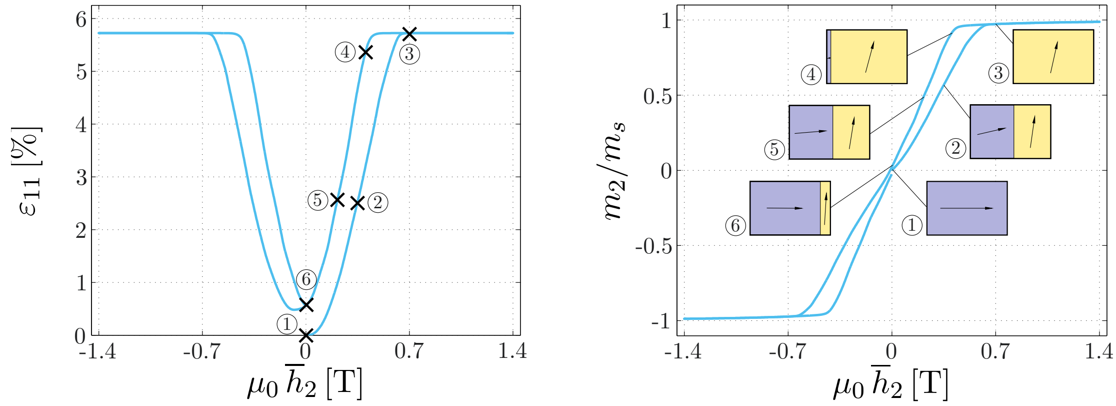

(a) (b)

**Figure 4.27:** Body area-averaged magnetic field-induced (a) strain and (b) magnetisation response under constant magnetic field $\mu_0\,\overline{h}_1 = 0.3\,\mathrm{T}$ and perpendicular cyclic magnetic field $\overline{h}_2$ loading of the quadratic specimen embedded in a free space box. The evolution of the body-averaged microstructure is sketched for selected loading states. Sketched mechanism: magnetisation vector rotation and martensite variant switching.

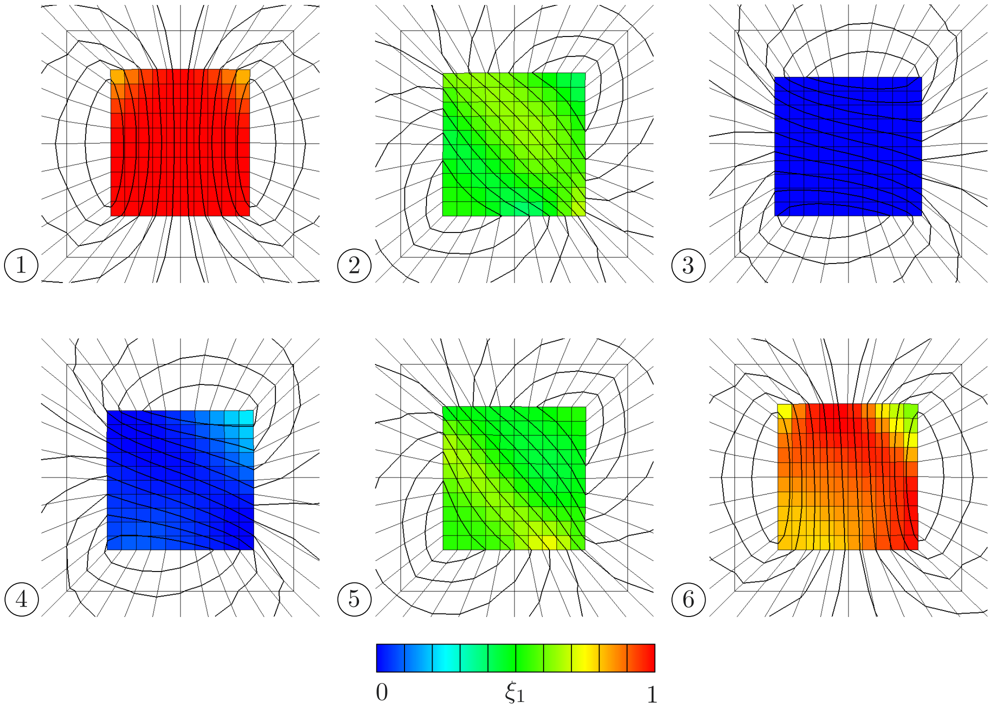

(a)

**Figure 4.28:** Spatial distributions of $\xi_1$ for selected load steps marked in Figure 4.27. In addition, iso-lines of the magnetic potential $\widetilde{\phi}$ are shown in black.

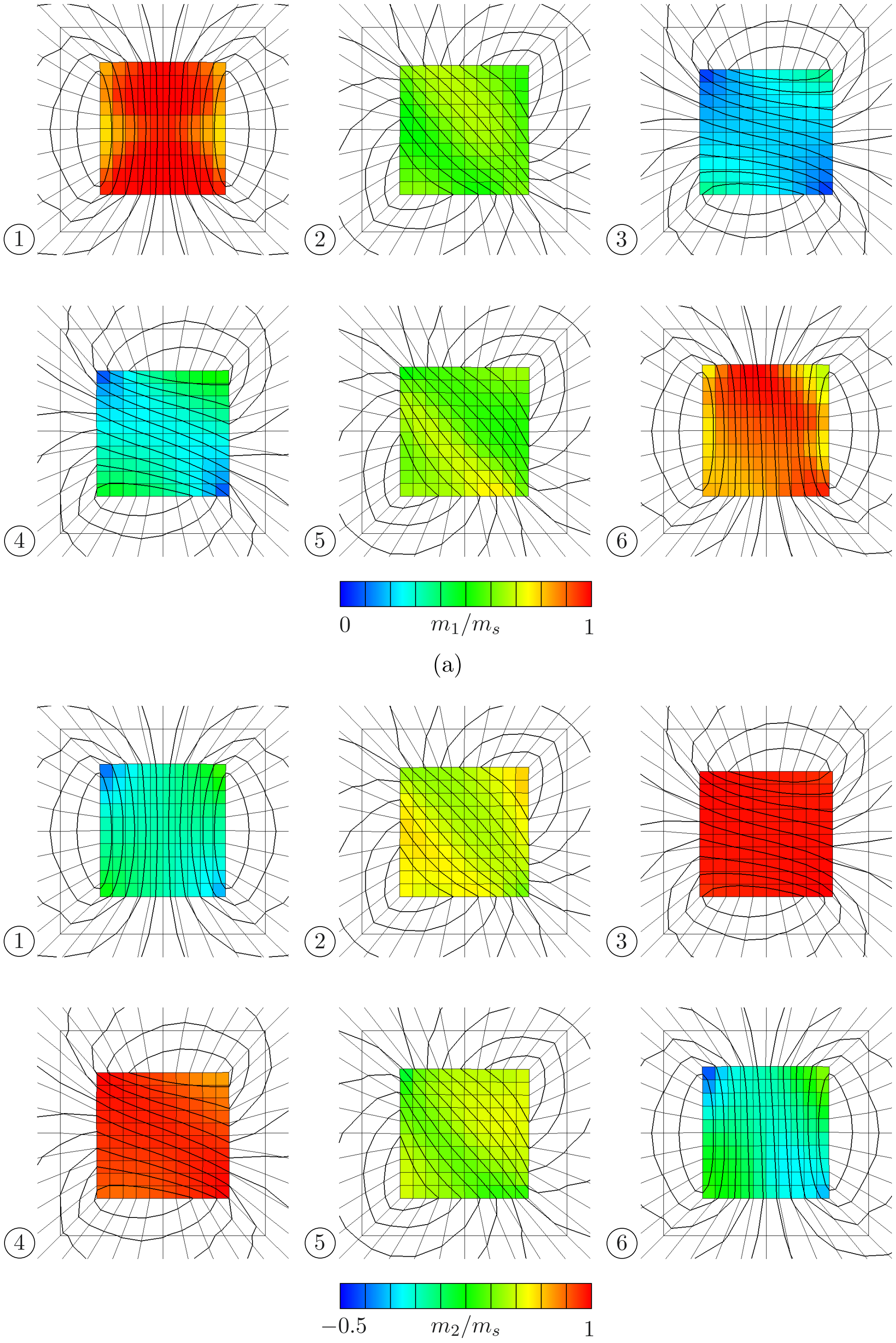

(a)

(b)

**Figure 4.29:** Spatial distributions of (a) $m_1/m_s$ and (b) $m_2/m_s$ for selected load steps marked in Figure 4.27. In addition, iso-lines of the magnetic potential $\widetilde{\phi}$ are shown in black.

### 4.4.6 Investigation of a complex geometry

In the final example, the response behaviour of an I-profile is investigated under constant prescribed tractions $\overline{t}_2$—favouring the initial second martensite variant—and cyclic magnetic field loading. One period of a triangle wave shaped magnetic field loading $\overline{h}_i$, favouring the $i$-th martensite variant, with a frequency of 250 Hz is applied. The boundary value problems are schematically sketched in Figure 4.30 for the magnetic field applied in (a) horizontal and (b) vertical direction.

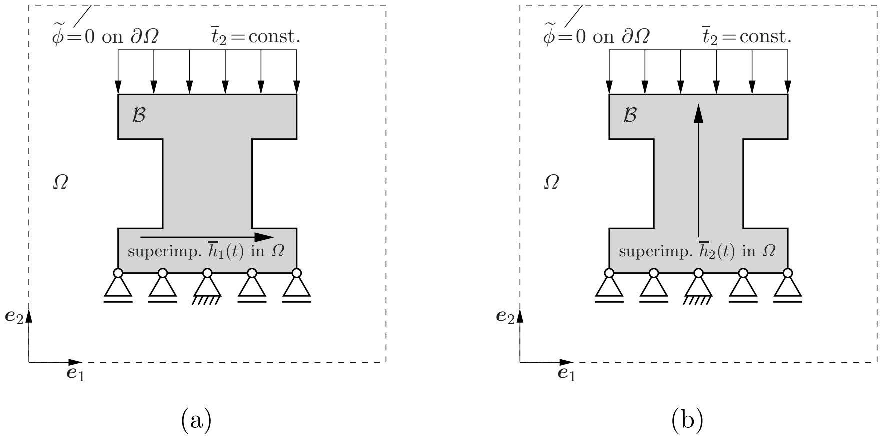
$\widetilde{\phi}=0$ on $\partial\Omega$
$\overline{t}_2=$const.
$\mathcal{B}$
$\Omega$
superimp. $\overline{h}_1(t)$ in $\Omega$
$e_2$
$e_1$
(a)
$\widetilde{\phi}=0$ on $\partial\Omega$
$\overline{t}_2=$const.
$\mathcal{B}$
$\Omega$
superimp. $\overline{h}_2(t)$ in $\Omega$
$e_2$
$e_1$
(b)

**Figure 4.30:** Schematic representation of the magnetomechanical BVP of an I-profile $\mathcal{B}$ embedded into a finite size free space box $\Omega$. Prescribed loading in terms of tractions $\overline{t}_2=$const. favouring the initial second martensite variant ($\xi_2=0.999$) and superimposed spatially homogeneous magnetic fields $\overline{h}_i(t)$ in (a) horizontal and (b) vertical direction.

Figure 4.31 shows (a) the strain where the lowest values are shifted to zero, and (b) the magnetisation response curves for the I-Profile under multiple constant prescribed tractions $\overline{t}_2$ and cyclic magnetic field $\overline{h}_i$ loading. Due to the shape of the body, the stress distribution inside the body is highly inhomogeneous under prescribed tractions. Firstly, the easy-axis response (e) is considered where the magnetic field $\overline{h}_2$ is applied parallel to the tractions. The tractions $\overline{t}_2$ applied on the surface are equivalent to applying a compression stress of $\overline{\sigma}_{22}=-10.0\,\text{MPa}$. The magnetisation response curve seems to consist of three nearly linear regions, with the highest slope around low magnetic fields. Even though the compression stress is larger than the blocking stress in all previous examples, the magnetic field is able to initialise a partial reorientation of the martensite variant, observable in the strain response curve. The width of the hysteresis curve is relatively small. Secondly, the hard-axis response (h) is considered where the magnetic field $\overline{h}_1$ is applied perpendicular to the tractions. The tractions $\overline{t}_2$ applied on the surface are, again, equivalent to applying a compression stress of $\overline{\sigma}_{22}=-10.0\,\text{MPa}$. The magnetisation response seems to be quite linear, but the slope decreases successively for larger magnetic fields. A partial variant reorientation into the magnetic field-favoured martensite variant is observable in the strain response curve. The width of the hysteresis

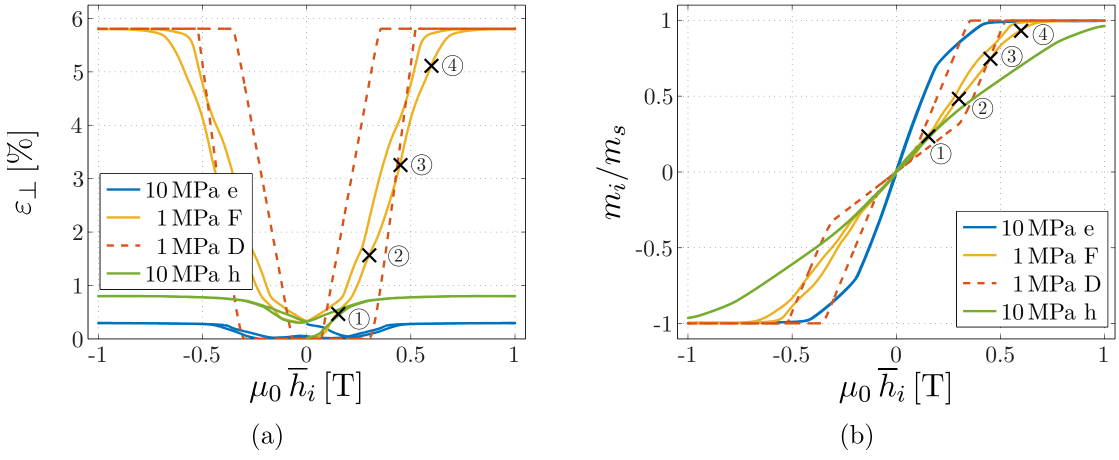

**Figure 4.31:** Body area-averaged magnetic field-induced (a) strain and (b) magnetisation response under multiple levels of constant compression stress $\overline{\sigma}_{22}$ that favours the initial second martensite variant and parallel (e) or perpendicular (h, F, D) cyclic magnetic field $\overline{h}_i$ loading of the I-profile embedded in a free space box. For $\overline{\sigma}_{22} = -1.0\,\text{MPa}$, the response behaviour of the finite element simulations (F) is compared to the response of a constitutive driver routine (D).

curve is also relatively small. Finally, the response behaviour under tractions $\overline{t}_2$ applied on the surface, that are equivalent to applying a compression stress of $\overline{\sigma}_{22} = -1.0\,\text{MPa}$, and cyclic perpendicular $\overline{h}_1$ magnetic field loading of a finite element simulation (F) is compared to the response behaviour of the constitutive driver routine (D). Due to the spatially highly inhomogeneous response of the I-profile, the predicted response behaviour of the constitutive driver routine is completely different to the body area-averaged response. The magnetisation response of the finite element simulations lies somewhere between the easy- and hard-axis magnetisation response. The strain response is shaped like “U”. Only an incomplete reorientation into the initial martensite variant occurs during unloading. A clearly but relatively small hysteretic behaviour is observable in both response curves. The spatial distribution of $\xi_1$, $m_1/m_s$, and $m_2/m_s$ is shown in Figure 4.32 for selected load steps marked in Figure 4.31.

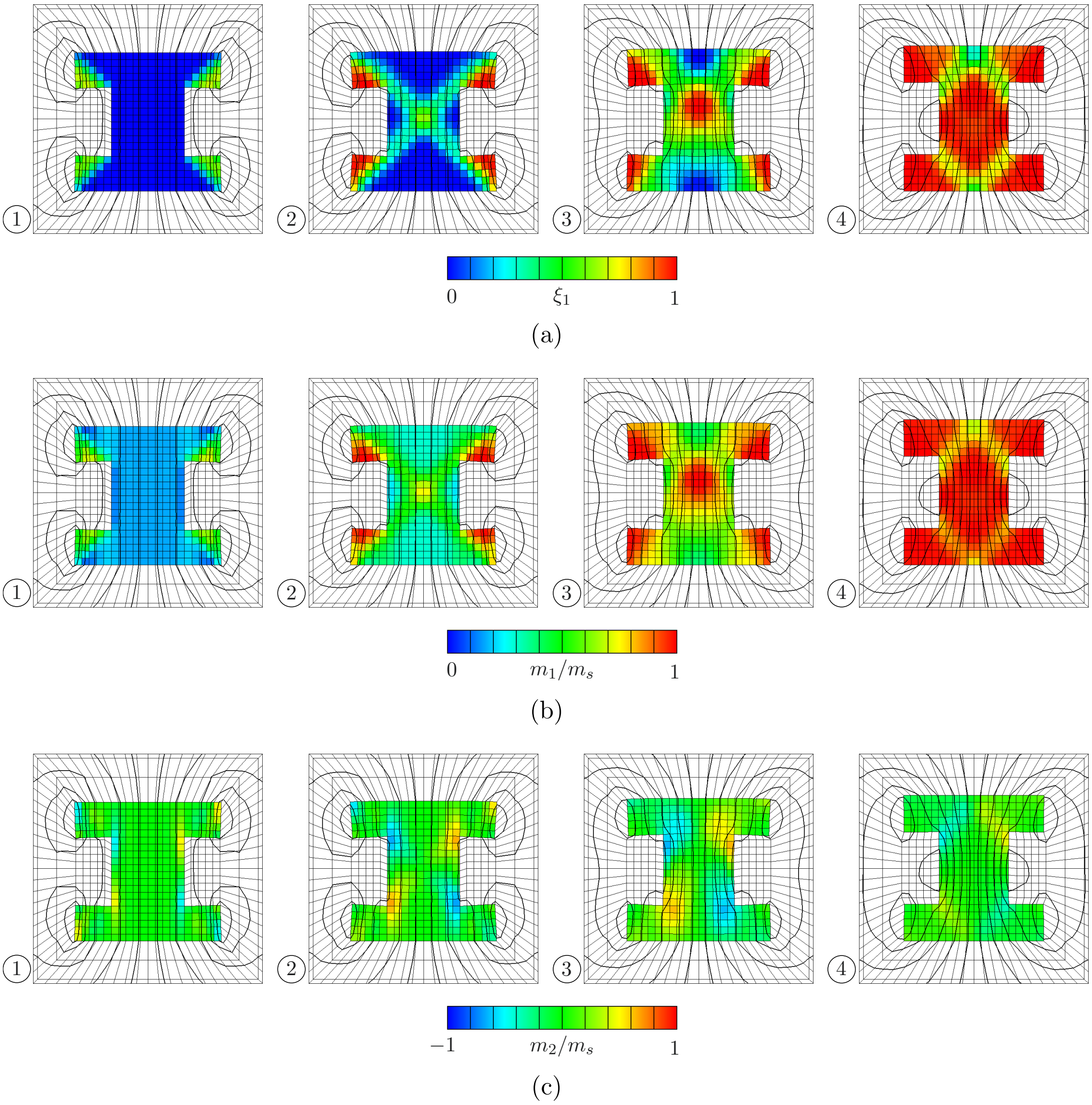

(a)

(b)

(c)

**Figure 4.32:** Spatial distributions of (a) $\xi_1$, (b) $m_1/m_s$, and (c) $m_2/m_s$ for selected load steps marked in Figure 4.31. In addition, iso-lines of the magnetic potential $\widetilde{\phi}$ are shown in black.

## 4.5 Summary and outlook

This chapter presented a micromagnetics-inspired finite element framework used for the modelling and simulation of the material behaviour and structural response of $Ni_2MnGa$ MSMA specimens embedded into finite size free space boxes. At first, a micromagnetics-inspired power type potential consisting of an energy potential and a dissipation functional was introduced, where the displacement field $\boldsymbol{u}$, the magnetic potential of the demagnetisation field $\tilde{\phi}$, and a set of microstructure-describing state variables $\boldsymbol{p}$ are the global primary field variables. The stationarity conditions of the power type potential are equivalent to solving the mechanical equilibrium equations, the Maxwell equations for the magnetostatic case, and the Biot equations in terms of evolution equations for the state variables. Secondly, the set of state variables that describe the state of the assumed underlying microstructure, in terms of a martensite variant volume fraction and some variables describing the magnetic state, was defined. A numerical homogenisation scheme was applied to derive the effective elastic strain energy density of the phase mixture that consists of two tetragonal martensite variants with different Bain strains. The magnetocrystalline anisotropy energy density that accounts for deviations of the (spontaneous) magnetisation vectors from their respective easy-axes was introduced for different parametrisations. The derivatives of the stored energy density of the body, the derivatives of the magnetisation, and the total magnetic field are part of the driving forces in the evolution equations of viscoplastic, respectively viscoelastic, type for the state variables. Due to the non-local nature of the demagnetisation self-field, the magnetostatic problem as well as the evolution equations for the state variables have to be solved simultaneously. The introduction of the state variables as global primary fields were therefore necessary. The underlying equations of the finite element implementation were derived from the stationarity conditions of the power type potential, subject to inequality constraints of the state variables. Two different regions, the magnetostrictive body and the surrounding free space, were considered. The displacement field and the state variables were solely resolved in elements of the body which was discretised using a mixed element formulation. The treatment of the inequality constraints necessitated the introduction of Karush-Kuhn-Tucker parameters at the global level in terms of additional nodal degrees of freedom. Fischer-Burmeister NCP functions were used to express the KKT-conditions in a residual format. Multiple numerical examples demonstrated the capabilities of the finite element framework. Body area-averaged strain and magnetisation response curves were compared to experimental data taken from the literature. This comparison demonstrated the advantages of the finite element simulations where inhomogeneous distributions of, e.g., the strain, the magnetisation, and the magnetic field occurred, over simulations performed using a demagnetisation tensor, where all quantities are by definition assumed to be homogeneously distributed inside the body. Finite element simulations of ellipsoidal bodies yielded the same homogeneous responses as were predicted by simulations utilising a demagnetisation tensor and therefore verified the finite element implementation.

In future work, the most important step is the extension to three-dimensional problems. This will allow the simulation of arbitrarily shaped bodies and make the comparison to all experimentally obtained response curves possible. In addition, more advanced material models will be employed, e.g. other numerical energy relaxation schemes may be applied to the elastic strain energy density of the phase mixture in terms of rank-one convexification w.r.t. laminates of first or second order. The general framework shall be applied to other material classes, for instance (giant) magnetostrictives such as Terfenol-D, Galfenol, and cobalt ferrite.

## 4.6 Appendix

### 4.6.1 Dependencies among the domain magnetisations

In Section 4.2, it was claimed, that $\theta_{2i} = -\,\theta_{2i-1}$ minimises the magnetocrystalline anisotropy energy density within the $i$-th variant of martensite at constant magnetisation, cf. (4.57). In the following proof—based on the derivation in [21]—, only the first variant of martensite is considered, i.e. $\xi_1 = 1$. The proof for the second martensite variant is analogously possible.

The magnetic state of the first martensite variant is characterised by the domain volume fraction $\gamma_1$ and the two angles $\theta_1$ and $\theta_2$. Assuming a coexistence of both domains, the lower and upper bound of the relative domain volume fraction are excluded, i.e. $\gamma_1 \neq 0$ and $\gamma_1 \neq 1$, since otherwise, the angle of the non-existing domain would be arbitrary. Additionally, the states $\theta_1 = -\,\theta_2 = \pm\,\pi/2$, which maximise the magnetocrystalline anisotropy energy density, are not considered.

Insertion of $\gamma_1 \sin(\theta_1) = [\,1 - \gamma_1\,] \sin(\theta_2) + m_{12}$, from (4.57), into (4.58) results in an alternative representation of the magnetocrystalline anisotropy energy density of the first martensite variant

$$\frac{\psi^{\mathrm{an}}_{M1}}{k_1} = \frac{m_{12}^2 + 2\,m_{12}\,[\,1-\gamma_1\,]\,\sin(\theta_2) + [\,1-\gamma_1\,]\,\sin^2(\theta_2)}{\gamma_1}\;. \tag{4.117}$$

The first and second partial derivative of (4.117)

$$\frac{1}{k_1}\,\frac{\partial \psi^{\mathrm{an}}_{M1}}{\partial \theta_2} = \frac{2\,[\,1-\gamma_1\,]}{\gamma_1}\,\cos(\theta_2)\,\left[\,m_{12} + \sin(\theta_2)\,\right]\;, \tag{4.118}$$

$$\frac{1}{k_1}\,\frac{\partial^2 \psi^{\mathrm{an}}_{M1}}{\partial \theta_2^2} = \frac{2\,[\,1-\gamma_1\,]}{\gamma_1}\,\left[\cos^2(\theta_2) - \sin(\theta_2)\,\left[\,m_{12} + \sin(\theta_2)\,\right]\right]\;. \tag{4.119}$$

are used to check the necessary and sufficient condition for a minimum, respectively maximum. The two solutions fulfilling $\partial_{\theta_2}\psi^{\mathrm{an}}_{M1} = 0$ are $m_{12} = -\sin(\theta_2)$ and $\cos(\theta_2) = 0$.

Inserting $m_{12} = -\sin(\theta_2)$ into (4.119) results in the sufficient condition for a minimum, viz.

$$k_1 \, \frac{2\,[\,1-\gamma_1\,]}{\gamma_1} \, \cos^2(\theta_2) > 0 \ , \quad \text{for} \quad \cos(\theta_2) \neq 0 \ . \tag{4.120}$$

Since the magnetisation (4.57) is assumed to remain constant, see (4.57), $m_{12} = -\sin(\theta_2)$ results in $\sin(\theta_1) = -\sin(\theta_2)$ and consequently $\theta_2 = -\theta_1$, even for $\cos(\theta_2) = 0$. Inserting $\cos(\theta_2) = 0$ into (4.119) results in the sufficient condition for a maximum, viz.

$$k_1 \, \frac{2\,[\,1-\gamma_1\,]}{\gamma_1} \, \big[ -\sin^2(\theta_2) - \sin(\theta_2)\, m_{12} \big] < 0 \ , \quad \text{for} \quad -1 < m_{12} < 1 \ , \tag{4.121}$$

Since the magnetisation (4.57) is assumed to remain constant, see (4.57), $m_{12} = \mp 1$ results in $\sin(\theta_1) = \mp 1$ and consequently $\sin(\theta_1) = -\sin(\theta_2)$, respectively $\theta_2 = -\theta_1 = \pm\,\pi/2$, and also $m_{12} = -\sin(\theta_2)$.

For $\cos(\theta_2) = 0$, the results of both possible solution state $\theta_2 = -\theta_1$, which is interpretable as a full alignment of the magnetisation in both domains with the magnetic hard-axis (maximum of the magnetocrystalline anisotropy energy density). In such a case, the domain volume fraction may take arbitrary values, even the excluded values $\gamma_1 = 0$, respectively $\gamma_1 = 1$, without having an influence on the magnetisation or the anisotropy energy density.

Insertion of $\theta_2 = -\theta_1$ together with $m_{12} = -\sin(\theta_2)$ ($\xi_1 = 1$) in (4.58), respectively (4.117), results in the magnetocrystalline anisotropy energy density of the first martensite variant

$$\frac{\psi^{\text{an}}_{M1}}{k_1} = \sin^2(\theta_1) = \sin^2(\theta_2) = m_{12}^2 \ , \tag{4.122}$$

even for the excluded values $\gamma_1 = 0$, respectively $\gamma_1 = 1$, at constant magnetisation, cf. (4.57).

In summary, the magnetocrystalline anisotropy energy density of the first martensite variant is minimised for $\theta_2 = -\theta_1$. The analogous derivation results in $\theta_4 = -\theta_3$ minimising the magnetocrystalline anisotropy energy density of the second martensite variant. As already mentioned in Section 4.2, the number on state variables is reduced by two and the number of inequality constraints reduces from fourteen (4.56) to four (4.59).

### 4.6.2 Constitutive driver routine

This sections deals with the derivation of a constitutive driver routine to calculate the response of macroscopically homogeneous states inside bodies under prescribed homogeneous stress $\overline{\boldsymbol{\sigma}}$ and prescribed homogeneous magnetic field $\overline{\boldsymbol{h}}$ loading. The strain $\boldsymbol{\varepsilon}(\boldsymbol{p})$ and magnetisation $\boldsymbol{m}(\boldsymbol{p})$ responses, which are also assumed to be homogeneous inside the body, are completely determined by the evolution of the state variables $\boldsymbol{p}$, introduced in Section 4.2. The constitutive driver routine is used for comparison to body area-averaged strain $\boldsymbol{\varepsilon}$ and magnetisation $\boldsymbol{m}$ response curves of finite element simulations.

Beginning with the energy potential (4.8), the displacement field $\boldsymbol{u}$ and the magnetic potential $\widetilde{\phi}$, respectively their gradients, viz. the strain $\boldsymbol{\varepsilon}$ (symmetric gradient) and the demagnetisation field $\widetilde{\boldsymbol{h}}$ (negative gradient), are directly expressed as functions of the state variables $\boldsymbol{p}$. Due to the linear relation of stress and strain in (4.47), the inverse relation is used to calculate the strain $\boldsymbol{\varepsilon}(\boldsymbol{\sigma}, \xi_i)$, viz.

$$\boldsymbol{\varepsilon} = \mathsf{E}^{-1} : \boldsymbol{\sigma} + \sum_{i=1}^{2} \xi_i \, \boldsymbol{\varepsilon}_i^{\mathrm{tr}} \; . \tag{4.123}$$

The inverse of the elasticity tensor is defined as the compliance tensor $\mathsf{S}$ and may be represented in terms of the compression-modulus $\kappa = E/[\,3\,[\,1 - 2\,\nu\,]\,]$ and the shear-modulus $\mu^{\mathrm{lam}}$

$$\mathsf{S} := \mathsf{E}^{-1} \widehat{=} \frac{1}{9\,\kappa}\,\delta_{ij}\,\delta_{kl} + \frac{1}{2\,\mu^{\mathrm{lam}}} \left[ \frac{1}{2}\,[\,\delta_{ik}\,\delta_{jl} + \delta_{il}\,\delta_{jk}\,] - \frac{1}{3}\,\delta_{ij}\,\delta_{kl} \right] \boldsymbol{e}_i \otimes \boldsymbol{e}_j \otimes \boldsymbol{e}_k \otimes \boldsymbol{e}_l \; . \tag{4.124}$$

For a prescribed homogeneous stress state, i.e. $\boldsymbol{\sigma} = \overline{\boldsymbol{\sigma}}$, (4.123) is completely determined by the variant volume fraction $\xi_1$ ($\xi_2 = 1 - \xi_1$), cf. [112]. Insertion of (4.123) into the elastic strain energy density (4.46) yields

$$C\psi^{\mathrm{el}} = \frac{1}{2}\boldsymbol{\sigma} : \mathsf{E}^{-1} : \boldsymbol{\sigma} = \frac{1}{2}\boldsymbol{\sigma} : \mathsf{S} : \boldsymbol{\sigma} \; , \tag{4.125}$$

which is independent of $\boldsymbol{p}$ and completely determined for $\boldsymbol{\sigma} = \overline{\boldsymbol{\sigma}}$. The contribution due to prescribed tractions $\overline{\boldsymbol{t}}$ on the Neumann surface are assumed to result in a homogeneous stress and strain state. In the absence of additional body forces, the reformulation of the surface integral yields

$$\begin{aligned} \int_{\partial\mathcal{B}_t} \overline{\boldsymbol{t}} \cdot \boldsymbol{u} \,\mathrm{d}a &= \int_{\partial\mathcal{B}_t} [\,\overline{\boldsymbol{\sigma}} \cdot \boldsymbol{n}\,] \cdot \boldsymbol{u} \,\mathrm{d}a = \int_{\mathcal{B}} \mathrm{div}_{\boldsymbol{x}}(\overline{\boldsymbol{\sigma}}^{\mathrm{t}} \cdot \boldsymbol{u}) \,\mathrm{d}v \\ &= \int_{\mathcal{B}} \nabla_{\boldsymbol{x}}^{\mathrm{sym}} \boldsymbol{u} : \overline{\boldsymbol{\sigma}} \,\mathrm{d}v + \int_{\mathcal{B}} \boldsymbol{u} \cdot \mathrm{div}_{\boldsymbol{x}} \overline{\boldsymbol{\sigma}} \,\mathrm{d}v = \int_{\mathcal{B}} \boldsymbol{\varepsilon} : \overline{\boldsymbol{\sigma}} \,\mathrm{d}v \; , \end{aligned} \tag{4.126}$$

where the strain $\boldsymbol{\varepsilon}$, introduced in (4.123), is completely determined by the volume fraction $\xi_1$. With (4.125) and (4.126) at hand, the incremental potential depends no longer on the displacement field $\boldsymbol{u}$ for homogeneous states.

**Remark 13** *For general cases, where the relation between the stress and the strain is nonlinear, the strain* $\boldsymbol{\varepsilon}$ *is iteratively determined until the norm of the difference of the stress* $\boldsymbol{\sigma} = \partial_{\boldsymbol{\varepsilon}} \psi^{\mathrm{mat}}$ *and the prescribed stress* $\overline{\boldsymbol{\sigma}}$ *falls below a certain tolerance value.*

A homogeneous magnetisation state yields the lowest possible magnetostatic energy of the demagnetisation field for ellipsoidal specimens, see [41], and the concept of the demagnetisation tensor is applicable, where the demagnetisation field $\widetilde{\boldsymbol{h}}$ depends directly on the magnetisation $\boldsymbol{m}$ and geometry dependent shape factors collected in the demagnetisation tensor $\boldsymbol{D}$, see, e.g., [115, 155], through

$$\widetilde{\boldsymbol{h}} = -\boldsymbol{D} \cdot \boldsymbol{m} \; . \tag{4.127}$$

This concept is also applicable for arbitrarily shaped bodies, which are homogeneously magnetised. In such a case, the average demagnetisation field $\langle \widetilde{\boldsymbol{h}} \rangle$ is related to the magnetisation by an average demagnetisation tensor $\langle \boldsymbol{D} \rangle$, cf. [65, 155]. The demagnetisation tensor $\boldsymbol{D}$ is either known for a given geometry or has to be calculated in advance in a magnetostatic finite element simulation.

**Remark 14** *The magnetisation* $\boldsymbol{m}$*, as introduced in (4.65) and occurring in (4.127), is assumed to be spatially homogeneously distributed inside the body on the considered macroscale and consequently identical to the body area-averaged magnetisation. Since it is an averaged, respectively homogenised, quantity, the distribution of the magnetisation might be inhomogeneous on the underlying microscale.*

Using (4.7) and (4.127), the integrals regarding the demagnetisation field $\widetilde{\boldsymbol{h}}$ in the energy potential (4.8) are replaced, cf. [41], by

$$-\frac{\mu_0}{2} \int\limits_{\Omega} \|\widetilde{\boldsymbol{h}}\|^2 \,\mathrm{d}v - \mu_0 \int\limits_{\mathcal{B}} \widetilde{\boldsymbol{h}} \cdot \boldsymbol{m} \,\mathrm{d}v = \frac{\mu_0}{2} \int\limits_{\mathcal{B}} \boldsymbol{m} \cdot \boldsymbol{D} \cdot \boldsymbol{m} \,\mathrm{d}v \; , \tag{4.128}$$

which depends, for a given demagnetisation tensor $\boldsymbol{D}$, only on the state variables $\boldsymbol{p}$, with $\boldsymbol{m}$ specified in (4.65), and no longer on the magnetostatic potential $\widetilde{\phi}$, respectively the demagnetisation field $\widetilde{\boldsymbol{h}}$. For homogeneous states, the energy potential (4.8) is reformulated using (4.123), (4.125), (4.126) and (4.128)

$$\Pi^{\mathrm{hom}} = \int\limits_{\mathcal{B}} \Big[ \psi^{\mathrm{mat}}(\overline{\boldsymbol{\sigma}}, \boldsymbol{p}) + \frac{\mu_0}{2} \boldsymbol{m}(\boldsymbol{p}) \cdot \boldsymbol{D} \cdot \boldsymbol{m}(\boldsymbol{p}) - \mu_0 \overline{\boldsymbol{h}} \cdot \boldsymbol{m}(\boldsymbol{p}) - \boldsymbol{\varepsilon}(\overline{\boldsymbol{\sigma}}, \boldsymbol{p}) : \overline{\boldsymbol{\sigma}} \Big] \,\mathrm{d}v \; , \tag{4.129}$$

with $\psi^{\mathrm{mat}}(\overline{\boldsymbol{\sigma}}, \boldsymbol{p}) = C\psi^{\mathrm{el}}(\overline{\boldsymbol{\sigma}}) + \psi^{\mathrm{an}}(\boldsymbol{p})$ defined in (4.64) and (4.125). Due to the assumption of homogeneous states inside $\mathcal{B}$, the volume integral (4.129) yields the volume of the body $V_{\mathcal{B}}$.

The magnetomechanical response is then modelled to be governed by the global rate-type variational principle, cf. (4.13) and (4.14),

$$\{\dot{\boldsymbol{p}}\} = \arg\inf_{\dot{\boldsymbol{p}}} \left[ \dot{\mathit{\Pi}}^{\text{hom}} + \int_{\mathcal{B}} \zeta(\dot{\boldsymbol{p}})\,\mathrm{d}v \right] \quad \text{subject to} \quad \boldsymbol{r}_{\text{c}}(\boldsymbol{p}) \le \boldsymbol{0}\;. \tag{4.130}$$

In analogy to the derivation of the time discrete evolution equations of the state variables $\boldsymbol{p}$ for the finite element implementation, see Section 4.2, the driving forces are derived as the negative gradient $-\partial_{\boldsymbol{p}}\mathit{\Pi}^{\,\text{hom}}$ in $\mathcal{B}$, viz.

$$\boldsymbol{\mathcal{F}}^{\,\text{hom}} := -\,\frac{\partial\left[\,\psi^{\text{mat}}(\overline{\boldsymbol{\sigma}},\boldsymbol{p}) + \dfrac{\mu_0}{2}\,\boldsymbol{m}(\boldsymbol{p})\cdot\boldsymbol{D}\cdot\boldsymbol{m}(\boldsymbol{p}) - \mu_0\,\overline{\boldsymbol{h}}\cdot\boldsymbol{m}(\boldsymbol{p}) - \boldsymbol{\varepsilon}(\overline{\boldsymbol{\sigma}},\boldsymbol{p}) : \overline{\boldsymbol{\sigma}}\,\right]}{\partial\boldsymbol{p}} \tag{4.131}$$

and thus

$$\boldsymbol{\mathcal{F}}^{\,\text{hom}} = \begin{bmatrix} \overline{\boldsymbol{\sigma}} : [\,\boldsymbol{\varepsilon}_1^{\text{tr}} - \boldsymbol{\varepsilon}_2^{\text{tr}}\,] + k_1\,[\,m_{21}^2 - m_{12}^2\,] + \mu_0\,m_s\,\boldsymbol{h}\cdot[\,\boldsymbol{m}_1^* - \boldsymbol{m}_2^*\,] \\ \mu_0\,m_s\,h_1\,\xi_1 \\ -2\,k_1\,\xi_1\,m_{12} + \mu_0\,m_s\,h_2\,\xi_1 \\ -2\,k_1\,\xi_2\,m_{21} + \mu_0\,m_s\,h_1\,\xi_2 \\ \mu_0\,m_s\,h_2\,\xi_2 \end{bmatrix}^{\text{t}} . \tag{4.132}$$

The driving forces in the homogeneous case (4.132) are in fact identical to the driving forces stated in (4.69), with $\boldsymbol{\sigma} = \overline{\boldsymbol{\sigma}}$. In analogy to the derivation in Section 4.2, the vector $\boldsymbol{r}^{\,\text{hom}}$ containing the residuals of the time discrete evolution equations for the homogeneous case may be derived and is defined as

$$\boldsymbol{r}^{\text{hom}} := \begin{bmatrix} \xi_1^{n+1} - \xi_1^n - \frac{\Delta t}{\eta_\xi}\,\text{sign}\left(\mathcal{F}_1^{\text{hom}^{n+1}}\right)\left\langle\left|\mathcal{F}_1^{\text{hom}^{n+1}}\right| - Y_\xi\right\rangle \\ m_{11}^{n+1} - m_{11}^n - \frac{\Delta t}{\eta_m}\,\mathcal{F}_2^{\text{hom}^{n+1}}/\xi_1 \\ m_{12}^{n+1} - m_{12}^n - \frac{\Delta t}{\eta_m}\,\mathcal{F}_3^{\text{hom}^{n+1}}/\xi_1 \\ m_{21}^{n+1} - m_{21}^n - \frac{\Delta t}{\eta_m}\,\mathcal{F}_4^{\text{hom}^{n+1}}/\xi_2 \\ m_{22}^{n+1} - m_{22}^n - \frac{\Delta t}{\eta_m}\,\mathcal{F}_5^{\text{hom}^{n+1}}/\xi_2 \end{bmatrix} . \tag{4.133}$$

The total residual of the homogeneous case contains the time discrete evolution equations (4.133), contributions due to the inequality constraints $\boldsymbol{r}_\text{c} \leq \boldsymbol{0}$ introduced in (4.60), cf. (4.82), and the Fischer-Burmeister functions, cf. (4.91), viz.

$$\boldsymbol{r}^\text{driver} = \begin{bmatrix} \boldsymbol{r}^\text{enh} \\ \boldsymbol{g} \end{bmatrix} = \begin{bmatrix} \boldsymbol{r}^\text{hom} + \boldsymbol{\lambda} \cdot \dfrac{\partial \boldsymbol{r}_\text{c}}{\partial \boldsymbol{p}} \\ \boldsymbol{g} \end{bmatrix} . \tag{4.134}$$

In this case, an enhanced driving force $\boldsymbol{r}^\text{enh}$ is formally introduced. Unlike in the finite element setting, where the nodal contributions account for the evolution due to contributions from all neighbouring elements, they are directly related to the time discrete evolution equations here. In combination with the Fischer-Burmeister functions $\boldsymbol{g}$, the additional terms prevent an inadmissible evolution of the state variables.

Unlike in previous works, where an optimiser was used to determine the evolution of the state variables, see [9, 10, 112, 114], the solution of the time discrete evolution equations satisfying the constraints of the state variables, viz. $\boldsymbol{r}^\text{driver} = \boldsymbol{0}$, is determined using the Newton-Raphson method. The constitutive driver routine including the Newton-Raphson uptate is outlined in Table 4.5. Some of the terms occurring in the Jacobian are different compared to the finite element setting, since all quantities depend on the state variables $\boldsymbol{p}$, see the appendix in Section 4.6.4.

**Remark 15** *Due to numerical reasons, again, slightly modified version of the constraints* $\boldsymbol{r}_\text{c}^*$ *introduced in (4.62) and the Fischer-Burmeister functions* $\boldsymbol{g}^*$ *introduced in (4.92) are used.*

**Table 4.5:** Constitutive driver routine.

0. *Initialisation:*

   Set load counter $n=0$, specify demagnetisation tensor $\boldsymbol{D}$, choose admissible initial configuration $\boldsymbol{p}_0$ satisfying the constraints and initialise the Lagrange multipliers $\boldsymbol{\lambda}_0=\boldsymbol{0}$.

1. *Load stepping:*

   Specify externally applied stress $\overline{\boldsymbol{\sigma}}_{n+1}$ and magnetic field $\overline{\boldsymbol{h}}_{n+1}$ loading, set iteration counter $k=0$, and set initial values for the state variables ${}^k\boldsymbol{p}_{n+1}=\boldsymbol{p}_n$ and Lagrange multipliers ${}^k\boldsymbol{\lambda}_{n+1}=\boldsymbol{\lambda}_n$.

2. *Residual vector:*

   Calculate the demagnetisation self field ${}^k\widetilde{\boldsymbol{h}}=-\boldsymbol{D}\cdot\boldsymbol{m}({}^k\boldsymbol{p}_{n+1})$, the total magnetic field ${}^k\boldsymbol{h}=\overline{\boldsymbol{h}}_{n+1}+{}^k\widetilde{\boldsymbol{h}}$ and the residual vector

$$
{}^k\boldsymbol{r}^{\text{driver}}=\begin{bmatrix}{}^k\boldsymbol{r}^{\text{enh}}({}^k\boldsymbol{p}_{n+1},{}^k\boldsymbol{\lambda}_{n+1})\\ {}^k\boldsymbol{g}({}^k\boldsymbol{p}_{n+1},{}^k\boldsymbol{\lambda}_{n+1})\end{bmatrix}=\begin{bmatrix}{}^k\boldsymbol{r}^{\text{hom}}({}^k\boldsymbol{p}_{n+1})+{}^k\boldsymbol{\lambda}_{n+1}\cdot\dfrac{\partial\boldsymbol{r}_{\text{c}}({}^k\boldsymbol{p}_{n+1})}{\partial{}^k\boldsymbol{p}_{n+1}}\\ {}^k\boldsymbol{g}({}^k\boldsymbol{p}_{n+1},{}^k\boldsymbol{\lambda}_{n+1})\end{bmatrix}
$$

3. *Newton update:*

   Check for convergence by calculating $\|{}^k\boldsymbol{r}^{\text{driver}}\|$:

   – if $\|{}^k\boldsymbol{r}^{\text{driver}}\|\leq\text{tol}$, with e.g. $\text{tol}=10^{-10}$, go to 4.

   – otherwise, calculate the Jacobian

$$
{}^k\boldsymbol{J}=\begin{bmatrix}\dfrac{\partial{}^k\boldsymbol{r}^{\text{enh}}({}^k\boldsymbol{p}_{n+1},{}^k\boldsymbol{\lambda}_{n+1})}{\partial{}^k\boldsymbol{p}_{n+1}} & \dfrac{\partial{}^k\boldsymbol{r}^{\text{enh}}({}^k\boldsymbol{p}_{n+1},{}^k\boldsymbol{\lambda}_{n+1})}{\partial{}^k\boldsymbol{\lambda}_{n+1}}\\ \dfrac{\partial{}^k\boldsymbol{g}({}^k\boldsymbol{p}_{n+1},{}^k\boldsymbol{\lambda}_{n+1})}{\partial{}^k\boldsymbol{p}_{n+1}} & \dfrac{\partial{}^k\boldsymbol{g}({}^k\boldsymbol{p}_{n+1},{}^k\boldsymbol{\lambda}_{n+1})}{\partial{}^k\boldsymbol{\lambda}_{n+1}}\end{bmatrix},
$$

   update the variables

$$
\begin{bmatrix}{}^{k+1}\boldsymbol{p}_{n+1}\\ {}^{k+1}\boldsymbol{\lambda}_{n+1}\end{bmatrix}=\begin{bmatrix}{}^{k}\boldsymbol{p}_{n+1}\\ {}^{k}\boldsymbol{\lambda}_{n+1}\end{bmatrix}-{}^k\boldsymbol{J}^{-1}\cdot{}^k\boldsymbol{r}^{\text{driver}},
$$

   set the iteration counter $k\Leftarrow k+1$ and return to 2.

4. *Postprocessing:*

   Calculate the strain $\boldsymbol{\varepsilon}_{n+1}$ (and magnetisation $\boldsymbol{m}_{n+1}$) of the current step as functions of ${}^k\boldsymbol{p}_{n+1}$. Save history data $\boldsymbol{p}_{n+1}={}^k\boldsymbol{p}_{n+1}$, set step counter $n\Leftarrow n+1$ and return to 1.

### 4.6.3 Shape functions

**Table 4.6:** Shape functions and the corresponding gradients of the eight-node incomplete quadratic serendipity and four-node bilinear element in the $\xi, \eta$-space, taken from [43], cf. Figure 4.4. Additionally, the degrees of freedom at the nodes in elements of the body $\mathcal{B}$ and the free space $\Omega \backslash \mathcal{B}$ are listed. The KKT-multipliers $\boldsymbol{\lambda}$ are not listed, since they are only resolved at $n_{\text{np}}^{\mathcal{B}\boldsymbol{p}}$ discrete nodes that belong to the body $\mathcal{B}$.

| Node $i$ | $\{N_i\}$ | $\{\partial N_i / \partial \xi\}$ | $\{\partial N_i / \partial \eta\}$ | Dof $\mathcal{B}$ | Dof $\Omega \backslash \mathcal{B}$ |
|---|---|---|---|---|---|
| 1 | $-0.25\,[1-\xi][1-\eta][1+\xi+\eta]$ | $0.25\,[1-\eta][2\,\xi+\eta]$ | $0.25\,[1-\xi][\xi+2\,\eta]$ | $\boldsymbol{u}, \widetilde{\phi}$ | $\widetilde{\phi}$ |
| 2 | $-0.25\,[1+\xi][1-\eta][1-\xi+\eta]$ | $0.25\,[1-\eta][2\,\xi-\eta]$ | $-0.25\,[1+\xi][\xi-2\,\eta]$ | $\boldsymbol{u}, \widetilde{\phi}$ | $\widetilde{\phi}$ |
| 3 | $-0.25\,[1+\xi][1+\eta][1-\xi-\eta]$ | $0.25\,[1+\eta][2\,\xi+\eta]$ | $0.25\,[1+\xi][\xi+2\,\eta]$ | $\boldsymbol{u}, \widetilde{\phi}$ | $\widetilde{\phi}$ |
| 4 | $-0.25\,[1-\xi][1+\eta][1+\xi-\eta]$ | $0.25\,[1+\eta][2\,\xi-\eta]$ | $-0.25\,[1-\xi][\xi-2\,\eta]$ | $\boldsymbol{u}, \widetilde{\phi}$ | $\widetilde{\phi}$ |
| 5 | $0.5\,[1-\xi^2][1-\eta]$ | $-[1-\eta]\xi$ | $-0.5\,[1-\xi^2]$ | $\boldsymbol{u}, \widetilde{\phi}$ | $\widetilde{\phi}$ |
| 6 | $0.5\,[1+\xi][1-\eta^2]$ | $0.5\,[1-\eta^2]$ | $-[1+\xi]\eta$ | $\boldsymbol{u}, \widetilde{\phi}$ | $\widetilde{\phi}$ |
| 7 | $0.5\,[1-\xi^2][1+\eta]$ | $-[1+\eta]\xi$ | $0.5\,[1-\xi^2]$ | $\boldsymbol{u}, \widetilde{\phi}$ | $\widetilde{\phi}$ |
| 8 | $0.5\,[1-\xi][1-\eta^2]$ | $-0.5\,[1-\eta^2]$ | $-[1-\xi]\eta$ | $\boldsymbol{u}, \widetilde{\phi}$ | $\widetilde{\phi}$ |
| 1 | $0.25\,[1-\xi][1-\eta]$ | $-0.25\,[1-\eta]$ | $-0.25\,[1-\xi]$ | $\boldsymbol{p}$ | – |
| 2 | $0.25\,[1+\xi][1-\eta]$ | $0.25\,[1-\eta]$ | $-0.25\,[1+\xi]$ | $\boldsymbol{p}$ | – |
| 3 | $0.25\,[1+\xi][1+\eta]$ | $0.25\,[1+\eta]$ | $0.25\,[1+\xi]$ | $\boldsymbol{p}$ | – |
| 4 | $0.25\,[1-\xi][1+\eta]$ | $-0.25\,[1+\eta]$ | $0.25\,[1-\xi]$ | $\boldsymbol{p}$ | – |

### 4.6.4 Stiffness matrix contributions

In the following representation, the brackets $\langle\!\langle \bullet \rangle\!\rangle$ marks entries that are only taken into account for $|\mathcal{F}_1|$ exceeding the corresponding threshold $Y_\xi$. The individual contributions of the stiffness matrices (4.100) – (4.106) introduced in Section 4.3 for the constitutive model introduced in Section 4.2 are specified as follows:

– of $\boldsymbol{K}^{AB}_{\boldsymbol{uu}}$ in (4.100)

$$\frac{\partial \boldsymbol{\sigma}}{\partial \boldsymbol{\varepsilon}} = \mathsf{E} \, , \tag{4.135}$$

– the non-zero contributions of $\boldsymbol{K}^{AF}_{\boldsymbol{up}}$ in (4.101)

$$\frac{\partial \boldsymbol{\sigma}}{\partial \xi_1} = \mathsf{E} : [\, \boldsymbol{\varepsilon}^{\mathrm{tr}}_2 - \boldsymbol{\varepsilon}^{\mathrm{tr}}_1 \,] \, , \tag{4.136}$$

– of $\boldsymbol{K}^{CF}_{\widetilde{\phi}\boldsymbol{p}}$ in (4.103)

$$\frac{\partial \boldsymbol{m}}{\partial \boldsymbol{p}} = m_s \begin{bmatrix} [\, m_{11} - m_{21} \,] & \xi_1 & 0 & \xi_2 & 0 \\ [\, m_{12} - m_{22} \,] & 0 & \xi_1 & 0 & \xi_2 \end{bmatrix} , \tag{4.137}$$

– the non-zero contributions of $\boldsymbol{K}^{EB}_{\boldsymbol{pu}}$ in (4.104)

$$\frac{\partial r^{\mathrm{evo}}_1}{\partial \boldsymbol{\varepsilon}} = \left\langle\!\!\left\langle \frac{\Delta\, t}{\eta_\xi} [\, \boldsymbol{\varepsilon}^{\mathrm{tr}}_2 - \boldsymbol{\varepsilon}^{\mathrm{tr}}_1 \,] : \mathsf{E} \right\rangle\!\!\right\rangle \, , \tag{4.138}$$

– of $\boldsymbol{K}^{ED}_{\boldsymbol{p}\widetilde{\phi}}$ in (4.105)

$$\frac{\partial \boldsymbol{r}^{\mathrm{evo}}}{\partial \widetilde{\boldsymbol{h}}} = \mu_0 \, m_s \begin{bmatrix} \left\langle\!\!\left\langle \frac{\Delta\, t}{\eta_\xi} [\, m_{11} - m_{21} \,] \right\rangle\!\!\right\rangle & \left\langle\!\!\left\langle \frac{\Delta\, t}{\eta_\xi} [\, m_{12} - m_{22} \,] \right\rangle\!\!\right\rangle \\ \frac{\Delta\, t}{\eta_m} & 0 \\ 0 & \frac{\Delta\, t}{\eta_m} \\ \frac{\Delta\, t}{\eta_m} & 0 \\ 0 & \frac{\Delta\, t}{\eta_m} \end{bmatrix} , \tag{4.139}$$

– of $\boldsymbol{K}^{EF}_{\boldsymbol{pp}}$ in (4.106)

$$\frac{\partial \boldsymbol{r}^{\text{evo}}}{\partial \boldsymbol{p}} = \begin{bmatrix} 1 & 0 & 0 & 0 & 0 \\ 0 & 1 & 0 & 0 & 0 \\ 0 & 0 & 1 & 0 & 0 \\ 0 & 0 & 0 & 1 & 0 \\ 0 & 0 & 0 & 0 & 1 \end{bmatrix} - \begin{bmatrix} \left\langle\!\!\left\langle \frac{\Delta\, t}{\eta_\xi} \frac{\partial \mathcal{F}_1}{\partial \boldsymbol{p}} \right\rangle\!\!\right\rangle \\ \boldsymbol{0} \\ \frac{\Delta\, t}{\eta_m} \frac{\partial \mathcal{F}_3/\xi_1}{\partial \boldsymbol{p}} \\ \frac{\Delta\, t}{\eta_m} \frac{\partial \mathcal{F}_4/\xi_2}{\partial \boldsymbol{p}} \\ \boldsymbol{0} \end{bmatrix} , \tag{4.140}$$

with

$$-\frac{\partial \mathcal{F}_1}{\partial \boldsymbol{p}} = \begin{bmatrix} [\,\boldsymbol{\varepsilon}^{\text{tr}}_2 - \boldsymbol{\varepsilon}^{\text{tr}}_1\,] : \boldsymbol{E} : [\,\boldsymbol{\varepsilon}^{\text{tr}}_2 - \boldsymbol{\varepsilon}^{\text{tr}}_1\,] \\ -\,\mu_0\, m_s\, h_1 \\ 2\, k_1\, m_{12} - \mu_0\, m_s\, h_2 \\ -2\, k_1\, m_{21} + \mu_0\, m_s\, h_1 \\ \mu_0\, m_s\, h_2 \end{bmatrix}^{\text{t}} ,$$

$$-\frac{\partial \mathcal{F}_3/\xi_1}{\partial \boldsymbol{p}} = \begin{bmatrix} 0 & 0 & 2\, k_1 & 0 & 0 \end{bmatrix} , \quad -\frac{\partial \mathcal{F}_4/\xi_2}{\partial \boldsymbol{p}} = \begin{bmatrix} 0 & 0 & 0 & 2\, k_1 & 0 \end{bmatrix} . \tag{4.141}$$

The dimensions of the stiffness matrices due to the contributions of the constraints at node G, see (4.107) – (4.110), are

$$\boldsymbol{K}^{GG}_{\boldsymbol{pp}} \in \mathbb{R}^{5\times 5} , \quad \boldsymbol{K}^{GG}_{\boldsymbol{p\lambda}} \in \mathbb{R}^{5\times 4} , \quad \boldsymbol{K}^{GG}_{\boldsymbol{\lambda p}} \in \mathbb{R}^{4\times 5} , \quad \boldsymbol{K}^{GG}_{\boldsymbol{\lambda\lambda}} \in \mathbb{R}^{4\times 4} . \tag{4.142}$$

The non-zero terms of (4.142) for the parametrisation and the corresponding constraints introduced in Section 4.2 are

$$\boldsymbol{K}^{GG}_{\boldsymbol{pp}}(2:3, 2:3) = \lambda^G_3 \left[ \frac{\boldsymbol{I}^{2\times 2}}{\|\boldsymbol{m}^*_1\|} - \frac{\boldsymbol{m}^*_1 \otimes \boldsymbol{m}^*_1}{[\,\boldsymbol{m}^*_1 \cdot \boldsymbol{m}^*_1\,]^{\frac{3}{2}}} \right] ,$$

$$\boldsymbol{K}^{GG}_{\boldsymbol{pp}}(4:5, 4:5) = \lambda^G_4 \left[ \frac{\boldsymbol{I}^{2\times 2}}{\|\boldsymbol{m}^*_2\|} - \frac{\boldsymbol{m}^*_2 \otimes \boldsymbol{m}^*_2}{[\,\boldsymbol{m}^*_2 \cdot \boldsymbol{m}^*_2\,]^{\frac{3}{2}}} \right] ,$$

$$\boldsymbol{K}^{GG}_{\boldsymbol{p\lambda}}(1,1) = -1 , \quad \boldsymbol{K}^{GG}_{\boldsymbol{p\lambda}}(1,2) = 1 ,$$

$$\boldsymbol{K}^{GG}_{\boldsymbol{p\lambda}}(2:3,3) = \frac{\boldsymbol{m}^*_1}{\|\boldsymbol{m}^*_1\|} , \quad \boldsymbol{K}^{GG}_{\boldsymbol{p\lambda}}(4:5,4) = \frac{\boldsymbol{m}^*_2}{\|\boldsymbol{m}^*_2\|} ,$$

$$
\begin{aligned}
\boldsymbol{K}^{GG}_{\boldsymbol{\lambda p}}(1,1) &= \frac{-\,r_1}{\sqrt{{r_1}^2+\lambda_1^{G2}}}-1\;, \quad \boldsymbol{K}^{GG}_{\boldsymbol{\lambda p}}(2,1) = \frac{r_2}{\sqrt{{r_2}^2+\lambda_2^{G2}}}+1\;,\\
\boldsymbol{K}^{GG}_{\boldsymbol{\lambda p}}(3,2:3) &= \frac{\boldsymbol{m}_1^{*\mathrm{t}}}{\|\boldsymbol{m}_1^*\|}\left[\frac{r_3}{\sqrt{{r_3}^2+\lambda_3^{G2}}}+1\right]\;,\\
\boldsymbol{K}^{GG}_{\boldsymbol{\lambda p}}(4,4:5) &= \frac{\boldsymbol{m}_2^{*\mathrm{t}}}{\|\boldsymbol{m}_2^*\|}\left[\frac{r_4}{\sqrt{{r_4}^2+\lambda_4^{G2}}}+1\right]\;,\\
\boldsymbol{K}^{GG}_{\boldsymbol{\lambda\lambda}}(i,i) &= \frac{\lambda_i^E}{\sqrt{{r_i}^2+\lambda_i^{G2}}}-1 \quad \text{with} \quad i=1,\dots,4\;.
\end{aligned} \tag{4.143}
$$

With (4.68) and (4.141) at hand, the contribution of the evolution equations to the Jacobian matrix in the constitutive driver routine, as outlined in the appendix in Section 4.6.2, is

$$
\frac{\partial \boldsymbol{r}^{\mathrm{hom}}}{\partial \boldsymbol{p}} = \begin{bmatrix} 1 & 0 & 0 & 0 & 0\\ 0 & 1 & 0 & 0 & 0\\ 0 & 0 & 1 & 0 & 0\\ 0 & 0 & 0 & 1 & 0\\ 0 & 0 & 0 & 0 & 1 \end{bmatrix} - \begin{bmatrix} \left\langle\!\!\left\langle \frac{\Delta t}{\eta_\xi}\frac{\partial \mathcal{F}_1^{\mathrm{hom}}}{\partial \boldsymbol{p}} \right\rangle\!\!\right\rangle \\ -\frac{\Delta t}{\eta_m}\,\mu_0\, m_s^2\, \boldsymbol{e}_1\cdot\boldsymbol{D}\cdot\frac{\partial \boldsymbol{m}^*}{\partial \boldsymbol{p}} \\ \frac{\Delta t}{\eta_m}\left[\frac{\partial \mathcal{F}_3/\xi_1}{\partial \boldsymbol{p}} - \mu_0\, m_s^2\, \boldsymbol{e}_2\cdot\boldsymbol{D}\cdot\frac{\partial \boldsymbol{m}^*}{\partial \boldsymbol{p}}\right] \\ \frac{\Delta t}{\eta_m}\left[\frac{\partial \mathcal{F}_4/\xi_2}{\partial \boldsymbol{p}} - \mu_0\, m_s^2\, \boldsymbol{e}_1\cdot\boldsymbol{D}\cdot\frac{\partial \boldsymbol{m}^*}{\partial \boldsymbol{p}}\right] \\ -\frac{\Delta t}{\eta_m}\,\mu_0\, m_s^2\, \boldsymbol{e}_2\cdot\boldsymbol{D}\cdot\frac{\partial \boldsymbol{m}^*}{\partial \boldsymbol{p}} \end{bmatrix}\;, \tag{4.144}
$$

wherein

$$
-\frac{\partial \mathcal{F}_1^{\mathrm{hom}}}{\partial \boldsymbol{p}} = \begin{bmatrix} 0 \\ -\mu_0\, m_s\, h_1 \\ 2\,k_1\, m_{12} - \mu_0\, m_s\, h_2 \\ -2\,k_1\, m_{21} + \mu_0\, m_s\, h_1 \\ \mu_0\, m_s\, h_2 \end{bmatrix}^{\mathrm{t}} + \mu_0\, m_s^2\,[\,\boldsymbol{m}_1^* - \boldsymbol{m}_2^*\,]\cdot\boldsymbol{D}\cdot\frac{\partial \boldsymbol{m}^*}{\partial \boldsymbol{p}}\;. \tag{4.145}
$$

# 5 Concluding remarks

The thesis dealt with the modelling and simulation of the microstructure evolution in functional magnetic materials under magnetomechanical loading conditions, in particular in single crystalline $Ni_2MnGa$ magnetic shape memory alloys. The objective was the development of suitable material models to capture and simulate the nonlinear, hysteretic, and stress-level dependent response of such materials and the embedding of these kinds of material models into a finite element framework. For the latter, one of the main challenges was the incorporation of the influence of the demagnetisation field that builds up as magnetisable specimens are subjected to externally applied magnetic fields. The demagnetisation field typically lowers the total magnetic field that is "visible" inside magnetisable specimens. Furthermore, since it is a non-local quantity, it heavily influences the evolution of the microstructure at every material point. Moreover, the demagnetisation effect depends on the shape of a specimen, such that simulated and experimentally determined response curves, when visualised as functions of the externally applied magnetic fields, e.g. strain and magnetisation responses, always show a structural response. In the following, the individual chapters are briefly summarised. An outlook on possible future research activities is given at the end of the chapter.

In Chapter 2, a material model for the simulation of $Ni_2MnGa$ MSMAs under magnetomechanical loading conditions was suggested. The chapter began by introducing the global primary fields and the micromagnetics-inspired variational framework, both being the basis for this and the two forthcoming chapters. The assumption of macroscopically homogeneous states allowed the reduction to a constrained minimisation problem to determine the evolution of the microstructure-describing state variables. The underlying microstructure, assumed to consist of two variants of twinned martensite with internal domains, was parametrised by a set of state variables. In addition, the stored energy densities of the individual martensite variants and the magnetocrystalline anisotropy energy densities were introduced. The effective or homogenised energy densities followed through appropriate mixture rules and energy relaxation concepts. Furthermore, a suitable dissipation potential was introduced. The shape dependency of the system response was captured by utilising the concept of demagnetisation factors. Several numerical examples demonstrated the prediction capabilities of the proposed model. To be precise, variant switching diagrams were introduced to visualise critical points during the martensite reorientation under magnetomechanial loading conditions. A closer look at strain and magnetisation response curves revealed that the model generally captures all key characteristics of the complex response behaviour of $Ni_2MnGa$. The effective response behaviour was connected to the predicted evolution of the microstructure. This analysis revealed that the model allows the individual and simultaneous occurrence of all mechanisms central to MSMA behaviour.

Chapter 3 was the first step taken in the implementation of energy relaxation-based material models into a finite element framework to simulate the material and structural behaviour of MSMA specimens. Inequality constraints that bound the state variables were directly taken into account in the variational framework. The dependency on the displacement field dropped out by assuming homogeneous stress and strain distributions. The first variation of a power-type potential served as a basis for the finite element implementation. By neglecting elastic strains, the microstructure consisting of two martensite variants with internal magnetic domains was parametrised, the magnetocrystalline anisotropy energy density as well as a dissipation function were specified, and the evolution equations were derived. A newly introduced mixed element formulation allows the monolithic solution of the magnetostatic boundary value problem and the evolution equations for the state variables, that are discretised as global degrees of freedom in this approach. The fulfilment of the Karush-Kuhn-Tucker conditions that arise due to the constraints was accomplished by nonlinear Fischer-Burmeister complementarity functions together with the introduction of the associated Lagrange-multipliers as additional nodal degrees of freedom. The finite element implementation was validated in comparison to simulations that utilised demagnetisation factors. Other simulations demonstrated the advantages of finite element simulations, in particular by comparing effective body-averaged response curves to experimental findings.

In Chapter 4, the ideas presented in Chapter 3 were extended by additionally incorporating the displacement field as a global degree of freedom. The focus lay on the monolithic solution of the fully coupled magnetomechanical boundary value problem and the evolution equations for the microstructure-describing state variables. Again, the first variation of a power-type potential served as the basis for the finite element implementation. The constitutive model was discussed in more detail. In particular, elastic strains were considered and multiple parametrisations of the underlying microstructure were introduced and connected. Energy relaxation concepts were applied to determine an effective energy density of the mixture of the martensite variants. In this chapter, the evolutions of all state variables—including those describing the magnetic state—were considered to be rate-dependent and dissipative. The previously introduced mixed element formulation was extended by additionally taking the displacement field into account. The constraints were treated in analogy to the previous chapter. Several numerical examples demonstrated the capabilities of the fully coupled finite element simulations in comparison to experimental findings and simulations that utilised demagnetisation factors. To be precise, body-averaged response curves, spatial distributions of various quantities, and the evolution of the underlying body-averaged microstructure were analysed and discussed for multiple load cases.

For the proposed energy relaxation-based material models, one possible next step would be the extension to three-dimensional problems to allow a comparison of experimental data with simulated response curves of the correct specimen geometry. This would necessitate a new parametrisation of the underlying microstructure in terms of martensite interface normals—only in the case of a Rank-one convexification approach—and the magnetic state. One may also consider taking the third tetragonal martensite variant into account. Instead of isotropic elastic properties, one could use elasticity tensors for tetragonal symmetry. This would require an experimental determination of the corresponding six material parameters. Other numerical energy relaxation schemes may be applied, e.g. higher order laminates or the consideration of magnetic compatibility. Another possibility would be the application of the general framework to the modelling of seven-layered 7M modulated nearly orthorombic martensite in $Ni_2MnGa$ or to other MSMAs. Furthermore, the framework might be applied to the modelling of (giant) magnetostrictive materials, for instance Terfenol-D, Galfenol, and cobalt ferrite, where the effect of magnetostriction would have to be taken directly into account. One possibility to reduce the numerical effort on the finite element level would be the introduction of effective magnetisation vectors, whose lengths are limited by a specific value, e.g. the saturation magnetisation, as global degree of freedom, cf. the micromagnetic theory, where the spontaneous magnetisation with constant length is one global degree of freedom. In such a case, the number of inequality constraints reduces to one. The magnetisation on the finite element level would then be connected to the local magnetisation at the material point level by, e.g., a penalty type approach, such as suggested by [113], where a global damage variable was connected to a local damage variable. In addition to the advantage of a reduced numerical effort on the finite element level, this approach would allow the use of basically arbitrary material models at the material point level.

# Bibliography

[1] URL `https://www.uni-due.de/ferroics/home`.

[2] URL `http://www.etrema.com/`.

[3] F. Albertini, L. Pareti, A. Paoluzi, L. Morellon, P. A. Algarabel, M. R. Ibarra, and L. Righi. Composition and temperature dependence of the magnetocrystalline anisotropy in $\mathrm{Ni}_{2+x}\mathrm{Mn}_{1+y}\mathrm{Ga}_{1+z}$ $(x + y + z = 0)$ Heusler alloys. *Applied Physics Letters*, 81(21):4032–4034, 2002. doi:10.1063/1.1525071.

[4] F. Albertini, F. Canepa, S. Cirafici, E. A. Franceschi, M. Napoletano, A. Paoluzi, L. Pareti, and M. Solzi. Composition dependence of magnetic and magnetothermal properties of Ni–Mn–Ga shape memory alloys. *Journal of Magnetism and Magnetic Materials*, 272–276(3):2111–2112, 2004. doi:10.1016/j.jmmm.2003.12.883.

[5] F. Auricchio, A.-L. Bessoud, A. Reali, and U. Stefanelli. A three-dimensional phenomenological model for magnetic shape memory alloys. *GAMM-Mitteilungen*, 34:90–96, 2011. doi:10.1002/gamm.201110014.

[6] T. Bartel. *Multiskalenmodellierung martensitischer Phasentransformationen in Formgedachtnislegierungen unter Verwendung relaxierter Energiepotenziale*. PhD thesis, Ruhr-University Bochum, 2009.

[7] T. Bartel and K. Hackl. A micromechanical model for martensitic phase-transformations in shape-memory alloys based on energy-relaxation. *Zeitschrift für Angewandte Mathematik und Mechanik*, 89:792–809, 2009. doi:10.1002/zamm.200900244.

[8] T. Bartel and A. Menzel. Modelling and simulation of cyclic thermomechanical behaviour of NiTi wires using a weak discontinuity approach. *International Journal of Fracture*, 202:281–293, 2016. doi:10.1007/s10704-016-0169-8.

[9] T. Bartel, B. Kiefer, K. Buckmann, and A. Menzel. A kinematically-enhanced relaxation scheme for the modeling of displacive phase transformations. *Journal of Intelligent Material Systems and Structures*, 26(6):701–717, 2015. doi:10.1177/1045389X14557507.

[10] T. Bartel, B. Kiefer, K. Buckmann, and A. Menzel. An energy-relaxation-based framework for the modelling of magnetic shape memory alloys — simulation of key response features under homogeneous loading conditions. *submitted for publication*, 2018.

[11] A. Bartels and J. Mosler. Efficient variational constitutive updates for Allen-Cahn-type phase field theory coupled to continuum mechanics. *Computer Methods in Applied Mechanics and Engineering*, 317:55–83, 2017. doi:10.1016/j.cma.2016.11.024.

[12] S. Bartels, C. Carstensen, K. Hackl, and U. Hoppe. Effective relaxation for microstructure simulations: Algorithms and applications. *Computational Mathematics and Engineering*, 193:5143–5175, 2004. doi:10.1016/j.cma.2003.12.065.

[13] D. P. Bertsekas. *Nonlinear Programming.* Athena Scientific, Belmont, MA, 2nd edition, 1999.

[14] A.-L. Bessoud and U. Stefanelli. Magnetic shape memory alloys: three-dimensional modeling and analysis. *Mathematical Models and Methods in Applied Sciences*, 21: 1043–1069, 2011. doi:10.1142/S0218202511005246.

[15] K. Bhattacharya. *Microstructure of Martensite — Why it Forms and How it Gives Rise to the Shape-memory Effect.* Oxford University Press, New York, 2003.

[16] A. Bhattacharyya, Y. Lagoudas, D. C. Wang, and V. K. Kinra. On the role of thermoelectric heat transfer in the design of sma actuators: theoretical modeling and experiment. *Smart Materials and Structures*, 4(4):252–263, 1995. doi:10.1088/0964-1726/4/4/005.

[17] M. A. Biot. *Mechanics of Incremental Deformations.* John Wiley & Sons, New York, 1965.

[18] W. F. Brown, Jr. *Micromagnetics*, volume 18 of *Interscience Tracts on Physics and Astronomy.* John Wiley & Sons, New York, 1963.

[19] W. F. Brown, Jr. *Magnetoelastic Interactions*, volume 9 of *Tracts in Natural Philosophy.* Springer-Verlag, New York, 1966.

[20] V. D. Buchelnikov and S. I. Bosko. The kinetics of phase transformations in ferromagnetic shape memory alloys Ni–Mn–Ga. *Journal of Magnetism and Magnetic Materials*, 258–259:497–499, 2003. doi:10.1016/S0304-8853(02)01070-3.

[21] K. Buckmann, B. Kiefer, T. Bartel, and A. Menzel. Simulation of magnetised microstructure evolution based on a micromagnetics-inspired FE framework: application to magnetic shape memory behaviour. *Archive of Applied Mechanics*, 2018. doi:10.1007/s00419-018-1482-7.

[22] W. J. Buehler, J. V. Gilfrich, and R. C. Wiley. Effect of low-temperature phase changes on the mechanical properties of alloys near composition tini. *Journal of Applied Physics*, 34(5):1475–1477, 1963. doi:10.1063/1.1729603.

[23] M. Canadija and J. Mosler. On the thermomechanical coupling in finite strain plasticity theory with non-linear kinematic hardening by means of incremental energy minimization. *International Journal of Solids and Structures*, 48:1120–1129, 2011. doi:10.1016/j.ijsolstr.2010.12.018.

[24] L. C. Chang and T. A. Read. Plastic deformation and diffusionless phase changes in metals — the gold-cadmium beta phase. *The Journal of The Minerals, Metals & Materials Society (TMS)*, 3(1):47–52, 1951. doi:10.1007/BF03398954.

[25] X. Chen. *Magneto-mechanical behaviors of ferromagnetic shape memory alloys.* Ph.D. dissertation, École Polytechnique Paris Tech, June 2013.

[26] X. Chen, Y. He, and Z. Moumni. Twin boundary motion in NiMnGa single crystals under biaxial compression. *Materials Letters*, 90:72–75, 2013. doi:10.1016/j.matlet.2012.08.107.

[27] X. Chen, Z. Moumni, Y. He, and W. Zhang. A three-dimensional model of magneto-mechanical behaviors of martensite reorientation in ferromagnetic shape memory alloys. *Journal of the Mechanics and Physics of Solids*, 64:249–286, 2014. doi:10.1016/j.jmps.2013.11.005.

[28] A. A. Cherechukin, I. E. Dikshtein, D. I. Ermakov, A. V. Glebov, V. V. Koledov, D. A. Kosolapov, V. G. Shavrov, A. A. Tulaikova, E. P. Krasnoperov, and T. Takagi. Shape memory effect due to magnetic field-induced thermoelastic martensitic transformation in polycrystalline Ni–Mn–Fe–Ga alloy. *Physics Letters A*, 291(2–3): 175–183, 2001. doi:10.1016/S0375-9601(01)00688-0.

[29] V. A. Chernenko, V. V. Kokorin, O. M. Babii, and I. K. Zasimchuk. Phase diagrams in the Ni–Mn–Ga system under compression. *Intermetallics*, 6(1):29–34, 1998. doi:10.1016/S0966-9795(97)00050-2.

[30] V. A. Chernenko, V. A. L'vov, P. Müllner, G. Kostorz, and T. Takagi. Magnetic-field-induced superelasticity of ferromagnetic thermoelastic martensites: experiment and modeling. *Physical Review B*, 134410(13):1–8, 2004. doi:10.1103/PhysRevB.69.134410.

[31] S. Chikazumi. *Physics of Ferromagnetism.* Clarendon Press, Oxford, 1997.

[32] R. Chulist, A. Böhm, T. Lippmann, W. Skrotzki, W.-G. Drossel, and R. Neugebauer. Twinning behaviour of textured polycrystalline Ni-Mn-Ga alloy after hot extrusion. *Materials Science Forum*, 635:195–199, 2010. doi:10.4028/www.scientific.net/MSF.635.195.

[33] A. E. Clark and H. S. Belson. Giant room-temperature magnetostrictions in $TbFe_2$ and $DyFe_2$. *Physical Review B*, 5(9):3642–3644, 1972. doi:10.1103/PhysRevB.5.3642.

[34] N. Creton and L. Hirsinger. Rearrangement surfaces under magnetic field and/or stress in Ni–Mn–Ga. *Journal of Magnetism and Magnetic Materials*, 290–291(2): 832–835, 2015. doi:10.1016/j.jmmm.2004.11.376.

[35] J. Cui, T. W. Shield, and R. D. James. Phase transformation and magnetic anisotropy of an iron-palladium ferromagnetic shape-memory alloy. *Acta Materialia*, 52(1):35–47, 2004. doi:10.1016/j.actamat.2003.08.024.

[36] B. D. Cullity. *Introduction to Magnetic Materials.* Addison-Wesley, Reading, MA, 1972.

[37] M. J. Dapino, R. C. Smith, L. E. Faidley, and A. B. Flatau. A coupled structural-magnetic strain and stress model for magnetostrictive transducers. *Journal of Intelligent Material Systems and Structures*, 11(2):135–152, 2000. doi:10.1106/MJ6A-FBP9-9M61-0E1F.

[38] A. DeSimone. Energy minimizers for large ferromagnetic bodies. *Archive for Rational Mechanics and Analysis*, 125:99–143, 1993. doi:10.1007/BF00376811.

[39] A. DeSimone. Coarse-grained models of materials with non-convex free-energy: Two case studies. *Computer Methods in Applied Mechanics and Engineering*, 193 (48–51):5129–5141, 2004. doi:10.1016/j.cma.2003.12.064.

[40] A. DeSimone and G. Dolzmann. Material instabilities in nematic elastomers. *Physica D*, 136(1–2):175–191, 2000. doi:10.1016/S0167-2789(99)00153-0.

[41] A. DeSimone and R. D. James. A constrained theory of magnetoelasticity. *Journal of the Mechanics and Physics of Solids*, 50(2):283–320, 2002. doi:10.1016/S0022-5096(01)00050-3.

[42] A. DeSimone, R. V. Kohn, S. Müller, and F. Otto. *Recent analytical developments in micromagnetics.* Elsevier, 2006.

[43] G. Dhatt, G. Touzot, and E. Lefrançois. *Finite element method.* Wiley, 2012.

[44] D. K. Dusthakar. *Computational modelling of single and polycrystalline ferroelectric materials.* PhD thesis, TU Dortmund, 2017.

[45] D. K. Dusthakar, A. Menzel, and B. Svendsen. Laminate-based modelling of single and polycrystalline ferroelectric materials - application to tetragonal barium titanate. *Mechanics of Materials*, 117:235–254, 2018. doi:10.1016/j.mechmat.2017.10.005.

[46] D. G. B. Edelen. On the existence of symmetry relations and dissipation potentials. *Archive for Rational Mechanics and Analysis*, 51:218–227, 1973. doi:10.1007/BF00276075.

[47] G. Engdahl, editor. *Handbook of Giant Magnetostrictive Materials.* Academic Press, San Diego, 2000.

[48] G. Ethiraj. *Computational Modeling of Ferromagnetics and Magnetorheological Elastomers.* PhD thesis, University of Stuttgart, 2014.

[49] G. Ethiraj and C. Miehe. Multiplicative magneto-elasticity of magnetosensitive polymers incorporating micromechanically-based network kernels. *International Journal of Engineering Science*, 102:93–119, 2016. doi:10.1016/j.ijengsci.2015.08.007.

[50] L. E. Faidley, M. J. Dapino, G. N. Washington, and T. A. Lograsso. Reversible strain in Ni–Mn–Ga with collinear field and stress. *Smart Structures and Materials*,

5761:501–512, 2005. doi:10.1117/12.600210.

[51] A. Fischer. A special newton-type optimization method. *Optimization*, 24:269–284, 1992. doi:10.1080/02331939208843795.

[52] A. Fujita, K. Fukamichi, F. Gejima, R. Kainuma, and K. Ishida. Magnetic properties and large magnetic-field-induced strains in off-stoichiometric Ni–Mn–Al Heusler alloys. *Applied Physics Letters*, 77(19):3054–3056, 2000. doi:10.1063/1.1323552.

[53] U. Gaitzsch, M. Pötschke, S. Roth, B. Rellinghaus, and L. Schultz. Mechanical training of polycrystalline 7 M $Ni_{50}Mn_{30}Ga_{20}$ magnetic shape memory alloy. *Scripta Materialia*, 57(6):493–495, 2007. doi:10.1016/j.scriptamat.2007.05.026.

[54] U. Gaitzsch, M. Pötschke, S. Roth, B. Rellinghaus, and L. Schultz. A 1% magnetostrain in polycrystalline 5M Ni–Mn–Ga. *Acta Materialia*, 57(2):365–370, 2009. doi:10.1016/j.actamat.2008.09.017.

[55] K. Gall and H. J. Maier. Cyclic deformation mechanisms in precipitated NiTi shape memory alloys. *Acta Materialia*, 50:4643–4657, 2002. doi:10.1016/S1359-6454(02)00315-4.

[56] Y. Ganor, D. Shilo, T. W. Shield, and R. D. James. Breaching the work output of ferromagnetic shape memory alloys. *Applied Physics Letters*, 93:122509–1–3, 2008. doi:10.1063/1.2982916.

[57] E. Gans, C. Henry, and G. P. Carman. Reduction in required magnetic field to induce twin-boundary motion in ferromagnetic shape memory alloys. *Journal of Applied Physics*, 95(11):6965–6967, 2004. doi:10.1063/1.1687292.

[58] J.-Y. Gauthier, A. Hubert, J. Abadie, C. Lexcellent, and N. Chaillet. Multistable actuator based on magnetic shape memory alloy. *Proceedings of the 10th International Conference on New Actuators*, 1:787–790, 2006.

[59] J.-Y. Gauthier, C. Lexcellent, A. Hubert, J. Abadie, and N. Chaillet. Modeling rearrangement process of martensite platelets in a magnetic shape memory alloy $Ni_2MnGa$ single crystal under magnetic field and (or) stress action. *Journal of Intelligent Material Systems and Structures*, 18(3):289–299, 2007. doi:10.1177/1045389X06066094.

[60] Y. Ge, O. Heczko, O. Söderberg, and V. K. Lindroos. Various magnetic domain structures in a Ni–Mn–Ga martensite exhibiting magnetic shape memory effect. *Journal of Applied Physics*, 96(4):2159–2163, 2004. doi:10.1063/1.1773381.

[61] N. I. Glavatska, A. A. Rudenko, I. N. Glavatskiy, and V. A. L'vov. Statistical model of magnetostrain effect in martensite. *Journal of Magnetism and Magnetic Materials*, 265(2):142–151, 2003. doi:10.1016/S0304-8853(03)00242-7.

[62] G. Gottstein, editor. *Physikalische Grundlagen der Materialkunde*. Springer, 2007.

[63] K. Haldar. *Magneto-thermo-mechanical coupling, stability analysis and phenomenological constitutive modeling of magnetic shape memory alloys.* Ph.D. dissertation, Texas A&M University, December 2012.

[64] K. Haldar, G. Chatzigeorgiou, and D. C. Lagoudas. Stability analysis of magnetostatic boundary value problems for magnetic SMAs. *Journal of Intelligent Material Systems and Structures*, 21(11):1103–1116, 2010. doi:10.1177/1045389X10375486.

[65] K. Haldar, B. Kiefer, and D. C. Lagoudas. Finite element analysis of the demagnetization effect and stress inhomogeneities in magnetic shape memory alloy samples. *Philosophical Magazine*, 91(32):4126–4157, 2011. doi:10.1080/14786435.2011.602031.

[66] B. Halphen and Q. S. Nguyen. Sur les matériaux standards généralisés. *Journal de Méchanique*, 14:39–63, 1975.

[67] R. F. Hamilton, C. Efstathiou, H. Sehitoglu, and Y. Chumlyakov. Thermal and stress-induced martensitic transformations in NiFeGa single crystals under tension and compression. *Scripta Materialia*, 54(3):465–469, 2006. doi:10.1016/j.scriptamat.2005.10.003.

[68] D. J. Hartl and D. C. Lagoudas. Aerospace applications of shape memory alloys. *Proceedings of the Institution of Mechanical Engineers*, 221:535–552, 2007. doi:10.1243/09544100JAERO211.

[69] Y. J. He, X. Chen, and Z. Moumni. Two-dimensional analysis to improve the output stress in ferromagnetic shape memory alloys. *Journal of Applied Physics*, 110:063905, 2011. doi:10.1063/1.3636366.

[70] Y. J. He, X. Chen, and Z. Moumni. Reversible-strain criteria of ferromagnetic shape memory alloys under cyclic 3D magneto-mechanical loadings. *Journal of Applied Physics*, 112(3):033902–1–11, 2012. doi:10.1063/1.4739711.

[71] O. Heczko. Magnetic shape memory effect and magnetization reversal. *Journal of Magnetism and Magnetic Materials*, 290–291(2):787–794, 2005. doi:10.1016/j.jmmm.2004.11.397.

[72] O. Heczko and L. Straka. Compositional dependence of structure, magnetization and magnetic anisotropy in Ni–Mn–Ga magnetic shape memory alloys. *Journal of Magnetism and Magnetic Materials*, 272–276(3):2045–2046, 2004. doi:10.1016/j.jmmm.2003.12.819.

[73] O. Heczko, A. Sozinov, and K. Ullakko. Giant field-induced reversible strain in magnetic shape memory NiMnGa alloy. *IEEE Transactions on Magnetics*, 36(5): 3266–3268, 2000. doi:10.1109/20.908764.

[74] O. Heczko, A. Sozinov, and K. Ullakko. Giant field-induced reverseble linear strain in magnetic shape memory NiMnGa at room temperature. In *2000 IEEE International Magnetics Conference (INTERMAG)*, page 617, 2000.

doi:10.1109/INTMAG.2000.872392.

[75] O. Heczko, N. Lanska, O. Soderberg, and K. Ullakko. Temperature variation of structure and magnetic properties of Ni–Mn–Ga magnetic shape memory alloys. *Journal of Magnetism and Magnetic Materials*, 242–245(2):1446–1449, 2002. doi:10.1016/S0304-8853(01)01087-3.

[76] O. Heczko, L. Straka, and K. Ullakko. Relation between structure, magnetization process and magnetic shape memory effect of various martensites occurring in Ni–Mn–Ga alloys. *Journal de Physique IV*, 112:959–962, 2003. doi:10.1051/jp4:20031040.

[77] C. P. Henry. *Dynamic actuation properties of Ni–Mn–Ga ferromagnetic shape memory alloys*. Ph.D. dissertation, Massachusetts Institute of Technology, May 2002.

[78] C. P. Henry, J. Feuchtwanger, D. Bono, M. Marioni, P. G. Tello, M. Richard, S. M. Allen, and R. C. O'Handley. AC performance and modeling of ferromagnetic shape memory actuators. In *Proceedings Volume 4333, Smart Structures and Materials 2001: Active Materials: Behavior and Mechanics*, 2001. doi:10.1117/12.432751.

[79] C. P. Henry, D. Bono, J. Feuchtwanger, S. M. Allen, and R. C. O'Handley. AC field-induced actuation of single crystal Ni–Mn–Ga. *Journal of Applied Physics*, 91:7810–7811, 2002. doi:10.1063/1.1449441.

[80] C. P. Henry, P. G. Tello, J. Bono, D. Hong, R. Wagner, J. Dai, and R. C. Allen, S. M. O'Handley. Frequency response of single-crystal Ni–Mn–Ga FSMAs. In *Proceedings Volume 5053, Smart Structures and Materials 2003: Active Materials: Behavior and Mechanics*, 2003. doi:10.1117/12.484343.

[81] F. E. Hildebrand. *Variational Multifield Modeling of the Formation and Evolution of Laminate Microstructure*. PhD thesis, University of Stuttgart, 2013.

[82] L. Hirsinger and C. Lexcellent. Internal variable model for magneto-mechanical behaviour of ferromagnetic shape memory alloys Ni–Mn–Ga. *Journal de Physique IV*, 112:977–980, 2003. doi:10.1051/jp4:20031044.

[83] L. Hirsinger, N. Creton, and C. Lexcellent. Stress-induced phase transformations in Ni–Mn–Ga alloys: experiments and modelling. *Materials Science and Engineering A*, 378(1–2):365–369, 2004. doi:10.1016/j.msea.2003.12.053.

[84] L. Hirsinger, N. Creton, and C. Lexcellent. From crystallographic properties to macroscopic detwinning strain and magnetisation of Ni–Mn–Ga magnetic shape memory alloys. *Journal de Physique IV*, 115:111–120, 2004. doi:10.1051/jp4:2004115014.

[85] A. Hubert and R. Schäfer. *Magnetic Domains*. Springer-Verlag, New York, 2001.

[86] T. J. R. Hughes. *The Finite Element Method*. Dover, 2000.

[87] R. D. James and D. Kinderlehrer. Frustration in ferromagnetic materials. *Continuum Mechanics and Thermodynamics*, 2:215–239, 1990. doi:10.1007/BF01129598.

[88] R. D. James and D. Kinderlehrer. Theory of magnetostriction with applications to $\mathrm{Tb}_x\mathrm{Dy}_{1-x}\mathrm{Fe}_2$. *Philosophical Magazine B*, 68(2):237–274, 1993. doi:10.1080/01418639308226405.

[89] R. D. James and M. Wuttig. Magnetostriction of martensite. *Philosophical Magazine A*, 77(5):1273–1299, 1998. doi:10.1080/01418619808214252.

[90] R. D. James, R. Tickle, and M. Wuttig. Large field-induced strains in ferromagnetic shape memory materials. *Materials Science and Engineering: A*, 273–275: 320–325, 1999. doi:10.1016/S0921-5093(99)00364-0.

[91] S. Jeong, K. Inoue, S. Inoue, K. Koterazawa, M. Taya, and K. Inoue. Effect of magnetic field on martensite transformation in a polycrystalline $\mathrm{Ni_2MnGa}$. *Materials and Engineering A*, 359(1–2):253–260, 2003. doi:10.1016/S0921-5093(03)00359-9.

[92] D. Jiles. *Introduction to Magnetism and Magnetic Materials*. Chapman and Hall, London, 1991.

[93] Y. M. Jin. Domain microstructure evolution in magnetic shape memory alloys: phase-field model and simulation. *Acta Materialia*, 57(8):2488–2495, 2009. doi:10.1016/j.actamat.2009.02.003.

[94] P. Junker and K. Hackl. Finite element simulations of poly-crystalline shape memory alloys based on a micromechanical model. *Computational Mechanics*, 47(5): 505–517, 2011. doi:10.1007/s00466-010-0555-4.

[95] T. Kakeshita, T. Takeuchi, T. Fukuda, T. Saburi, R. Oshima, S. Muto, and K. Kishio. Magnetic field-induced martensitic transformation and giant magnetostriction in Fe–Ni–Co–Ti and ordered $\mathrm{Fe_3Pt}$ shape memory alloys. *Material Transactions, JIM*, 41(8):882–887, 2000. doi:10.2320/matertrans1989.41.882.

[96] T. Kakeshita, T. Takeuchi, T. Fukuda, M. Tsujiguchi, T. Saburi, R. Oshima, and S. Muto. Giant magnetostriction in an ordered $\mathrm{Fe_3Pt}$ single crystal exhibiting a martensitic transformation. *Applied Physics Letters*, 77(10):1502–1504, 2000. doi:10.1063/1.1290694.

[97] S. V. Kankanala and N. Triantafyllidis. On finitely strained magnetorheological elastomers. *Journal of Mechanics and Physics of Solids*, 52:2869–2908, 2004. doi:10.1016/j.jmps.2004.04.007.

[98] H. E. Karaca, I. Karaman, D. C. Lagoudas, H. J. Maier, and Y. I. Chumlyakov. Recoverable stress-induced martensitic transformation in a ferromagnetic CoNiAl alloy. *Scripta Materialia*, 49(9):831–836, 2003. doi:10.1016/S1359-6462(03)00470-6.

[99] H. E. Karaca, I. Karaman, B. Basaran, Y. I. Chumlyakov, and H. J. Maier. Magnetic field and stress induced martensite reorientation in NiMnGa ferromag-

netic shape memory alloy single crystals. *Acta Materialia*, 54(1):233–245, 2006. doi:10.1016/j.actamat.2005.09.004.

[100] I. Karaman, H. E. Karaca, B. Basaran, D. C. Lagoudas, Y. I. Chumlyakov, and H. J. Maier. Stress-assisted reversible magnetic field-induced phase transformation in $Ni_2MnGa$ magnetic shape memory alloys. *Scripta Materialia*, 55(4):403–406, 2006. doi:10.1016/j.scriptamat.2006.03.061.

[101] I. Karaman, B. Basaran, H. E. Karaca, A. I. Karsilayan, and Y. I. Chumlyakov. Energy harvesting using martensite variant reorientation mechanism in a NiMnGa magnetic shape memory alloy. *Applied Physics Letters*, 90(17):172505–1–3, 2007. doi:10.1063/1.2721143.

[102] R. A. Kellogg, A. B. Flatau, A. E. Clark, M. Wun-Fogle, and T. A. Lograsso. Temperature and stress dependencies of the magnetic and magnetostrictive properties of $Fe_{0.81}Ga_{0.19}$. *Journal of Applied Physics*, 91(10):7821–7823, 2002. doi:10.1063/1.1452216.

[103] F. Khelfaoui, M. Kohl, J. Buschbeck, O. Heczko, S. Fähler, and L. Schultz. A fabrication technology for epitaxial Ni-Mn-Ga microactuators. *The European Physical Journal Special Topics*, 158(1):167–172, 2008. doi:10.1140/epjst/e2008-00671-5.

[104] J. Kiang and L. Tong. Modelling of magneto-mechanical behaviour of Ni–Mn–Ga single crystals. *Journal of Magnetism and Magnetic Materials*, 292:394–412, 2005. doi:10.1016/j.jmmm.2004.11.481.

[105] J. Kiang and L. Tong. Three-dimensional constitutive equations for Ni–Mn–Ga single crystals. *Journal of Magnetism and Magnetic Materials*, 313(1):214–229, 2007. doi:10.1016/j.jmmm.2007.01.016.

[106] B. Kiefer. *A Phenomenological Constitutive Model for Magnetic Shape Memory Alloys*. Ph.D. dissertation, Department of Aerospace Engineering, Texas A&M University, College Station, TX, December 2006.

[107] B. Kiefer and D. C. Lagoudas. Phenomenological modeling of ferromagnetic shape memory alloys. *Proceedings of SPIE: Smart Structures and Materials*, 5387:164–176, 2004. doi:10.1117/12.540081.

[108] B. Kiefer and D. C. Lagoudas. Magnetic field-induced martensitic variant reorientation in magnetic shape memory alloys. *Philosophical Magazine*, 85(33–35): 4289–4329, 2005. doi:10.1080/14786430500363858.

[109] B. Kiefer and D. C. Lagoudas. Application of a magnetic SMA constitutive model in the analysis of magnetomechanical boundary value problems. In *Proceedings of SPIE 6170, Smart Structures and Materials 2006: Active Materials: Behavior and Mechanics, San Diego*, 2006. doi:10.1117/12.658560.

[110] B. Kiefer and D. C. Lagoudas. Modeling the coupled strain and magnetization response of magnetic shape memory alloys under magnetomechanical load-

ing. *Journal of Intelligent Material Systems and Structures*, 20(2):143–170, 2009. doi:10.1177/1045389X07086688.

[111] B. Kiefer, H. E. Karaca, D. C. Lagoudas, and I. Karaman. Characterization and modeling of the magnetic field-induced strain and work output in $Ni_2MnGa$ shape memory alloys. *Journal of Magnetism and Magnetic Materials*, 312(1):164–175, 2007. doi:10.1016/j.jmmm.2006.09.035.

[112] B. Kiefer, K. Buckmann, and T. Bartel. Numerical energy relaxation to model microstructure evolution in functional magnetic materials. *GAMM-Mitteilungen*, 38(1):171–196, 2015. doi:10.1002/gamm.201510009.

[113] B. Kiefer, T. Waffenschmidt, R. Sprave, and A. Menzel. A gradient-enhanced damage model coupled to plasticity—multi-surface formulation and algorithmic concepts. *International Journal of Damage Mechanics*, 27(2):253–295, 2018. doi:10.1177/1056789516676306.

[114] B. Kiefer, T. Bartel, and K. Buckmann. *A variational framework for the modeling of phase transforming solids using energy relaxation methods — application to conventional and magnetic SMA*. Springer, submitted for publication (2016).

[115] C. Kittel. Physical theory of ferromagnetic domains. *Reviews of Modern Physics*, 21(4):541–583, 1949. doi:10.1103/RevModPhys.21.541.

[116] C. Kittel. *Introduction to Solid State Physics*. John Wiley & Sons, 1996.

[117] M. Kohl, D. Brugger, M. Ohtsuka, and T. Takagi. A novel actuation mechanism on the basis of ferromagnetic SMA thin films. *Sensors and Actuators A*, 114(2–3): 445–450, 2004. doi:10.1016/j.sna.2003.11.006.

[118] M. Kohl, D. Brugger, M. Ohtsuka, and B. Krevet. A ferromagnetic shape memory actuator designed for large 2d optical scanning. *Sensors and Actuators A*, 135(1): 92–98, 2007. doi:10.1016/j.sna.2006.08.014.

[119] M. Kohl, S. Y. Reddy, F. Khelfaoui, B. Krevet, A. Backen, S. Fähler, T. Eichhorn, G. Jakob, and A. Mecklenburg. Recent progress in FSMA microactuator developments. *Materials Science Forum*, 635:145–154, 2010. doi:10.4028/www.scientific.net/MSF.635.145.

[120] M. Kohl, R. Yin, V. Pinneker, Y. Ezer, and A. Sozinov. A miniature energy harvesting device using martensite variant reorientation. *Materials Science Forum*, 738–739:411–415, 2013. doi:10.4028/www.scientific.net/MSF.738-739.411.

[121] M. Kök, Z. D. Yakinci, A. Aydogdu, and Y. Aydogdu. Thermal and magnetic properties of $Ni_{51}Mn_{28.5}Ga_{19.5}B$ magnetic-shape-memory alloy. *Journal of Thermal Analysis and Calorimetry*, 115:555–559, 2014. doi:10.1007/s10973-013-3365-z.

[122] N. C. Koon, A. I. Schimdler, and F. L. Carter. Giant magnetostriction in cubic rare earth-iron compounds of the type $RFe_2$. *Physics Letters A*, 37(5):413–414, 1971. doi:10.1016/0375-9601(71)90610-4.

[123] B. Krevet, M. Kohl, P. Morrison, and S. Seelecke. Magnetization- and strain-dependent free energy model for FEM simulation of magnetic shape memory alloys. *The European Physical Journal Special Topics*, 158(1):205–211, 2008. doi:10.1140/epjst/e2008-00677-y.

[124] D. C. Lagoudas, editor. *Shape Memory Alloys: Modeling and Engineering Applications*. Springer-Verlag, New York, 2008.

[125] D. C. Lagoudas, B. Kiefer, and A. J. Broederdorf. Accurate interpretation of magnetic shape memory alloy experiments utilizing coupled magnetostatic analysis. In *Proceedings of ASME, International Mechanical Engineering Congress and Exposition 2006*, volume IMECE2006-15296, pages 311–321, 2006. doi:10.1115/IMECE2006-15296.

[126] Y.-W. Lai. *Magnetic microstructure and actuation dynamics of NiMnGa magnetic shape memory materials*. Ph.D. dissertation, Technische Universität Dresden, January 2009.

[127] L. D. Landau and E. M. Lifshitz. On the theory of the dispersion of magnetic permeability in ferromagnetic bodies. *Physikalische Zeitschrift der Sowjetunion*, 8:153–169, 1935. doi:10.1016/B978-0-08-036364-6.50008-9.

[128] A. N. Lavrov, S. Komiya, and Y. Ando. Magnetic shape-memory effects in a crystal. *Nature*, 418:385–386, 2002. doi:10.1038/418385a.

[129] L. J. Li, J. Y. Li, Y. C. Shu, H. Z. Chen, and J. H. Yen. Magnetoelastic domains and magnetic field-induced strains in ferromagnetic shape memory alloys by phase-field simulation. *Applied Physics Letters*, 92:172504–1–3, 2008. doi:10.1063/1.2918127.

[130] L. J. Li, C. H. Lei, Y. C. Shu, and J. Y. Li. Phase-field simulation of magnetoelastic couplings in ferromagnetic shape memory alloys. *Acta Materialia*, 59(7):2648–2655, 2011. doi:10.1016/j.actamat.2011.01.001.

[131] Y. Li, J. Chengbao, T. Liang, Y. Ma, and H. Xu. Martensitic transformation and magnetization of ni–fe–ga ferromagnetic shape memory alloys. *Scripta Materialia*, 48(9):1255–1258, 2003. doi:10.1016/S1359-6462(03)00048-4.

[132] Y. Liang, Y. Sutou, T. Wada, C.-C. Lee, M. Taya, and T. Mori. Magnetic field-induced reversible actuation using ferromagnetic shape memory alloys. *Scripta Materialia*, 48(10):1415–1419, 2003. doi:10.1016/S1359-6462(03)00110-6.

[133] H. H. Liebermann and C. D. Graham, Jr. Plastic and magnetoplastic deformation of dy single crystals. *Acta Metallurgica*, 25(7):715–720, 1977. doi:10.1016/0001-6160(77)90086-4.

[134] A. A. Likhachev and K. Ullakko. Magnetic-field-controlled twin boundaries motion and giant magneto-mechanical effects in Ni–Mn–Ga shape memory alloy. *Physics Letters A*, 275(1–2):142–151, 2000. doi:10.1016/S0375-9601(00)00561-2.

[135] A. A. Likhachev and K. Ullakko. Quantitative model of large magnetostrain effect in ferromagnetic shapell memory alloys. *The European Physical Journal B*, 14(2): 263–267, 2000. doi:10.1007/s100510050128.

[136] A. A. Likhachev, A. Sozinov, and K. Ullakko. Different modeling concepts of magnetic shape memory and their comparison with some experimental results obtained in Ni–Mn–Ga. *Materials Science and Engineering A*, 378(1–2):513–518, 2004. doi:10.1016/j.msea.2003.10.353.

[137] D. G. Luenberger. *Linear and Nonlinear Programming*. Addison-Wesley, Reading, MA, 2nd edition, 1984.

[138] M. A. Marioni, R. C. O'Handley, and S. M. Allen. Analytical model for field-induced strain in ferromagnetic shape-memory alloy polycrystals. *Journal of Applied Physics*, 91(10):7807–7809, 2002. doi:10.1063/1.1453935.

[139] M. A. Marioni, R. C. O'Handley, and S. M. Allen. Pulsed magnetic field-induced actuation of Ni–Mn–Ga single crystals. *Applied Physics Letters*, 83:3966–3968, 2003. doi:10.1063/1.1626021.

[140] V. V. Martynov and V. V. Kokorin. The crystal structure of thermally- and stress-induced martensites in $Ni_2MnGa$ single crystals. *Journal de Physique III*, 2(5): 739–749, 1992. doi:10.1051/jp3:1992155.

[141] C. Mennerich. *Phase-field modeling of multi-domain evolution in ferromagnetic shape memory alloys and of polycrystalline thin film growth*. PhD thesis, Karlsruher Institut für Technologie (KIT), 2013.

[142] C. Mennerich, F. Wendler, M. Jainta, and B. Nestler. A phase-field model for the magnetic shape memory effect. *Archives of Mechanics*, 63(5–6):549–571, 2011.

[143] C. Mennerich, F. Wendler, M. Jainta, and B. Nestler. Rearrangement of martensitic variants in $Ni_2MnGa$ studied with the phase-field method. *The European Physical Journal B*, 86(4):171: 1–9, 2013. doi:10.1140/epjb/e2013-30941-6.

[144] T. Merzouki, A. Duval, and T. B. Zineb. Finite element analysis of a shape memory alloy actuator for a micropump. *Simulation Modelling Practice and Theory*, 27: 112–126, 2012. doi:10.1016/j.simpat.2012.05.006.

[145] C. Miehe. Strain-driven homogenization of inelastic microstructures and composites based on an incremental variational formulation. *International Journal for Numerical Methods in Engineering*, 55(11):1285–1322, 2002. doi:10.1002/nme.515.

[146] C. Miehe and G. Ethiraj. A geometrically consistent incremental variational formulation for phase field models in micromagnetics. *Computer Methods in Applied Mechanics and Engineering*, 245–246:331–347, 2012. doi:10.1016/j.cma.2012.03.021.

[147] C. Miehe, B. Kiefer, and D. Rosato. An incremental variational formulation of dissipative magnetostriction at the macroscopic continuum level. *International Journal of Solids and Structures*, 48(13):1846–1866, 2011.

doi:10.1016/j.ijsolstr.2011.02.011.

[148] C. Miehe, D. Rosato, and B. Kiefer. Variational principles in dissipative electro-magneto-mechanics: A framework for the macro-modeling of functional materials. *International Journal for Numerical Methods in Engineering*, 86(10):1225–1276, 2011. doi:10.1002/nme.3127.

[149] M. B. Moffet, A. E. Clark, M. Wun-Fogle, J. Linberg, J. P. Teter, and E. A. McLaughlin. Characterization of Terfenol-d for magnetostrictive transducers. *Journal of the Acoustical Society of America*, 89(3):1448–1455, 1991. doi:10.1121/1.400678.

[150] H. Morito, A. Fujita, K. Fukamichi, R. Kainuma, K. Ishida, and K. Oikawa. Magnetocrystalline anisotropy in single-crystal Co–Ni–Al ferromagnetic shape-memory alloy. *Applied Physics Letters*, 81(9):1657–1659, 2002. doi:10.1063/1.1503851.

[151] H. Morito, A. Fujita, K. Oikawa, K. Ishida, K. Fukamichi, and R. Kainuma. Stress-assisted magnetic-field-induced strain in Ni–Fe–Ga–Co ferromagnetic shape memory alloys. *Applied Physics Letters*, 90(6):062505, 2007. doi:10.1063/1.2450667.

[152] H. Morito, K. Oikawa, A. Fujita, K. Fukamichi, R. Kainuma, and K. Ishida. Stress-assisted large magnetic-field-induced strain in single-variant co–ni–ga ferromagnetic shape memory alloy. *Journal of Physics: Condensed Matter*, 21(25): 256002, 2009. doi:10.1088/0953-8984/21/25/256002.

[153] H. Morito, K. Oikawa, A. Fujita, K. Fukamichi, R. Kainuma, and K. Ishida. Large magnetic-field-induced strain in co–ni–al single-variant ferromagnetic shape memory alloy. *Scripta Materialia*, 63(4):379–382, 2010. doi:10.1016/j.scriptamat.2010.04.026.

[154] C. B. Morrey. Quasi-convexity and the lower semicontinuity of multiple integrals. *Pacific Journal of Mathematics*, 2(1):25–53, 1952. doi:10.2140/pjm.1952.2-1.

[155] R. Moskowitz and E. Della Torre. Theoretical aspects of demagnetization tensors. *IEEE Transactions on Magnetics*, 2(4):739–744, 1966. doi:10.1109/TMAG.1966.1065973.

[156] J. Mosler, O. Shchyglo, and H. Montazer Hojjat. A novel homogenization method for phase field approaches based on partial rank-one relaxation. *Journal of the Mechanics and Physics of Solids*, 68:251–266, 2014. doi:10.1016/j.jmps.2014.04.002.

[157] P. Müllner, V. A. Chernenko, M. Wollgarten, and G. Kostorz. Large cyclic deformation of a Ni-Mn-Ga shape memory alloy induced by magnetic fields. *Journal of Applied Physics*, 92(11):6708–6713, 2002. doi:10.1063/1.1513875.

[158] P. Müllner, V. A. Chernenko, and G. Kostorz. A microscopic approach to the magnetic-field-induced deformation of martensite (magnetoplasticity). *Journal of Magnetism and Magnetic Materials*, 267(3):325–334, 2003. doi:10.1016/S0304-8853(03)00400-1.

[159] P. Müllner, V. A. Chernenko, and G. Kostorz. Stress-induced twin rearrangement resulting in change of magnetization in a Ni–Mn–Ga ferromagnetic martensite. *Scripta Materialia*, 49(2):129–133, 2003. doi:10.1016/S1359-6462(03)00219-7.

[160] P. Müllner, V. A. Chernenko, and G. Kostorz. Large cyclic magnetic-field-induced deformation in orthorhombic (14M) Ni–Mn–Ga martensite. *Journal of Applied Physics*, 95(3):1531–1536, 2004. doi:10.1063/1.1639144.

[161] S. J. Murray. *Magneto-mechanical properties and applications of Ni–Mn–Ga ferromagnetic shape memory alloy.* Ph.D. dissertation, Massachusetts Institute of Technology, February 2000.

[162] S. J. Murray, M. Farinelli, C. Kantner, J. K. Huang, S. M. Allen, and R. C. O'Handley. Field-induced strain under load in Ni–Mn–Ga magnetic shape memory materials. *Journal of Applied Physics*, 83(11):7297–7299, 1998. doi:10.1063/1.367758.

[163] S. J. Murray, R. Hayashi, M. A. Marioni, S. M. Allen, and R. C. O'Handley. Magnetic and mechanical properties of fenicoti and nimnga magnetic shape memory alloys. *Proceedings of SPIE*, 3675:204–211, 1999. doi:10.1117/12.352794.

[164] S. J. Murray, M. Marioni, S. M. Allen, R. C. O'Handley, and T. A. Lograsso. 6 % magnetic-field-induced strain by twin-boundary motion in ferromagnetic Ni–Mn–Ga. *Applied Physics Letters*, 77(6):886–888, 2000. doi:10.1063/1.1306635.

[165] S. J. Murray, M. A. Marioni, A. M. Kukla, J. Robinson, R. C. O'Handley, and S. M. Allen. Large field induced strain in single crystalline Ni–Mn–Ga ferromagnetic shape memory alloy. *Journal of Applied Physics*, 87(9):5774–5776, 2000. doi:10.1063/1.372518.

[166] S. J. Murray, R. C. O'Handley, and S. M. Allen. Model for discontinuous actuation of ferromagnetic shape memory alloy under stress. *Journal of Applied Physics*, 89 (2):1295–1301, 2001. doi:10.1063/1.1285867.

[167] H. P. Myers. *Introductory Solid State Physics.* CRC Press, 1997.

[168] M. L. Néel. Propriétés magnétiques des ferrites ; ferrimagnétisme et antiferromagnétisme. *Annales de Physique*, 12(3):137–198, 1948. doi:10.1051/anphys/194812030137.

[169] R. C. O'Handley. Model for strain and magnetization in magnetic shape-memory alloys. *Journal of Applied Physics*, 83(6):3263–3270, 1998. doi:10.1063/1.367094.

[170] R. C. O'Handley. *Modern Magnetic Materials.* John Wiley & Sons, New York, 2000.

[171] R. C. O'Handley and S. M. Allen. *Shape-Memory Alloys, Magnetically Activated Ferromagnetic Shape-Memory Materials. In Encyclopedia of Smart Materials.* New York: Wiley, 2002. doi:10.1002/0471216275.esm072.

[172] R. C. O'Handley, S. M. Allen, D. I. Paul, C. P. Henry, M. Marioni, D. Bono, C. Jenkins, A. Banful, and R. Wager. Magnetic field-induced strain in single crystal Ni–Mn–Ga. *Proceedings of SPIE*, 5053:200–206, 2003. doi:10.1117/12.498549.

[173] R. C. O'Handley, D. I. Paul, S. M. Allen, M. Richard, J. Feuchtwanger, B. Peterson, R. Techapiesancharoenkij, M. Barandiaran, and L. P. Model for temperature dependence of field-induced strain in ferromagnetic shape memory alloys. *Materials Science and Engineering: A*, 438–440:445–449, 2006. doi:10.1016/j.msea.2006.02.197.

[174] K. Oikawa, L. Wulff, T. Iijima, F. Gejima, and K. Ishida. Promising ferromagnetic ni–co–al shape memory alloy system. *Applied Physics Letters*, 79:3290–3292, 2001. doi:10.1063/1.1418259.

[175] K. Oikawa, T. Ota, T. Ohmori, Y. Tanaka, H. Morito, A. Fujita, R. Kainuma, K. Fukamichi, and K. Ishida. Magnetic and martensitic phase transitions in ferromagnetic ni–ga–fe shape memory alloys. *Applied Physics Letters*, 81:5201–5203, 2002. doi:10.1063/1.1532105.

[176] A. Ölanger. The crystal structure of aucd. *Zeitschrift für Kristallographie - Crystalline Materials*, 83(1–6):145–148, 1932. doi:10.1524/zkri.1932.83.1.145.

[177] M. Ortiz and E. Repetto. Nonconvex energy minimization and dislocation structures in ductile single crystals. *Journal of the Mechanics and Physics of Solids*, 47:397–462, 1999. doi:10.1016/S0022-5096(97)00096-3.

[178] M. Ortiz and L. Stainier. The variational formulation of viscoplastic constitutive updates. *Computer Methods in Applied Mechanics and Engineering*, 171:419–444, 1999. doi:10.1016/S0045-7825(98)00219-9.

[179] K. Otsuka and C. M. Wayman, editors. *Shape Memory Materials*. Cambridge University Press, 1998.

[180] L. P., M. Sasmaz, E. Cesari, J. M. Barandiarán, J. Gutiérrez, and V. A. Chernenko. Martensitic transformation and magnetic field induced effects in $Ni_{42}Co_8Mn_{39}Sn_{11}$ metamagnetic shape memory alloy. *Acta Materialia*, 109:170–176, 2016. doi:10.1016/j.actamat.2016.02.046.

[181] Q. Pan and R. D. James. Micromagnetic study of $Ni_2MnGa$ under applied field (invited). *Journal of Applied Physics*, 87(9):4702–4706, 2000. doi:10.1063/1.373134.

[182] M. Pasquale. Mechanical sensors and actuators. *Sensors and Actuators A*, 106 (1–3):142–148, 2003. doi:10.1016/S0924-4247(03)00153-5.

[183] A. Peng, Y. J. He, and Z. Moumni. A phase-field model on the hysteretic magneto-mechanical behaviors of ferromagnetic shape memory alloy. *Acta Materialia*, 88: 13–24, 2015. doi:10.1016/j.actamat.2015.01.044.

[184] S. Piratla. Fully-coupled characterization of thermo-electro-magneto-mechanical materials. Master's thesis, The Ohio State University, 2009.

[185] J. Pons, V. A. Chernenko, E. Cesari, and V. A. L'vov. Stress-strain-temperature behaviour for martensitic transformation in Ni–Mn–Ga single crystal compressed along ⟨001⟩ and ⟨110⟩ axes. *Journal de Physique IV*, 112:939–942, 2003. doi:10.1051/jp4:20031035.

[186] T. Sakamoto, T. Fukuda, T. Kakeshita, T. Takeuchi, and K. Kishio. Magnetic field-induced strain in iron-based ferromagnetic shape memory alloys. *Journal of Applied Physics*, 93(10):8647–8649, 2003. doi:10.1063/1.1540132.

[187] E. K. Salje. *Phase Transitions in Ferroelastic and Co-elastic Crystals.* Cambridge University Press, 1993.

[188] E. Schlömann. A sum rule concerning the inhomogeneous demagnetizing field in nonellipsoidal samples. *Journal of Applied Physics*, 33(9):2825–2826, 1962. doi:10.1063/1.1702557.

[189] M. Schmidt-Baldassari. Numerical concepts for rate-independent single crystal plasticity. *Computer Methods in Applied Mechanics and Engineering*, 192:1261–1280, 2003. doi:10.1016/S0045-7825(02)00563-7.

[190] H. Sehitoglu, R. Anderson, I. Karaman, K. Gall, and Y. Chumlyakov. Cyclic deformation behavior of single crystal NiTi. *Materials Science and Engineering: A*, 314:67–74, 2001. doi:10.1016/S0921-5093(00)01924-9.

[191] T. W. Shield. Magnetomechanical testing machine for ferromagnetic shape-memory alloys. *Review of Scientific Instruments*, 74(9):4077–4088, 2003. doi:10.1063/1.1599072.

[192] R. C. Smith. *Smart Material Systems: Model Development.* Society for Industrial and Applied Mathematics, Philadelphia, PA, 2005.

[193] O. Söderberg. *Novel Ni–Mn–Ga alloys and their magnetic shape memory behaviour.* PhD thesis, Helsinki University of Technology, 2004.

[194] O. Söderberg, A. Sozinov, and V. K. Lindroos. *Giant Magnetostrictive Materials. The Encyclopedia of Materials: Science and Technology.* Elsevier Science, 2004.

[195] A. Sozinov, A. A. Likhachev, N. Lanska, and K. Ullakko. Giant magnetic-field-induced strain in NiMnGa seven-layered martensitic phase. *Applied Physics Letters*, 80(10):1746–1748, 2002. doi:10.1063/1.1458075.

[196] A. Sozinov, A. A. Likhachev, and K. Ullakko. Crystal structures and magnetic anisotropy properties of Ni–Mn–Ga martensitic phases with giant magnetic-field-induced strain. *IEEE Transactions on Magnetics*, 38(5):2814–2816, 2002. doi:10.1109/TMAG.2002.803567.

[197] A. Sozinov, A. A. Likhachev, N. Lanska, O. Söderberg, K. Ullakko, and V. K. Lindroos. Effect of crystal structure on magnetic-field-induced strain in Ni–Mn–Ga. *Proceedings of SPIE*, 5053:586–594, 2003. doi:10.1117/12.484353.

[198] A. Sozinov, A. A. Likhachev, N. Lanska, O. Söderberg, K. Koho, K. Ullakko, and V. K. Lindroos. Stress-induced variant rearrangement in Ni–Mn–Ga single crystals with nonlayered tetragonal martensitic structure. *Journal de Physique IV France*, 115:121–128, 2004. doi:10.1051/jp4:2004115015.

[199] J. M. Stephan, E. Pagounis, M. Laufenberg, O. Paul, and P. Ruther. A novel concept for strain sensing based on the ferromagnetic shape memory alloy NiMnGa. *IEEE Sensors Journal*, 11(11):2683–2689, 2011. doi:10.1109/JSEN.2011.2157489.

[200] L. Straka. *Magnetic and Magneto-Mechanical Properties of Ni-Mn-Ga Magnetic Shape Memory Alloys*. PhD thesis, Helsinki University of Technology, 2007.

[201] L. Straka and O. Heczko. Superelastic response of Ni–Mn–Ga martensite in magnetic fields and a simple model. *IEEE Transactions on Magnetics*, 39(5):3402–3404, 2003. doi:10.1109/INTMAG.2003.1230416.

[202] L. Straka and O. Heczko. Reversible 6% strain of Ni–Mn–Ga martensite using opposing external stress in static and variable magnetic fields. *Journal of Magnetism and Magnetic Materials*, 290–291(2):829–831, 2005. doi:10.1016/j.jmmm.2004.11.375.

[203] L. Straka and O. Heczko. Magnetization changes in Ni–Mn–Ga magnetic shape memory single crystal during compressive stress reorientation. *Scripta Materialia*, 54(9):1549–1552, 2006. doi:10.1016/j.scriptamat.2006.01.028.

[204] L. Straka, O. Heczko, V. Novak, and N. Lanska. Study of austenite-martensite transformation in Ni–Mn–Ga magnetic shape memory alloy. *Journal de Physique IV*, 112:911–915, 2003. doi:10.1051/jp4:20031029.

[205] M. R. Sullivan and H. D. Chopra. Temperature- and field-dependent evolution of micromagnetic structure in ferromagnetic shape-memory alloys. *Physical Review B*, 70(9):094427–1–094427–8, 2004. doi:10.1103/PhysRevB.70.094427.

[206] I. Suorsa, J. Tellinen, E. Pagounis, I. Aaltio, and K. Ullakko. Applications of magnetic shape memory actuators. In *Proceedings of the 8th International Conference on New Actuators*, 2002.

[207] I. Suorsa, J. Tellinen, K. Ullakko, and E. Pagounis. Voltage generation induced by mechanical straining in magnetic shape memory materials. *Journal of Applied Physics*, 95(12):8054–8058, 2004. doi:10.1063/1.1711181.

[208] Y. Sutou, N. Kamiya, T. Omori, R. Kainuma, K. Ishida, and K. Oikawa. Stress-strain characteristics in ni–ga–fe ferromagnetic shape memory alloys. *Applied Physics Letters*, 84:1275–1277, 2004. doi:10.1063/1.1642277.

[209] R. Techapiesancharoenkij, J. Kostamo, S. M. Allen, and R. C. O'Handley. Frequency response of acoustic-assisted Ni–Mn–Ga ferromagnetic-shape-memory-alloy actuator. *Journal of Applied Physics*, 105:093923, 2009. doi:10.1063/1.3125307.

[210] J. Tellinen, I. Suorsa, A. Jääskeläinen, I. Aaltio, and K. Ullakko. Basic properties of magnetic shape memory actuators. *Proceedings of International Conference Actuator*, 8:566–569, 2002.

[211] R. Tickle. *Ferromagnetic shape memory materials.* Ph.D. dissertation, University of Minnesota, May 2000.

[212] R. Tickle and R. D. James. Magnetic and magnetomechanical properties of $Ni_2MnGa$. *Journal of Magnetism and Magnetic Materials*, 195(3):627–638, 1999. doi:10.1016/S0304-8853(99)00292-9.

[213] R. Tickle, R. D. James, T. Shield, M. Wuttig, and V. V. Kokorin. Ferromagnetic shape memory in the NiMnGa system. *IEEE Transactions on Magnetics*, 35(5): 4301–4310, 1999. doi:10.1109/20.799080.

[214] E. Trémolet de Lacheisserie. *Magnetostriction Theory and Applications of Magnetoelasticity.* CRC Press, Boca Raton, FL, 1993.

[215] K. Ullakko, J. K. Huang, C. Kantner, R. C. O'Handley, and V. V. Kokorin. Large magnetic-field-induced strains in $Ni_2MnGa$ single crystals. *Applied Physics Letters*, 69(13):1966–1968, 1996. doi:10.1063/1.117637.

[216] K. Ullakko, Y. Ezer, A. Sozinov, G. Kimmel, P. Yakovenko, and V. K. Lindroos. Magnetic-field-induced strains in polycrystalline Ni–Mn–Ga at room temperature. *Scripta Materialia*, 44(3):475–480, 2001. doi:10.1016/S1359-6462(00)00610-2.

[217] A. N. Vasil'ev, A. D. Bozhko, V. V. Khovailo, I. E. Dikshtein, V. G. Shavrov, V. D. Buchelnikov, M. Matsumoto, S. Suzuki, T. Takagi, and J. Tani. Structural and magnetic phase transitions in shape-memory alloys $Ni_{2+x}Mn_{1-x}Ga$. *Physical Review B*, 59(2):1113–1120, 1999. doi:10.1103/PhysRevB.59.1113.

[218] M. Šilhavý. *The Mechanics and Thermodynamics of Continuous Media.* Springer, Berlin, 1997.

[219] T. Wada, Y. Liang, H. Kato, T. Tagawa, M. Taya, and T. Mori. Structural change and straining in fe–pd polycrystals by magnetic field. *Materials Science and Engineering: A*, 361(1–2):75–82, 2003. doi:10.1016/S0921-5093(03)00444-1.

[220] J. Wang and P. Steinmann. A variational approach towards the modeling of magnetic field-induced strains in magnetic shape memory alloys. *Journal of the Mechanics and Physics of Solids*, 60(6):1179–1200, 2012. doi:10.1016/j.jmps.2012.02.003.

[221] J. Wang and P. Steinmann. Finite element simulation of the magneto-mechanical response of a magnetic shape memory alloy sample. *Philosophical Magazine*, 93 (20):2630–2653, 2013. doi:10.1080/14786435.2013.782443.

[222] J. Wang and P. Steinmann. On the modeling of equilibrium twin interfaces in a single-crystalline magnetic shape memory alloy sample. I: theoretical formulation. *Continuum Mechanics and Thermodynamics*, 26(4):563–592, 2014.

doi:10.1007/s00161-013-0319-4.

[223] J. Wang and P. Steinmann. On the modeling of equilibrium twin interfaces in a single-crystalline magnetic shape memory alloy sample. II: numerical algorithm. *Continuum Mechanics and Thermodynamics*, 28(3):669–698, 2016. doi:10.1007/s00161-014-0403-4.

[224] J. Wang and P. Steinmann. On the modeling of equilibrium twin interfaces in a single-crystalline magnetic shape-memory alloy sample—III: Magneto-mechanical behaviors. *Continuum Mechanics and Thermodynamics*, 28:885–813, 2016. doi:10.1007/s00161-015-0452-3.

[225] W. H. Wang, G. D. Liu, and G. H. Wu. Magnetically controlled high damping in ferromagnetic $Ni_{52}Mn_{24}Ga_{24}$ single crystal. *Applied Physics Letters*, 89(10): 101911, 2006. doi:10.1063/1.2345462.

[226] P. J. Webster, K. R. A. Ziebeck, S. L. Town, and M. S. Peak. Magnetic order and phase transformation in $Ni_2MnGa$. *Philosophical Magazine B*, 49(3):295–310, 1984. doi:10.1080/13642817408246515.

[227] P. Wriggers. *Nonlinear Finite Element Methods.* Springer, 2008.

[228] G. H. Wu, W. H. Wang, J. L. Chen, L. Ao, Z. H. Liu, and W. S. Zhan. Magnetic properties and shape memory of fe-doped $ni_{52}mn_{24}ga_{24}$ single crystals. *Applied Physics Letters*, 80(4):634–636, 2002. doi:10.1063/1.1447003.

[229] M. Wuttig, L. Liu, K. Tsuchyia, and R. D. James. Occurrence of ferromagnetic shape memory alloys (invited). *Journal of Applied Physics*, 87(9):4707–4711, 2000. doi:10.1063/1.373135.

[230] M. Wuttig, J. Li, and C. Cracinescu. A new ferromagnetic shape memory alloy system. *Scripta Materialia*, 44(10):2393–2397, 2001. doi:10.1016/S1359-6462(01)00939-3.

[231] T. Yamamoto, M. Taya, Y. Sutou, Y. Liang, T. Wada, and L. Sorensen. Magnetic field-induced reversible variant rearrangement in Fe–Pd single crystals. *Acta Materialia*, 52(17):5083–5091, 2004. doi:10.1016/j.actamat.2004.07.014.

[232] I. K. Zasimchuk, V. V. Kokorin, V. V. Martynov, A. V. Tkachenko, and V. A. Chernenko. Crystal structure of martensite in Heusler alloy $Ni_2MnGa$. *Physics of Metals and Metallography*, 69(6):104–108, 1990.

[233] M. Zeng, S. W. Or, and H. L. W. Chan. Ultrahigh anisotropic damping in ferromagnetic shape memory Ni–Mn–Ga single crystal. *Journal of Alloys and Compounds*, 493(1–2):565–568, 2010. doi:10.1016/j.jallcom.2009.12.156.

[234] J. X. Zhang and L. Q. Chen. Phase-field model for ferromagnetic shape-memory alloys. *Philosophical Magazine Letters*, 85(10):533–541, 2005. doi:10.1080/09500830500385527.

[235] H. Ziegler. *Some Extremum Principles in Irreversible Thermodynamics with Application to Continuum Mechanics*. North-Holland, 1963.

# Curriculum Vitae

## Personal Data

| | |
|---|---|
| Name | Karsten Buckmann |
| Date of Birth | September 16, 1985 |
| Place of Birth | Datteln, Germany |
| Nationality | German |

## Professional Occupation

| | |
|---|---|
| 09/2012 – 08/2018 | Scientific Assistant, Institute of Mechanics, TU Dortmund University |

## University Education

| | |
|---|---|
| 08/2012 | Academic Degree: Diploma (Dipl.-Ing.) |
| 10/2005 – 08/2012 | Studies of Mechanical Engineering, TU Dortmund University |
| 01/2011 – 04/2012 | Student Assistant, Institute of Mechanics, TU Dortmund University |
| 07/2010 – 11/2010 | Internship, Siemens Energy, Mülheim/Ruhr |
| 05/2008 – 12/2009 | Student Assistant, Institute of Mechanics, TU Dortmund University |

## School Education

| | |
|---|---|
| 08/1996 – 06/2005 | Secondary School, Städtisches Gymnasium Selm |

# Publication series of the Institute of Mechanics

## published to date:

| | |
|---|---|
| 2010/01 | Palnau, V.: Implementierung eines netzfreien Diskretisierungsverfahrens und seine Anwendung auf die Scherbandanalyse. ISBN 978-3-921823-51-4 |
| 2010/02 | Klusemann, B.: Application of homogenization methods and crystal plasticity to the modeling of heterogeneous materials of technological interest. ISBN 978-3-921823-53-8 |
| 2011/01 | Hortig, C.: Local and non-local thermomechanical modeling and finite-element simulation of high-speed cutting. ISBN 978-3-921823-54-5 |
| 2011/02 | Parvizian, F.: Modeling of microstructure evolution in aluminum alloys during hot extrusion. ISBN 978-3-921823-56-9 |
| 2011/03 | Noman, M.: Characterization and model identification for the simulation of the forming behavior of ferritic steels. ISBN: 978-3-921823-55-2 |
| 2011/04 | Kayser, T.: Characterization of microstructure in aluminum alloys based on electron backscatter diffraction. ISBN: 978-3-921823-57-6 |
| 2011/05 | Bargmann, S.: Computational modeling of material behavior on different scales based on continuum mechanics. ISBN: 978-3-921823-58-3 |
| 2013/01 | Waffenschmidt, T.: Modelling and simulation of adaptation and degradation in anisotropic biological tissues. ISBN: 978-3-921823-61-3 |
| 2015/01 | Ostwald, R.: Modelling and simulation of phase-transformations in elastoplastic polycrystals. ISBN: 978-3-921823-66-8 |
| 2016/01 | Subramanian, M.: Phenomenological modelling and simulation of ferroelectric ceramics. ISBN: 978-3-921823-74-3 |
| 2016/02 | Clausmeyer, T.: Evolution of plastic anisotropy in metals. ISBN 978-3-921823-76-7 |
| 2017/01 | Holtermann, R.: Computational multiscale modelling of grinding processes. ISBN 978-3-921823-86-6 |
| 2017/02 | Bartels, A.: Modelling of evolving microstructures at different scales. ISBN 978-3-921823-93-4 |

2017/03 Dusthakar Kumar Rao, D. K.: Computational modelling of single and polycrystalline ferroelectric materials. ISBN 978-3-921823-94-1

2019/01 Buckmann, K.: Microstructure evolution in functional magnetic materials. ISBN 978-3-947323-09-8